

## Energy Effectiveness and Operational Safety of Low-Powered Ocean-going Cargo Ship in Various (Heavy) Operating Conditions

Sui, C.

**Publication date**

2021

**Document Version**

Final published version

**Citation (APA)**

Sui, C. (2021). *Energy Effectiveness and Operational Safety of Low-Powered Ocean-going Cargo Ship in Various (Heavy) Operating Conditions*. [Dissertation (TU Delft), Delft University of Technology].

**Important note**

To cite this publication, please use the final published version (if applicable).  
Please check the document version above.

**Copyright**

Other than for strictly personal use, it is not permitted to download, forward or distribute the text or part of it, without the consent of the author(s) and/or copyright holder(s), unless the work is under an open content license such as Creative Commons.

**Takedown policy**

Please contact us and provide details if you believe this document breaches copyrights.  
We will remove access to the work immediately and investigate your claim.

# **Energy Effectiveness and Operational Safety of Low-Powered Ocean-going Cargo Ship in Various (Heavy) Operating Conditions**

**Congbiao SUI 随从标**



# **Energy Effectiveness and Operational Safety of Low-Powered Ocean-going Cargo Ship in Various (Heavy) Operating Conditions**

## **Dissertation**

for the purpose of obtaining the degree of doctor  
at Delft University of Technology,  
by the authority of the Rector Magnificus Prof.dr.ir. T.H.J.J. van der Hagen,  
chair of the Board for Doctorates  
to be defended publicly on  
Monday 12 July 2021 at 10:00 o'clock

by

**Congbiao SUI**

Master of Engineering in Power Engineering,  
Harbin Engineering University, China  
born in Fuyang, Anhui, China



This dissertation has been approved by the promotor.

Composition of the doctoral committee:

|                      |  |
|----------------------|--|
| Rector Magnificus,   | Chairperson                                |
| Prof.ir. J.J. Hopman | Delft University of Technology, promotor   |
| Dr.ir. P. de Vos     | Delft University of Technology, copromotor |

*Independent members:*

|                             |                                |
|-----------------------------|--------------------------------|
| Prof.dr.ir. B.J. Boersma    | Delft University of Technology |
| Prof.dr.ir. J. Westerweel   | Delft University of Technology |
| Prof.dr. Y. Li              | Harbin Engineering University  |
| Prof.dr.ing. B.O. el Moctar | University of Duisburg-Essen   |

*Other members:*

|               |                                |
|---------------|--------------------------------|
| Ir. K. Visser | Delft University of Technology |
|---------------|--------------------------------|

*Keywords:* ship propulsion system, hybrid propulsion, propulsion control, power take off/in, fuel consumption, emissions, energy conversion effectiveness, diesel engine, mean value first principle engine model, engine dynamic behaviour, low-powered ship, ship operational safety

*Printed by:* Ipskamp Printing

*Cover by:* Congbiao SUI

Copyright © 2021 by Congbiao SUI

All rights reserved. No part of this publication may be reproduced, stored in a retrieval system, or transmitted, in any form or by any means, electronic, mechanical, photocopying, recording or otherwise, without the prior written permission of the author.

ISBN 978-94-6421-410-9

An electronic copy of this dissertation is available at <https://repository.tudelft.nl/>

# Contents

|   |           |
|---|-----------|
| <b>Summary .....</b>  | <b>v</b>  |
| <b>1 Introduction .....</b>   | <b>1</b>  |
| 1.1 Background.....   | 1         |
| 1.1.1 Challenges of shipping industry .....   | 1         |
| 1.1.2 Weaknesses of EEDI (Energy Efficiency Design Index) .....   | 2         |
| 1.2 Research motivation .....   | 3         |
| 1.3 Research questions .....  | 4         |
| 1.4 Research approach.....  | 5         |
| 1.5 Research boundaries .....   | 10        |
| 1.6 Thesis outline.....   | 11        |
| 1.7 Contributions .....   | 13        |
| <b>2 Energy Effectiveness of Ocean-Going Cargo Ship under Various Operating Conditions .....</b>                              | <b>15</b> |
| 2.1 Introduction .....  | 15        |
| 2.2 The propulsion and electric power systems of the benchmark ship .....   | 18        |
| 2.3 Energy conversion effectiveness and fuel index.....   | 20        |
| 2.3.1 Energy conversion effectiveness .....   | 20        |
| 2.3.2 Fuel index .....  | 22        |
| 2.4 Propulsion system model description and philosophy .....  | 23        |
| 2.4.1 Diesel engine model .....   | 24        |
| 2.4.2 Ship resistance model .....   | 24        |
| 2.4.3 Propeller model.....  | 25        |
| 2.4.4 Wake factor, thrust deduction factor and relative rotative efficiency model .....                                       | 25        |
| 2.4.5 Mechanical transmission losses.....   | 25        |
| 2.5 Different ship propulsion control and electric power generation modes.....  | 26        |
| 2.5.1 Ship propulsion control modes .....   | 26        |
| 2.5.2 Electric power generating modes.....  | 28        |
| 2.6 Results and discussions .....   | 28        |
| 2.6.1 Fuel consumption and fuel index.....  | 28        |
| 2.6.2 Energy effectiveness and efficiencies.....  | 30        |
| 2.7 Summary and Conclusions .....   | 33        |
| <b>3 Fuel Consumption and Emissions of Ocean-Going Cargo Ship with Hybrid Propulsion and Different Fuels over Voyage.....</b> | <b>35</b> |
| 3.1 Introduction .....  | 35        |
| 3.2 Hybridisation of the Benchmark Chemical Tanker .....  | 38        |
| 3.3 Mean Value Indicators of Fuel Consumption and Emissions .....   | 39        |
| 3.4 Engine emissions model .....  | 40        |
| 3.5 Ship mission profile.....   | 40        |

|  |            |
|--|------------|
| 3.5.1 Transit in open sea .....  | 40         |
| 3.5.2 Manoeuvring in coastal and port areas .....  | 42         |
| 3.6 Results and discussions .....  | 43         |
| 3.6.1 Average Ship Transport Performance Over Transit Voyage in Open Sea.....  | 43         |
| 3.6.2 Average Ship Transport Performance Over Manoeuvring in Close-To-Port Areas   | 46         |
| 3.6.3 Fuel Consumption and Emissions of the Whole Voyage.....  | 48         |
| 3.7 Summary and Conclusions .....  | 48         |
| <b>4 Mean Value First Principle Modelling of Two-Stroke Marine Diesel Engine .....</b>                                   | <b>51</b>  |
| 4.1 Introduction .....   | 52         |
| 4.2 Concepts and definitions of the mean value first principle engine model.....   | 54         |
| 4.2.1 In-cylinder processes of two-stroke marine diesel engine.....  | 54         |
| 4.2.2 Volume and resistance elements in MVFPP engine model .....   | 56         |
| 4.2.3 Mass flows of in-cylinder process in MVFPP two-stroke engine model .....   | 57         |
| 4.3 Closed cylinder process model .....  | 59         |
| 4.4 Gas exchange process model.....  | 60         |
| 4.4.1 Blowdown model.....  | 60         |
| 4.4.2 Scavenging model.....  | 61         |
| 4.4.3 Expelling model.....   | 68         |
| 4.5 Engine model validation.....   | 69         |
| 4.6 Results and discussions .....  | 71         |
| 4.7 Summary and Conclusions .....  | 74         |
| <b>5 Integrated Ship Propulsion and Manoeuvring Model .....</b>  | <b>75</b>  |
| 5.1 Introduction .....   | 75         |
| 5.2 Coordinate system of 3DOF manoeuvring model.....   | 77         |
| 5.3 Equations of ship motions .....  | 77         |
| 5.4 Hydrodynamic forces and moments .....  | 78         |
| 5.4.1 Forces and moment on hull .....  | 79         |
| 5.4.2 Force by propeller.....  | 82         |
| 5.4.3 Forces and moment by rudder .....  | 83         |
| 5.4.4 Hydrodynamic mass and moment of inertia.....   | 85         |
| 5.4.5 Calibrating parameters.....  | 86         |
| 5.5 Model validation and verification.....   | 87         |
| 5.5.1 Propulsion validation .....  | 88         |
| 5.5.2 Turning circle validation and verification .....   | 88         |
| 5.5.3 Zigzag validation and verification .....   | 93         |
| 5.5.4 Inertia and crash stop validation and verification.....  | 98         |
| 5.5.5 Uncertainty and sensitivity analysis .....   | 104        |
| 5.6 Summary and Conclusions .....  | 108        |
| <b>6 Engine Behaviour of Low-Powered Ocean-Going Cargo Ship under Various Propulsion and Manoeuvring Operations.....</b> | <b>111</b> |
| 6.1 Introduction .....   | 111        |
| 6.2 Low-powered ocean-going chemical tanker.....   | 112        |
| 6.3 Engine static behaviour and operational limits.....  | 113        |
| 6.3.1 Engine mechanical loading.....   | 113        |
| 6.3.2 Engine thermal loading.....  | 114        |

|  |            |
|--|------------|
| 6.3.3 Compressor surge .....   | 116        |
| 6.4 Engine dynamic behaviour in different ship operations .....  | 117        |
| 6.4.1 Ship acceleration.....   | 117        |
| 6.4.2 Ship deceleration .....  | 120        |
| 6.4.3 Ship crash stop.....   | 122        |
| 6.4.4 Ship turning .....   | 125        |
| 6.5 Engine operational limits and ship thrust limit.....   | 127        |
| 6.6 Summary and Conclusions .....  | 129        |
| <b>7 Effects of Adverse Sea Conditions on Propulsion and Manoeuvring Performance of Low-Powered Ocean-Going Cargo Ship .....</b> | <b>131</b> |
| 7.1 Introduction .....   | 131        |
| 7.2 Definition of adverse sea conditions and safety criteria.....  | 134        |
| 7.3 Wind- and waves-induced steady forces and moments .....  | 135        |
| 7.3.1 Wind-induced steady forces and moment.....   | 136        |
| 7.3.2 Waves-induced steady forces and moments .....  | 137        |
| 7.4 Propeller wake fluctuation in waves.....   | 140        |
| 7.5 Verification of wind and waves model .....   | 141        |
| 7.6 Ship propulsion and manoeuvring performance in adverse sea .....   | 142        |
| 7.6.1 Ship sailing in head sea .....   | 142        |
| 7.6.2 Ship acceleration in head sea.....   | 146        |
| 7.6.3 Ship turning to head sea.....  | 150        |
| 7.7 Influence of operational measures .....  | 154        |
| 7.7.1 Propeller pitch.....   | 154        |
| 7.7.2 Power-take-in (PTI) .....  | 155        |
| 7.8 Summary and Conclusions .....  | 156        |
| <b>8 Suggestions on Amendments of IMO's EEDI.....</b>  | <b>159</b> |
| 8.1 Introduction .....   | 159        |
| 8.2 Recommended EEDI formula.....  | 160        |
| 8.3 Minimum propulsion power guidelines.....   | 163        |
| 8.4 Installing a larger engine on the benchmark ship .....   | 164        |
| 8.4.1 EEDI of the ship with larger engine .....  | 165        |
| 8.4.2 Ship fuel consumption and energy effectiveness with larger engine.....   | 167        |
| 8.4.3 Ship propulsion capability in adverse sea with larger engine.....  | 169        |
| 8.5 Summary and Conclusions .....  | 169        |
| <b>9 Conclusions and Recommendations .....</b>   | <b>171</b> |
| 9.1 Addressing the research questions .....  | 171        |
| 9.2 Recommendations for future research .....  | 174        |
| <b>A. Calibration and validation of ship propulsion system model.....</b>  | <b>177</b> |
| A.1 Correction of towing tank measurement data .....   | 177        |
| A.2 Calibration of component models to testbed and towing tank measurements.....   | 179        |
| A.2.1 Fuel consumption and emissions of diesel engines .....   | 179        |
| A.2.2 Ship resistance .....  | 183        |
| A.2.3 Propeller open water characteristics .....   | 184        |
| A.2.4 Wake factor, thrust deduction factor and relative rotative efficiency .....  | 185        |

|  |            |
|--|------------|
| A.3 Static matching and validation of the ship propulsion system model.....                  | 185        |
| <b>B. Selecting a Sea Margin for typical sailing condition .....</b>                         | <b>187</b> |
| <b>C. Corrections of Fuel Consumption and Emissions for Different Fuel Types .....</b>       | <b>189</b> |
| <b>D. Mission Profile in Open Sea.....</b>   | <b>191</b> |
| <b>E. Details of blowdown and scavenging models of two-stroke marine diesel engine .....</b> | <b>193</b> |
| E.1 Blowdown .....   | 193        |
| E.2 Two-stage scavenging .....   | 195        |
| E.2.1 Stage I: Two-zone scavenging model.....  | 195        |
| E.2.2 Stage II: Perfect mixing model.....  | 198        |
| <b>F. Engine components models .....</b>   | <b>199</b> |
| F.1 Turbocharger model.....  | 199        |
| F.1.1 Buchi balance.....   | 199        |
| F.1.2 Compressor and turbine characteristics .....   | 199        |
| F.1.3 Compressor surge index.....  | 200        |
| F.1.4 Turbocharger mechanical efficiency.....  | 200        |
| F.2 Air cooler model .....   | 201        |
| F.3 Auxiliary blower and non-return valve models .....                                       | 201        |
| F.4 Exhaust valve temperature model.....   | 202        |
| F.5 Engine mechanical and heat losses models .....   | 202        |
| <b>G. Correction of C4-55 Characteristics.....</b>   | <b>203</b> |
| G.1 Correction factors of the delivered power and shaft speed.....                           | 203        |
| G.2 Correction factors of C4-55 propeller characteristics.....                               | 204        |
| <b>References .....</b>  | <b>207</b> |
| <b>Acknowledgements.....</b>   | <b>217</b> |
| <b>Curriculum Vitae.....</b>   | <b>219</b> |

# Summary

Ocean shipping, which carries more than 80% of world trade by volume, remains the backbone of international merchandise trade. Due to the increasingly high fuel price, social concerns on the environmental impact and the mandatory and strict emission control regulations worldwide, the shipping industry is striving to reduce its fuel consumption and emissions. New ship designs need to achieve a small EEDI (Energy Efficiency Design Index) to meet the requirements of IMO (International Maritime Organization). However, the current EEDI is not able to accurately evaluate the real lifetime carbon emissions of the ship. Under the guidance of current EEDI regulation, the ship designers, owners and policymakers could be misled to adopt the configurations that are underperforming or even leading to an increase of CO<sub>2</sub> emissions in reality. A technically easy and effective solution to meet the EEDI requirement is to lower the installed engine power and thus the ship design speed. However, reducing the installed engine power could lead to an underpowered ship, which is believed to be vulnerable and unsafe as it could have insufficient power for propulsion and steering in adverse weather conditions.

There is an enormous variety in the assessment methodology of transport performance of ships, including IMO's EEDI. However, the effects of different technical and operational measures on the fuel consumption and emissions performance of typical cargo ships have rarely been investigated systematically with a proper performance assessment methodology. Due to the serious safety concerns on the underpowered ships when sailing in adverse sea conditions, many researches have been conducted to assess ship safety in different sea conditions, but previous researches have mainly focused on the ship manoeuvrability and seakeeping performance. The interactions between the engine, the propeller, the ship, and the waves, etc., in adverse sea conditions are very complicated and highly dynamic, and the ship safety in adverse weather conditions is highly related to the engine behaviour. However, researches providing detailed insights of the engine behaviour especially the dynamic behaviour when the ship is sailing and manoeuvring in adverse sea conditions are very limited. The research in this dissertation tries to fill the above-mentioned knowledge gaps. The main research question addressed in this dissertation is:

*What is the transport performance of ocean-going cargo ships with small EEDI when sailing in realistic operating conditions; are these ships safe when sailing in heavy operating conditions; and, how to improve both the transport performance and operational safety of ocean-going cargo ships by using the short-term applicable ship propulsion options?*

The ship transport performance investigated in this dissertation includes the energy conversion performance, fuel consumption performance and emissions performance. Based on the analysis of energy conversion, fuel consumption and exhaust emissions processes in the 'tank to wheel' power chain of the ship propulsion and electric generation systems, the ship transport performance has been defined and quantified by three indicators, i.e., energy

conversion effectiveness, fuel index, and emissions index. When taking the ship mission profiles into account, the mean energy conversion effectiveness, fuel index and emissions index, which are averaged over the whole voyage of the ship, are defined. An integrated ship propulsion and electric generating systems model of a benchmark chemical tanker is developed, calibrated and validated. Based on the simulation model and the defined energy conversion effectiveness, fuel index and emissions indices, the ship transport performance of the ocean-going cargo ship under various operating conditions is systematically and quantitatively investigated. In particular, the influences of the operational ship speed reduction, propulsion control, PTO (power-take-off) / PTI (power-take-in), and using LNG (liquefied natural gas) as the fuel as well as the combination of these measures on the ship transport performance over the whole voyage taking ship mission profiles into account have been systematically investigated.

The operational safety investigated in this dissertation includes both engine operational safety and ship operational safety. Based on the analysis of the engine and ship operational limits, the ship operational safety has been defined and quantified using the engine mechanical and thermal loading limits, engine speed limits, compressor surge limit and ship thrust limit. The ship 3DOF (degree-of-freedom) manoeuvring and motions (surge, sway and yaw) model and the wind and waves disturbances model have been integrated with the ship propulsion and electric generating systems model. Based on the integrated systems model and the defined engine and ship operational limits, the ship operational safety of the low-powered ocean-going cargo ship under various operating conditions has been systematically and quantitatively investigated. The engine dynamic behaviour during ship acceleration, deceleration, crash stop, and turning in normal sea condition have been investigated. The ship propulsion and manoeuvring performance when sailing in head sea and turning to head sea in adverse sea conditions (BF7 and BF8) have been investigated. The influences of propeller pitch and PTO/PTI on the ship thrust limit and engine behaviour have also been investigated.

To effectively reduce the fuel consumption and greenhouse gas emissions, the operational ship speed reduction and optimisation of the ship mission profiles over the voyage should still be the primary measures for the ocean-going cargo ships in short term future. Generating the electric power by the shaft generator (in PTO mode) rather than the auxiliary generators will further reduce the fuel consumption. Using LNG as the marine fuel helps to reduce the CO<sub>2</sub> emissions and especially pollutant emissions (such as NO<sub>x</sub>) over the whole voyage. Sailing the ship in PTI mode on LNG will reduce the local pollutant emissions in coastal and port areas significantly. However, the methane emissions from LNG engines as well as the life-cycle emissions of natural gas should be minimised as much as possible, as methane is actually a more potent greenhouse gas than CO<sub>2</sub>. The dynamic engine behaviour as well as the influence of PTO/PTI and propeller pitch should be taken into account when assessing the ship operational safety in adverse sea conditions. To protect the engine from mechanical and thermal overloading, compressor surge and over-speeding during dynamic ship operations and/or in high sea states, the engine and propeller should be carefully controlled. The shaft generator/motor can work as a motor (in PTI mode) when the ship needs more propulsion power especially in (heavy) adverse weather conditions. As a conclusion, in the short-term future, a

PTO/PTI system together with using LNG as the fuel, which forms a hybrid electric power generation system and a hybrid propulsion system, will help improve both the ship transport performance in normal sea conditions and the ship operational safety in (heavy) adverse sea conditions.

Last but not least, as a reflection of the research in this dissertation, suggestions on amendments of IMO's current EEDI has been provided. A proposal on the formula calculating the attained EEDI of ships in a more realistic way, in which a representative ship operating profile and multiple engine operating points are considered, has been made. The proposal for amending the current EEDI formula tries to make the EEDI calculation more realistic and representative when evaluating ship transport performance at the design stage. Moreover, it can also partly solve another weakness of the current EEDI with respect to the issues of underpowered ships, because the ship designer is able to install a larger engine by selecting a sufficiently large engine margin according to the proposal.



# Samenvatting

Zeevaart, dat naar volume meer dan 80% van de wereldhandel vervoert, blijft de ruggengraat van de internationale handel in goederen. Vanwege de steeds hogere brandstofprijzen, maatschappelijke zorgen over de milieu-impact en de verplichte en strikte emissiebeheersingsvoorschriften wereldwijd, streeft de scheepvaart ernaar om het brandstofverbruik en de uitstoot te verminderen. Nieuwe scheepsontwerpen moeten een kleine EEDI (Energy Efficiency Design Index) behalen om te voldoen aan de eisen van IMO (International Maritime Organization). Het huidige EEDI is echter niet in staat om de werkelijke CO<sub>2</sub>-uitstoot van het schip nauwkeurig te evalueren. Onder begeleiding van de huidige EEDI-regelgeving kunnen scheepsontwerpers, eigenaren en beleidsmakers worden misleid om configuraties over te nemen die ondermaats presteren of zelfs leiden tot een toename van de CO<sub>2</sub>-uitstoot in de praktijk. Een technisch eenvoudige en effectieve oplossing om aan de EEDI-eis te voldoen, is om het geïnstalleerde motorvermogen en daarmee de ontwerpsnelheid van het schip te verlagen. Het verminderen van het geïnstalleerde motorvermogen zou echter kunnen leiden tot een schip met ondermaats vermogen, waarvan wordt aangenomen dat het kwetsbaar en onveilig is omdat het onvoldoende vermogen zou hebben voor voortstuwing en besturing in ongunstige weersomstandigheden.

Er is een enorme variatie in de beoordelingsmethodiek van transportprestaties van schepen, waaronder IMO's EEDI. De effecten van verschillende technische en operationele maatregelen op het brandstofverbruik en de emissieprestaties van typische vrachtschepen zijn echter zelden systematisch onderzocht met een deugdelijke methode voor prestatiebeoordeling. Vanwege de ernstige bezorgdheid over de veiligheid van schepen met een te laag vermogen bij het varen in ongunstige zeecondities, zijn er veel onderzoeken uitgevoerd om de veiligheid van schepen in verschillende zeecondities te beoordelen, maar eerdere onderzoeken waren vooral gericht op de manoeuvreerbaarheid van het schip en de zeewaardigheid. De interacties tussen de motor, de propeller, het schip en de golven, enz., zijn in ongunstige zeeomstandigheden zeer gecompliceerd en zeer dynamisch, en de veiligheid van het schip in ongunstige weersomstandigheden is sterk gerelateerd aan het gedrag van de motor. Onderzoeken die gedetailleerde inzichten verschaffen in het motorgedrag, met name het dynamische gedrag wanneer het schip vaart en manoeuvreert in ongunstige zeecondities, zijn echter zeer beperkt. Dit proefschrift tracht de bovengenoemde kennislacunes op te vullen. De belangrijkste onderzoeksvraag die in dit proefschrift aan de orde komt, is:

*Wat is de transportprestatie van zeegaande vrachtschepen met kleine EEDI onder realistische bedrijfsomstandigheden; zijn deze schepen veilig tijdens het varen onder zware bedrijfsomstandigheden; en, hoe kunnen zowel de transportprestaties als de operationele veiligheid van zeegaande vrachtschepen worden verbeterd door gebruik te maken van de op korte termijn toepasbare opties voor scheepsvoortstuwing?*

De prestaties van het scheepstransport die in dit proefschrift worden onderzocht, omvatten de prestaties op het gebied van energieconversie, brandstofverbruik en emissieprestaties. Op basis van de analyse van energieconversie, brandstofverbruik en uitlaatemissieprocessen in de 'tank-to-wheel'-stroomketen van de scheepsvoortstuwings- en elektrische opwekkingssystemen, zijn de prestaties van het scheepstransport gedefinieerd en gekwantificeerd aan de hand van

drie indicatoren, namelijk de doeltreffendheid van de energieomzetting, brandstofindex en emissie-index. Rekening houdend met de missieprofielen van het schip, worden de gemiddelde effectiviteit van de energieomzetting, de brandstofindex en de emissie-index, die gemiddeld zijn over de hele reis van het schip, bepaald. Een model voor geïntegreerde scheepsvoortstuwing en elektrische opwekkingssystemen van een benchmark chemicaliëntanker wordt ontwikkeld, gekalibreerd en gevalideerd. Op basis van het simulatiemodel en de gedefinieerde energieomzettingseffectiviteit, brandstofindex en emissie-indices worden de transportprestaties van het zeeschip onder verschillende bedrijfsomstandigheden systematisch en kwantitatief onderzocht. In het bijzonder de invloeden van de operationele scheepsnelheidsreductie, voortstuwingsregeling, power-take-in / power-take-off en het gebruik van LNG als brandstof, evenals de combinatie van deze maatregelen op de transportprestaties van het schip gedurende de hele reis rekening houdend met de missieprofielen van schepen zijn systematisch onderzocht.

De operationele veiligheid die in dit proefschrift wordt onderzocht, omvat zowel de operationele veiligheid van de motor als de operationele veiligheid van het schip. Op basis van de analyse van de bedrijfslimieten van de motor en het schip, is de bedrijfsveiligheid van het schip bepaald en gekwantificeerd met behulp van de mechanische en thermische belastingslimieten van de motor, de motortoerental limieten, de pieklimiet van de compressor en de stuwkrachtlimiet van het schip. Het schip 3DOF (degree-of-freedom) manoeuvreer- en bewegingsmodel (surge, slingeren en gieren) en het wind- en golfverstoringsmodel zijn geïntegreerd met het model voor scheepsvoortstuwing en elektrische opwekkingssystemen. Op basis van het model van geïntegreerde systemen en de gedefinieerde bedrijfslimieten voor motoren en schepen, is de operationele veiligheid van het zeegaande vrachtschip met laag vermogen onder verschillende bedrijfsomstandigheden systematisch en kwantitatief onderzocht. Het dynamische gedrag van de motor tijdens het versnellen, vertragen, het stoppen van een crash en het draaien in normale zeecondities is onderzocht. De voortstuwings- en manoeuvreerprestaties van het schip bij het varen op kopzee en het keren naar kopzee bij ongunstige zeecondities (BF7 en BF8) zijn onderzocht. De invloeden van de spoed van de schroef en PTO / PTI op de stuwkrachtgrens van het schip en het motorgedrag zijn ook onderzocht.

Om het brandstofverbruik en de uitstoot van broeikasgassen effectief te verminderen, moeten de operationele snelheidsreductie en optimalisatie van de scheepsmissieprofielen tijdens de reis op korte termijn nog steeds de belangrijkste maatregelen zijn voor de zeegaande vrachtschepen. Door de elektrische stroom op te wekken door de asgenerator (PTO-modus) in plaats van door de hulpgeneratoren, wordt het brandstofverbruik verder verlaagd. Het gebruik van LNG als scheepsbrandstof helpt om de CO<sub>2</sub>-uitstoot en vooral de uitstoot van verontreinigende stoffen (zoals NO<sub>x</sub>) over de hele reis te verminderen. Door het schip in PTI-modus op LNG te varen, wordt de lokale uitstoot van verontreinigende stoffen in kust- en havengebieden aanzienlijk verminderd. De methaanemissies van LNG-motoren en de levenscyclusemissies van aardgas moeten echter zoveel mogelijk worden geminimaliseerd, aangezien methaan eigenlijk een krachtiger broeikasgas is dan CO<sub>2</sub>. Bij het beoordelen van de operationele veiligheid van het schip in ongunstige zeeomstandigheden moet rekening worden gehouden met het dynamische motorgedrag en de invloed van de PTO / PTI en de spoed van de schroef. Om de motor te beschermen tegen mechanische en thermische overbelasting, compressorstoten en te hoge snelheden tijdens dynamische scheepsoperaties en / of op volle zee, moeten de motor en de propeller zorgvuldig worden gecontroleerd. De asgenerator / motor kan in PTI-modus als motor werken wanneer het schip met name bij (zware) ongunstige

weersomstandigheden meer voortstuwingsvermogen nodig heeft. Concluderend, op korte termijn zal een PTO / PTI-systeem samen met het gebruik van LNG als brandstof, dat een hybride elektriciteitsopwekkingssysteem en een hybride voortstuwingssysteem vormt, bijdragen aan het verbeteren van zowel de prestaties van het scheepstransport onder normale zeecondities en de operationele veiligheid van het schip in (zware) ongunstige zeeomstandigheden.

Last but not least zijn, als weerspiegeling van het onderzoek in dit proefschrift, suggesties gedaan voor wijzigingen van IMO's huidige EEDI. Er is een voorstel gedaan voor de formule om de behaalde EEDI van schepen op een meer realistische manier te berekenen, waarbij een representatief scheepsoperatieprofiel en meerdere motorbedrijfspunten in aanmerking worden genomen. Het voorstel tot wijziging van de huidige EEDI-formule probeert de EEDI-berekening realistischer en representatiever te maken bij het evalueren van de vervoersprestaties van schepen in de ontwerpfase. Bovendien kan het ook gedeeltelijk een andere zwakte van het huidige EEDI oplossen met betrekking tot de problemen van ondermaatse schepen, omdat de scheepsontwerper in staat is om een grotere motor te installeren door een voldoende grote motormarge te selecteren volgens het voorstel.

# **1 Introduction**

## **1.1 Background**

### **1.1.1 Challenges of shipping industry**

As over 80% of world trade by volume and more than 70% of its value are carried by sea, ocean shipping remains the backbone of international merchandise trade and manufacturing supply chain (UNCTAD, 2019). However, on the other hand, shipping industry is facing increasing social concerns over its environmental impact and maritime safety issues. Looking into the future, the shipping industry needs to address the challenges in balancing between the transportation benefits, the environmental impact and the maritime safety (UNCTAD, 2018).

Shipping has been considered as a relatively energy-efficient, environment-friendly and sustainable mode of mass transport of cargo (Chapman, 2007). But, in terms of total amount, shipping industry consumes more fuel in comparison with other transport modes (Shi, 2013) and shipping-related emissions contribute significantly to the global air pollution and long-term global warming (Taljegard et al., 2014; Moreno-Gutiérrez et al., 2019). Correlated with fuel consumption, shipping is responsible for approximately 3.1% of annual global CO<sub>2</sub> and approximately 2.8% of annual GHGs (greenhouse gases) on a CO<sub>2</sub>e (CO<sub>2</sub> equivalent) basis (IMO, 2015). Approximately 15% and 13% of global human-made NO<sub>x</sub> and SO<sub>x</sub> emissions come from the shipping industry. Depending on future economic and energy developments, it is projected that maritime CO<sub>2</sub> emissions could increase significantly by 50% to 250% in the period from 2012 to 2050, which is the so-called BAU (business as usual) projection (IMO, 2015). Moreover, as fuel cost accounts for approximately 50% to 60% of the total operational cost of a ship (Perera et al., 2015), a significant fuel consumption reduction will contribute to a considerable save of a ship's operational cost.

Consequently, the shipping industry is striving to reduce its fuel consumption and

emissions due to the increasingly high fuel price, social concerns on the environmental impact and the resulting mandatory and strict emission control regulations worldwide (Andersson et al., 2016). Nevertheless, currently, diesel engines remain the dominant marine prime movers for ship propulsion and heavy fuel oil (HFO), which accounts for 79% of total fuel consumption by energy content in 2018, remains the dominant fuel in international shipping (IMO, 2020). In the short-term, diesel engines will continue to provide the most propulsion and auxiliary power for ships in the coming decades (Geertsma et al., 2018). To address the current and future challenges, depending on the technological development, commercial motivation, public perception and political acceptability, the shipping industry needs to consider and adopt the appropriate ship powering and propulsion options that are applicable in short-, medium- and long-term time frames as identified in Figure 1.1 (Carlton et al., 2013).

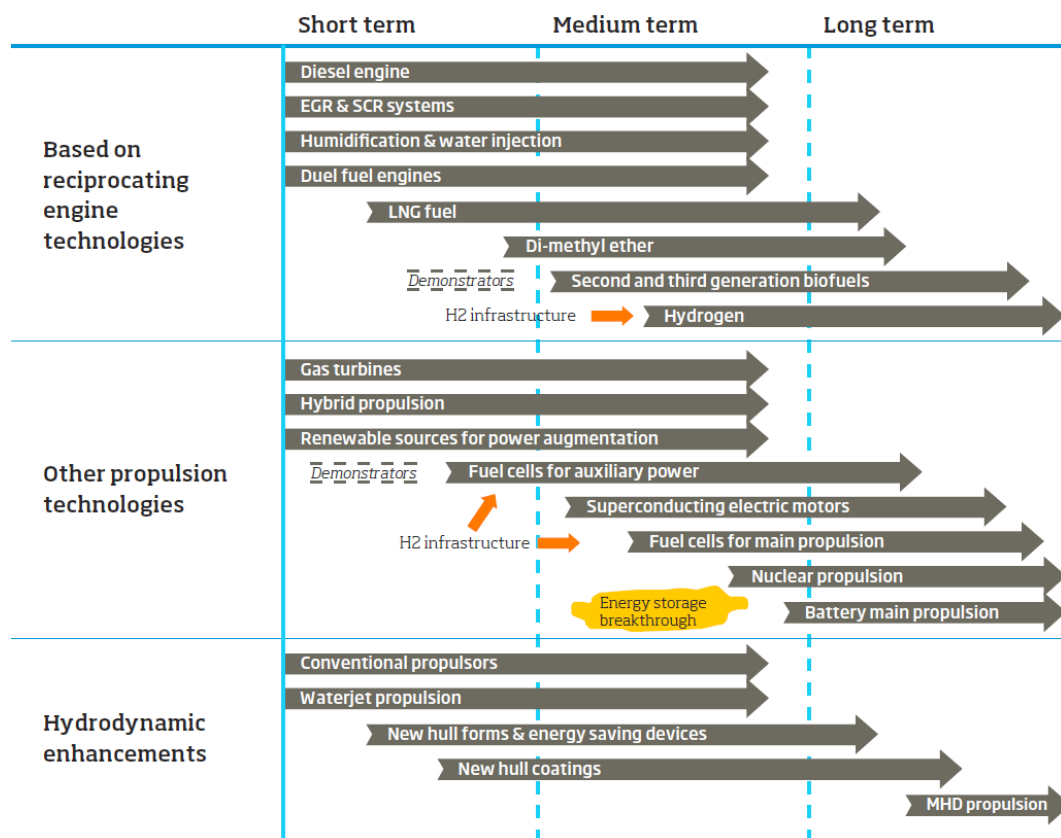


Figure 1.1: Potential phasing of different ship propulsion technologies in time (Carlton et al., 2013)

### 1.1.2 Weaknesses of EEDI (Energy Efficiency Design Index)

Aiming at promoting the application of more energy efficient (less polluting) equipment and engines on ships to reduce the environmental impact from shipping industry, the Energy Efficiency Design Index (EEDI), which is the most important technical measure, has been made mandatory for new ships by the International Maritime Organization (IMO) (MEPC, 2011). The current EEDI, in a simplest form, is actually the ratio between the ship's CO<sub>2</sub> production potential (environmental cost) and the cargo capacity and speed of the ship (social benefit) for the design point. New ship designs need to meet the EEDI requirements, i.e., the attained EEDI

of the ship should be no more than the required EEDI for their ship types; and this has to be verified by an independent organisation to obtain the certification. The requirement for EEDI compliance will become more stringent in the coming years.

The current EEDI, which provides an important guidance for the ship design, considers only one operating point (the nominal design point) of the ship. However, the nominal design condition does not accurately represent the actual operating conditions of the ship in reality, and consequently the current EEDI is not able to accurately evaluate the real lifetime carbon emissions of the ship (Trivyza et al., 2020). Without taking ship's representative and realistic operating profile instead of only one design speed (in calm water conditions) into account, a lower EEDI ship design does not necessarily lead to less fuel consumption and emissions when the ship sails with a certain mission profile over the actual voyage. As a result, under the guidance of current EEDI regulation, the ship designers, owners and policymakers could be misled to adopt the configurations that are underperforming or even leading to an increase of CO<sub>2</sub> emissions in reality (Jacobs et al., 2016; Lindstad et al., 2019; Trivyza et al., 2020).

Moreover, compared to adopting innovative ship design concepts and energy efficient technologies, a technically easy and effective solution to meet the EEDI requirement is to lower the installed engine power and thus to reduce ship design speed (Mundt et al., 2019). However, if reducing the installed engine power has been chosen to achieve a small EEDI, it could lead to an underpowered ship, which is believed to be vulnerable and unsafe as the engine may not be capable of providing sufficient power for ship propulsion and steering under adverse weather conditions (Papanikolaou et al., 2016). Based on the statistical analysis of marine accidents (Ventikos et al., 2015; Shigunov et al., 2019a), it is inferred that a quite number of underpowered ships are currently sailing at sea worldwide, especially the ships with small EEDI that is achieved by simply reducing the installed engine power. Marine accidents could happen if the underpowered ships unfortunately sail in storms, which could lead to disastrous consequences on human lives, the society and even the marine environment.

## **1.2 Research motivation**

Although fundamental ship propulsion system theory is well-known and is at a mature stage of development, there is still an enormous variety in the assessment methodology of (environmental) transport performance of ships, including IMO's EEDI as mentioned previously. The effects of different technical and operational measures on the fuel consumption and emissions performance of typical cargo ships have rarely been investigated systematically with a proper performance assessment methodology. Hybrid propulsion and using liquefied natural gas (LNG) as the alternative fuel, which are considered as the promising and attractive solutions to reducing the environmental impact and operational costs of ships, have been applied on automobiles and some small ships. Nevertheless, research investigating the fuel consumption and emissions over the total voyage of ocean-going cargo ships with a hybrid propulsion and different fuels taking the ship mission profiles into account is limited.

As it has raised serious safety concerns on the underpowered ships when sailing in adverse sea conditions, many researches have been conducted to assess ship safety in different sea

conditions. However, researches on ship safety in adverse sea conditions have mainly focused on the ship manoeuvrability and seakeeping performance, etc.; while researches providing detailed insights of the engine behaviour especially the dynamic behaviour when the ship is sailing and manoeuvring in adverse sea conditions are very limited. The interactions between the engine, the propeller, the ship, and the waves, etc., in adverse sea conditions are very complicated and highly dynamic, and the ship safety in adverse weather conditions is highly related to the engine behaviour. So, a detailed and systematic investigation on the engine behaviour (including both static and dynamic behaviour) taking the dynamic interactions between the sea, the ship and its propulsion system under various operating conditions into account is important and necessary; however, the research in this respect is still limited.

The research in this dissertation tries to fill the above-mentioned knowledge gaps.

### 1.3 Research questions

The main research question addressed in this dissertation is:

***What is the transport performance of ocean-going cargo ships with small EEDI when sailing in realistic operating conditions; are these ships safe when sailing in heavy operating conditions; and, how to improve both the transport performance and operational safety of ocean-going cargo ships by using the short-term applicable ship propulsion options?***

To avoid ambiguity and to define the research scope, some terminologies and concepts used in this thesis are clarified as follows:

- **Transport performance** investigated in this thesis includes the energy conversion performance, fuel consumption performance and emission performance of the ship. Both economic cost and environmental impact need to be considered when evaluating the transport performance of cargo ships.
- **Operational safety** investigated in this thesis includes both engine operational safety and ship operational safety. The engine operational safety is indicated by the engine thermal loading, mechanical loading, compressor surge and engine over-speeding, which could lead to engine failure. The ship operational safety is indicated by the ship thrust availability especially when operating in adverse sea conditions. Ship thrust unavailability in adverse sea conditions could be caused by: insufficient driving power (engine and/or motor power); thrust decrease due to propeller wake variation, ventilation and propeller emergence, etc.; or even complete loss of thrust due to engine failure.

To answer the main research question, the following sub-questions will be addressed.

**Q1. How to define and quantify the transport performance of cargo ships?**

**Q2. What is the influence of various short-term applicable technical and operational measures on the transport performance of cargo ships?**

**Q3. How to improve ship transport performance by using the short-term applicable ship propulsion options?**

**Q4. How to define and quantify ship operational safety?**

**Q5. What is the influence of various ship operations and adverse sea conditions on ship operational safety?**

**Q6. How to improve ship operational safety by using the short-term applicable ship propulsion options?**

## 1.4 Research approach

The research in this dissertation has been divided into two parts, in which Part 1 studies the ship transport performance, and Part 2 studies the ship operational safety. Sub-questions Q1, Q2 and Q3 are addressed in Part 1; while Q4, Q5 and Q6 are addressed in Part 2. Both parts of the research are conducted based on the methodologies including the case study of a benchmark ship, system modelling, and simulation results analysis, etc., as illustrated in Figure 1.2 and Figure 1.3.

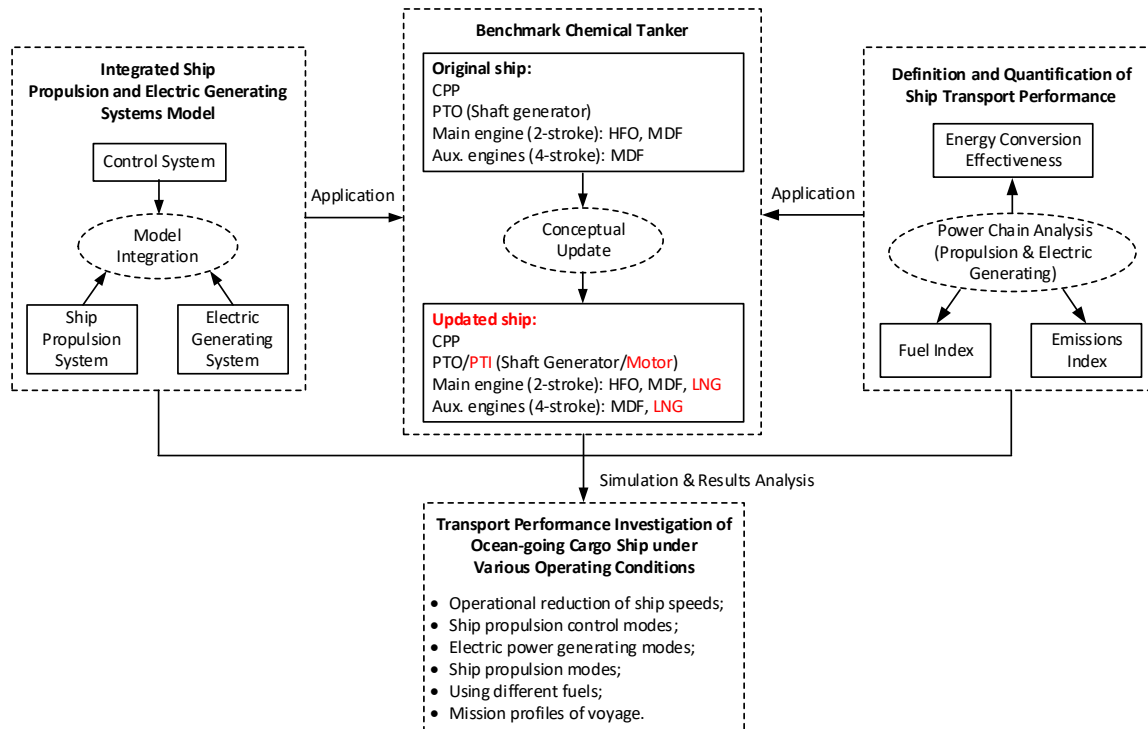


Figure 1.2: Research approach for Part 1 (Ship transport performance)



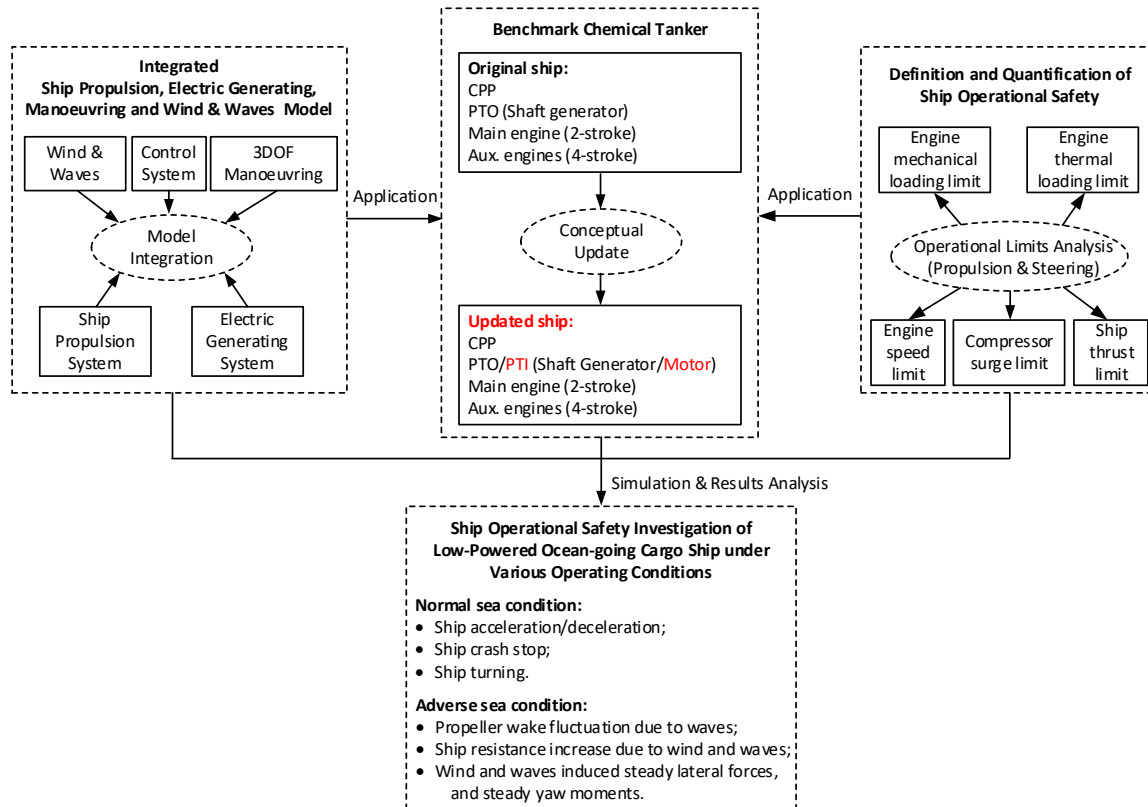


Figure 1.3: Research approach for Part 2 (Ship Operational Safety)

A 13000 DWT chemical tanker (shown in Figure 1.4), for which ample real ship measurement data (both towing tank and full-scale) are available, has been chosen as a benchmark ocean-going cargo ship for the study in this thesis because it represents a "normal" type of ship that takes its share in the daily business of transportation of goods. The propulsion system of the chemical tanker consists of a two-stroke diesel engine working as the main engine, a controllable pitch propeller (CPP) and the shafting system. The electric power generation system includes a shaft generator (power take off, PTO) driven by the main engine and three auxiliary generators driven by three auxiliary four-stroke diesel engines.



Figure 1.4: 13000 DWT Chemical Tanker 'Castillo de Tebra' (built by Ningbo Xinle Shipbuilding Group CO. LTD (China)).

Hybrid ship propulsion and using LNG (liquefied natural gas) as the fuel are considered as two of the promising and short-term applicable ship propulsion options for ocean-going cargo ships. In order to investigate the potential influence of the adoption of hybrid ship propulsion and LNG on the transport performance and operational safety of the ocean-going cargo ship, the ship propulsion and electric generating systems of the benchmark chemical tanker have been conceptually updated. Due to the conceptual update of the ship, the shaft generator can also work as a shaft motor in PTI (power take in) mode and the engines can also use LNG as their fuels.

The first part of the research (Part 1: ship transport performance) is illustrated in Figure 1.2. Based on the analysis of the ‘tank to wheel’ power chain (from fuel energy flow to ship mobility power) of the ship propulsion and electric generating systems, the ship transport performance has been defined and quantified using three indicators, namely the energy conversion effectiveness, fuel index and emissions index. An integrated ship propulsion and electric generating systems model of the benchmark ship will be developed, calibrated and validated. Based on the simulation model and the defined energy conversion effectiveness, fuel index and emissions indices, the ship transport performance of the ocean-going cargo ship under various operating conditions will be systematically and quantitatively investigated. In particular, the influence of the operational reduction of ship speeds, ship propulsion control modes, electric power generating modes, ship propulsion modes, using different fuels as well as ship mission profiles on the ship transport performance over the total voyage will be investigated.

The second part of the research (Part 2: ship operational safety) is illustrated in Figure 1.3. Based on the analysis of the engine and ship operational limits, the ship operational safety has been defined and quantified using the engine mechanical and thermal loading limits, engine speed limits, compressor surge limit and ship thrust limit. The ship 3DOF (degree-of-freedom) manoeuvring and motions (surge, sway and yaw) model and the wind and waves disturbances model will be integrated with the ship propulsion and electric generating systems model. Based on the integrated systems model and the defined engine and ship operational limits, the ship operational safety of the low-powered ocean-going cargo ship under various operating conditions will be systematically and quantitatively investigated. In particular, the influence of ship operations, which includes ship acceleration, deceleration, crash stop and ship turning, etc., in normal sea condition; and wind and waves disturbances, which include propeller wake fluctuation and wind and waves induced steady forces (added resistance, steady lateral forces and steady yaw moments), in adverse sea conditions on the engine and ship operational safety will be investigated.

Modelling and simulation have played an important role in the research in this dissertation. To avoid ambiguity and for convenience when discussing the modelling processes and the procedures evaluating the credibility of these processes, a clear and consistent terminology and methodical framework needs to be defined (Schlesinger, 1979; Refsgaard and Henriksen, 2004). The terminology used in this dissertation is modified from that was proposed in (Schlesinger, 1979) and later extended in (Refsgaard and Henriksen, 2004). The important elements and the interrelationships of them in the terminology of modelling and simulation are illustrated in Figure 1.5 and explained in the following.

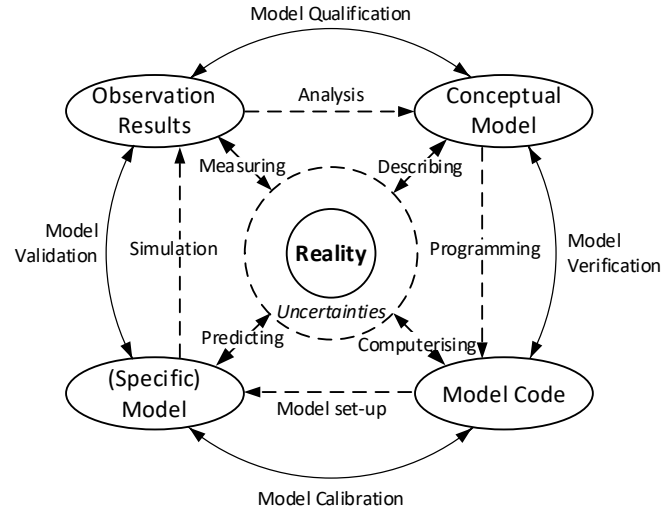


Figure 1.5: Modelling the reality. Modified after (Schlesinger, 1979) and (Refsgaard and Henriksen, 2004)

- **Reality:** “An entity, situation, or system which has been selected for analysis.” (Schlesinger, 1979). In this research, it is understood as the ship propulsion system, electric generating system, manoeuvring system, control system, disturbances of the sea, ship transport performance and operational safety, etc, which are investigated.
- **Observation Results:** “In science, observation involves the perception and recording of data via the use of scientific instruments. The term may also refer to any data collected during the scientific activity. Observations can be qualitative, that is, only the absence or presence of a property is noted, or quantitative if a numerical value is attached to the observed phenomenon by counting or measuring.” (Wikipedia, 2020). In this research, the observation results include the test data that has been measured during the engine test, ship and propeller model tests, and ship sea trial test, etc.
- **Conceptual Model:** “Verbal description, equations, governing relationships, or ‘natural laws’ that purport to describe reality.” (Schlesinger, 1979). In this research, the conceptual model includes both the mathematical expressions (equations) and the descriptions that define and describe, for instance, the energy conversion processes in the ship propulsion and generating systems, the gas exchange processes of the engine, the ship propulsion and control modes, the concepts of ship transport performance and operational safety, etc.
- **Model Code:** “A mathematical formulation in the form of a computer program that is so generic that it, without program changes, can be used to establish a model with the same basic type of equations (but allowing different input variables and parameter values) for different study areas (systems and/or processes).” (Refsgaard and Henriksen, 2004). In this dissertation, the model code is understood as the MATLAB/Simulink program for computerising and implementing the mathematical models of the ship propulsion and manoeuvring, etc.
- **(Specific) Model:** A specific model established for a particular system or process that is (to be) investigated, including input data and parameter values (Refsgaard and

Henriksen, 2004). In this research, it is understood as the model of the benchmark chemical tanker, which has been calibrated using the specific data of the chemical tanker. Based on the specific model, the transport performance and operational safety of the benchmark chemical tanker can be predicted and investigated.

- **Model Qualification:** *“Determination of adequacy of the conceptual model to provide an acceptable level of agreement for the domain of intended application. This is in other words the scientific confirmation of the theories/hypotheses included in the conceptual model.”* (Schlesinger, 1979; Refsgaard and Henriksen, 2004). In this research, for instance, the test-data-based fitting engine model is adequate for studying the ship transport performance, but not for ship operational safety, which needs a more detailed thermodynamic-based mean value first principle engine model.
- **Model Verification:** *“Substantiation that a model code is in some sense a true representation of a conceptual model within certain specified limits or ranges of application and corresponding ranges of accuracy.”* (Refsgaard and Henriksen, 2004). In this research, it is understood that the mathematical models of, for instance, the ship propulsion and manoeuvring systems, must be correctly programmed and calculated in the MATLAB/Simulink environment.
- **Model Calibration:** *“The procedure of adjustment of parameter values of a model to reproduce the response of reality within the range of accuracy specified in the performance criteria.”* (Refsgaard and Henriksen, 2004). In this research, for instance, the parameters in the engine model of the benchmark chemical tanker need to be set or tuned so that the model can to some extent reproduce the engine behaviour that is of interest with satisfactory accuracy.
- **Model Validation:** *“Substantiation that a (specific) model within its domain of applicability possesses a satisfactory range of accuracy consistent with the intended application of the model.”* (Schlesinger, 1979; Refsgaard and Henriksen, 2004). In this research, for instance, when the calibrated engine model, propeller model, ship resistance model, rudder model and ship manoeuvring model, etc., are matched and integrated together, the ship propulsion and manoeuvring system as a whole should be able to simulate and predict the engine thermal and mechanical loading during different ship propulsion and manoeuvring operations with satisfactory accuracy.
- **Model Set-up:** *“Establishment of a specific model using a (generic) model code. This requires, among other things, the definition of boundary and initial conditions and parameter assessment from field and laboratory data.”* (Refsgaard and Henriksen, 2004). In this research, for instance, the parameters in the engine model of the benchmark ship are set and/or estimated according to the engine specification data and test data, etc. The inputs to the engine model, such as the engine speed command and the loading (modes) setting (generator law or propeller law), etc., need to be set. Initial conditions of the engine, such as the initial engine speed, fuel rack position, temperatures and pressures in different components of the engine, etc., need to be defined, and in MATLAB/Simulink the initial conditions are always defined in the

integrator and/or memory blocks.

- **Simulation:** “*Use of a validated model to gain insight into reality and obtain predictions*” (Refsgaard and Henriksen, 2004). In this research, for instance, using the validated ship propulsion and manoeuvring model, insights into the energy conversion processes in the propulsion system and the engine behaviour during various ship operations will be provided, and the ship transport performance and operational safety will be predicted and assessed.
- **Uncertainties:** Uncertainties always exist in the observation results, conceptual models, model codes and specific models, etc. Uncertainties will cause errors or deviations when measuring, describing, computerising and predicting the reality.

## 1.5 Research boundaries

The research in this thesis has covered a wide scope in terms of different research fields and disciplines that have been involved. It is necessary to clarify the research boundaries to limit the research both in scope and depth in order to reach the research goals effectively and efficiently. Therefore, some assumptions and simplifications at different levels throughout the research in this dissertation have been made.

Among others, the following research boundaries of this thesis are clarified:

- (1) The research focuses on the transport performance and operational safety of ocean-going (or seagoing) cargo ships rather than any other types of vessels.
- (2) In this thesis, the short-term applicable alternative ship propulsion technologies focus only on hybrid ship propulsion and using LNG as the fuel.
- (3) When conceptually updating the propulsion and electric generating systems of the benchmark ship, i.e., hybridizing the ship propulsion and using LNG as the fuel, the details of the update will not be considered. For instance, the details of how the engines are updated, how the shaft generator/motor is updated and how different fuels are stored and managed onboard the ship, etc., will be left out of scope of the research.
- (4) When investigating the transport performance of the ship, the research in this thesis focuses on ship propulsion and electric generating systems, while the energy conversion, fuel consumption and emissions of the heating plant and other systems of the ship are not considered.
- (5) When investigating the ship operational safety in the adverse sea conditions, only influence of wind and waves induced steady forces (including added resistance, steady lateral forces and steady yaw moments), and propeller wake fluctuation due to waves will be considered, while the propeller ventilation and propeller emergence will be left out of scope assuming that the ship has enough propeller immersion.
- (6) When investigating the ship operational safety, ship safety issues with regard to marine accidents, such as ship collision, contact, grounding and capsizing, etc., which could be caused by ship thrust unavailability in certain situations will not be considered. Also, the possible ultimate disastrous consequences on human lives, impact on society and

the marine environment, etc., which are caused by the ship accidents will be left out of the scope of this thesis.

## **1.6 Thesis outline**

Part 1 of the research includes Chapters 2 and 3; while Part 2 includes Chapters 4, 5, 6 and 7. Based on the research of Part 1 and Part 2, suggestions on amendments of IMO's current EEDI will be provided in Chapter 8. The conclusions and recommendations of Part 1 and Part 2 will be combined and discussed in Chapter 9. The outline and structure of this thesis are illustrated in Figure 1.6.

This thesis is organised as follows:

### **Chapter 2: Energy Effectiveness of Ocean-Going Cargo Ship under Various Operating Conditions**

In Chapter 2, a theoretical framework evaluating the ship transport performance has been introduced. The 'point value' indicators (at each ship speed) have been defined for evaluating the energy conversion performance the ship. The benchmark ocean-going chemical tanker has been chosen for the research in this thesis. The integrated ship propulsion and electric power generating systems model has been developed, calibrated and validated. Based on the theoretical framework and the simulation model, the effects of operational reduction of the ship speed, different ship propulsion control and electric power generation modes on the ship transport performance in realistic sailing conditions have been investigated.

### **Chapter 3: Fuel Consumption and Emissions of Ocean-Going Cargo Ship with Hybrid Propulsion and Different Fuels over Voyage**

In Chapter 3, the benchmark chemical tanker has been conceptually updated so that the ship can also sail in PTI (power-take-in) mode and/or using LNG (liquefied natural gas) as the fuel. The 'mean value' indicators (weighted over the voyage) have been defined for evaluating the fuel consumption and emissions performance of the ship over the total voyage. Based on the conceptual hybridisation, the influence of sailing on different fuel types and PTI propulsion mode as well as ship operational speeds, propulsion control modes and electric power generation modes on the fuel consumption and emissions performance over the total voyage of the ship, including the transit in open sea and manoeuvre in close-to-port areas, has been investigated.

### **Chapter 4: Mean Value First Principle Modelling of Two-Stroke Marine Diesel Engine**

In Chapter 4, to predict the engine thermal loading, mechanical loading and compressor surge limits as well as other engine behaviour, which are highly related to the engine operational safety, a thermodynamic-based mean value first principle parametric (MVFP) model for the two-stroke marine diesel engine has been developed, calibrated and validated. The MVFP engine model includes the closed cylinder process model, gas exchange process model, turbocharger model, air cooler model, auxiliary blower model, exhaust valve temperature model, engine mechanical and heat losses models, etc. The MVFP model is able to predict the engine's behaviour in various operating conditions, including both steady (static) and transient

(dynamic) operating conditions.

### **Chapter 5: Integrated Ship Propulsion and Manoeuvring Model**

In Chapter 5, the 3DOF (degree-of-freedom) ship manoeuvring model including ship motions of surge, sway and yaw is developed, calibrated and validated. The MVFPP engine model (introduced in Chapter 4) and the 3DOF ship manoeuvring model are integrated into the ship propulsion and electric power generating system model (introduced in Chapter 2 and updated in Chapter 3) for investigating the engine and ship operational safety in Chapter 6 and Chapter 7.

### **Chapter 6: Engine Behaviour of Low-Powered Ocean-Going Cargo Ship under Various Propulsion and Manoeuvring Operations**

In Chapter 6, based on the integrated ship propulsion and manoeuvring model, the engine behaviour under different ship propulsion and manoeuvring operations, including ship acceleration, deceleration, crash stop and turning in normal sea condition, are investigated. The engine operational safety will be defined and quantified. The relationship between the engine operational limits and ship thrust limits will be investigated.

### **Chapter 7: Effects of Adverse Sea Conditions on Propulsion and Manoeuvring Performance of Low-Powered Ocean-Going Cargo Ship**

In Chapter 7, the waves and wind disturbances models are integrated into the ship propulsion and manoeuvring model. Based on the simulation model, the effects of adverse sea conditions on the propulsion and manoeuvring performance of the low-powered ocean-going cargo ship will be investigated. In particular, the influences of the propeller wake fluctuation due to waves, and wind and waves induced steady forces and moments acting on ship hull will be studied as they ultimately have an impact on the engine loading. The engine behaviour and ship thrust availability for ship propulsion and steering in various adverse sea conditions will be investigated. The impact of different operational measures including changing propeller pitch and PTO/PTI operations on the ship thrust limits will be studied.

### **Chapter 8: Suggestions on Amendments of IMO's EEDI**

In Chapter 8, as a reflection of the research in this dissertation, suggestions on amendments of IMO's current EEDI will be provided.

### **Chapter 9: Conclusions and Recommendations**

In Chapter 9, the findings and conclusions of the research in this thesis will be summarised. The research questions will be answered. The limitations and uncertainties of this research as well as the recommendations for future research will be discussed.



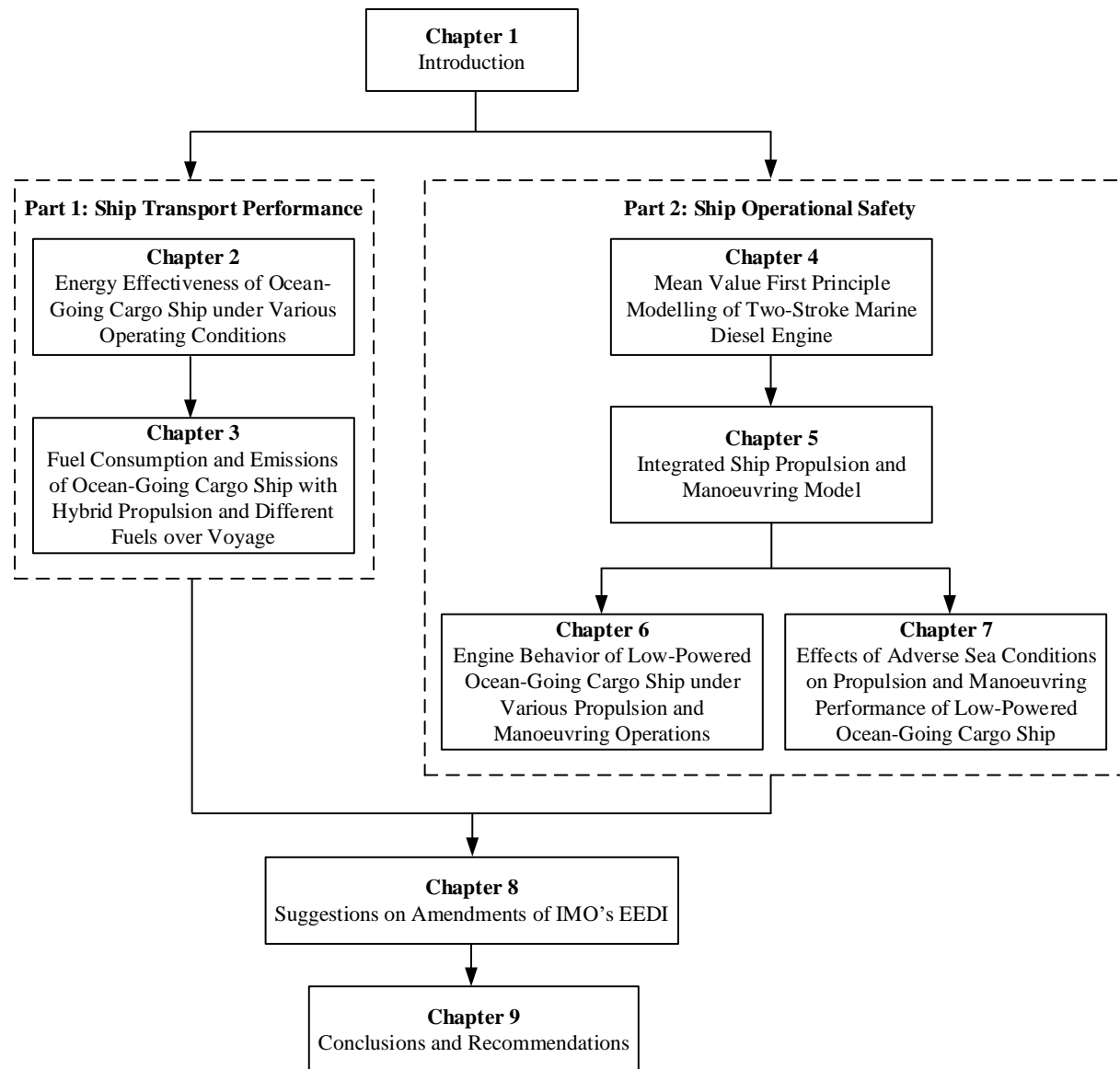


Figure 1.6: Thesis outline and structure

## 1.7 Contributions

The main contributions of this thesis with respect to understanding and assessing the transport performance of ocean-going cargo ships are as follows:

- clearing up some confusion in the existing terminology by developing a consistent and comprehensive theoretical framework of the energy conversion of cargo ships in Chapter 2 and published in (Sui et al., 2019a);
- a ship propulsion system model calibrated and validated with testbed, towing tank and full-scale sea trial measurement data, which is rare, as these measurements are both difficult and expensive, in Chapter 2 and published in (Sui et al., 2019a).
- a quantitative and systematic investigation and evaluation of the influence of



operational reduction of ship speeds, propulsion control modes and electric power generation modes on ship energy conversion performance in realistic operating conditions; a close look inside the stages of the energy conversion process of the ship propulsion and electric generating systems, providing a deeper insight into the influence of individual “nodes” and “links” of the power chain on the overall performance in Chapter 2 and published in (Sui et al., 2019a);

- a quantitative and systematic investigation and evaluation of the potential influence of the application of the hybrid ship propulsion and using LNG as the fuels as well as various propulsion control and power management strategies on the ocean-going cargo ship in reducing the fuel consumption and emissions over the total voyage, including transiting in open sea and manoeuvring in coastal and close-to-port area, by taking ship mission profiles into account in Chapter 3 and published in (Sui et al., 2020).

The main contributions with regard to understanding and assessing the operational safety of low-powered ocean-going cargo ships are as follows:

- a Mean Value First Principle Parametric (MVFPP) engine model of the two-stroke marine uniflow diesel engine that can accurately predict engine behaviour including engine thermal loading, mechanical loading and compressor surge, etc., in various static and dynamic operating conditions with detailed information. In particular, a novel mean value first principle gas exchange model for the two-stroke uniflow marine diesel engines, including the two-zone scavenging model, blowdown model and the expelling process model in Chapter 4;
- an integrated model of ship propulsion, electric generating, ship manoeuvring and wind and waves disturbances, which is able to predict the engine and ship behaviour in various ship operations and sea conditions with detailed information in Chapter 5 and Chapter 7.
- a quantitative and systematic investigation and evaluation of the engine behaviour of a low-powered ocean-going cargo ship with small EEDI under various ship operations including ship acceleration/deceleration, crash stop and ship turning, etc.; in particular, providing a detailed insight of the engine performance in various ship operations in normal sea condition in Chapter 6.
- a quantitative and systematic investigation and evaluation of the engine behaviour and ship thrust availability of a low-powered ocean-going cargo ship with small EEDI under the disturbances of adverse sea conditions including propeller wake fluctuation and wind and waves induced steady forces acting on the hull; in particular, providing a detailed insight of the engine performance when the ship is sailing and manoeuvring in adverse sea conditions in Chapter 7.

The main contributions with respect to improving IMO’s EEDI regulations:

- a proposal on the formula calculating the attained EEDI of ships in a more realistic way, in which a representative ship operating profile and multiple engine operating points are considered in Chapter 8.

## **2 Energy Effectiveness of Ocean-Going Cargo Ship under Various Operating Conditions\***

### **2.1 Introduction**

Almost 70 years ago, in (Gabrielli and Von Karman, 1950), Gabrielli and Von Karman asked the question, ‘What Price Speed?’. In this classic paper, the economic cost for faster travel by means of various transport modes was investigated from an efficiency perspective. Today, due to increasing economic and environmental pressure, high maximum speed is no longer the highest priority in design and operation for transportation vehicles, especially for maritime transport (Lindstad and Eskeland, 2015). Thus, priority has shifted to the question ‘What Price Transportation?’ rather than ‘What Price Speed?’ (Eyring et al., 2010; Shi, 2013).

Fuel consumption significantly influences the economic cost of transportation and directly results in the emission of carbon dioxide (CO<sub>2</sub>), which is a major greenhouse gas. Consequently, the overall fuel consumption includes not only the economic cost, but also the environmental impact (Psaraftis and Kontovas, 2010). The increasing worldwide concerns regarding the environmental impact of maritime transportation thus necessitate proper evaluation and reduction of fossil fuel consumption of commercial ships, particularly cargo ships. In order to facilitate the ship performance evaluation, during both the ship preliminary design stage and operation stage (Coraddu et al., 2014), a consistent and comprehensive theoretical framework is indispensable. During ship operation, propulsion control, power and energy management, and ship operational speeds significantly influence the fuel consumption performance of ships (Klein Woud and Stapersma, 2002; Armstrong and Banks, 2015; Geertsma et al., 2017a), so,

---

\* This chapter is based on (Sui et al., 2019a).

quantitative and systematic investigations in this regard are needed when trying to improve the transport performance of ships.

### **Existing frameworks and terminology**

It is difficult to properly assess the ship transport performance due to the large amounts of influencing variables (Coraddu et al., 2015). Indicators and criteria need to be identified when evaluating transport performance of ships (Misra, 2016). Thus, research has been performed to quantify the transport performance of ships and marine vehicles (Papanikolaou, 2014; Stapersma, 2017). The EEDI (Energy Efficiency Design Index) proposed by IMO (International Maritime Organisation) (IMO, 2014), which for merchant ships is the obligatory indicator defining the ship energy efficiency, is in principle the ratio of penalty to benefit of the energy conversion of ships (Stapersma, 2016a). As such, the EEDI has a close relationship to the energy conversion effectiveness that will be introduced in this thesis. The main difference is however that the energy conversion effectiveness is defined for different ship speeds and for representative environmental conditions, while the EEDI is not. In (Papanikolaou, 2005), the *transport efficiency* is defined as the ratio of the total installed power to the vessel's deadweight or payload times the ship service speed. In (Akagi, 1991), the *reciprocal transportation efficiency* is defined as a function of the ship displacement, maximum ship speed and total installed power. In (Akagi and Morishita, 2001), the *specific power* is analysed as a function of the ship payload, maximum ship speed and total installed power. In (Kennell, 1998), a *transport factor* is defined as a function of the ship's displacement, the design speed and the total installed power. The above-mentioned indicators of ship transport performance are essentially the same or similar while they may be termed differently by different researchers.

### **Influence of ship operations**

Reducing the fuel consumption is an effective solution to decrease the transportation cost and the emission of greenhouse gases (Stapersma, 2010a; Bialystocki and Konovessis, 2016). Although the design of the ship propulsion system initially influences the fuel consumption behaviour of the ship (Altosole et al., 2007), ship operation plays a crucial role in the fuel consumption reduction as well (Roskilly et al., 2015; Andersson et al., 2016). A practical and widely adopted practice to reduce fuel consumption of cargo ships is reducing ship speed, both during design (decrease design speed) and operationally (slow steaming) (Psaraftis and Kontovas, 2013; Lee et al., 2015). However, using only one single design point to calculate EEDI rather than the actual operation on the basis of ship missions during its lifetime, IMO strives to reduce installed power and thus design ship speed to achieve a smaller EEDI, raising serious concerns regarding the safety of ships in adverse conditions (Papanikolaou et al., 2016; Bitner-Gregerse et al., 2016). Instead, designing the ship with a higher design speed and reducing actual operational speed during missions could be more effective and, more importantly, safer (Yasukawa et al., 2017).

Ship propulsion control and energy management also influence the fuel consumption performance of ships significantly (Kanellos et al., 2014; Geertsma et al., 2017a; Geertsma et al., 2017b). In (Geertsma et al., 2017b), in a case study of a patrol vessel, Geertsma et al. find that propulsion control strategy can save up to 30% of fuel, while also reducing thermal engine loading and acceleration time. Further in (Geertsma et al., 2018), Geertsma et al. propose an

adaptive pitch control strategy to optimise the fuel consumption, ship manoeuvrability, engine thermal loading and propeller cavitation noise. In (Buhaug et al., 2009), an assessment of the energy-saving potential using known technology and practices has shown that a proper energy management can reduce CO<sub>2</sub> emissions (CO<sub>2</sub>/ton-mile) by 1-10% as a result of reduction of fuel consumption. In (Figari and Guedes Soares, 2009), Figari, et al. propose a ‘dynamic set point’ propulsion control scheme with respect to the ‘static combinator’ control scheme for the best use of the ship propulsion system in terms of power, fuel consumption and exhaust emissions for a ferry.

### **Requirement of a flexible simulation tool**

Simulation models can be categorized into two main groups: first principle and empirical models (Del Re et al., 2010). First principle models provide the ability to gain physical insight in the investigated systems and not just the superficial and direct results and therefore have always been the first choice of researchers (Guzzella and Onder, 2009; Del Re et al., 2010). First principle models have to be limited however, both in scope and depth, to balance the usefulness and effectiveness with required calculation time of the chosen models (Bossel, 1994; Refsgaard and Henriksen, 2004). In order to get effective high-performance models, one of the common ways is combining the first principle and empirical approaches, from different aspects or at different levels, resulting in hybrid models (Asprion et al., 2013). In (Figari and Campora, 2003), a ship propulsion system model, which includes amongst others a complex two-zone crank angle diesel engine model based on Wiebe shaped combustion, but on the other hand a simple one-dimensional lookup table for the ship resistance model and simple two-dimensional lookup tables for the propeller model, is developed and used to analyse the components and system responses at off-design and transient conditions. For a better balance in (Schulten, 2005; Grimmelius et al., 2007; Sui et al., 2017; Geertsma et al., 2017b), ship propulsion system models containing different mean value first principle (MVFP) models of a diesel engine are developed for the investigation of ship performance. In (Vrijdag, 2009), in order to investigate the control of propeller cavitation in operational conditions, a complex propeller model and propulsion control model can be found in the ship propulsion system model while the diesel engine is modelled as a set of lookup tables. Thus, the complexity and focus of models depend on the goals pursued by researchers using the model.

### **Existing problems and knowledge gap**

The existing terminology defining the ship transport performance is considered to be inconsistent and confusing. The current terminology mixes up the concepts of ‘energy effectiveness’, ‘energy efficiency’ and ‘energy factor’ when defining the ship transport performance. Moreover, most of the indicators only take the power chain of ‘shaft to wheel’ (from installed power to ship mobility power) rather than ‘tank to wheel’ (from fuel energy flow to ship mobility power) into consideration neglecting power generation, which can make significant differences to the overall transport performance of ships. When the engines are considered, most of the research of ship transport performance only focus on the input and output ends of the power chain of the energy conversion and fail to clarify the individual contributions of each part of the power chain to the overall performance. In addition, in most research, indicators of ship transport performance, including IMO’s EEDI, are only investigated

at one single ship speed, often the design ship speed, rather than at various operational ship speeds and only in calm water conditions, which rarely is the case according to (Faltinsen, 1980).

The influence of propulsion control strategy on the fuel consumption performance have been researched for ships whose operating conditions change frequently, such as navy frigates, patrol vessels and Ro-Ro Pax ferries etc. However, quantitative and systematic investigations of the influence on the fuel consumption of ocean-going cargo ships, which consume much more fuel than any other ship type, by propulsion control as well as the adoption of a shaft generator (power-take-off, PTO) are scarce. This gap in maritime research is addressed in this chapter.

The goals and outline of this chapter are:

- 1) To introduce the propulsion and electric generating systems of the benchmark chemical tanker, which provides all the opportunities to systematically investigate the transport performance of ocean-going cargo ships (Section 2.2).
- 2) To introduce a transport performance indicator termed as the energy conversion effectiveness. This performance indicator can be calculated for different ship speeds and representative environmental conditions and encompasses all energy conversions on board of ships (Section 2.3).
- 3) To develop a theoretic ship propulsion system model and to calibrate (the parameters of) the model with extensive tank and on-board measurement data taken on board of a typical chemical tanker (i.e., full-scale measurements). The model is “balanced”, i.e., approximately equal level-of-detail of component models (Section 2.4).
- 4) To introduce different ship propulsion control modes and electric power generating modes investigated in this thesis (Section 2.5).
- 5) To investigate the effects of different ship propulsion control and electric power generation modes on the energy conversion effectiveness and other performance variables in realistic sailing conditions (Section 2.6).
- 6) The summary and conclusions of this chapter will be provided in Section 2.7.

## **2.2 The propulsion and electric power systems of the benchmark ship**

The layout of the power plant, i.e., propulsion and electric power system, of the benchmark chemical tanker (Figure 1.4) is shown in Figure 2.1. The benchmark ship has a propulsion system, in which a controllable pitch propeller (CPP) directly driven by a two-stroke main diesel engine is installed. Ships equipped with CPP have better manoeuvrability and are more adaptable to different operating conditions (Klein Woud and Stapersma, 2002). With an appropriate control strategy, ship performance can be improved by the application of CPP (Geertsma et al., 2017a). However, for large ocean-going ships such as container ships, tankers and bulk carriers, fixed pitch propellers (FPP) are the most common choice, as these ships do not need a particularly good manoeuvrability and FPP offers the highest efficiency (MAN, 2018). So, the benchmark chemical tanker chosen in this study has a unique propulsion system compared to most of ships of the same or similar types.

The propulsion system with CPP allows to investigate ship performance when operating in different propulsion control modes, i.e., Constant Revolution Mode, Constant Pitch mode and Combinator mode. The electric power generation system of the chemical tanker consists of a shaft generator that is powered by the main engine through a PTO (power-take-off) gearbox and three auxiliary generators driven by three auxiliary diesel engines. The chemical tanker having a power generating system with PTO and auxiliary generators provides the opportunity to investigate the influence on the ship performance of different electric power generation modes, i.e., Aux mode and PTO mode. Both the propulsion control modes and electric power generation modes will be elaborated in section 2.5. Some general information of the ship and power plant of the chemical tanker is presented in Table 2.1 to Table 2.3.

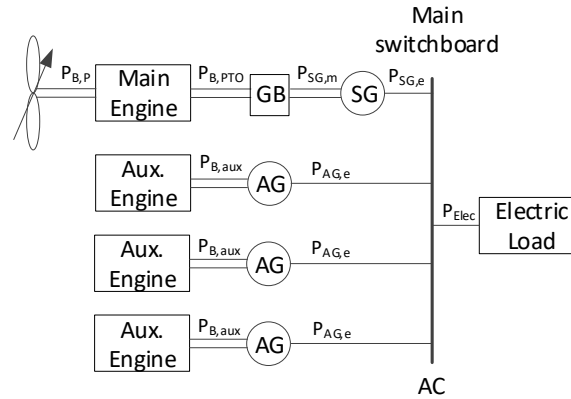


Figure 2.1: Layout of the chemical tanker power plant (i.e., propulsion system and electric power generation + distribution system).

Table 2.1: Ship and propeller particulars of the benchmark chemical tanker.

| Principle Particulars of the Chemical Tanker |        | Parameters of the Propeller |           |
|--|--------|-----------------------------|-----------|
| Length Between Perpendiculars (m)            | 113.80 | Manufacturer                | MAN ALPHA |
| Breadth Molded (m)                           | 22.00  | Kind of Propeller           | CPP       |
| Depth Molded (m)                             | 11.40  | Number of Units (-)         | 1         |
| Design Draught (m)                           | 8.50   | Rated Speed (rpm)           | 167       |
| Design Displacement (m <sup>3</sup> )        | 16988  | Number of Blades (-)        | 4         |
| Dead Weight Tonnage (ton)                    | 13000  | Diameter (m)                | 4.30      |
| Design Speed (kn)                            | 13.30  |                             |           |

Table 2.2: Parameters of the main engine and auxiliary engines

| Parameters                    | Main Engine                       | Auxiliary Engine              |
|-------------------------------|-----------------------------------|-------------------------------|
| Engine Type                   | MAN 6S35ME-B9.3-TII<br>(2-stroke) | DAIHATSU 6DE-18<br>(4-stroke) |
| Number of engines (-)         | 1                                 | 3                             |
| Rated Power (kW)              | 4170                              | 750                           |
| Rated Speed (rpm)             | 167                               | 900                           |
| Stroke (m)                    | 1.55                              | 0.28                          |
| Bore (m)                      | 0.35                              | 0.185                         |
| Mean Effective Pressure (MPa) | 1.67                              | 2.21                          |

Table 2.3: General information of the electric power generation system

| Auxiliary Gensets        |     | Shaft Generator          |      |
|--------------------------|-----|--------------------------|------|
| Number of Sets (-)       | 3   | Number of sets (-)       | 1    |
| Engine output (kW)       | 750 | PTO gearbox output (kW)  | 1100 |
| Generator output (kW)    | 712 | Generator output (kW)    | 1045 |
| Engine Speed (rpm)       | 900 | PTO input speed (rpm)    | 167  |
| Generator Speed (rpm)    | 900 | Generator Speed (rpm)    | 1800 |
| Generator Frequency (Hz) | 60  | Generator Frequency (Hz) | 60   |

## 2.3 Energy conversion effectiveness and fuel index

### 2.3.1 Energy conversion effectiveness

When evaluating the transport performance of ships that transport goods from one port to another the ultimate ship mission must be taken into account (Stapersma, 2017), i.e., the ship mobility power to move a certain useful weight with a certain speed should be added to the end of the power chain of the ship propulsion, as illustrated by Figure 2.2. The main power is provided by the main engine for ship propulsion which overcomes ship resistance at a certain ship speed indicated by the ship effective power (Harvald, 1983; Molland et al., 2011). The auxiliary power is provided by the auxiliary engines, or by the main engine in PTO (power-take-off) mode, to support the ship auxiliary systems, the crew and the cargo, etc., mainly indicated by the electric power for on-board loads. The key connection between the main power and auxiliary power lines in case of PTO is the mechanical "splitting" hub working together with an electrical "merging" hub (Figure 2.2).



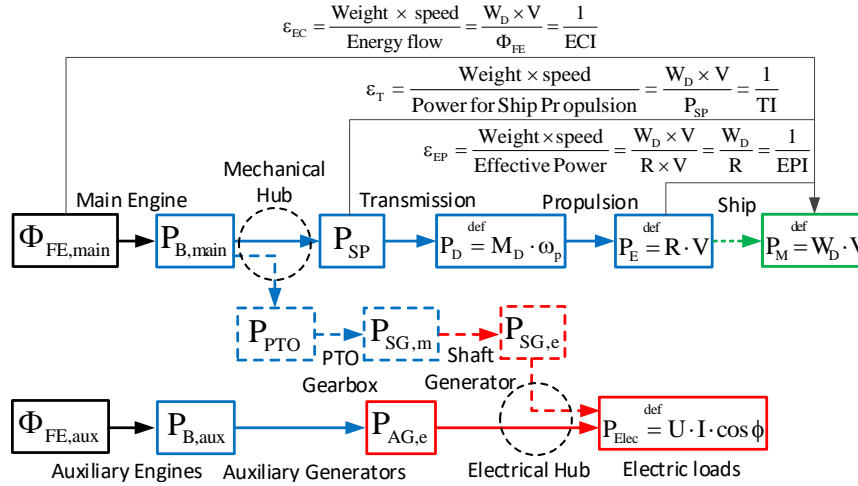


Figure 2.2: Energy conversion in the propulsion system and electric power generating system

In (Gabrielli and Von Karman, 1950), in order to evaluate the transportation performance of ships, the effective power index  $EPI$  (equal to the resistance/weight ratio) is defined by equation (2.1). Note that the resistance/weight ratio which was originally termed as the coefficient of the specific resistance symbolized as  $\varepsilon$  by Gabrielli and Von Karman was actually an index (cost/benefit) and hence will be called an effective power index  $EPI$  in this thesis.

$$EPI = \frac{P_{E,\max}}{W_G \cdot V_{\max}} = \frac{R_{\max}}{W_G} \quad (2.1)$$

where,  $P_{E,\max}$  is the maximum ship effective power, [W];  $R_{\max}$  is the maximum ship resistance, [N];  $W_G$  is the ship gross weight, [N] and  $V_{\max}$  is the maximum ship velocity, [m/s].

However, the effective power index  $EPI$  defined by equation (2.1) to evaluate the ship transportation performance has a number of drawbacks. Firstly, the maximum ship speed and the corresponding maximum ship effective power are used in the definition, which is not representative for ship's operations in reality. Secondly, in the original paper, Gabrielli and Von Karman themselves had already argued that a certain useful load which the ship transports rather than the gross weight of the ship should be used when evaluating the economic performance of transportation of the ship. They failed to do this finally due to lack of exact information. Last but not least, the definition by equation (2.1) only takes the hull resistance into account, i.e., excluding the ship propulsion and power generation. This, nowadays, cannot be neglected when analysing the energy conversion performance of the whole ship.

To solve the first and the second problems, in this thesis the definition of the effective power index  $EPI$  has been improved to equation (2.2). The maximum ship speed and the corresponding maximum ship effective power have been replaced with the operational ones during real ship sailing. The ship gross weight has been replaced by ship dead weight, which following IMO is considered the "useful" weight.

$$EPI = \frac{P_E}{W_D \cdot V} = \frac{R}{W_D} \quad (2.2)$$

where,  $P_E$  is the ship effective power, [W];  $R$  is the ship resistance, [N];  $V$  is the ship speed,



[m/s] and  $W_D$  is the dead weight of the ship, [N].

Extending the concept of the effective power index introduced by (Gabrielli and Von Karman, 1950), the *transport effectiveness*  $\varepsilon_T$  of ships is defined by equation (2.3):

$$\varepsilon_T = \frac{W_D \cdot V}{P_{SP}} \quad (2.3)$$

where,  $P_{SP}$  is the power required for ship propulsion, [W].

Note that effectiveness essentially is a benefit/cost ratio. In the definition of the transport effectiveness  $\varepsilon_T$  by equation (2.3), the ship propulsion and transmission system are included. In order to also include the engine power generation and take both the main engine and auxiliary engines into account, the *energy conversion effectiveness*  $\varepsilon_{EC}$  is defined according to (Stapersma, 2017) by equation (2.4):

$$\varepsilon_{EC} = \frac{W_D \cdot V}{\Phi_{FE,main} + \Phi_{FE,aux}} \quad (2.4)$$

where,  $\Phi_{FE,main}$  is the fuel energy flow into the main engine, [J/s];  $\Phi_{FE,aux}$  is the fuel energy flow into the auxiliary engines, [J/s].

Decomposing the energy conversion effectiveness  $\varepsilon_{EC}$  unveils the different elements of the power chain of the ship. Equation (2.5) shows that the energy conversion effectiveness  $\varepsilon_{EC}$  is the product of familiar component efficiencies, a power distribution factor  $\varepsilon_{hub}$  and a ship effective power effectiveness  $\varepsilon_{EP}$ :

$$\varepsilon_{EC} = \underbrace{\frac{P_{B,main} + P_{B,aux}}{\Phi_{FE,main} + \Phi_{FE,aux}}}_{\eta_{eng}} \cdot \underbrace{\frac{P_{SP}}{P_{B,main} + P_{B,aux}}}_{\varepsilon_{hub}} \cdot \frac{P_D}{P_{SP}} \cdot \frac{P_E}{P_D} \cdot \underbrace{\frac{W_D \cdot V}{P_E}}_{\varepsilon_{EP}} = \eta_{eng} \cdot \varepsilon_{hub} \cdot \underbrace{\eta_{TRM} \cdot \eta_D \cdot \varepsilon_{EP}}_{\varepsilon_T} \quad (2.5)$$

Where,  $P_{B,main}$  is the power of the main engine, [W];  $P_{B,aux}$  is the power of the auxiliary engines, [W];  $P_D$  is the delivered power to the propeller, [W].

The hub distribution factor  $\varepsilon_{hub}$  defined in equation (2.5) includes the engine power required for ship propulsion, since only that power in the end is "useful" and benefits the mobility power, and the engine power produced by both main and auxiliary engines. Note that the introduction of the hub distribution factor also makes it possible to define the combined engine efficiency that takes all power generation on board into account and consequently all fuel consumption. The hub distribution factor  $\varepsilon_{hub}$  is determined by the loads according to which the power distribution or energy management decisions are made, put even more poignantly, the hub distribution factor  $\varepsilon_{hub}$  actually is an "energy management factor" rather than an "energy usage efficiency".

### 2.3.2 Fuel index

Fuel consumption of the ship at each operating point are quantified by the fuel index ( $FI$ , g/(ton·mile)), which is defined by equation (2.6).

$$FI = \frac{\Phi_{Fuel,main} + \Phi_{Fuel,aux}}{m_D \cdot V} \quad (2.6)$$

where,  $\Phi_{Fuel,main}$  is the fuel mass flow into the main engine, [g/h];  $\Phi_{Fuel,aux}$  is the fuel mass flow into the auxiliary engines, [g/h];  $m_D$  is the dead weight tonnage of the ship, [ton]; and  $V$  is the ship speed, [kn].

Note that an index essentially is the inverse of effectiveness, i.e., a cost/benefit ratio.

## 2.4 Propulsion system model description and philosophy

The models of the main components of the ship propulsion system (Figure 2.1), although having a first principle structure with normalised input and output variables, basically are empirical models fitted with a finite number of parameters (rather than look-up tables in which the measured test data are stored directly). The component models are given in this section and they have been calibrated first to available test data (component level) as presented in Appendix A.2. The component models have been integrated into the overall ship propulsion and electric generating system model of the chemical tanker using first principle balances as shown in Figure 2.3. In this case the propulsion system model can be validated by sea trial test data (system level) of the real ship and the actual matching of engine, propeller and ship can be established as shown in Appendix A.3. This is able to make the subsequent results of the analysis realistic as the model is based on hard full-scale data.

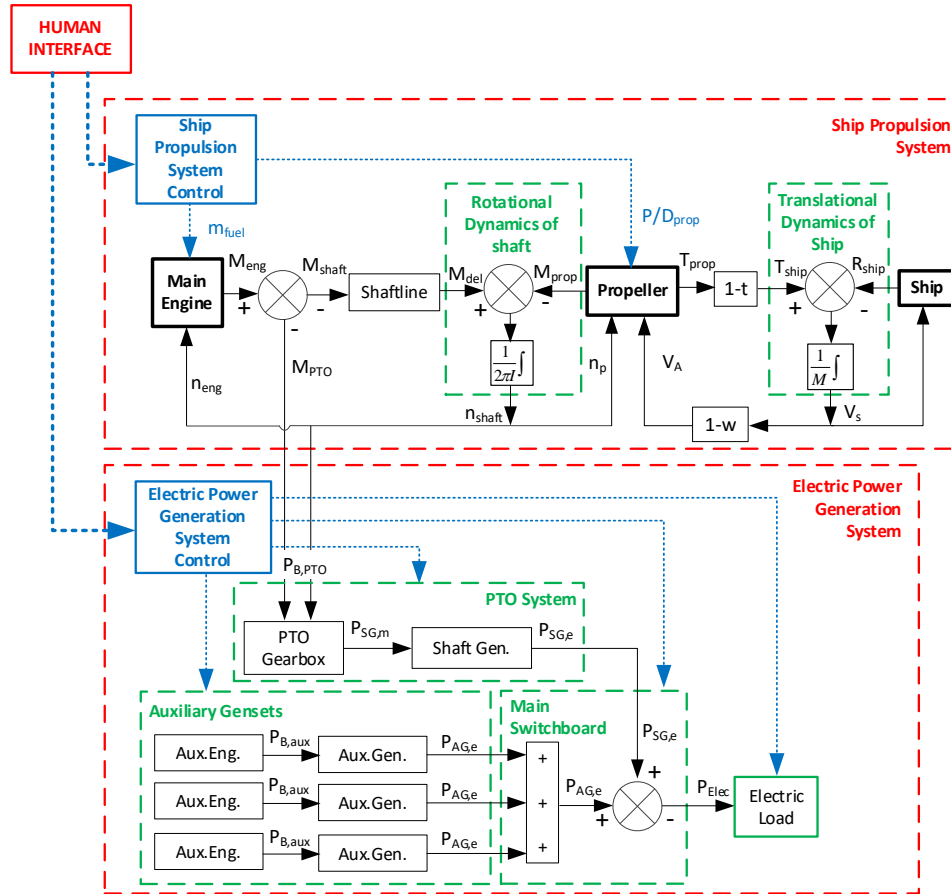


Figure 2.3: Structure scheme of integrated ship propulsion and electric generating systems model of the chemical tanker

For the sake of convenience in modelling and analysis of the ship propulsion system, some variables used in the model of ship propulsion system have been normalised by relating the off-design condition variables to the corresponding variables of a known nominal condition (Klein Woud and Stapersma, 2002) as presented in equation (2.7).

$$X^* = \frac{X}{X_{nom}} \quad (2.7)$$

Where,  $X^*$  is the normalised variables,  $X$  is the relevant variables to be normalised and  $X_{nom}$  is the corresponding nominal value of the variables.

#### 2.4.1 Diesel engine model

The fuel consumption is calculated using the engine torque model introduced in (Shi, 2013), in which the engine torque  $M_{eng}$  is modelled as a function of engine speed  $n_{eng}$  and the injected fuel per cycle  $m_f$  expressed by equation (2.8). This equation essentially is a Taylor series approximation of a function of two variables up to second order terms, including the cross product. The engine torque  $M_{eng}$ , injected fuel per cycle  $m_f$  and the engine speed  $n_{eng}$  have all been normalised as  $M^*$ ,  $m_f^*$  and  $N^*$  according to equation (2.7).

$$\begin{aligned} M^* &= f(m_f^*, N^*) \\ &= 1 - a \cdot (1 - m_f^*) + b \cdot (1 - m_f^*)^2 - c \cdot (1 - N^*) + d \cdot (1 - N^*)^2 + 2 \cdot e \cdot (1 - m_f^*) \cdot (1 - N^*) \end{aligned} \quad (2.8)$$

Where,  $a$ ,  $b$ ,  $c$ ,  $d$  and  $e$  are constants that can be determined using the engine test data.

#### 2.4.2 Ship resistance model

In (Klein Woud and Stapersma, 2002) the specific resistance of ship hull  $C_E$ , which is a non-dimensional parameter indicating the ship resistance characteristics when amongst others ship size, speed and hull form are given. It is defined by equation (2.9).

$$C_E = \frac{P_E}{\rho \cdot \nabla^{2/3} \cdot v_s^3} \quad (2.9)$$

Where,  $P_E$  is the ship effective power (W);  $\rho$  is the density of water ( $\text{kg/m}^3$ );  $\nabla$  is the displacement volume of the hull ( $\text{m}^3$ );  $v_s$  is the ship velocity (m/s).

In this thesis, the ship specific resistance  $C_E$  instead of ship resistance or ship effective power, which is the result of the former, is modelled as a function of ship speed  $v_s$  by equation (2.10). The variables in the following equations have been normalised according to equation (2.7). Both the viscous resistance at lower ship speeds and wave-making resistance at higher ship speeds are modelled by equation (2.10). The wave-making resistance, which takes a very small part of the total resistance at low ship speeds and will increase rapidly at high ship speeds, is modelled as an exponential function of the ship speed. The viscous resistance consists of the basic viscous resistance, a linear correction and nonlinear correction, the latter two contributions being the result of viscous effect at lower Reynolds and being modelled as a linear slope and exponential function respectively.

$$C_E^* = \underbrace{1 - a_{CE}}_{\text{Basic viscous resistance}} + \underbrace{k_{CE} \cdot (v_s^* - 1)}_{\text{Linear correction viscous resistance}} + \underbrace{c_{CE} \cdot (e^{d_{CE} \cdot v_s^*} - e^{d_{CE}})}_{\text{Nonlinear correction viscous resistance}} + \underbrace{a_{CE} \cdot e^{b_{CE} \cdot (v_s^* - 1)}}_{\text{Wavemaking resistance}} \quad (2.10)$$

Viscous Resistance

Where,  $a_{CE}$ ,  $b_{CE}$ ,  $c_{CE}$ ,  $d_{CE}$  and  $k_{CE}$  are constant coefficients, which have been calibrated using ship resistance data as shown in Appendix A.

### 2.4.3 Propeller model

The propeller model introduced in (Klein Woud and Stapersma, 2002) has been applied, as shown in equation (2.11) and (2.12). The propeller thrust coefficient  $K_T$ , torque coefficient  $K_Q$  and advance ratio  $J$  have been normalised as  $K_T^*$ ,  $K_Q^*$  and  $J^*$ .

$$K_T^* = 1 + a_{prop} \cdot (J^* - 1) + c_{prop} \cdot (J^* - 1)^2 \quad (2.11)$$

$$K_Q^* = 1 + b_{prop} \cdot (J^* - 1) + d_{prop} \cdot (J^* - 1)^2 \quad (2.12)$$

Where,  $a_{prop}$ ,  $b_{prop}$ ,  $c_{prop}$  and  $d_{prop}$  are constant coefficients, which have been calibrated using the data of propeller open water characteristics as shown in Appendix A.

### 2.4.4 Wake factor, thrust deduction factor and relative rotative efficiency model

The wake factor  $w$ , thrust deduction factor  $t$  and relative rotative efficiency  $\eta_R$  are modelled as a quadratic function of ship speed  $v_s$  by equations (2.13), (2.14) and (2.15) respectively. Again, these essentially are Taylor series approximations of a function of one variable up to second order terms. The variables in the equations have already been normalised.

$$w^* = 1 - c_w \cdot (1 - v_s^*) + d_w \cdot (1 - v_s^*)^2 \quad (2.13)$$

$$t^* = 1 - c_t \cdot (1 - v_s^*) + d_t \cdot (1 - v_s^*)^2 \quad (2.14)$$

$$\eta_R^* = 1 - c_{\eta R} \cdot (1 - v_s^*) + d_{\eta R} \cdot (1 - v_s^*)^2 \quad (2.15)$$

### 2.4.5 Mechanical transmission losses

The method proposed in (Godjevac et al., 2016) is used to model the transmission losses of propulsion shaft line and PTO gearbox of the ship. The gearbox and shaft losses are presented as a torque loss  $M_{loss}$ , which is expressed as function of the input torque  $M_{in}$  and input speed  $N_{in}$ , shown in equation (2.16). The variables in the equation have already been normalised.

$$M_{loss}^* = k_a \cdot M_{in}^* + k_b \cdot N_{in}^* + k_c \quad (2.16)$$

Where,  $k_a$  is the coefficient related to the torque,  $k_b$  is the coefficient related to the rotational speed and  $k_c$  is the coefficient related to the constant torque loss.

## 2.5 Different ship propulsion control and electric power generation modes

In this thesis, different propulsion control modes as well as different electric power generation modes are taken into consideration to conduct a systematic ship propulsion behaviour investigation.

### 2.5.1 Ship propulsion control modes

A controllable pitch propeller, driven by the main engine is installed in the propulsion system of the chemical tanker. Theoretically, the chemical tanker propulsion system can work in three different control modes, namely Constant Revolution Mode, Constant Pitch mode and Combinator mode as presented in Table 2.4.

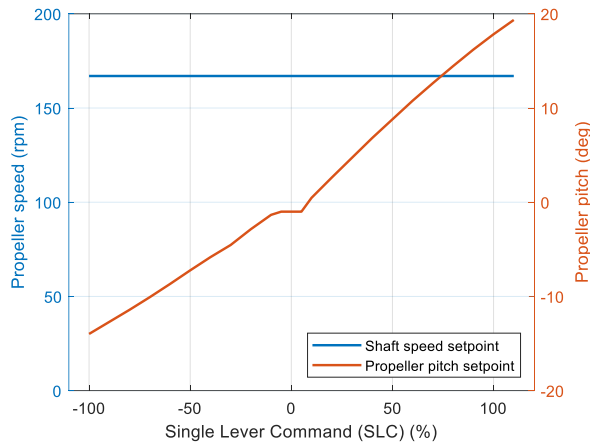
Table 2.4: Ship propulsion control modes

|                          |  |
|--------------------------|--|
| Constant Revolution Mode | CONSTANT revolution & CHANGING pitch (Generator Law)                                     |
| Constant Pitch Mode      | CONSTANT pitch & CHANGING revolution until minimum revolution is reached (Propeller Law) |
| Combinator Mode          | CHANGING pitch & CHANGING revolution (limited by minimum and maximum revolution)         |

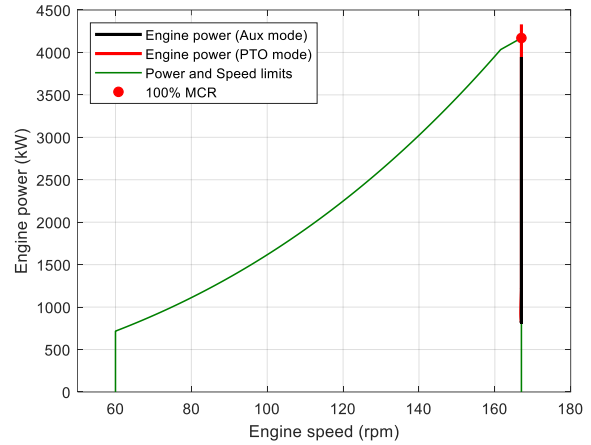
The propeller revolution and propeller pitch are predefined in combinator curves and controlled simultaneously by single lever command (SLC) for these three different propulsion control modes. In each combinator curve, for a given SLC, there will be a certain corresponding propeller revolution and propeller pitch. In constant revolution mode, the ship speed will be controlled by changing the propeller pitch and keeping the propeller revolution constant (Figure 2.4(a)). In the constant pitch mode, the ship speed will be controlled by changing the propeller revolution and keeping the propeller pitch constant until the propeller revolution reaches the minimum revolution limit (Figure 2.5(a)). In the combinator mode, the ship speed will be controlled by changing the propeller revolution (limited by the minimum and maximum revolutions) and pitch simultaneously (Figure 2.6(a)).

The mechanical power, which is either provided by the main engine to the shaft generator through the PTO gearbox in PTO mode or is provided by the auxiliary engine directly to the auxiliary generator in Aux. mode, is 350kW and assumed to be constant. Setting the sea margin as 15% (Appendix B), the operational results in terms of main engine speed and power under the three control modes and the two electric power generation modes are shown in Figure 2.4(b), Figure 2.5(b) and Figure 2.6(b) respectively.

When the electric power is generated in PTO mode, the main engine needs to provide extra power to the shaft generator in addition to the power required by the propulsion system. If the main engine is operating in the high engine speed region, in practice ship speed should be reduced somewhat or, for the sake of the engine operation safety, the electric power generation mode should be switched from PTO mode to Aux mode or the propeller pitch should be reduced slightly to keep the engine power inside the engine operating envelope.

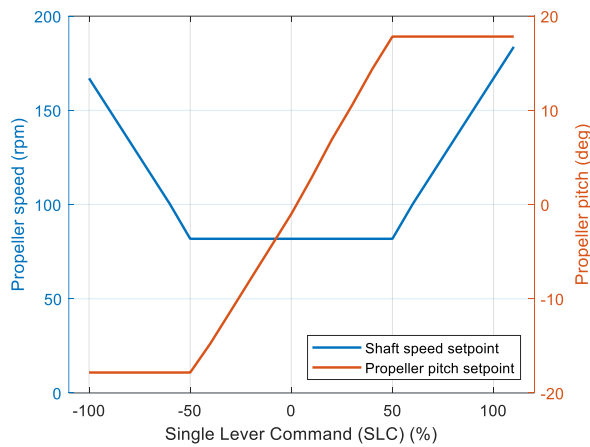


(a) Combinator Curve

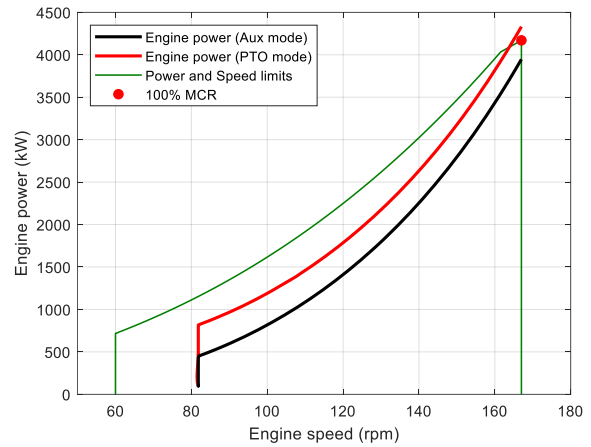


(b) Main Engine Power

Figure 2.4: Constant Revolution control mode.

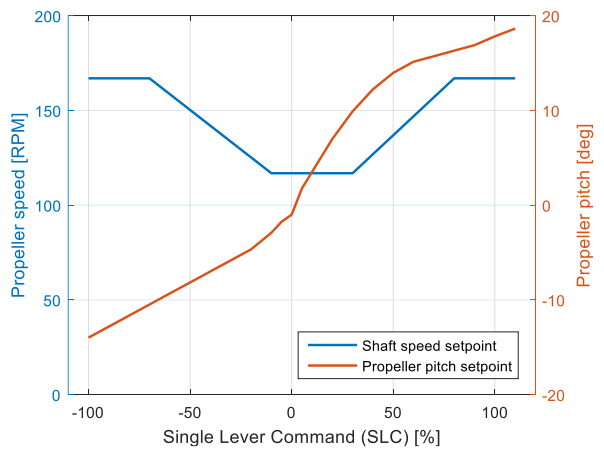


(a) Combinator Curve

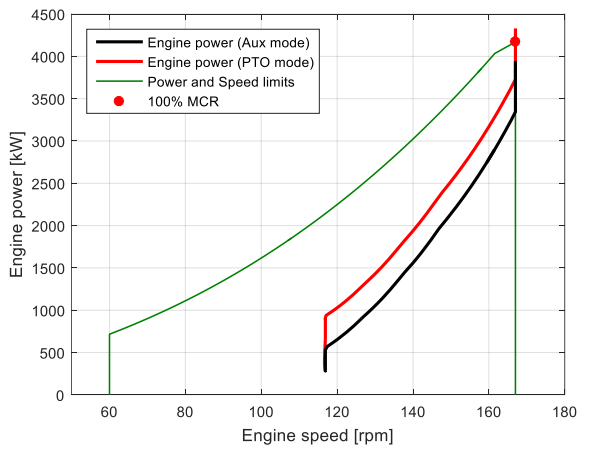


(b) Main Engine Power

Figure 2.5: Constant Pitch control mode.



(a) Combinator Curve



(b) Main Engine Power

Figure 2.6: Combinator control mode.

### 2.5.2 Electric power generating modes

The electric power generation system of the chemical tanker consists of three auxiliary generators driven by three auxiliary engines and one shaft generator driven by the main engine through a PTO gearbox. The electric power required by the on-board electric loads can be provided either by the shaft generator (PTO mode) or by the auxiliary generators (Aux. mode), or even by both the shaft generator and auxiliary generators working in parallel (Combined mode) when a large amount of electric power is needed in some special cases. The latter mode will however not be investigated in this thesis. Table 2.5 presents the electric power generation modes investigated in this thesis.

Table 2.5: Investigated electric power generation modes

|          |  |
|----------|--|
| PTO mode | Shaft generator ON & auxiliary generator OFF |
| Aux mode | Shaft generator OFF & auxiliary generator ON |

## 2.6 Results and discussions

The fuel consumption performance under different propulsion control modes as well as different power generation modes at nominal sea margin ( $SM = 15\%$ , see Appendix B) has been investigated and the results are presented in Figure 2.7 - Figure 2.14. Note that, in reality, the diesel fuel type in ship operation is heavy fuel oil (HFO) for the main engine and marine diesel fuel (MDF) for the auxiliary engines. However, the test results of fuel consumption and emissions for developing and calibrating the models of both the main engine and the auxiliary engines have been corrected at ISO (International Organization for Standardization) standard reference conditions using the standard LHV (Lower Heating Value) of the fuel oil (42,700 kJ/kg), referring to ISO 15550:2016 and ISO 3046-1:2002. Therefore, the fuel consumption during real ship operation has been corrected accordingly as shown in Appendix C in details.

The onboard electric loads are modelled as constant, i.e., 350 kW. The shaft generator and auxiliary generators are modelled by constant energy conversion efficiencies (which is consistent with the constant auxiliary power assumption and the practice of switching on/off auxiliary generators to ensure proper loading of the engines). The efficiencies of the shaft generator and auxiliary generators are both set as 95%.

### 2.6.1 Fuel consumption and fuel index

The combined engine power and fuel flow at different propulsion control modes and power generation modes are shown in Figure 2.7 (a) and (b) respectively. According to Figure 2.7 (a), the combined engine power in PTO mode is slightly higher than that of Aux mode because of the power losses in the PTO gearbox through which the power from the main engine is transmitted to the shaft generator while the power from auxiliary engine is directly transmitted to the auxiliary generator. According to Figure 2.7 (b), the combined fuel flow at Aux mode is higher than that at PTO mode especially at low ship speeds due to the higher specific fuel consumption at Aux mode (Figure 2.8 (a)). For the same ship speeds, especially at low ship speeds, the constant revolution mode requires the highest engine power and fuel flow followed by the combinator mode and the constant pitch mode requires the lowest. This in fact is mainly

caused by the lower propeller efficiency when the pitch is reduced in case of constant revolution and combinator mode compared with the constant pitch mode, as will be elaborated in the next section.

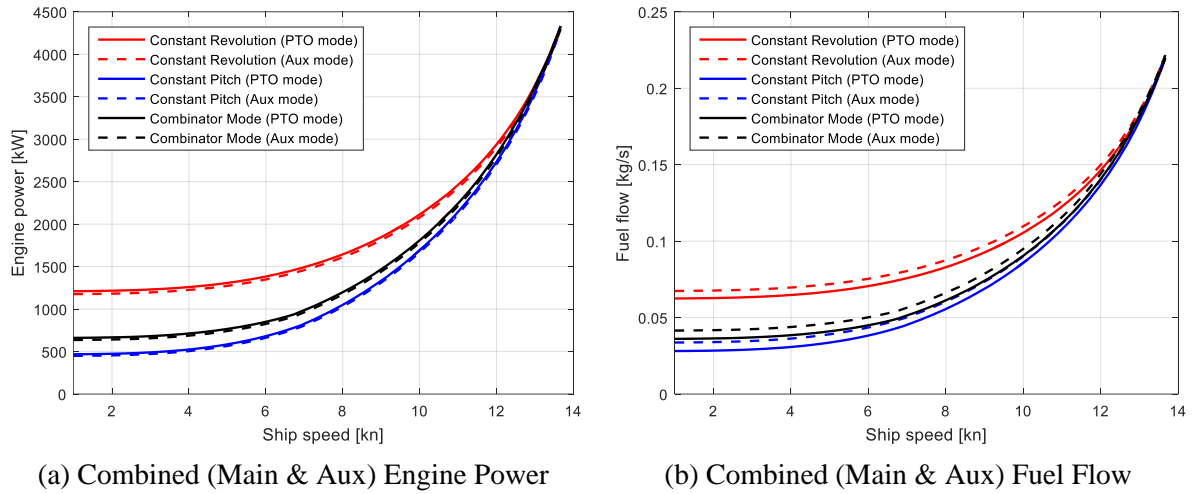


Figure 2.7: Engine Power and Fuel Flow (SM=15%)

The combined specific fuel consumption ( $sfc$ ) under constant revolution control mode is better (lower) than the constant pitch mode and the combinator mode especially at low ship speeds (Figure 2.8 (a)) while the results of fuel index ( $FI$ ) under the three different propulsion control modes are contrary (Figure 2.8 (b)). The reason is that the main engine almost operates in the same region of specific fuel consumption under the three different control modes at high ship speeds while it runs in quite different regions at low ship speeds and for the 2-stroke engines in the benchmark ship the constant revolution mode runs through a better region of  $sfc$  compared with the other two modes (note that for 4-stroke engines constant revolution normally has a worse  $sfc$  compared to constant pitch propeller curve). The fuel index is determined by the fuel consumption flow at a certain ship speed when the ship dead weight remains the same. The constant revolution control mode has a higher fuel consumption flow compared with the other two modes especially at low ship speeds as already shown in Figure 2.7 (b). Furthermore, the lowest fuel index under different propulsion control modes occurs at different ship speeds. It shows the fact that the fuel consumption can be reduced by slow steaming of the ship although the specific fuel consumption of the engines will increase with the reduction of the ship speed. Note that engine specific fuel consumption  $sfc$  is a combined value for main and auxiliary engines (if applicable).



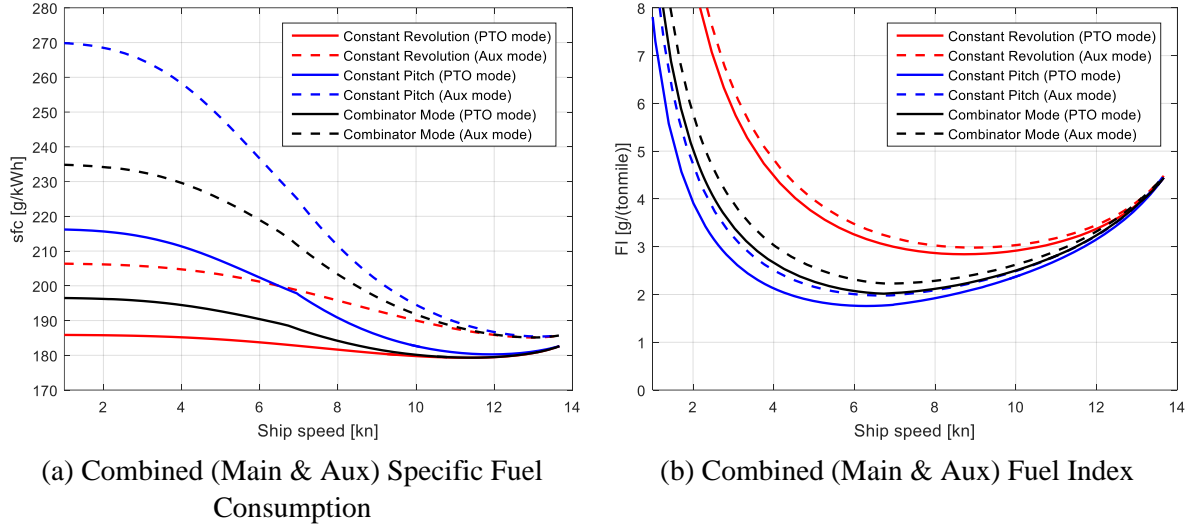


Figure 2.8: Fuel Consumption (SM=15%)

When looking at the electric power generation modes, the combined specific fuel consumption is higher at Aux mode than that at PTO mode especially at low ship speeds (Figure 2.8 (a)). The reason is that, at low ship speeds, the engine power required for propulsion is low and the engine power for electric loads is relatively higher than at high ship speeds. Consequently, the auxiliary engine with higher specific fuel consumption contributes relatively more engine power at low ship speeds resulting in higher combined specific fuel consumption at Aux mode. The difference between operating the shaft generator or auxiliary gensets also has some influence on the combined fuel index and the PTO mode has a lower fuel index in all the three propulsion control modes (Figure 2.8 (b)).

The first lesson is that specific fuel consumption of the engine gives misleading trends and should not be used when considering the overall energy conversion in the ship. Instead, the fuel index should be used since it contains information of the propeller efficiency and auxiliary power conversion as well and therefore is a real system performance indicator unlike *sfc*.

### 2.6.2 Energy effectiveness and efficiencies

The energy conversion effectiveness  $\varepsilon_{EC}$  (Figure 2.10) is actually the inverse of the fuel index and thus the energy conversion effectiveness  $\varepsilon_{EC}$  has the inverse trend as that of the fuel index *FI*. The highest values of the energy conversion effectiveness correspond to the lowest values of the fuel index. In fact, the energy conversion effectiveness  $\varepsilon_{EC}$  is determined by the combined engine efficiency  $\eta_{eng}$  (Figure 2.9), the hub distribution factor  $\varepsilon_{hub}$  (Figure 2.11), the transmission efficiency  $\eta_{TRM}$  (Figure 2.12), the propulsive efficiency  $\eta_D$  (Figure 2.13) and the ship effective power effectiveness  $\varepsilon_{EP}$  which is actually the ratio of ship dead weight to ship resistance  $W_D/R$  (Figure 2.14).

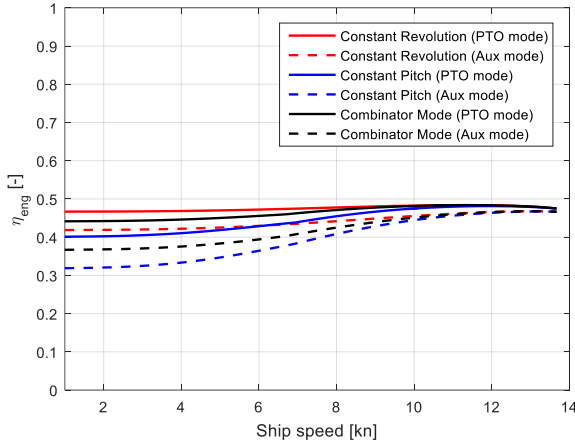


Figure 2.9: Combined (Main &amp; Aux) Engine Efficiency

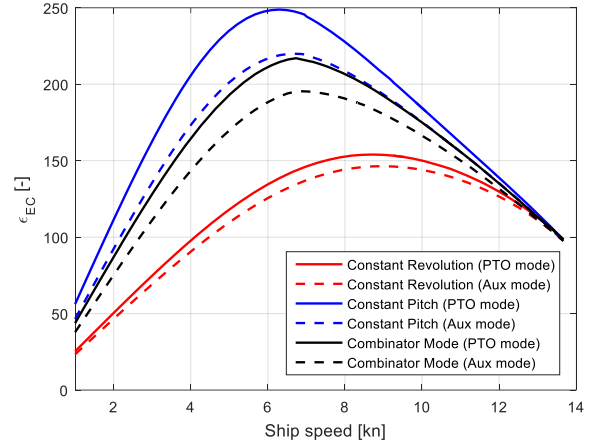


Figure 2.10: Energy Conversion Effectiveness

The combined engine efficiency  $\eta_{eng}$  is actually the inverse of the combined engine specific fuel consumption  $sfc$ . The hub distribution factor  $\epsilon_{hub}$  is determined by the propulsion load provided that the electrical load is kept constant, or rather, the hub distribution factor will increase if the power required for ship propulsion increases. Both increasing the ship speed and changing propulsion control modes from constant pitch mode to constant revolution mode will increase the power required for propulsion and consequently influence the hub distribution factor. In the latter case, it can be explained by the propulsive efficiency  $\eta_D$  of different control modes. At certain ship speeds, in particular at low ship speeds, constant revolution mode with smaller propeller pitch results in lower propulsive efficiency, so the propeller needs more power from engine for ship propulsion. The hub distribution factor at PTO mode is slightly higher than that at Aux mode, because the engine power for electric system at PTO mode is slightly higher than that at Aux mode due to the power losses in the PTO gearbox. The transmission efficiency  $\eta_{TRM}$  of the shaftline does not change much with the ship speed and propulsion control modes having limited influence on the overall performance of the entire power chain.

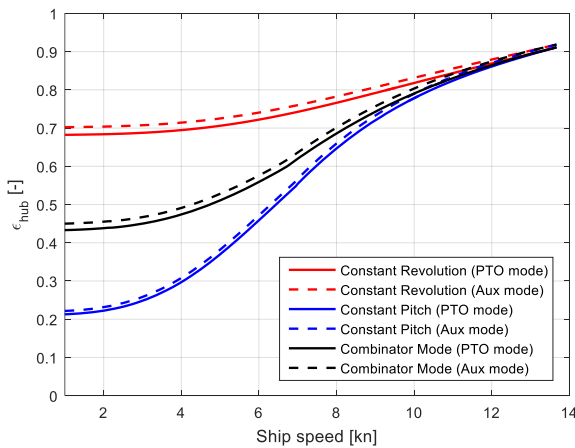


Figure 2.11: Hub Distribution Factor

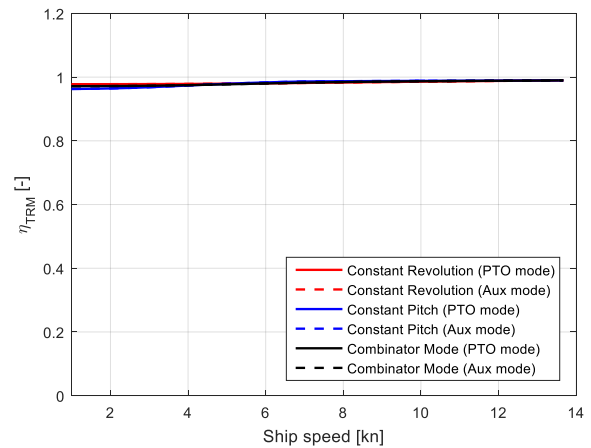


Figure 2.12: Transmission Efficiency

The propulsive efficiency  $\eta_D$  is mainly determined by the propeller efficiency considering

the fact that the ship hull efficiency does not vary too much under different operating conditions. At high ship speeds, the propulsive efficiency under different propulsion control modes shows very small differences because both the propeller speed and pitch are almost the same to obtain the corresponding high ship speeds. When the ship slows down, the propulsive efficiency under all the three different propulsion control modes decreases as a result of the different combinations of propeller speed and pitch to obtain the required low ship speeds. The decrease of propulsive efficiency under constant revolution propulsion control mode is the fastest, followed by the combinator control mode while for the constant pitch control mode the propulsive efficiency changes slowest. In other words, the constant pitch control mode shows the best propulsive efficiency when the ship sails at low speeds while the constant revolution mode has the worst propulsive efficiency and the combinator control modes lies in between. When the ship is operating under constant revolution mode, in order to reduce the ship speed, the propeller pitch has to be reduced, consequently decreasing the propeller efficiency. In fact, the propeller pitch has a dominating effect on the propeller efficiency while the propeller speed hardly has an influence when the ship sails under certain resistance conditions.

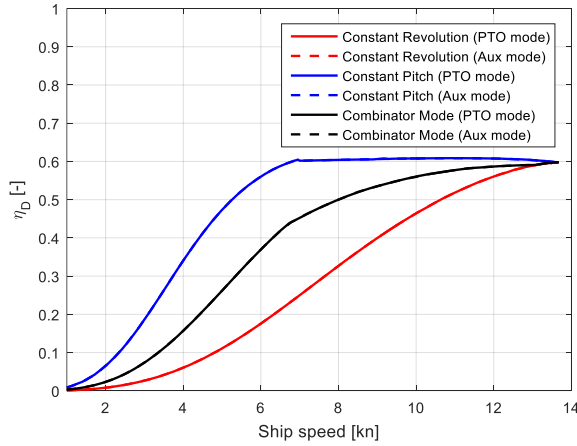


Figure 2.13: Propulsive Efficiency

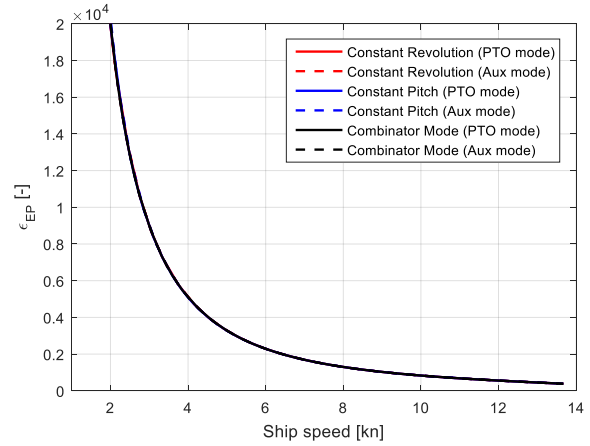


Figure 2.14: Ship Effective Power Effectiveness

The ship effective power effectiveness  $\epsilon_{EP}$ , i.e., the ratio of ship dead weight to resistance  $W_D/R$ , under the three different propulsion control modes will be obviously the same when the ship sails at the same speeds. When the ship slows down, the ship effective power effectiveness  $\epsilon_{EP}$  will increase accordingly, in other words, the power needed for ship propulsion to transport a certain useful load will be reduced significantly when reducing the ship speed. As a consequence, the required engine power will be reduced by a great deal when the ship sails at slow speeds especially when the propulsive efficiency  $\eta_D$  does not change much, for example when the ship is operated under the constant pitch control modes or the ship is propelled by a fixed pitch propeller (FPP) that is the most common case for large ocean-going cargo ships nowadays. In fact, the ship effective power effectiveness  $\epsilon_{EP}$  is the core reason why ship transportation is the most efficient when compared to other transportation modes and the absolute size of useful weight  $W_D$  makes it the most important transportation mode in terms of transport volume as well.

The result of course is that slow steaming within a certain ship speed range will reduce the

fuel consumption. Generating the electric power by the shaft generator (PTO mode) rather than by the auxiliary generators (Aux mode) also saves fuel. Constant revolution control mode consumes more fuel than the other two modes especially at low ship speeds. However, the benchmark chemical tanker operates in constant revolution mode most of the time during transport because of the installed shaft generator, which needs to run at constant revolution. When the ship is operating at constant pitch and combinator modes, where the shaft speed will change significantly with SLC, the onboard electric power will be provided by the auxiliary generators rather than the shaft generator to provide electricity with stable frequency and voltage for the onboard grid.

When comparing the fuel index and energy conversion effectiveness of the ship under constant revolution mode, where the electric power is generated in PTO mode, with those under constant pitch and combinator modes, where the electric power is generated in Aux mode, the disadvantages brought by the constant revolution mode at low ship speeds are essentially the results of the decreased propeller pitch, leading to a lower propeller efficiency which is not compensated by the better specific fuel consumption of the engine and the advantages of the shaft generator.

## 2.7 Summary and Conclusions

This chapter has cleared up some confusion in the existing terminology by developing a consistent and comprehensive theoretical framework of the energy conversion of ships. With the new framework, in addition to having an overall look at the whole power chain, this chapter also has a close look inside the stages of the energy conversion process, providing a deeper insight into the influence of individual “nodes” and “links” of the power chain on the overall performance. The influence on the transport performance by ship operations is provided through a quantitative and systematic investigation on the impact of operational reduction of ship speeds, propulsion control modes and electric power generation modes.

According to results of the ship performance investigation, the most efficient and practical way to reduce the fuel index of a cargo ship not surprisingly is to reduce the ship speed. However, the engine *specific* fuel consumption may increase with the reduction of the ship speed, which is a misleading result. In this chapter *operational* reduction of ship speed has been investigated given a fixed nominal or design speed. In fact, under IMO, ships are designed to be slower by selecting propulsion systems with smaller engines in the design stage to achieve a lower EEDI, which has raised serious concerns regarding ship safety in adverse weather conditions. However, designing the ship for a higher speed but reducing *actual* operational speed during missions will be more effective and safer.

Alternative propulsion control modes also result in differences in the fuel consumption performance especially at low ship speeds. In terms of the fuel index, the constant pitch control mode shows the best performance during various operational conditions while the constant revolution mode is the worst especially during low ship speeds. In terms of the specific fuel consumption of the engines, the constant revolution mode shows a better behaviour compared with the other two control modes in particular at low ship speeds. But, this is a misleading result.

The propulsive efficiency and the effective power effectiveness are the core factors that have a dominating influence on the overall performance of the power chain. The effective power effectiveness presents the core reason why bigger and slower ships are more energy efficient. However, the reduction of the propulsive efficiency at lower ship speed will severely limit the increase of the energy conversion effectiveness that would be possible from the effective power effectiveness, i.e., the favourable weight/resistance ratio at low speeds.

The energy management of the power chain, which is quantified by the hub distribution factor, has a large impact on the energy conversion effectiveness of the ship. The more the power is distributed for ship propulsion compared to the power provided for example to the electrical loads onboard, the higher the energy conversion effectiveness will be, which means the ship will be more efficient. Investigation of the influence on the energy conversion effectiveness by the power-take-off (PTO) shows that, under the same propulsion control mode, generating the electric power by the shaft generator rather than the auxiliary generator also reduces fuel consumption of the ship but the effect is relatively minor.

However, in this chapter, only *point* values of the performance parameters have been investigated while in the end *mean* values weighted over realistic mission profiles must give the real answers, and this will be addressed in Chapter 3.

### **3 Fuel Consumption and Emissions of Ocean-Going Cargo Ship with Hybrid Propulsion and Different Fuels over Voyage\***

#### **3.1 Introduction**

Ship mission profile during the voyage has a significant influence on the fuel consumption and exhaust emissions of ships (Klein Woud and Stapersma, 2002). Therefore, the ship mission profiles should be taken into consideration when evaluating ship transport performance (Stapersma, 2017). However, one of the major drawbacks of the present IMO (International Maritime Organization)'s EEDI (Energy Efficiency Design Index) is that it only considers one operating point without taking the ship's representative mission profiles into account. On the contrary, the EEOI (Energy Efficiency Operational Indicator), which is also developed by IMO, is calculated for a voyage or a number of voyage legs based on real operating conditions (MEPC, 2009). In (Acomi and Acomi, 2014), based on a case study of a handy size Chemical/Product Tanker of 38,000 DWT (Deadweight Tonnage), Acomi, et al. investigate the voyage energy efficiency by calculating the EEOI of the ship using both commercial software and onboard measures. In (Coraddu et al., 2014), in the case study of a RoPax vessel, Coraddu et al. estimate the ship operational performance of the ship voyage using the EEOI as the measure by real data statistics and numerical simulations. In (Hou et al., 2019), Hou et al. optimise the vessel speed of an ice zone ship to find a minimum EEOI in an ice zone. In (Safaei et al., 2015), in the case study of a VLCC (Very Large Crude Carrier) tanker, Safaei et al. address the reduction in fuel consumption of the ship voyage using route optimisation considering ship profile and sea

---

\* This chapter is based on (Sui et al., 2020).

conditions. In (Zaccone et al., 2018), in the case study of a bulk carrier, Zaccone et al. develop a 3D dynamic programming optimisation method to select the optimal path and speed profile for the ship voyage aiming to minimise the voyage fuel consumption and taking also into account ship safety and comfort. However, most of the research focuses on route planning and ship speed profile when studying the ship voyage optimisation. During ship operation, propulsion control (Geertsma et al., 2017b; Geertsma et al., 2018), power management (Vu et al., 2015; Zhao et al., 2016; Kalikatzarakis et al., 2018) and ship operational speeds (Psaraftis and Kontovas, 2013; Lee et al., 2015) will significantly influence the fuel consumption and emissions performance of ships. However, quantitative and systematic investigations on the influence of various ship operations, including propulsion control, power management and operational speeds, on the ship performance of the whole voyage are still limited.

Hybrid propulsion, which is a combination of mechanical and electrical propulsion, is a promising option to improve the economic, environmental and operational performance of ships (Carlton et al., 2013; Bouman et al., 2017). In the basic form of the hybrid propulsion system, the propeller can be mechanically driven by an internal combustion engine and/or electrically driven by an electric motor, which may also be able to work as an electric generator. If the electric motor is powered by a hybrid power supply, such as diesel generator(s), natural gas generator(s), fuel cells and/or batteries, it will be a hybrid propulsion with a hybrid power supply system (Geertsma et al., 2017a). The operation modes of a hybrid propulsion system include power take off (PTO); slow power take in (PTI); boost power take in (Kwasieckyj, 2013). Among others, the benefits of a hybrid propulsion include reduced fuel consumption; reduced CO<sub>2</sub> emissions and other pollutants; possibility to sail and operate with zero emission in coastal and port areas; greater redundancy; noise reduction; lower maintenance (Carlton et al., 2013; Bennabi et al., 2016). However, different ship types can benefit differently from the hybrid propulsion due to their diverse operational profiles (Bennabi et al., 2016; Jafarzadeh and Schjøberg, 2018). In (Jafarzadeh and Schjøberg, 2018), Jafarzadeh and Schjøberg study the operational profiles of eight different ship types, including tankers, bulk carriers, general cargo ships, container ships, Ro-Ro ships, reefers, offshore ships and passenger ships, aiming to identify what ship types are able to benefit from hybrid propulsion. Hybrid ship propulsion is typically applied on naval vessels, towing vessels, offshore vessels and passenger ships including ferries. However, the current applications and research of hybrid propulsion are mainly limited on small ships, while the applications and research on large ocean-going vessels are rare.

To improve the safety and operability of ocean-going cargo ships and to reduce their global greenhouse gas emissions and the local pollutant emissions in coastal and port areas, few studies on the potential applications of hybrid propulsion and power supply system on the big ocean-going cargo ships can be found. In (Yum et al., 2016), based on a multi-physical domain model, a conceptual hybrid propulsion system for a very large crude oil carrier (VLCC) has been studied for the potential benefit of improving the ship's safety and operability in heavy sea conditions without reducing the system efficiency. In (Dedes et al., 2016) and (Kern et al., 2019), the potential benefits of hybrid propulsion for large ocean-going cargo vessels to increase fuel efficiency and reduce greenhouse gas emissions and pollutant emissions are investigated as well.

In (Sui et al., 2019b), the impact of battery–hybrid propulsion on the fuel consumption and emissions of an ocean-going chemical tanker when sailing in coastal and port areas during port approaches has been investigated. However, it is concluded that the battery–hybrid propulsion for ocean-going cargo ships, even when only sailing at low ship speed in close-to-port areas for a short time, is still not a realistic option nowadays even though it can produce zero local emissions; the main reason is that the required battery capacity is very large and the weight of the battery becomes unacceptable.

Using LNG (liquefied natural gas) as the alternative marine fuel is another promising and attractive solution to reducing the local and regional environmental impact and operational costs of ships (Brynolf et al., 2014; Wei and Geng, 2016). Compared to using conventional marine fuels, using LNG produces significantly less pollutant emissions, such as NO<sub>x</sub>, SO<sub>x</sub> and PM (particle matter), and CO<sub>2</sub> emissions will also be reduced as well (Burel et al., 2013; Carlton et al., 2013). Another driver for using LNG as a marine fuel is the current favourable fuel price compared to the increasing price of conventional fuel oil (Thomson et al., 2015). However, one of the disadvantages in the use of LNG as marine fuel is that it may have a worse impact on climate change (global warming) than using conventional fuels, when taking the life-cycle emissions of methane (CH<sub>4</sub>), which is a worse greenhouse gas than CO<sub>2</sub>, into consideration (Brynolf et al., 2014; Thomson et al., 2015). Currently, a relatively small number of ships run on LNG and adopting LNG as a fuel is attractive for ships sailing on fixed routes and large ships sailing in short sea and coastal areas, especially in emission control areas (ECAs) (AEsoy et al., 2011; Acciaro, 2014; Schinas and Butler, 2016). With more stricter emissions regulations coming into force and more infrastructure of LNG fuel growing worldwide, larger ocean-going vessels are expected to select LNG as a fuel in the foreseeable future (Schinas and Butler, 2016). There are many publications indicating the potential benefits of using LNG as a marine fuel, however, quantitative investigations on the impact of using LNG as a fuel on the fuel consumption and emissions of ships over the whole voyage, taking the ship’s operational profile into consideration, are limited.

This chapter will therefore investigate the potential influence of the application of the hybrid ship propulsion and electric power generation system with different fuels as well as various propulsion control and power management strategies on the ocean-going cargo ship in reducing the fuel consumption and emissions over the whole voyage.

The main goals and outline of this chapter are:

- 1) To introduce the conceptual hybrid propulsion and electric power generation system of the benchmark ocean-going chemical tanker (Section 3.2).
- 2) To explain the “average” indicators of the fuel consumption and emissions performance of the ship taking the ship mission profiles of both the transit voyage in open sea and manoeuvre in close-to-port areas into consideration (Section 3.3).
- 3) To present the emissions models of both the main engine (two-stroke diesel engine) and the auxiliary engines (four-stroke diesel engine) (Section 3.4).
- 4) To introduce the ship mission profiles of the transit voyage sailing in open sea and the close-to-port manoeuvre in coastal and port areas (Section 3.5).



- 5) To quantitatively and systematically investigate the influence of the ship operational speeds, propulsion control modes, electric power generation modes, sailing on different fuel types and PTI propulsion mode on the fuel consumption and emissions performance over the whole voyage, including the transit in open sea and manoeuvre in close-to-port areas (Section 3.6).
- 6) In Section 3.7, the summary and conclusions of this chapter will be provided.

### 3.2 Hybridisation of the Benchmark Chemical Tanker

In the benchmark chemical tanker, originally, the shaft generator can only work in PTO mode (Figure 2.1) as introduced in Chapter 2. In order to investigate the potential fuel consumption and emissions performance of a hybrid ocean-going cargo ship especially when sailing in coastal and harbour areas, in this chapter, the original propulsion system and electric power generation system of the benchmark chemical tanker have been conceptually hybridised. In the conceptual hybrid ship propulsion and electric power generation system (Figure 3.1), the shaft generator can also work as a shaft motor in PTI (power take in) mode. To investigate the influence of sailing on different fuels on the fuel consumption and emissions of the ship, both the main engine and auxiliary engines have been assumed (conceptually updated) that they can also use LNG (liquefied natural gas) as their fuels. The details of how the engines will be updated and how different fuels will be stored and managed onboard the ship, which are out of the scope of this thesis, has not been considered. So, after the updates, the benchmark ocean-going chemical tanker will have a hybrid ship propulsion and electric generation system. The power chain of the updated propulsion and electric generating systems is shown in Figure 3.2.

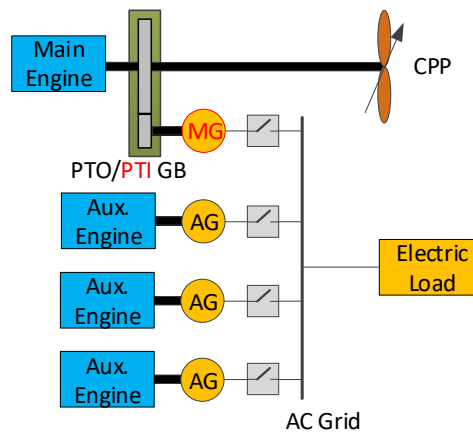


Figure 3.1: Layout of the updated chemical tanker propulsion system and electric generating system

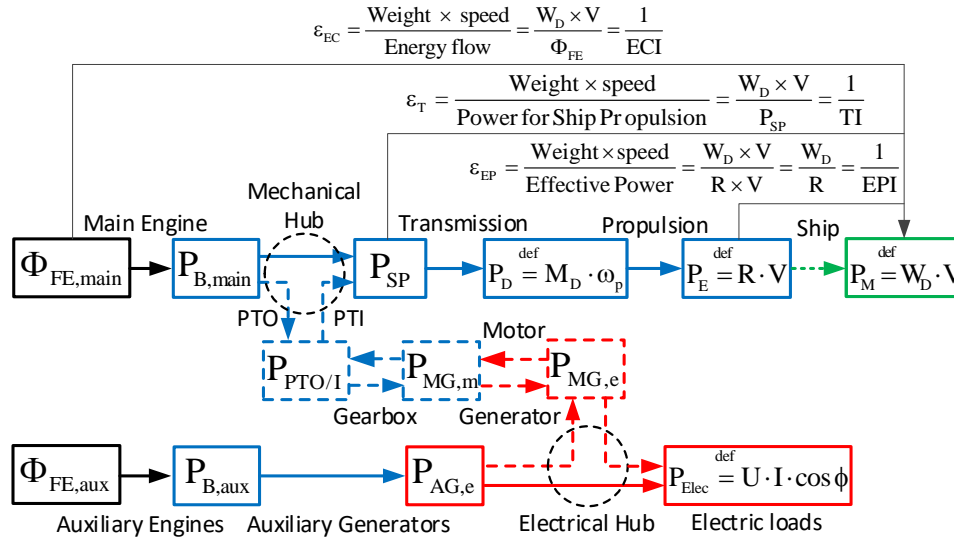


Figure 3.2: Energy conversion in the updated propulsion system and electric power generating system

### 3.3 Mean Value Indicators of Fuel Consumption and Emissions

When taking the ship mission profile into account and in order to express the ship performance as a single value, an operational average value of energy effectiveness and energy (fuel) index has been introduced in (Stapersma, 2017).

The mean energy conversion effectiveness  $\bar{\epsilon}_{EC}$  over voyage, which is the weighted average value over the mission profile of the ship that will be defined later in the section 3.5, is defined in Equation (3.1).

$$\bar{\epsilon}_{EC} = \frac{\sum_i W_{D,i} \cdot V_i \cdot \Delta t_i}{\sum_i (\Phi_{FE,main,i} + \Phi_{FE,aux,i}) \cdot \Delta t_i} \quad (3.1)$$

where  $W_{D,i}$ ,  $V_i$ ,  $\Phi_{FE,main,i}$ ,  $\Phi_{FE,aux,i}$  and  $\Delta t_i$  are the ship dead weight (N), ship speed (m/s), energy flow into main engine (J/s), energy flow into auxiliary engines (J/s) and time of duration in each part of the voyage (h).

Same as for the definition of the mean energy conversion effectiveness, the mean fuel index  $\overline{FI}$  (g/(ton·mile)) and mean emission index  $\overline{EI}$  (g/(ton·mile)) averaged over the whole voyage of the ship are defined by Equation (3.2) and (3.3), respectively.

$$\overline{FI} = \frac{\sum_i (\Phi_{Fuel,main,i} + \Phi_{Fuel,aux,i}) \cdot \Delta t_i}{\sum_i M_{D,i} \cdot V_i \cdot \Delta t_i} \quad (3.2)$$

$$\overline{EI} = \frac{\sum_i (\Phi_{Emission,main,i} + \Phi_{Emission,aux,i}) \cdot \Delta t_i}{\sum_i M_{D,i} \cdot V_i \cdot \Delta t_i} \quad (3.3)$$

where  $\Phi_{Fuel,main,i}$ ,  $\Phi_{Fuel,aux,i}$ ,  $\Phi_{Emission,main,i}$ ,  $\Phi_{Emission,aux,i}$  and  $M_{D,i}$  are the fuel mass flow into

the main engine (g/h), fuel mass flow into auxiliary engines (g/h), emission mass flow generated by the main engine (g/h), emission mass flow generated by auxiliary engines (g/h) and dead weight tonnage of the ship (t) in each part of the voyage, respectively.

### 3.4 Engine emissions model

The emissions are modelled as functions of the engine torque and engine speed, which has a similar form as that of the engine torque model (see equation (2.8)), i.e. the second order Taylor expansion of two variables, including the cross product as shown in equation (3.4).

$$\begin{aligned}\Phi_{em}^* &= f_2(M^*, N^*) \\ &= 1 - a_{em} \cdot (1 - N^*) + b_{em} \cdot (1 - N^*)^2 - c_{em} \cdot (1 - M^*) \\ &\quad + d_{em} \cdot (1 - M^*)^2 + 2 \cdot e_{em} \cdot (1 - N^*) \cdot (1 - M^*)\end{aligned}\quad (3.4)$$

where  $M^*$ ,  $N^*$  and  $\Phi_{em}^*$  are the normalised engine torque, engine speed, fuel mass injected per cycle, emission mass flow, which are normalised by dividing the relevant variables using the corresponding nominal value of the variables;  $a_{em} \sim e_{em}$  ( $a_{NOx} \sim e_{NOx}$  and  $a_{HC} \sim e_{HC}$ ) are constant coefficients, which can be determined using engine test data.

Only the emissions of the carbon dioxide CO<sub>2</sub>, NO<sub>x</sub> and HC (hydrocarbons) are investigated in this thesis. The carbon dioxide is the direct product of the complete combustion of the fuel. So, the CO<sub>2</sub> emission is directly determined by the fuel consumption. More details on the calibration of the NO<sub>x</sub> and HC emissions models of the main engine and auxiliary engines can be found in Appendix A. The NO<sub>x</sub> emission and HC emission as well as the fuel consumption of the main engine and auxiliary engines have been corrected accordingly when different fuels including HFO, MDF and LNG have been used as shown in Appendix C in details.

### 3.5 Ship mission profile

It is assumed that the ship displacement is the design displacement and does not change during the whole voyage including both transit in open sea and manoeuvre in close-to-port areas. In normal sea condition, when sailing in open sea, the ship sails in deep water and the ship resistance addition (10%) is mainly due to the sea state; while, when sailing in coastal and port areas, the ship resistance addition (10%) is mainly due to the shallow water and the effect of sea state is neglected. According to the above assumptions, in normal sea condition, the sea margins when sailing in both open sea and close-to-port area are 15% due to the combined effects of the ship fouling, displacement, sea state and water depth.

#### 3.5.1 Transit in open sea

A combination of ship mission and sea condition profiles for three different voyages of the chemical tanker sailing at open sea has been defined as shown in Table 3.1. Each voyage is divided into three parts, namely Transit A, Transit B and Transit C. In different parts of the voyage the ship speed, transport distance and sea condition, which is represented by the sea

margin (SM), are different. Transit A is in a calm sea condition (low sea margin, 5%), Transit B is in heavy weather (high sea margin, 30%) and Transit C is in a normal sea condition (15% sea margin). The three voyages (I, II and III) have the same total distance (650 n miles) and the same average sea margin (15%), which is defined by Equation (3.5), but have different average ship speeds from fast (13.5 kn) to slow steaming (10 kn).

$$\overline{SM} = \frac{\sum_i SM_i \cdot P_{E,i} \cdot \Delta t_i}{\sum_i P_{E,i} \cdot \Delta t_i} \quad (3.5)$$

where  $\overline{SM}$  is the average sea margin of each voyage obtained by averaging the power over the whole voyage;  $SM_i$  is the sea margin of each part of the voyage;  $P_{E,i}$  is the ship effective power at design draft with clean hull and calm weather;  $\Delta t_i$  is the time of duration in each part of the voyage.

Table 3.1: Ship mission profiles when sailing in open sea.

| Ship Missions and Sea Conditions                 |                                 | Voyages |       |       |
|--|---------------------------------|---------|-------|-------|
|  |                                 | I       | II    | III   |
| Transit A<br>(Calm Sea State:<br>$SM = 5\%$ )    | Ship Speed $V_A$ (kn)           | 13.90   | 12    | 10    |
|  | Time $T_A$ (h)                  | 4.27    | 7.89  | 7.89  |
|  | Sea Margin $SM_A$ (-)           | 1.05    | 1.05  | 1.05  |
| Transit B<br>(Heavy Sea State:<br>$SM = 30\%$ )  | Ship Speed $V_B$ (kn)           | 12      | 12    | 10    |
|  | Time $T_B$ (h)                  | 5.26    | 5.26  | 5.26  |
|  | Sea Margin $SM_B$ (-)           | 1.3     | 1.3   | 1.3   |
| Transit C<br>(Normal Sea State:<br>$SM = 15\%$ ) | Ship Speed $V_C$ (kn)           | 13.66   | 12    | 10    |
|  | Time $T_C$ (h)                  | 38.62   | 41.02 | 51.85 |
|  | Sea Margin $SM_C$ (-)           | 1.15    | 1.15  | 1.15  |
| The whole transit<br>voyage                      | Average Ship Speed (kn)         | 13.50   | 12.00 | 10.00 |
|  | Total Transit Time (h)          | 48.15   | 54.17 | 65.00 |
|  | Total Transit Distance (n mile) | 650     | 650   | 650   |
|  | Average Sea Margin (-)          | 1.15    | 1.15  | 1.15  |

The average ship speeds for the three voyages are systematically going down from voyage I (13.5 kn) to voyage III (10 kn) and transit time is going up accordingly. However, to make it more realistic, for voyage I with average ship speeds of 13.5 kn, the ship speeds of Transit B (where the ship is in heavy weather and the sea margin is 30%) are reduced to 12 kn, because of the high sea state, while the speed loss is assumed to be recovered in part C of the transit. For the voyage II and voyage III in which the average speeds are 12 kn and 10 kn, respectively, the ship speed during the whole voyage remains the same. The detailed determination of the mission profiles when the ship transits in open sea can be found in Appendix D.

For each ship voyage, the influence of different ship propulsion control modes and electric power generation modes on the fuel consumption and emissions of the ship over the whole

voyage will be investigated. The ship propulsion control modes (Constant Revolution Mode and Constant Pitch Mode) and electric power generation modes (PTO Mode and Aux Mode) have been introduced in previous chapter in details.

Note that, if the commanded ship speed cannot be reached within the power limit of the main engine because of providing PTO power, the shaft generator will be shut down and the electric power needed by the ship will be supplied by auxiliary generators, such as Transit A and Transit C of voyage I during which the PTO switch is turned off and the main engine only provides power for propulsion due to the demanded high ship speeds under the corresponding sea margin shown in Table 3.1.

### 3.5.2 Manoeuvring in coastal and port areas

The ship mission profile during the close-to-port manoeuvre is shown in Table 3.2. The ship speed is 7 knots in coastal areas and 5 knots in port areas. The sailing time and sailing distance of the ship in the same area (approaching and leaving) are combined together, respectively, in the ship mission profile in Table 3.2. In coastal areas, the total sailing distance when approaching and leaving the harbour is 40 nautical miles and the total sailing time is 5.71 h. In port areas, the total sailing distance is 10 nautical miles and the total sailing time is 2 h. The sea margin when the ship is sailing in coastal and port areas is assumed to be normal, i.e., 15% sea margin, and the added ship resistance is because of the smaller depth in coastal and port areas compared with the open sea, where the sea state is the main reason for the added ship resistance.

Table 3.2: Ship mission profile sailing in coastal and port areas

| Sailing Area  | Ship Mission Profile      |      |
|---|---------------------------|------|
| Coastal Area  | Ship Speed (kn)           | 7    |
|   | Sailing Distance (n mile) | 40   |
|   | Sailing Time (h)          | 5.71 |
| Port Area   | Ship Speed (kn)           | 5    |
|   | Sailing Distance (n mile) | 10   |
|   | Sailing Time (h)          | 2    |
| The whole harbour<br>approaching and<br>leaving manoeuvre | Average speed (kn)        | 6.49 |
|   | Total Time (h)            | 7.71 |
|   | Total Distance (n mile)   | 50   |

Five different operation cases of the ship are studied to investigate the influence of the ship propulsion and the electric generation modes of a hybrid propulsion ship on the fuel consumption and emissions performance during the close-to-port manoeuvre.

- In case I, the main engine burning heavy fuel oil (HFO) provides power for the ship propulsion and onboard electric loads through shaft generator in PTO mode, while the auxiliary engines are shut down.
- In case II, it is the same as case I except that the fuel burnt by the main engine is

changed from heavy fuel oil (HFO) to marine diesel fuel (MDF).

- In case III, it is also the same as case I except that the fuel for the main engine is changed from HFO to LNG (liquefied natural gas).
- In case IV, the auxiliary engines burning marine diesel fuel (MDF) provide power for the ship propulsion through shaft motor in PTI mode and onboard electric loads, while the main engine is shut down.
- In case V, it is the same as case IV except that the fuel for the auxiliary engines is changed from MDF to LNG.

So, in case I, case II and case III, the ship propulsion system works in PTO mode but on different fuels; while in case IV and case V, the ship propulsion system works in PTI mode but on different fuels. Only the constant revolution mode, in which the ship speed is controlled by changing the propeller pitch and the propeller revolution is kept constant, will be studied during the close-to-port manoeuvre.

## **3.6 Results and discussions**

Note that, the onboard electric loads are modelled by a constant value, which is set as 350 kW. The shaft generator/motor and the auxiliary generators are modelled by constant energy conversion efficiencies. The energy conversion efficiencies of both the generator(s) and motor are set as 95% in the model.

### **3.6.1 Average Ship Transport Performance Over Transit Voyage in Open Sea**

#### **(1) Influence of Different Operation Modes**

The influence of different propulsion control modes and electric power generation modes on the ship performance when sailing in the open sea has been investigated from the voyage perspective. In this section, the fuels for the main engine and the auxiliary engines are set as HFO and MDF, respectively. The average energy conversion effectiveness of the ship over the voyage is shown in Figure 3.3. In voyage I, where the average ship speed is 13.5 kn, different propulsion control and electric power generation modes do not make much difference on the average energy conversion effectiveness (around 100). The reason is that the propeller pitch of the two control modes is almost the same to reach that high ship speed. However, in voyage II and III, where the average ship speeds are 12 kn and 10 kn, respectively, the differences are much more obvious. The average energy conversion effectiveness will increase with the decrease in the average ship speed. Taking the constant revolution control and PTO electric generation modes, for example, the energy conversion effectiveness will increase from 100 to 130 and 150 when the average ship speed decreases from 13.5 kn (voyage I) to 12 kn (voyage II) and 10 kn (voyage III). The major reason is the increase in the ship weight/resistance ratio when reducing the ship speed and it is also the main reason why ship “slow steaming” can save fuel consumption over the voyage.

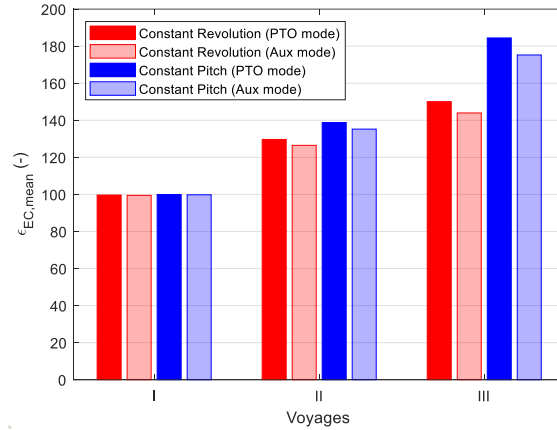


Figure 3.3: Mean value of energy conversion effectiveness.

The “average” ship performance in terms of the fuel and emissions indices during the whole voyage of the ship are presented in Figure 3.4. The average fuel index (Figure 3.4(a)) and the average CO<sub>2</sub> emission index (Figure 3.4 (b)) of the ship over the voyage are in fact the inverse of the average energy conversion effectiveness, so they have the inverse trends. For example, in constant pitch control mode and PTO electric generation mode, the fuel index will decrease from 4.37 to 3.15 and 2.37 (g/(ton·mile)), and the CO<sub>2</sub> emission index will decrease from 14.03 to 10.11 and 7.61 (g/(ton·mile)) when the average ship speed reduces from 13.5 to 12 and 10 (kn). Moreover, during the ship voyage, controlling the ship speed in constant pitch mode rather than the constant revolution mode, and providing the electric power by the shaft generator instead of the auxiliary generator will also reduce the fuel consumption and CO<sub>2</sub> emission over the voyage.

When the average ship speed decreases, the average NO<sub>x</sub> and HC emission index over the whole voyage will also reduce as shown in Figure 3.4(c) and Figure 3.4(d). For instance, under constant pitch and PTO electric generation mode, the NO<sub>x</sub> emission index decreases from 0.33 to 0.24 and 0.17 (g/(ton·mile)) and the HC index reduces from 0.0118 to 0.0098 and 0.0081 (g/(ton·mile)). The constant pitch mode has a lower average NO<sub>x</sub> emission index (Figure 3.4 (c)) than the constant revolution mode. Generating the electric power in PTO mode during the ship voyage will also reduce the NO<sub>x</sub> emission in constant pitch operating mode, while it will increase the NO<sub>x</sub> emission in constant revolution mode. The constant revolution mode has lower HC emission index (Figure 3.4 (d)) than the constant pitch mode especially at low average ship speeds. Unlike the average fuel consumption, CO<sub>2</sub> emission and NO<sub>x</sub> emission, the average HC emission over the voyage will increase when the electric power is provided by the shaft generator (PTO mode). According to the simulation results of the defined three voyages, an effective way to reduce the fuel consumption and emissions indexes is to reduce the average ship speed of the voyage, i.e., slow steaming. Different propulsion control modes and power generation modes also make some differences on the average fuel consumption and emissions indexes of the voyage especially at low ship speeds.

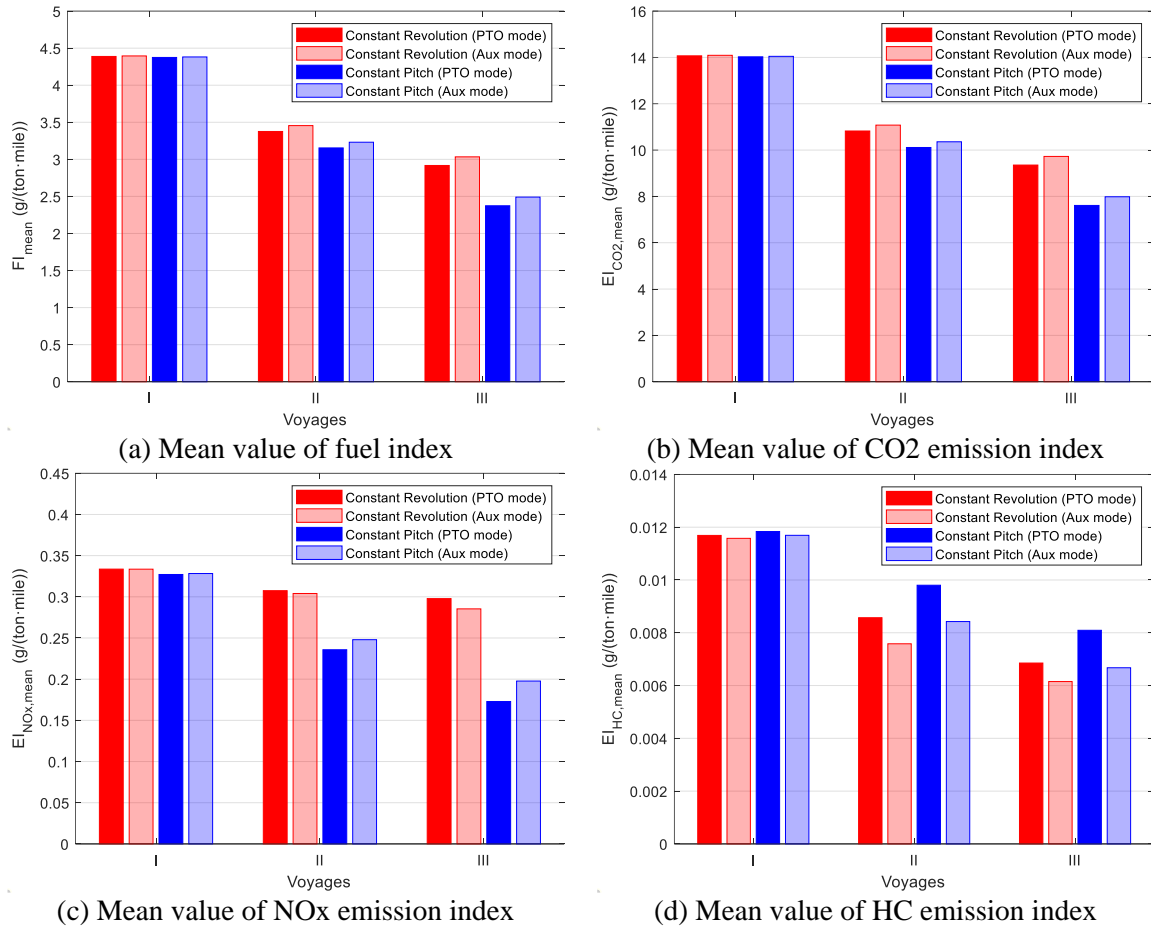


Figure 3.4: Mean value of fuel and emissions indices

## (2) Influence of Sailing on Different Fuels

In this section, when investigating the influence of different fuel types on the fuel consumption and emissions over the whole transit voyage, only voyage II, in which the ship sails at 12 knots while at sea, will be looked into. The propulsion control mode is set as constant pitch mode and the electric generation mode is set as PTO mode. The average fuel and emissions indices of the ship over the whole transit voyage when sailing on different fuels, i.e., HFO, MDF and LNG, are shown in Figure 3.5. The average fuel index of the ship (Figure 3.5 (a)) when sailing on LNG (2.727 g/(ton·mile)) is about 13.5% less compared with sailing on HFO (3.154 g/(ton·mile)) and 12.5% less than MDF (3.117 g/(ton·mile)). The average CO<sub>2</sub> emission index of the ship (Figure 3.5 (b)) when sailing on LNG (7.50 g/(ton·mile)) is about 25.8% less compared with sailing on HFO (10.11 g/(ton·mile)) and 25% less than MDF (10.00 g/(ton·mile)). Note that, the lower heating values (LHV) and the conversion factors between fuel consumption and CO<sub>2</sub> emissions are different for different fuels. The average NO<sub>x</sub> emission index of the ship (Figure 3.5 (c)) when sailing on MDF (0.196 g/(ton·mile)) is about 17% less than sailing on HFO (0.236 g/(ton·mile)), while sailing on LNG (0.039 g/(ton·mile)) can further reduce the NO<sub>x</sub> emission index by 80% compared with sailing on MDF. However, the average HC emission index (Figure 3.5 (d)) of the ship when sailing on LNG (0.065 g/(ton·mile)) is much higher than sailing on HFO (0.0098 g/(ton·mile)) and MDF (0.0065 g/(ton·mile)).



g/(ton·mile)), which is one of the major disadvantages of using LNG as the marine fuel. This is primarily caused by methane slip and unburnt methane during engine operations.

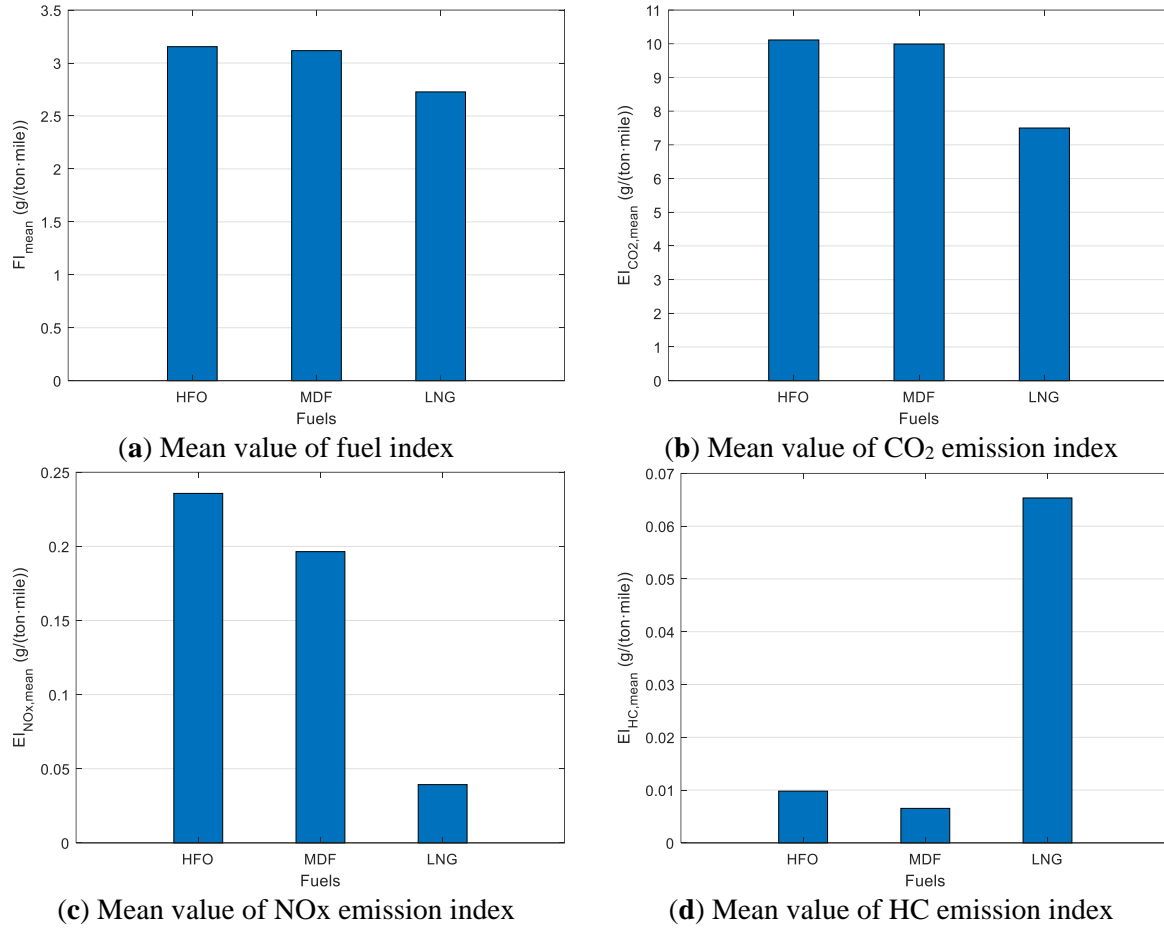


Figure 3.5: Mean value of fuel and emissions indices when using different fuels

### 3.6.2 Average Ship Transport Performance Over Manoeuvring in Close-To-Port Areas

The fuel consumption and emissions performance of the ship during manoeuvre in close-to-port areas under five different operation cases introduced in Section 3.5.2 are investigated. The fuel consumption and emissions of the ship during the whole close-to-port manoeuvre are shown in Figure 3.6. The average fuel indices (Figure 3.6 (a)) and CO<sub>2</sub> emission indices (Figure 3.6(b)) of the ship when sailing on main engine in PTO mode (Case I, II and III) are lower than sailing on auxiliary engines in PTI mode (Case IV and V). However, sailing on auxiliary engines in PTI mode can reduce the local NO<sub>x</sub> (Figure 3.6 (c)) and HC emissions indices (Figure 3.6 (d)) significantly compared with sailing on the main engine in PTO mode.

When sailing on conventional fuels (Case I, II and IV), the fuel index and CO<sub>2</sub> emission index in case I, which are 3.10 and 9.93 (g/(ton·mile)), respectively, are slightly higher than those in Case II, which are 3.06 and 9.81 (g/(ton·mile)); but they are notably lower than those in Case IV, which are 4.25 and 13.62 (g/(ton·mile)), respectively. However, the NO<sub>x</sub> and HC emission indices in Case I, which are 0.35 and 0.0074 (g/(ton·mile)), respectively, are much higher than those in Case II, which are 0.28 and 0.0049 (g/(ton·mile)), respectively; the NO<sub>x</sub> and HC emission indices in Case IV, which are 0.17 and 0.0029 (g/(ton·mile)), respectively, are

further lower than Case II. The reason is that the fuel consumption performance of the main engine (two-stroke) is better than that of the auxiliary engine (four-stroke) burning MDF while the NOx and HC emission performance of the main engine is worse especially when burning HFO compared with the auxiliary engine.

Sailing on LNG (Case III and V) instead of conventional fuels in coastal and port areas can both reduce fuel consumption and CO<sub>2</sub> emission indices of the ship, in particular the local NOx emission index (0.058 g/(ton·mile) in Case III and 0.035 g/(ton·mile) in Case V) will decrease significantly. However, the local HC emission index (0.049 g/(ton·mile) in Case III and 0.029 g/(ton·mile) in Case V) is much higher when sailing on LNG than sailing on HFO and MDF.

Therefore, comparing the five cases, in order to reduce the ship emissions significantly when manoeuvring in close-to-port areas, the ship should be driven by the auxiliary engines through PTI mode. However, a balance between CO<sub>2</sub> and NOx emissions on the one hand and HC emissions on the other needs to be made when selecting to sail the ship on LNG rather than the conventional fuels. Note that, as mentioned earlier, the methane emissions of LNG have no direct health effects on humans. At the same time, it is actually a more potent greenhouse gas than CO<sub>2</sub>. So, from reducing the local pollution point of view, driving the ship in PTI mode and using LNG as the fuel when manoeuvring in close-to-port areas is a better choice compared to the other cases.

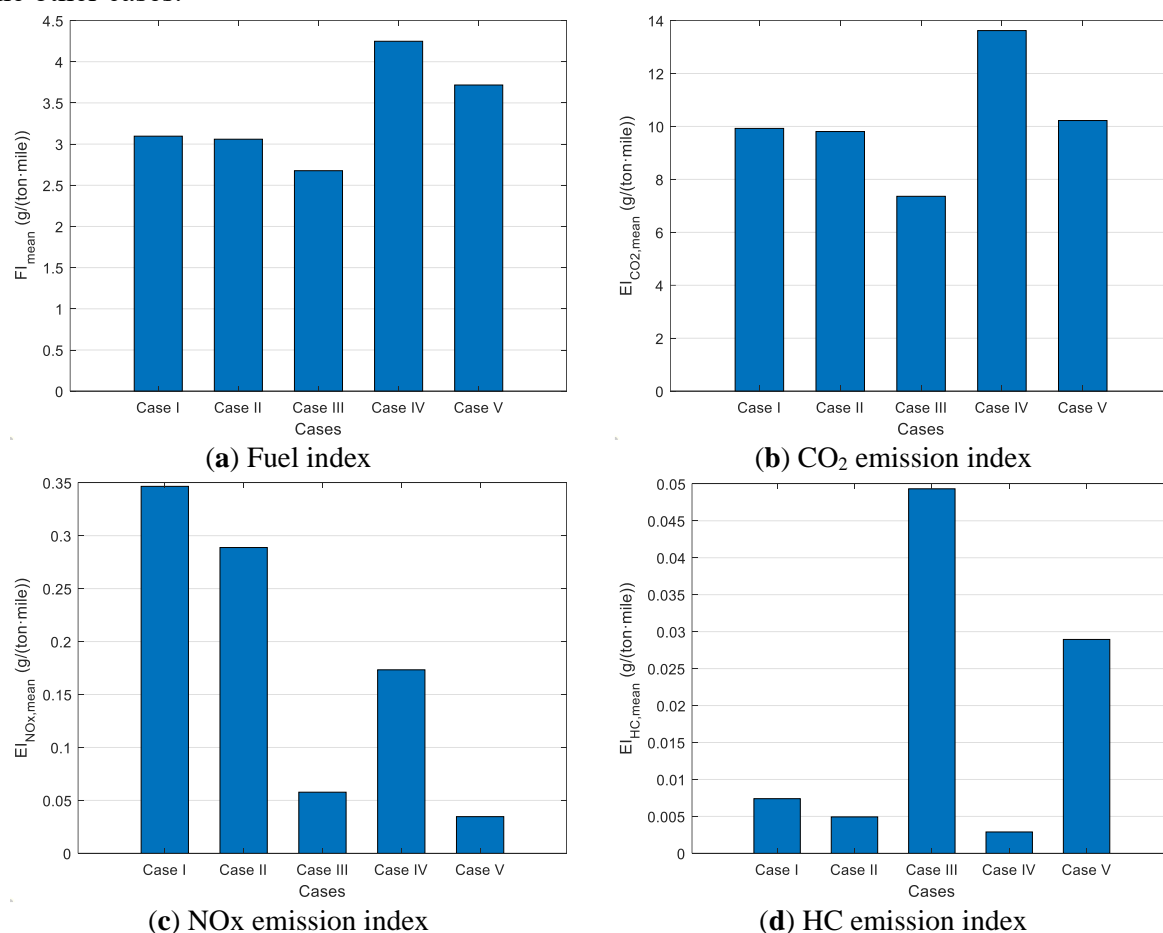


Figure 3.6: Fuel and emissions indices in different cases

### 3.6.3 Fuel Consumption and Emissions of the Whole Voyage

In summary, the average fuel and emissions indexes of the ship over the whole voyage, including transit at open sea, approaching and leaving harbour manoeuvre, are shown in Table 3.3. According to the previous discussions in Sections 3.6.1 and 3.6.2, there are many different combinations of ship operation cases during the whole voyage. For simplicity, only two cases sailing the ship on two different fuels, i.e., HFO and LNG, have been selected and are shown in Table 3.3. The propulsion control modes for transit in open sea and manoeuvring in close-to-port areas are set as constant pitch mode and constant revolution mode, respectively; the electric power generation modes for the whole voyage are set as PTO mode. Compared to transit in open sea, harbour approaching and leaving manoeuvres only take a small part of the total voyage, so, the results of the total voyage shown in Table 3.3 are mainly determined by the fuel and emissions indexes of the voyage when sailing at open sea.

Table 3.3: Average fuel and emissions indexes of the whole voyage

| Fuel Type                             | HFO    | LNG    |
|---------------------------------------|--------|--------|
| $\overline{FI}$ (g/(ton·mile))        | 3.15   | 2.72   |
| $\overline{EI}_{CO_2}$ (g/(ton·mile)) | 10.10  | 7.49   |
| $\overline{EI}_{NOx}$ (g/(ton·mile))  | 0.24   | 0.041  |
| $\overline{EI}_{HC}$ (g/(ton·mile))   | 0.0096 | 0.0642 |

## 3.7 Summary and Conclusions

In this chapter, the influences of the ship propulsion control modes, electric power generation modes, ship operational speeds, propulsion modes as well as sailing on different fuels on the fuel consumption and emissions of an ocean-going benchmark chemical tanker have been investigated taking the ship's operational profiles into account. The current IMO's EEDI considers only one operating point when estimating ship energy efficiency, however, a lower EEDI does not necessarily mean less ship fuel consumption and emissions when sailing with a certain mission profile over the whole voyage. So, the mean value indicators weighted over the ship mission profile should be used when estimating the fuel consumption and emissions performance of the ship over the voyage.

When transiting in open sea, reducing the ship average operational speed will effectively reduce both the fuel consumption and emissions of the ship over the voyage. To reduce the ship operational speed, reducing the propeller revolution rather than the propeller pitch is more preferable, as pitch reduction will reduce the propeller efficiency and consequently increase the fuel consumption especially for voyage where the ship speed is reduced. Generating the electric power by the shaft generator (PTO mode) rather than the auxiliary generator (Aux mode) will further reduce the fuel consumption while the NOx and HC emissions could increase. However, compared to the propulsion control modes, the electric generation modes have relatively minor influence on fuel consumption and emissions of the ship.

When the ship is sailing and manoeuvring in the coastal and port areas, changing the fuel

for the main engine from heavy fuel oil (HFO) to marine diesel fuel (MDF) will reduce the NO<sub>x</sub> and HC emissions significantly while slightly reducing the fuel consumption and CO<sub>2</sub> emissions. Providing the power for ship propulsion (PTI mode) and onboard electric loads by the auxiliary engines and shutting down the main engine will further reduce the local NO<sub>x</sub> and HC emissions significantly while the fuel consumption and CO<sub>2</sub> emission will increase notably mainly due to the lower engine efficiency of the auxiliary engines.

Using LNG (liquefied natural gas) as the fuel for both the main and auxiliary engines will reduce the NO<sub>x</sub> emission significantly compared to using HFO (heavy fuel oil) or MDF (marine diesel fuel). So, sailing the ship on LNG in close-to-port areas will produce much less local environmental impact due to the much less local pollutant emissions. In particular, sailing the ship in PTI mode on LNG will further reduce the local pollutant emissions in coastal and port areas. The fuel consumption and CO<sub>2</sub> emission of the ship will also decrease notably over the whole voyage when sailing on LNG instead of HFO and MDF. However, the hydrocarbon (HC) emission is much higher when using LNG as a marine fuel than traditional diesel fuel due to the methane (CH<sub>4</sub>) slip and unburnt methane during engine operations and although it has no direct effects on human health, it may have a worse impact on climate change (global warming) when taking the life-cycle emissions of natural gas into consideration (although the lifetime of the emitted substance should then also be taken into account, which is outside the scope of this research). It is clear either way that methane emissions from LNG engines should be minimised as much as possible.



## **4 Mean Value First Principle Modelling of Two-Stroke Marine Diesel Engine\***

The engine model used for investigating the ship transport performance (Chapter 2 and Chapter 3) is actually a test-data-based fitting model, which only considers the fuel consumption, emissions, engine torque and engine speed. The (quasi)static test-data-based fitting engine model is adequate to predict the fuel consumption and emissions performance of the ocean-going cargo ship, as for most of the time during a voyage the ship will operate at steady conditions; and transport performance of the ocean-going cargo ship in steady operating conditions is much more important than that during the short transient operations. However, when investigating the ship operational safety (Chapter 6 and Chapter 7), the capability of the ship propulsion plant to accelerate the ship, to crash-stop the ship, to turn the bow of the ship into head sea, and to respond to the dynamic seaway in adverse sea conditions, etc., needs to be evaluated. Since the interactions between the engine, the propeller, the ship and the high sea states are highly dynamic rather than static, not only static but also dynamic behaviour of the ship and the propulsion system should be evaluated, taking not only the static load limits of the main engine but also the dynamic load limits into account (Holt and Nielsen, 2021). A static engine model that only considers static engine torque or power and only takes the static engine operational profile into account is inadequate for predicting the engine's dynamic (over)loading conditions, and may lead to misleadingly optimistic predictions as will be discussed in details in Chapter 6 and Chapter 7. So, correctly modelling the main engine as well as the ship propulsion system is a critical aspect when investigating ship propulsion and manoeuvring performance in adverse sea conditions. The engine model needs to provide more information

---

\* A small part of this chapter has been published in (Sui et al., 2017).

of the engine, including especially the engine thermal loading, mechanical loading and compressor surge, etc., in various operating conditions including both static (steady) and dynamic (transient) operations. For this purpose, the thermodynamic-based mean value first principle parametric (MVFPP) engine model has been developed and will be introduced in details in this chapter.

## 4.1 Introduction

Due to the well-developed technology and high propulsion efficiency, two-stroke marine diesel engines have been dominantly used as the main propulsion engines of the large ocean-going cargo ships such as tankers, bulk carriers and container ships (MAN, 2018), which together account for 91% of the world cargo-carrying fleet in terms of dead-weight tons (dwt) (Carlton et al., 2013; UNCTAD, 2019). In the coming decades, two-stroke marine diesel engines will continue to provide the most propulsion power for the international shipping (Geertsma et al., 2018; IMO, 2020).

With the rapid development of testing, modelling and computing technology, diesel engines have been investigated quite deeply and in considerable details. A great variety of diesel engine models have been developed using different methods and with different levels of details due to various research and application purposes. In order of complexity, the engine models can be recognized as: models only consisting of lookup tables and/or best-fit polynomials, transfer function models, mean value models, filling and emptying (zero- or one-dimensional crank angle models), phenomenological multizone models, and CFD (Computational Fluid Dynamics) models (Schulten, 2005). Generally, an engine model with higher fidelity (which is different than accuracy) is more complex, requiring more input parameters, longer calculation time and always are more difficult to adapt to different operating conditions (Payri et al., 2011; Guan et al., 2014). However, for investigating the engine performance in a larger system such as ship propulsion and manoeuvring systems under various operating conditions, the mean value first principle models are preferable compared with the other types of engine models (Schulten, 2005; Sui et al., 2017; Theotokatos et al., 2018).

To predict the engine behaviour including engine thermal loading, mechanical loading and compressor surge, etc., under various ship propulsion and manoeuvring operations and in different sea conditions, a mean value first principle parametric (MVFPP) model for the two-stroke marine diesel engine has been developed and applied in this thesis. The MVFPP engine model, which is thermodynamic-based, includes the analytical models of the closed in-cylinder process, the gas exchange process and the turbocharger, etc. The model is able to predict the engine's behaviour in both steady (static) and transient (dynamic) operating conditions. For instance, the fuel consumption, air mass flow, scavenge efficiency, air excess ratio, temperatures and pressures in different component volumes, engine torque and speed, heat and mechanical losses, etc., which have the time scale of each operating cycle can be calculated by the MVFPP engine model with a satisfactory accuracy and calculation speed. The thermodynamic-based MVFPP model was originally developed by Delft University of Technology (the Netherlands) and Netherlands Defence Academy (Grimmelius et al., 2007; Sui et al., 2017). The model has been updated and used for many different research applications. In (Grimmelius and Stapersma,

2000) the engine thermal loading prediction and control optimization for marine diesel engines using the MVFPP model have already been studied. In (Schulten and Stapersma, 2003), the mean value model of the gas exchange process for four-stroke diesel engines have been updated. In (Schulten, 2005), the updated MVFPP model for four-stroke diesel engines have been integrated into the ship propulsion and manoeuvring system and the interaction between diesel engines, ship and propellers during manoeuvring has been investigated. In (Stapersma, 2008), an analytic parametric turbocharger model replacing the compressor and turbine maps is introduced into the MVFPP model for investigating the influence of turbocharger matching on ship propulsion performance. In (Geertsma et al., 2017b) and (Geertsma et al., 2018) the MVFPP engine model with a simplified gas exchange process model has been used to investigate the influence of different propeller control strategies on the performance of the ship propulsion performance. In (Sapra et al., 2017), using the MVFPP engine model the influence of the engine back pressure on the thermal loading has been investigated to define the back pressure limits. However, the above-mentioned MVFPP engine models have been mainly applied for four-stroke engines, while for modelling two-stroke diesel engines the model, especially the gas exchange process model, needs to be updated, as the gas exchange process in two-stroke (marine) diesel engines is very different from four-stroke engines.

Modern low speed two-stroke marine diesel engines have uniflow scavenging and large stroke/bore ratios, which are beneficial to the scavenging efficiency and energy efficiency (Stapersma, 2010b). For two-stroke diesel engines, the scavenging process, which is driven by the pressure difference between the inlet receiver and the outlet receiver, is a crucial part of the engine cycle. The scavenging process of two-stroke diesel engines have the important functions of disposing the exhaust gas out of the cylinders, supplying the fresh air to the cylinders for combustion and cooling the hot cylinder parts. Consequently, the performance of a two-stroke diesel engine is highly influenced by the scavenging process (Liu et al., 2014; He and Wei, 2017).

To predict the scavenging process of the two-stroke diesel engines for various applications, scavenging models can be divided into three categories: one-stage models, multi-zone models and CFD models (Sher, 1990; Ding et al., 2019). One-stage models, which include the perfect displacement model and the perfect mixing model, are not realistic for predicting the scavenging process of modern two-stroke diesel engines as the perfect displacement model overestimates while the perfect mixing model underestimates the scavenging performance (Sher, 1990). Due to the large stroke/bore ratios of modern two-stroke marine diesel engines, multi-zone models are preferable for accurate predictions of the scavenging performance (Sher, 1990; Ding et al., 2019; Foteinos et al., 2019). The widely used multi-zone scavenging models such as the Maekawa two-zone model, the Benson and Brandham two-zone model, the Benson three-zone model and the Sher 'S' shape model have been well summarised in (Sher, 1990). However, most of the multi-zone models are empirical or semi-empirical models, which need empirical or experimental parameters of the engine, rather than the first principle models. CFD models are capable of providing very detailed information of the scavenging process for a better understanding of the gas exchange process (Andersen et al., 2013; Sigurdsson et al., 2014), for optimising the cylinder design (Lamas and Rodríguez Vidal, 2012; He and Wei, 2017) and for



developing empirical scavenging models (Cagin et al., 2016; Foteinos et al., 2019). However, CFD models are not very practical for predicting the overall engine performance (Sher, 1990), as the computational cost remains high in terms of both resources and time (Cagin et al., 2016).

In (Ding et al., 2019), a two-zone semi-empirical crank angle model for the scavenging process of the Super-Long-Stroke two-stroke uniflow marine diesel engine has been introduced. The two-zone scavenging model in (Ding et al., 2019) is in effect a combination of the perfect displacement model and the perfect mixing model. In this thesis, an analytical solution of the two-zone model for the mean value first principle modelling of the scavenging process of a two-stroke marine diesel engine has been developed. The two-zone scavenging model is developed for the mean value first principle model of the two-stroke marine diesel engine, which will be further integrated into a larger system, i.e. the ship propulsion and manoeuvring system, for predicting the engine and ship performance under various operating conditions.

Therefore, in this thesis, the MVFPP engine model has been further updated for modelling the two-stroke marine diesel engine, in particular, the gas exchange process model has been largely improved. This chapter will thus mainly focus on the modelling of gas exchange process of the two-stroke marine diesel engine.

The main goals and outline of this chapter are:

- 1) The important concepts and definitions of the mean value first principle model of two-stroke diesel engines will be explained (Section 4.2);
- 2) The mean value first principle model of the closed cylinder process of the diesel engine based on Seiliger cycle will be briefly presented (Section 4.3);
- 3) The mean value first principle model of the gas exchange process of the two-stroke uniflow marine diesel engine, including blowdown, scavenging and expelling processes, will be introduced in details (Section 4.4);
- 4) The engine components models including the models of turbocharger, air cooler, auxiliary blower, exhaust valve temperature, engine mechanical losses and heat losses, etc., will be introduced in Appendix F. The mean value first principle model of the two-stroke marine diesel engine will be validated by the engine test data (Section 4.5);
- 5) Some simulation results of the gas exchange process of the two-stroke marine diesel engine using the MVFPP engine model will be presented and discussed (Section 4.6);
- 6) The summary and conclusions of this chapter will be provided (Section 4.7).

## **4.2 Concepts and definitions of the mean value first principle engine model**

### **4.2.1 In-cylinder processes of two-stroke marine diesel engine**

The in-cylinder processes of a two-stroke marine diesel engine cycle include the closed cylinder process and the gas exchange process as illustrated in Figure 4.1. For a two-stroke diesel engine in the case where the exhaust valve closes (EC) after the inlet ports closes (IC), the closed cylinder process starts from EC and ends at EO (exhaust valve opens).

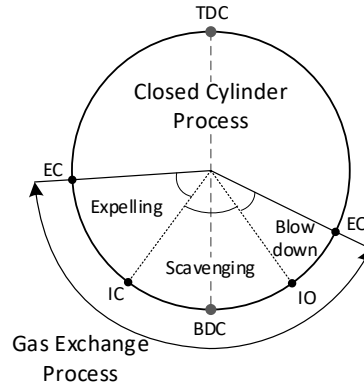


Figure 4.1: In-cylinder processes of two-stroke diesel engine cycle (IC before EC)

The closed cylinder process of four-stroke diesel engines has been modelled by the 6-point Seiliger process (1-2-3-4-5-6) (Figure 4.2) in (Sui et al., 2017). In this thesis, the same 6-point Seiliger process model with some updates is applied for modelling the closed cylinder process of the two-stroke marine diesel engine. According to the 6-point Seiliger process, the closed cylinder process is characterised by the following five stages:

- 1-2: Polytropic compression;
- 2-3: Isochoric combustion;
- 3-4: Isobaric combustion and expansion;
- 4-5: Isothermal combustion and expansion;
- 5-6: Polytropic expansion indicating a net heat loss, used when there is no combustion in this stage (basic); or, 5-6: Polytropic expansion indicating a net heat input caused by late combustion during expansion (advanced).

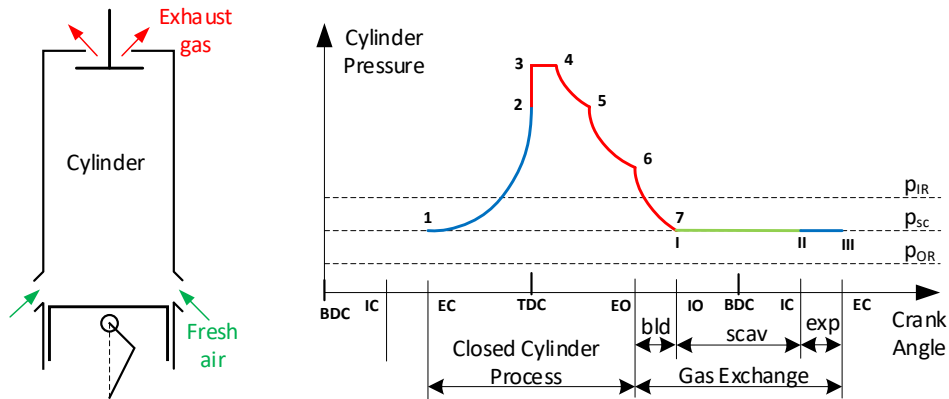


Figure 4.2: Conceptual model of in-cylinder pressure of a two-stroke turbocharged diesel engine (IC before EC)

The gas exchange process (6-7-I-II-III) (Figure 4.2) starts immediately when the exhaust valve opens (EO) after the closed cylinder process and ends at EC. In this thesis, three processes during the gas exchange process, i.e. the blowdown, scavenging and expelling process (Figure

4.2), for a two-stroke diesel engine have been distinguished based on the theories in (Stapersma, 2010c) and (Ding et al., 2019).

- Blowdown (6-7):

When the exhaust valve opens, due to the higher pressure in the cylinder than the pressure in the outlet receiver, part of the gases in the cylinder will blow out entering the outlet receiver automatically. The remaining gases in the cylinder continue their expansion process while the blowdown gases entering the outlet receiver together with the outgoing gases from the cylinder during the following processes will build up the pressure in the outlet receiver before the turbine.

- Scavenging (I-II):

When the inlet ports open, due to the pressure difference between the inlet receiver and the outlet receiver, scavenging gases will flow through the cylinder driving the remaining exhaust gases out of the cylinder and providing fresh air in the cylinder.

- Expelling (II-III):

When the inlet ports are closed and the exhaust valve is still open (IC before EC), a part of the gases in the cylinder will be expelled by the upward moving piston. There will be an air loss during the expelling process.

#### 4.2.2 Volume and resistance elements in MVFPP engine model

According to the information in the project guide of MAN 6S35ME two-stroke diesel engine (MAN, 2014), the layout diagram of the engine is shown in Figure 4.3. The model structure of the two-stroke marine diesel engine is shown in Figure 4.4. Different components in the model, including the air filter, compressor, air cooler, auxiliary blow/non-return valve, inlet receiver, cylinder(s), outlet receiver, turbine and silencer, are connected with each other by the mass flow, temperature and pressure. When modelling the components, the resistance element and volume element method introduced in (Schulten and Stapersma, 2003), which is akin to the lumped parameters modelling approach (Barton, 1992; Hangos and Cameron, 2001; Colonna and van Putten, 2007; van Putten and Colonna, 2007), has been used. The mass flow is calculated as a function of the pressure difference over the component using the resistance element; while the mass, temperature and pressure in a volume is calculated using the volume element, which is actually an integrator (breaking the algebraic loops), based on the mass balance, energy balance and the ideal gas law.

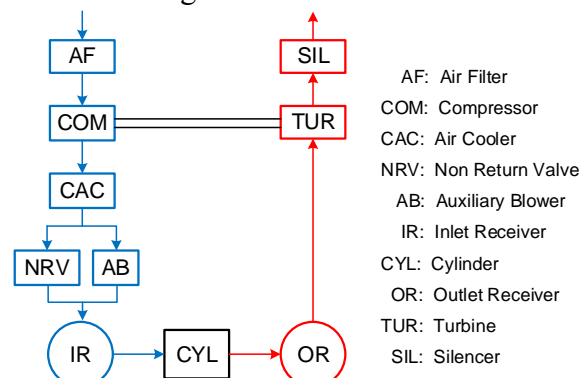


Figure 4.3: Layout diagram of MAN6S35ME two-stroke marine diesel engine

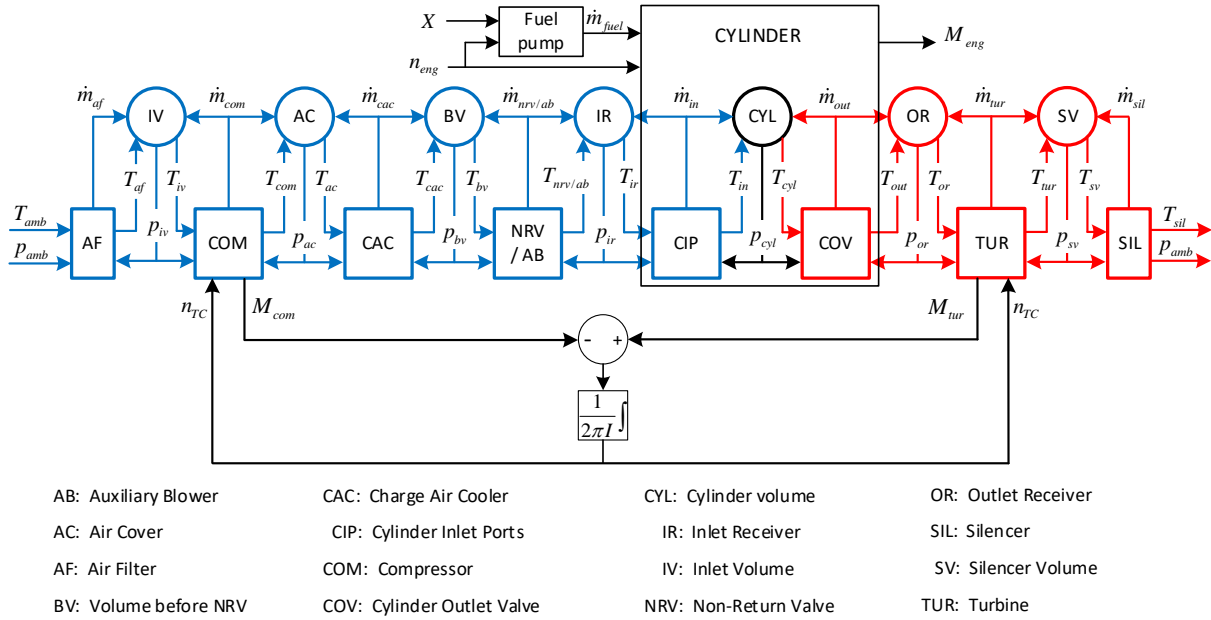


Figure 4.4: Model structure of two-stroke marine diesel engine (updated from (Schulten, 2005) for two-stroke engine)

In a volume element, the mass ' $m$ ' is accumulated at a certain temperature ' $T$ ' and pressure ' $p$ ' and it consists of pure air ' $m_a$ ' and the stoichiometric exhaust gas ' $m_g$ ' as shown in equation (4.1). The composition of the mass is specified by the air mass ratio ' $x$ ' defined by equation (4.2). So, ' $x$ ' indicates the purity of the mass and ' $x=1$ ' means the pure air while ' $x=0$ ' means the stoichiometric combustion gas.

$$m = m_a + m_g \quad (4.1)$$

$$x = \frac{m_a}{m} \quad (4.2)$$

Through the resistance element, the ingoing or outgoing mass flows with certain temperature and composition enter or exit the volume elements. For instance, there is an ingoing mass flow ' $\dot{m}_{in}$ ', which has temperature ' $T_{in}$ ' and composition ' $x_{in}$ ' entering the cylinder volume through the inlet ports; and an outgoing mass flow ' $\dot{m}_{out}$ ', which has temperature ' $T_{out}$ ' and composition ' $x_{out}$ ' exiting the cylinder volume through the outlet valves.

#### 4.2.3 Mass flows of in-cylinder process in MVFPP two-stroke engine model

In the model of the gas exchange process, the mass flow is a key variable that is used for calculating the gas composition, scavenging efficiency, the pressure and temperature in both cylinder and the inlet and outlet receivers. The illustration of the relationships of the mass flows of a two-stroke diesel engine during a work cycle is shown in Figure 4.5.

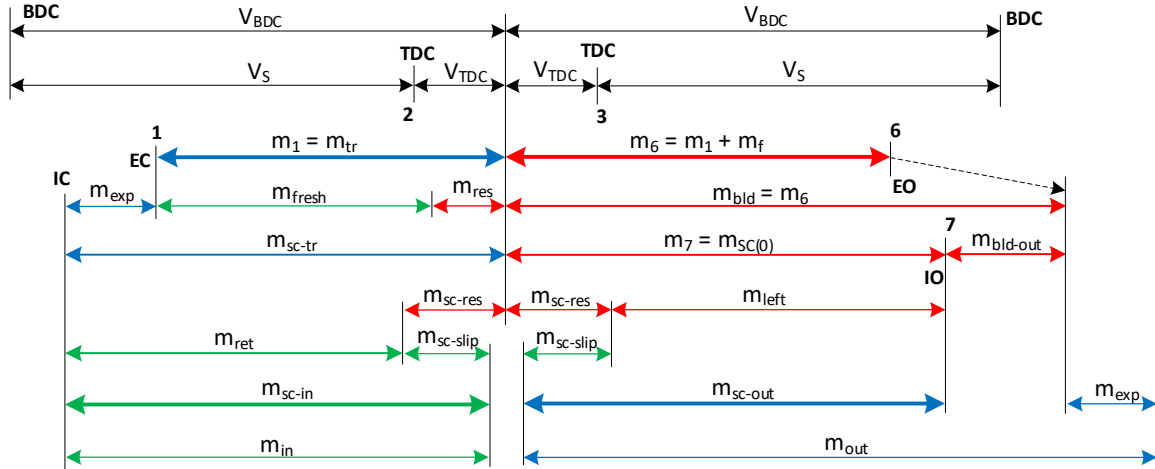


Figure 4.5: Partition of mass flows of a two-stroke diesel engine

The total trapped mass  $m_{tr} (= m_1)$  in the closed cylinder when the exhaust valve closes (EC) consists of the mixture of the fresh air  $m_{fresh}$  and the residual combustion gas  $m_{res}$ .

$$m_1 = m_{tr} = m_{fresh} + m_{res} \quad (4.3)$$

During the closed cylinder process, an amount of fuel will be injected into the cylinder and combusted into gases. So, the mass of in-cylinder gasses at the end of the cylinder process  $m_6$  will be increased by the injected fuel mass  $m_f$  if the combustion is complete.

$$m_6 = m_1 + m_f \quad (4.4)$$

During the blowdown, a part of the in-cylinder gases  $m_{bld-out}$  will blow out to the outlet receiver and the remaining gases  $m_7$  in the cylinder forming the initial mass for the subsequent scavenging process  $m_{sc}(0) (=m_7)$ .

$$m_{bld} = m_6 = m_{sc}(0) + m_{bld-out} \quad (4.5)$$

During the scavenging process, the majority of the exhaust gas  $m_{left}$  will leave the cylinder while a small part of the foul gas  $m_{sc-res}$  remains in the cylinder as a residual.

$$m_{sc}(0) = m_{left} + m_{sc-res} \quad (4.6)$$

The combustion gas that flows out of the cylinder during scavenging  $m_{sc-out}$  includes the left exhaust gas  $m_{left}$  and the fresh air that slips through the engine  $m_{sc-slip}$ .

$$m_{sc-out} = m_{left} + m_{sc-slip} \quad (4.7)$$

For a two-stroke diesel engine, the total fresh air required by the engine  $m_{in}$  for scavenging the cylinder and combustion is supplied only during the scavenging process as there is no inlet stroke, which only exists in the gas exchange process of four-stroke engines.

$$m_{in} = m_{sc-in} \quad (4.8)$$

During scavenging, the fresh air flow  $m_{sc-in}$  is partly retained in the cylinder ( $m_{ret}$ ) while another part slips through the engine ( $m_{sc-slip}$ ).

$$m_{sc-in} = m_{ret} + m_{sc-slip} \quad (4.9)$$

After scavenging, the trapped mass in the cylinder  $m_{sc-tr}$  includes the mixture of the retained

air  $m_{ret}$  and the residual combustion gas  $m_{sc-res}$ .

$$m_{sc-tr} = m_{ret} + m_{sc-res} \quad (4.10)$$

During the extra expelling process, a part of the trapped mixture after the scavenging  $m_{exp}$  will be expelled out of the cylinder and flow into the outlet receiver. Therefore, the total trapped mass in the cylinder  $m_{tr}$  for the closed cycle process when the exhaust valve is closed (EC) will be reduced and there will be a fresh air loss during the extra expelling.

$$m_{tr} = m_{sc-tr} - m_{exp} \quad (4.11)$$

The total mass flow coming out of the engine  $m_{out}$  includes the blowdown flow  $m_{bld-out}$ , scavenging outgoing flow  $m_{sc-out}$  and the expelling flow  $m_{exp}$ .

$$m_{out} = m_{bld-out} + m_{sc-out} + m_{exp} \quad (4.12)$$

### 4.3 Closed cylinder process model

The five Seiliger stages (Seiliger, 1922; 1926) are parameterised by the Seiliger parameters as shown in Table 4.1. The three combustion stages, i.e., the isochoric combustion, the isobaric combustion and the isothermal combustion are characterised by the combustion parameters  $a$ ,  $b$  and  $c$  respectively. The polytropic compression is parameterised by the polytropic compression exponent  $n_{comp}$  and the effective compression ratio  $r_c$ ; while the polytropic expansion is indicated by the polytropic expansion exponent  $n_{exp}$  and the expansion ratio  $r_e$ . For a certain engine, the effective compression ratio  $r_c$ , which depends on the geometry of the combustion chamber and the timing of inlet valve closing (IC), can be set as constant. The polytropic compression exponent  $n_{comp}$  can also be regarded as constant during the compression process under various operating conditions according to the real process. The expansion ratio  $r_e$  depends on the combustion parameters  $b$  and  $c$  and the timing of the exhaust valve opening (EO), only the latter being constant. The polytropic expansion exponent  $n_{exp}$  is assumed to be constant for the basic Seiliger process but like  $a$ ,  $b$ , and  $c$  is a variable for the advanced Seiliger process (Sui et al., 2017). In this thesis, the basic Seiliger process has been used, so  $n_{exp}$  has been set as a constant in the model.

Once all the Seiliger parameters are known, the pressures, temperatures, work and heat in the various stages of the Seiliger cycle can be calculated according to Table 4.1 and Table 4.2. For details on the influence of the Seiliger parameters on the engine performance and how to determine the Seiliger parameters, please refer to (Stapersma, 2010b; Ding, 2011; Stapersma, 2016b; Sui et al., 2017), where the closed cylinder process of diesel engines has been investigated and analysed extensively.

Table 4.1: Seiliger process definition and parameters (Stapersma, 2010b)

| Seiliger stage | Volume $V$              | Pressure $p$                       | Temperature $T$                      | Seiliger parameters |
|----------------|-------------------------|------------------------------------|--------------------------------------|---------------------|
| 1-2            | $\frac{V_1}{V_2} = r_c$ | $\frac{p_2}{p_1} = r_c^{n_{comp}}$ | $\frac{T_2}{T_1} = r_c^{n_{comp}-1}$ | $r_c, n_{comp}$     |
| 2-3            | $\frac{V_3}{V_2} = 1$   | $\frac{p_3}{p_2} = a$              | $\frac{T_3}{T_2} = a$                | $a$                 |
| 3-4            | $\frac{V_4}{V_3} = b$   | $\frac{p_4}{p_3} = 1$              | $\frac{T_4}{T_3} = b$                | $b$                 |
| 4-5            | $\frac{V_5}{V_4} = c$   | $\frac{p_4}{p_5} = c$              | $\frac{T_5}{T_4} = 1$                | $c$                 |
| 5-6            | $\frac{V_6}{V_5} = r_e$ | $\frac{p_5}{p_6} = r_e^{n_{exp}}$  | $\frac{T_6}{T_5} = r_e^{1-n_{exp}}$  | $r_e, n_{exp}$      |

Table 4.2: Specific work and heat in Seiliger process

| Seiliger stage | Work $W$ (J)   | Heat $Q$ (J)  |
|----------------|--|---|
| 1-2            | $W_{12} = \bar{m}_{12} \cdot \frac{\bar{R}_{12}}{n_{comp} - 1} \cdot (T_1 - T_2)$          | $Q_{12} = \bar{m}_{12} \cdot \frac{\bar{K}_{12} - n_{comp}}{n_{comp} - 1} \cdot \bar{c}_{v,12} \cdot (T_2 - T_1)$ |
| 2-3            | $W_{23} = 0$   | $Q_{23} = \bar{m}_{23} \cdot \bar{c}_{v,23} \cdot (T_3 - T_2)$  |
| 3-4            | $W_{34} = \bar{m}_{34} \cdot \bar{R}_{34} \cdot (T_4 - T_3)$                               | $Q_{34} = \bar{m}_{34} \cdot \bar{c}_{p,34} \cdot (T_4 - T_3)$  |
| 4-5            | $W_{45} = \bar{m}_{45} \cdot \bar{R}_{45} \cdot T_4 \cdot \ln\left(\frac{V_5}{V_4}\right)$ | $Q_{45} = \bar{m}_{45} \cdot \bar{R}_{45} \cdot T_4 \cdot \ln\left(\frac{V_5}{V_4}\right)$                        |
| 5-6            | $W_{56} = \bar{m}_{56} \cdot \frac{\bar{R}_{56}}{n_{exp} - 1} \cdot (T_5 - T_6)$           | $Q_{56} = \bar{m}_{56} \cdot \frac{n_{exp} - \bar{K}_{56}}{n_{exp} - 1} \cdot \bar{c}_{v,56} \cdot (T_6 - T_5)$   |

## 4.4 Gas exchange process model

### 4.4.1 Blowdown model

The blowdown process (6-7) starts immediately when the exhaust valve opens (EO) after the closed cylinder process. During the blowdown process, a part of the gases leaves the cylinder and the rest of the gases remain in the cylinder. It is assumed that the remaining gases in the cylinder continues the polytropic expansion with an increasing cylinder volume (from  $V_6$  to  $V_7$ ). The pressure in the cylinder  $p_7$  after blowdown is assumed to be the scavenging pressure  $p_{scav}$ , which is higher than the pressure in the outlet receiver  $p_{or}$ . The left part of the gases that blows down out of the cylinder continues the expansion in the outlet receiver. The details of the blowdown model can be found in Appendix E.

The temperature and the remaining mass in the cylinder after blowdown are calculated by equations (4.13) and (4.14) respectively. The mass and temperature of the blowdown-out gases into the outlet receiver during blowdown are calculated by equations (4.15) and (4.16) respectively.

$$T_7 = T_6 \cdot \left( \frac{p_7}{p_6} \right)^{\frac{n_{\text{exp}} - 1}{n_{\text{exp}}}} \quad (4.13)$$

$$m_7 = \frac{p_{\text{scav}} \cdot V_{IO}}{R_7 \cdot T_7} \quad (4.14)$$

$$m_{\text{bld-out}} = m_6 - m_7 \quad (4.15)$$

$$T_{\text{bld-out}} = \frac{m_6 \cdot T_{\text{bld}} - m_7 \cdot T_7}{m_{\text{bld-out}}} \cdot \left( \frac{1}{\kappa_{\text{bld}}} + \frac{\kappa_{\text{bld}} - 1}{\kappa_{\text{bld}}} \cdot \frac{p_{\text{or}}}{p_{\text{scav}}} \right) \quad (4.16)$$

The composition of the gases during blowdown is the same as that in cylinder at the end of the closed cylinder process, which is calculated by the closed cylinder process model.

$$x_7 = x_{\text{bld-out}} = x_6 \quad (4.17)$$

#### 4.4.2 Scavenging model

##### (1) Two zones and two stages during scavenging

According to the newly developed two-zone scavenging model, during the scavenging process, the cylinder volume is divided into two zones, i.e., A zone and B zone (Figure 4.6).

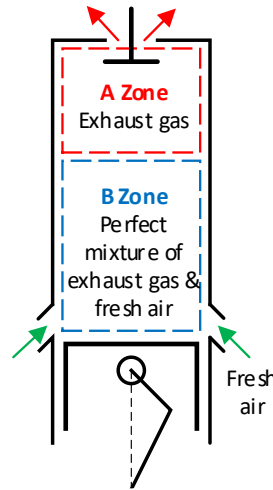


Figure 4.6: Two zones of scavenging model for Super-Long-Stroke two-stroke diesel engine

- A Zone:

A Zone, which is near to the exhaust valve, contains only 'pure' exhaust gas that is left from the previous cycle after blowdown. It is assumed that A zone is a zero-dimensional volume, in which the state in A zone is homogeneous.

- B Zone:



B Zone, which is near to the inlet ports, contains a perfect mixture of the exhaust gas and the fresh air. It is assumed that B zone is also a zero-dimensional volume, in which the entering fresh air perfectly mixes with the initially existing exhaust gas and reaches a homogeneous state immediately.

As mentioned previously, neither a perfect displacement model (with B zone containing pure fresh air) nor a perfect mixing model (without A zone) is realistic for long-stroke two-stroke marine diesel engines. So, in order to make it more realistic for predicting the scavenge process of two-stroke engines, the new model combines the perfect displacement model and perfect mixing model (Figure 4.6).

The mass ratios of gas in A zone  $S_A$  and B zone  $S_B$  to that in the whole cylinder volume, which quantify the size of A zone and B zone in terms of mass during scavenging, are defined by equations (4.18) and (4.19):

$$S_A \stackrel{def}{=} \frac{m_A}{m_A + m_B} \quad (4.18)$$

$$S_B \stackrel{def}{=} \frac{m_B}{m_A + m_B} = 1 - S_A \quad (4.19)$$

where,  $m_A$  is the gas mass of A zone,  $m_B$  is the gas mass of B zone.

The mass ratio  $S_A$  decreases from an initial value  $S_A(0)$  to, if the scavenging time is sufficiently long, zero during the scavenging process. Depending on the developments of the two zones, two stages of the scavenging process are distinguished, i.e., stage I and stage II.

- Stage I:

During stage I, both A zone and B zone exist in the cylinder. B zone grows from an initial size during the scavenging process and pushes A zone out of the cylinder to the outlet receiver. A zone will decrease gradually and finally disappear (mass ratio  $S_A$  equals 0) if the scavenging mass flow and scavenging time are sufficient.

- Stage II:

During stage II, A zone has been expelled out of the cylinder and only B zone exists in the cylinder, so B zone is of the same size as the whole cylinder volume. Note that stage II cannot occur if the scavenging time is insufficiently long and, in this case, only stage I exists during the scavenging process.

## (2) Mean value scavenging mass flow and relative scavenging time

### *Mean value scavenging mass flow of the engine*

In the mean value model, all the mass flows in the engine have been averaged over the full cycle (Stapersma, 2010a). So, accordingly the mean value scavenging mass flow is calculated by equation (4.20).

$$\dot{m}_{sc-in} \stackrel{def}{=} \frac{i \cdot \int_{t_{IO}}^{t_{IC}} \tilde{m}_{sc-in} \cdot dt}{t_{cycle}} \quad (4.20)$$

where,  $i$  is the number of the cylinders of the engine;  $\tilde{m}_{sc-in}$  is the real ingoing scavenging mass flow per cylinder of the engine;  $t_{cycle}$  is the time of the full cycle and is calculated by  $t_{cycle} = k/N$ , in which  $N$  is the engine rotational speed and  $k$  is the number of revolutions per cycle (for two-stroke engine  $k=1$ , and for four-stroke engine  $k=2$ );  $t_{IO}$  and  $t_{IC}$  are the time when the inlet ports open and close respectively.

It is assumed that the pressures in both the cylinder and the inlet receiver are constant during the scavenging process. As a result, the scavenging mass flow  $\tilde{m}_{sc-in}$ , which can be calculated by the resistance element of the inlet ports introduced in (Schulten and Stapersma, 2003), is also constant. So, the mean value scavenging mass flow of the engine is calculated by equation (4.21).

$$\dot{m}_{sc-in} = \tilde{m}_{sc-in} \cdot \frac{t_{sc} \cdot N \cdot i}{k} \quad (4.21)$$

where,  $t_{sc} (=t_{IC} - t_{IO})$  is the real time interval over the scavenging process, which can be calculated by the scavenging valve timing and the engine speed.

### **Scavenging time constant**

The ideal scavenging process can be modelled by the ‘perfect displacement model’, where the volume of B zone containing only fresh air increases from zero to the size of whole cylinder volume, pushing A zone containing only exhaust gas out of the cylinder. Based on the perfect displacement model, all the exhaust gases will be perfectly pushed out of the cylinder volume by the fresh scavenging air and there will be no residual gas left in the cylinder after scavenging. To express the scavenging time in a mean value model, the scavenging time constant  $\tau_{sc}$  is defined by equation (4.22) based on the time when A zone disappears from the cylinder volume in a perfect displacement model.

$$\tau_{sc} \stackrel{def}{=} \frac{V}{\tilde{V}_{sc-in}} \cdot \frac{p}{p_{sc-in}} \quad (4.22)$$

where,  $V$  is the volume of the cylinder, which is assumed to be constant during the scavenging process ( $V=V_{IO}$ );  $p$  is the pressure in the cylinder;  $\tilde{V}_{sc-in}$  is the real scavenging volume flow per cylinder of the engine at inlet receiver condition, which is calculated by equation (4.23);  $p_{sc-in}$  is the pressure of the ingoing scavenging mass, which is same as the pressure in the inlet receiver  $p_{ir}$  ( $p_{sc-in} = p_{ir}$ ).

$$\tilde{V}_{sc-in} = \frac{R_{sc-in} \cdot T_{sc-in}}{p_{sc-in}} \cdot \tilde{m}_{sc-in} \quad (4.23)$$

### **Relative scavenging time**

The scavenging time has been normalised (and nondimensionalised) against the scavenging time constant as the relative scavenging time as shown in equation (4.24). Combining equations (4.21) to (4.24), the relative scavenging time is calculated by equation (4.25).

$$t_{sc,r} \stackrel{def}{=} \frac{t_{sc}}{\tau_{sc}} \quad (4.24)$$

$$t_{sc,r} = \frac{R_{sc-in} \cdot T_{sc-in} \cdot \dot{m}_{sc-in}}{p \cdot V} \cdot \frac{k}{i \cdot N} \quad (4.25)$$

### (3) Two-stage scavenging model

According to the mean value scavenging model, the temperature  $T$ , mass  $m$  and composition  $x$  of the gases in the cylinder are calculated by equations (4.26), (4.27) and (4.28) respectively. Note that the temperature  $T$  and the mass  $m$  in the cylinder have been normalised as the temperature ratio  $y = T/T_{sc-in}$  and the mass ratio  $m/m(0)$  by dividing ingoing scavenging air temperature  $T_{sc-in}$  and the initial mass in the cylinder  $m(0)$  respectively as shown in equations (4.26) and (4.27). The composition  $x$ , which is the air mass ratio indicating the purity of the gases, is defined as the ratio of the air mass  $m_{air}$  to the total mass of the gases  $m$ , i.e.,  $x = m_{air}/m$ . For details of the scavenging model in different stages and zones, please refer to Appendix E.

$$y \stackrel{def}{=} \frac{T}{T_{sc-in}} = \begin{cases} \frac{y(0)}{1 + t_{sc,r} \cdot \left[ y(0) - \frac{1}{\gamma} \right]} & t_{sc,r} \leq t_{sc,r,I} \\ \frac{y_{II}(0)}{1 + [y_{II}(0) \cdot \gamma - 1] \cdot \left[ 1 - e^{-\frac{1}{\gamma}(t_{sc,r} - t_{sc,r,I})} \right]} & t_{sc,r} > t_{sc,r,I} \end{cases} \quad (4.26)$$

$$\frac{m}{m(0)} = \begin{cases} 1 + t_{sc,r} \cdot \left[ y(0) - \frac{1}{\gamma} \right] & t_{sc,r} \leq t_{sc,r,I} \\ y(0) \cdot \left\{ \gamma - \left[ \gamma - \frac{1}{y_{II}(0)} \right] \cdot e^{-\frac{1}{\gamma}(t_{sc,r} - t_{sc,r,I})} \right\} & t_{sc,r} > t_{sc,r,I} \end{cases} \quad (4.27)$$

$$x = \frac{m_a}{m} = \begin{cases} \frac{x_{sc-in} \cdot y(0) - x(0) \cdot \frac{1}{\gamma} \cdot t_{sc,r} + x(0)}{1 + t_{sc,r} \cdot \left[ y(0) - \frac{1}{\gamma} \right]} & t_{sc,r} \leq t_{sc,r,I} \\ x_{sc-in} - \frac{[x_{sc-in} - x_{II}(0)] \cdot e^{-\frac{1}{\gamma}(t_{sc,r} - t_{sc,r,I})}}{1 + [y_{II}(0) \cdot \gamma - 1] \cdot \left[ 1 - e^{-\frac{1}{\gamma}(t_{sc,r} - t_{sc,r,I})} \right]} & t_{sc,r} > t_{sc,r,I} \end{cases} \quad (4.28)$$

Where,  $y(0)$  and  $x(0)$  are the initial temperature ratio and the initial air mass ratio in the

cylinder respectively;  $y_{II}(0)$  and  $x_{II}(0)$  are the initial temperature ratio and the initial air mass ratio of stage II respectively;  $\gamma$  ( $\gamma = c_{p,B} / c_{p,sc-in}$ ) is the specific heat ratio of gases in B zone and that of the ingoing scavenging air (see Appendix E);  $t_{sc,r,I}$  is the end time of stage I (see Appendix E).

#### (4) Mean value parameters of outgoing scavenging flow

The above introduced model is for calculating the condition in the cylinder. However, for calculating the condition in the outlet receiver, the parameters of the outgoing scavenging flow, such as the mass, mean value composition and mean value temperature of the outgoing flow, need to be calculated.

##### *Mass of outgoing scavenging flow*

According to the mass balance in the cylinder volume expressed by equation (4.29), the normalized mass of outgoing scavenging flow is calculated by equation (4.30).

$$m = m(0) + m_{sc-in} - m_{sc-out} \quad (4.29)$$

$$\frac{m_{sc-out}}{m(0)} = 1 + y(0) \cdot t_{sc,r} - \frac{m}{m(0)} \quad (4.30)$$

##### *Mean value composition of outgoing scavenging flow*

According to the composition balance in the cylinder volume expressed by equation (4.31), the average air mass ratio of the outgoing scavenging flow is calculated by equation (4.32).

$$m \cdot x = m(0) \cdot x(0) + m_{sc-in} \cdot x_{sc-in} - m_{sc-out} \cdot \bar{x}_{sc-out} \quad (4.31)$$

$$\bar{x}_{sc-out} = \frac{x(0) + y(0) \cdot t_{sc,r} \cdot x_{sc-in} - m/m(0) \cdot x}{1 + y(0) \cdot t_{sc,r} - m/m(0)} \quad (4.32)$$

##### *Mean value temperature of outgoing scavenging flow*

The energy balance for the cylinder volume with the assumption of no work and no heat exchange with the cylinder wall is expressed by equation (4.33).

$$c_v \cdot [m \cdot T - m(0) \cdot T(0)] = c_{p,sc-in} \cdot T_{sc-in} \cdot m_{sc-in} - \bar{c}_{p,sc-out} \cdot \bar{T}_{sc-out} \cdot m_{sc-out} \quad (4.33)$$

According to the assumption that the pressure in the (constant) cylinder volume is constant ( $p \cdot V = \text{constant}$ ) during scavenging process and based on the ideal gas law ( $p \cdot V = m \cdot R \cdot T$ ), it can be concluded that the internal energy change in the cylinder volume is zero, i.e.,  $c_v \cdot [m \cdot T - m(0) \cdot T(0)] = 0$ . So, the mean temperature of the scavenging flow out of the cylinder over the total outgoing mass is calculated by equation (4.34).

$$\bar{T}_{sc-out} = \frac{1}{\bar{\gamma}} \cdot \frac{T_{sc-in} \cdot m_{sc-in}}{m_{sc-out}} \quad (4.34)$$

Where,  $\bar{\gamma}$  is the ratio of the mean value specific heat ratio of outgoing scavenging mass

and that of the ingoing scavenging air ( $\bar{\gamma} \stackrel{def}{=} \bar{c}_{p,sc-out} / c_{p,sc-in}$ ), which is assumed to be the same as  $\gamma$ . So, the normalised mean temperature of the outgoing scavenging flow is calculated by equation (4.35).

$$\bar{y}_{sc-out} \stackrel{def}{=} \frac{\bar{T}_{sc-out}}{T_{sc-in}} = \frac{1}{\gamma} \cdot \frac{y(0) \cdot t_{sc,r}}{1 + y(0) \cdot t_{sc,r} - m/m(0)} \quad (4.35)$$

## (5) Scavenging efficiency and slip factors

### *Scavenging efficiency*

For the cylinder volume, the mass ‘ $m$ ’ could also be thought of two ‘partitions’, i.e. a part originating from the ingoing scavenging mass flowing through the cylinder volume but retained in the volume after a certain time interval ‘ $m_{ret}$ ’ and another part that originally was present within the volume and still was there as residual mass after a certain time ‘ $m_{res}$ ’ as shown in equation (4.36). For two-stroke engines, the scavenging efficiency  $\eta_{sc}$  is defined as the scavenging air mass retained in the volume  $m_{ret}$  divided by the mass in the cylinder volume as shown in equation (4.37). So, ‘ $\eta_{sc}=1$ ’ means an ideally scavenged volume containing no residual gas.

$$m = m_{ret} + m_{res} \quad (4.36)$$

$$\eta_{sc} \stackrel{def}{=} x_{ret} = \frac{m_{ret}}{m} \quad (4.37)$$

The relationship between the scavenging efficiency  $\eta_{sc}$  and the trapped air mass ratio in the cylinder  $x$  is shown in equation (4.38).

$$\eta_{sc} = \frac{x - x(0)}{x_{sc-in} - x(0)} \quad (4.38)$$

where,  $x(0)$  is the initial air mass ratio in the cylinder when the scavenging process starts;  $x_{sc-in}$  is the air mass ratio of the ingoing scavenging mass flow, which normally is the pure fresh air ( $x_{sc-in}=1$ ).

### *Scavenging slip factor*

A scavenging slip factor is defined as the scavenging air mass flowing through the cylinder volume divided by the scavenging air mass retained in the cylinder during scavenging process as shown in equation (4.39).

$$s_{sc} \stackrel{def}{=} \frac{m_{sc-slip}}{m_{ret}} = \frac{m_{sc-in} - m_{ret}}{m_{ret}} \quad (4.39)$$

The relationship of the scavenging slip factor with the scavenging efficiency and the air mass ratio in cylinder is expressed by equation (4.40).

$$s_{sc} = \frac{y \cdot t_{sc,r}}{x_{ret}} - 1 = \frac{x_{sc-in} - x(0)}{x - x(0)} \cdot y \cdot t_{sc,r} - 1 \quad (4.40)$$

Note that, during scavenging process, fresh air slip can only occur in the two-zone

scavenging model if the scavenging time is sufficient to reach stage II. If the scavenging time is insufficiently long, there will be no fresh air slip during the scavenging process, which means the scavenging slip factor  $s_{sc}$  is zero.

### ***Real slip factor***

However, the scavenging slip factor is not the real slip factor of the gas exchange process for a two-stroke diesel engine as more scavenging air trapped in the cylinder during the scavenging process will be pushed out of the cylinder during the subsequent expelling process. A real slip factor of the gas exchange process is defined as the total mass of the fresh air flowing through the cylinder volume divided by the fresh air mass trapped in the cylinder volume at the end of the gas exchange process (Stapersma, 2010b) as shown in equation (4.41).

$$s = \frac{\overset{def}{m}_{slip}}{m_{fresh}} = \frac{m_{in} - m_{fresh}}{m_{fresh}} \quad (4.41)$$

The relationship of the real slip factor with the scavenging slip factor and the air mass ratio in cylinder is expressed by equation (4.42).

$$\begin{aligned} s &= \frac{V_{IC}}{V_{EC}} \cdot (s_{sc} + 1) - 1 \\ &= \frac{V_{IC}}{V_{EC}} \cdot \frac{x_{sc-in} - x(0)}{x - x(0)} \cdot y \cdot t_{sc,r} - 1 \end{aligned} \quad (4.42)$$

where,  $V_{IC}$  and  $V_{EC}$  are the cylinder volumes at IC (Inlet ports close) and EC (Exhaust valve close) respectively.

### **(6) Influence of initial size of A zone on scavenging process**

The initial size of A zone  $S_A(0)$  has a significant influence on the scavenging process, which has been shown in Figure 4.7 to Figure 4.10. For analysing the influence of the initial size of A zone, a case, where  $T_{in}=50^\circ\text{C}$ ,  $T(0)=550^\circ\text{C}$ ,  $x(0)=0.2$  and  $\gamma=1$ , has been assumed and the results in Figure 4.7 to Figure 4.10 are based on this case. According to the two-zone scavenging model, it will be a ‘perfect displacement’ model when  $S_A(0)$  is unity and a ‘perfect mixing’ model when  $S_A(0)$  is zero. During the scavenging process, the in-cylinder temperature will drop faster in stage I than in stage II as shown in Figure 4.7. With a higher  $S_A(0)$ , the temperature will drop faster and the final temperature will be lower within a limited scavenging time. In particular, if  $S_A(0)=1$  (a perfect displacement model) the in-cylinder temperature will drop to the temperature of the ingoing scavenging flow when the relative scavenging time is unity ( $t/\tau_{sc}=1$ ). The in-cylinder mass (Figure 4.8) actually has an inverse trend as that of the temperature because  $m \cdot T$  in the cylinder is constant according to the model. In stage I, both the mass in B zone and mass in the whole cylinder volume increase linearly.

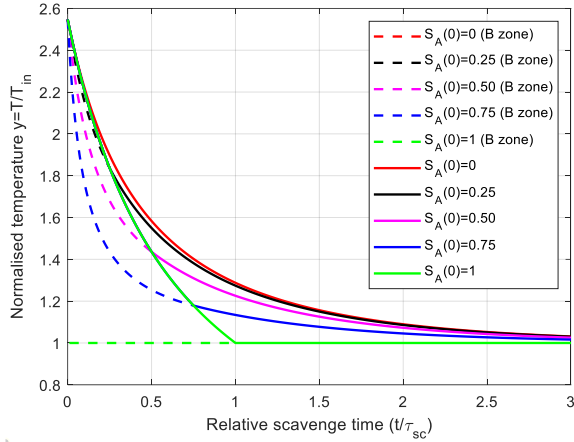


Figure 4.7: Normalised temperature in cylinder

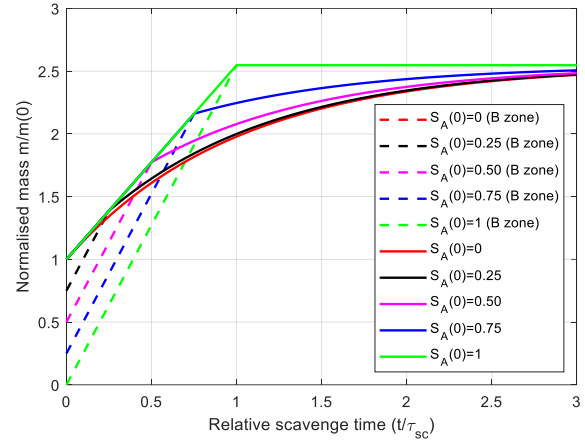


Figure 4.8: Normalised mass in cylinder

The purity (air mass ratio or air fraction) in cylinder (Figure 4.9) increases from an initial value higher than zero, which in this case is assumed as 0.2, due to the fact that normally there will be some unburnt air existing in the residual gas from last cycle. The scavenging efficiency (Figure 4.10) increases from zero and is normally lower than the purity as it indicates the fresh air fraction which is less than the total air fraction. Both the purity and scavenging efficiency after scavenging process will be higher with a larger  $S_A(0)$  if the scavenging time is sufficiently long.

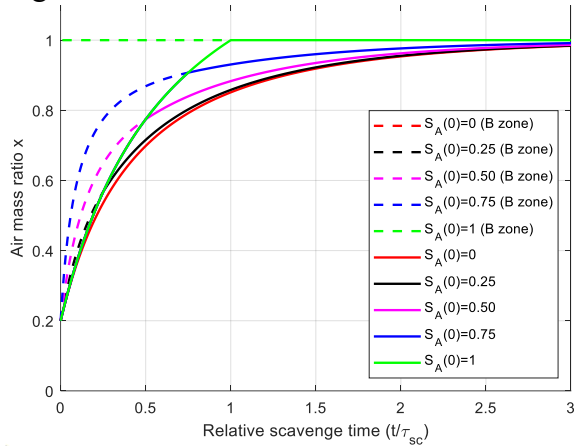


Figure 4.9: Air mass ratio (purity) in cylinder

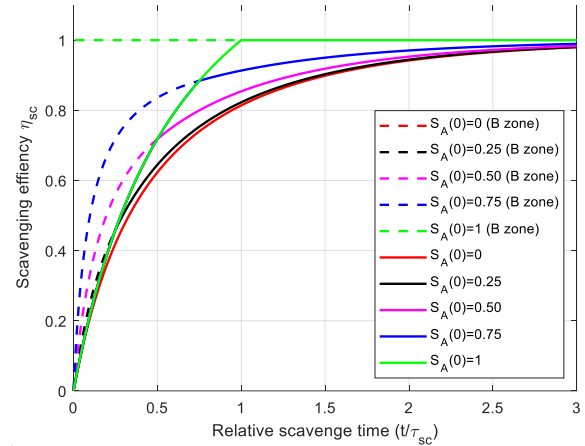


Figure 4.10: Scavenging efficiency

#### 4.4.3 Expelling model

The expelling process starts as soon as the inlet ports are closed while the exhaust valves are still open. A homogeneous state is assumed for the gases in the cylinder during the expelling process. It is also assumed that the cylinder pressure is constant during the expelling process and equals the cylinder pressure during scavenging process. Similar to A zone in scavenging process, the temperature in the cylinder during expelling can be proven to be constant. So, the trapped condition and composition in cylinder after the expelling process remain the same as the trapped condition and composition after the scavenging process, although the volume and mass will be reduced because of the upward moving piston, as shown in equations (4.43) to (4.47).

$$x_1 = x_{sc-tr} \quad (4.43)$$

$$p_1 = p_{scav} \quad (4.44)$$

$$T_1 = T_{sc-tr} \quad (4.45)$$

$$V_1 = V_{EC} \quad (4.46)$$

$$m_1 = \frac{p_1 \cdot V_1}{R_1 \cdot T_1} \quad (4.47)$$

The mass of the gases expelled out of the cylinder entering the outlet receiver is calculated by equation (4.48), and the temperature and composition are calculated by equations (4.49) and (4.50) respectively.

$$m_{exp} = m_{sc-tr} - m_1 \quad (4.48)$$

$$T_{exp} = T_{sc-tr} \quad (4.49)$$

$$x_{exp} = x_{sc-tr} \quad (4.50)$$

## 4.5 Engine model validation

The models of engine components, including the turbocharger, air cooler, auxiliary blower, non-return valve, as well as exhaust valve temperature model, and engine mechanical and heat losses models are introduced in Appendix F.

The mean value model of the two-stroke marine diesel engine MAN6S35ME-B9.3 (4170 kW @ 167 rpm) is verified, calibrated and validated before it is further integrated into the ship propulsion system model, using the engine test data provided by the engine manufacturer. The engine model is validated by comparing the simulation results with the engine test data of the mass flows, Buchi pressures and temperatures, turbocharger speed, in-cylinder compression and maximum pressures and the specific fuel consumption as shown in Figure 4.11 to Figure 4.16. The engine has been measured at different loads (100%, 90%, 75%, 50% and 10% of nominal load) while keeping the engine rotational speed constant at nominal speed (167 rpm). The simulation results are generated by running the engine model (quasi-)statically by decreasing the engine load (from 100% to 10% of nominal power) along the generator law (constant engine rotational speed at 167 rpm). So, only (quasi-)static simulation results of the engine model along the generator law have been validated and the simulation results have shown a good consistency with the engine test data. Although the simulation results along the propeller law have not been validated due to the lack of test data of the same engine, the results have been checked and verified with the test data of another engine from the same engine family, which has the same nominal rotational speed but a higher nominal power. Note that, the ‘sharp changes’ in the simulation results happening at around 35% of nominal engine power as shown in Figure 4.11 to Figure 4.16 are caused by the operation of the auxiliary blower.

When reducing the engine load, the fuel mass flow injected into the engine cylinders for combustion will decrease (Figure 4.11), and consequently the energy in the exhaust gas flowing out of the cylinders into the outlet receiver also decreases. As a result, the temperature and pressure in the outlet receiver before the turbine decreases (Figure 4.12 and Figure 4.13). The



turbocharger rotational speed will drop (Figure 4.14) due to the less enthalpy of the exhaust flow into the turbine. The compressor that is driven by the turbine has less power to charge the air, so, the temperature and pressure after the compressor as well as the charging air mass flow will decrease (Figure 4.11, Figure 4.12 and Figure 4.13). The in-cylinder compression pressure and the maximum combustion pressure are also dropping with the decreasing engine load (Figure 4.15). The engine specific fuel consumption will, however, first decrease and then increase sharply at low loads and reaches the lowest at around 70% nominal power (Figure 4.16). Note that, the temperature after turbine will first decrease slightly and then increase at low loads before the blower starts operating (Figure 4.12), and that is caused by the dropping turbine efficiency at low engine loads. The auxiliary blower operating at low engine loads helps to boost the air charging when the turbocharger is not able to provide sufficient air to the engine. As a result, the air and exhaust mass flows increase sharply, while the temperatures in the outlet receiver and after the turbine will drop.

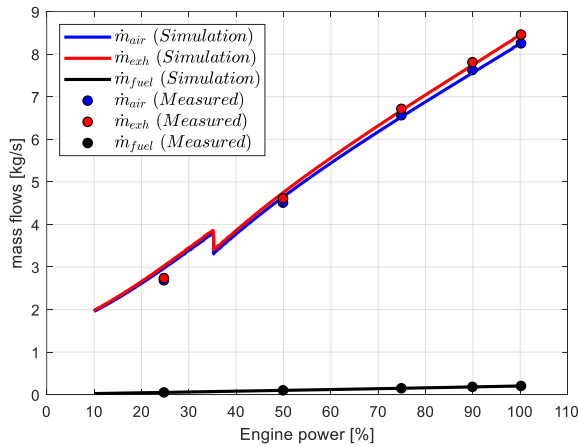


Figure 4.11: Mass flows

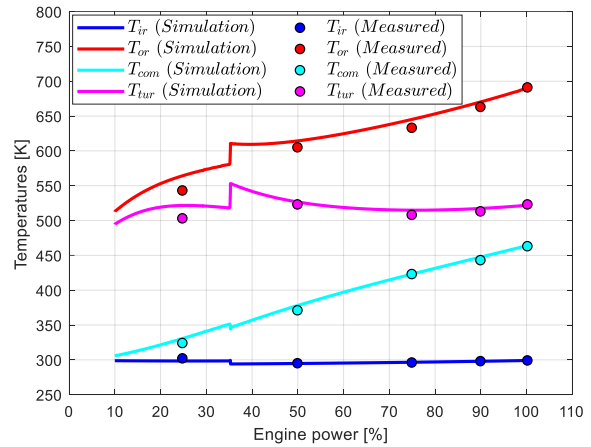


Figure 4.12: Buchi temperatures

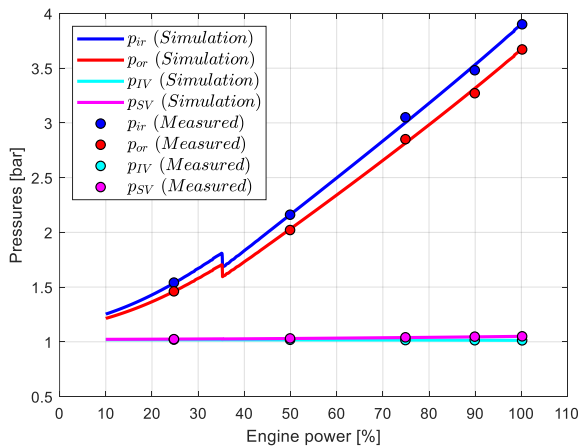


Figure 4.13: Buchi pressures

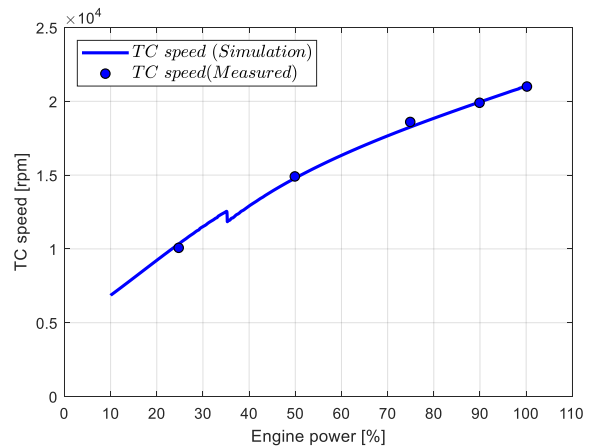


Figure 4.14: Turbocharger rotational speed

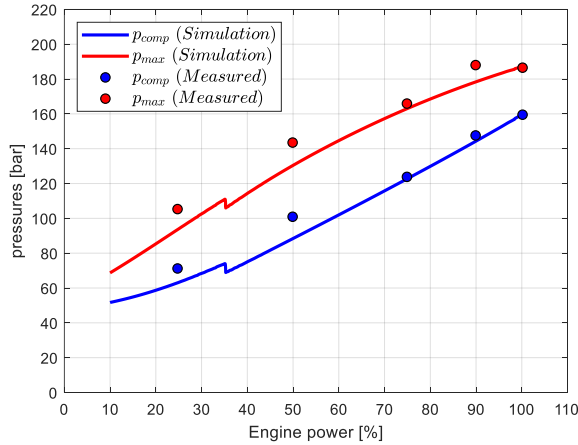


Figure 4.15: In-cylinder pressures

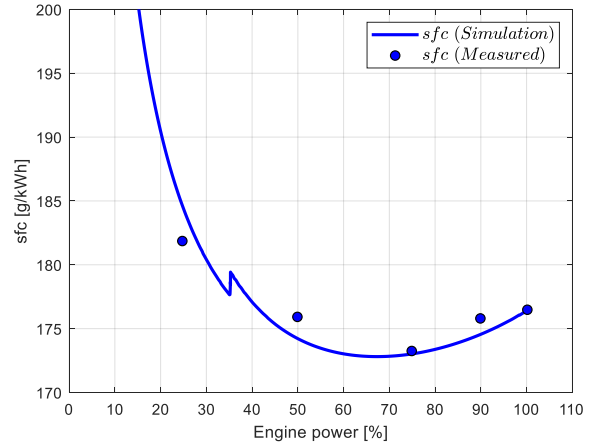


Figure 4.16: Specific fuel consumption

## 4.6 Results and discussions

Some simulation results (along the generator law) of the gas exchange process of the MAN 6S35ME two-stroke diesel engine are shown in Figure 4.17 to Figure 4.22. The scavenging efficiency (Figure 4.17) is around 0.91 at high engine loads (55%-100% of nominal engine power) and decreases quickly at low loads (below 40% of nominal power) although the operation of the auxiliary blower helps to increase it to a certain extent. The scavenging slip factor  $s_{sc}$  (Figure 4.17) is zero, which means there is no fresh air slipping from the cylinder during the scavenging process (Figure 4.19). It is still in stage I until the scavenging process ends, because the relative scavenging time  $t_{sc,r}$  is not long enough and less than the relative end time of stage I  $t_{sc,r,I}$  (Figure 4.18), which is caused by the insufficient scavenging air mass flow. However, the real slip factor of the engine  $s$ , which is highly determined by the expelling process, is as high as 0.43 and keeps constant at various loads (Figure 4.17). According to equation (4.42), if scavenging slip factor is zero, the real slip factor will be determined by the ratio of the cylinder volumes at IO and EC, which are constant if no variable valve timing is applied at different engine loads. The relative end time of stage I ( $t_{sc,r,I} = \gamma \cdot S_A(0)$ ) is constant because the initial size of A zone  $S_A(0)$  ( $= 0.82$ ) and the specific heat ratio  $\gamma$  ( $=1$ ) are set as constant in the model.

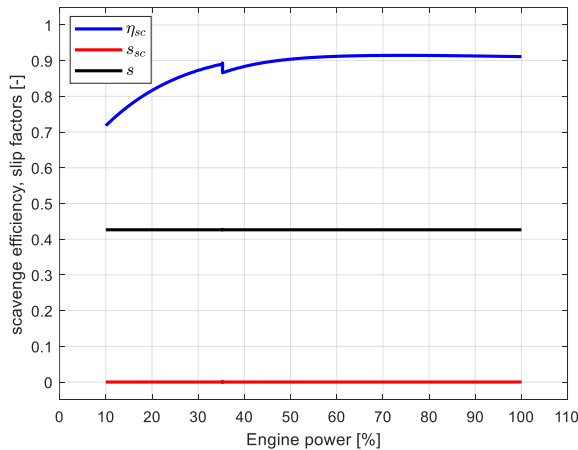


Figure 4.17: Scavenge efficiency, slip factors

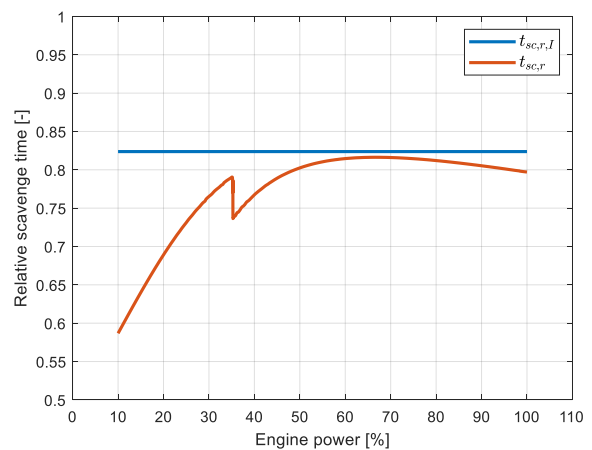


Figure 4.18: Relative scavenging time

As there is no fresh air slipping from the cylinder during scavenging process ( $\dot{m}_{sc-slip} = 0$ ), the retained scavenging air  $\dot{m}_{ret}$  is the same as the ingoing scavenging air  $\dot{m}_{sc-in}$  and the left exhaust gas  $\dot{m}_{left}$  from the cylinder is the same as the outgoing scavenging gas  $\dot{m}_{sc-out}$  as shown in Figure 4.19. The trapped mass in the cylinder  $\dot{m}_{sc-tr}$  after scavenging process is higher than the scavenging air  $\dot{m}_{sc-in}$  due to the existing residual gas after scavenging  $\dot{m}_{sc-res}$ . As there is a noticeable amount of fresh air loss  $\dot{m}_{slip}$  during the expelling process, the fresh air trapped in the cylinder after expelling process  $\dot{m}_{fresh}$  will be less than the scavenging air that enters the cylinder  $\dot{m}_{sc-in}$  (Figure 4.20(a)). The gases expelled out of the cylinder during expelling process  $\dot{m}_{exp}$  is even higher than those blown out during the blowdown process  $\dot{m}_{bld-out}$  (Figure 4.20(b)). And the majority of the expelled gas during expelling process is air due to the high air fraction  $x_{exp}$ , which is as high as 0.96 (Figure 4.21).

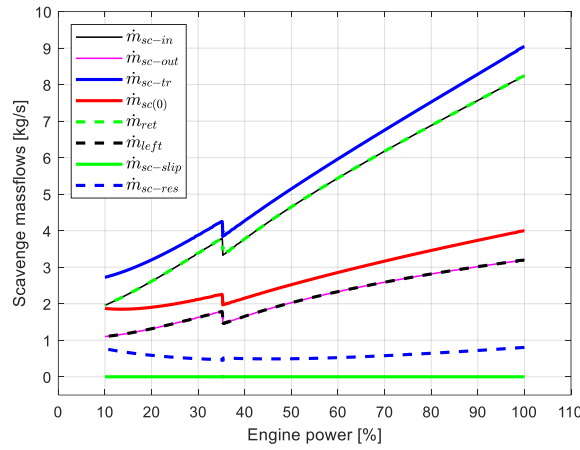
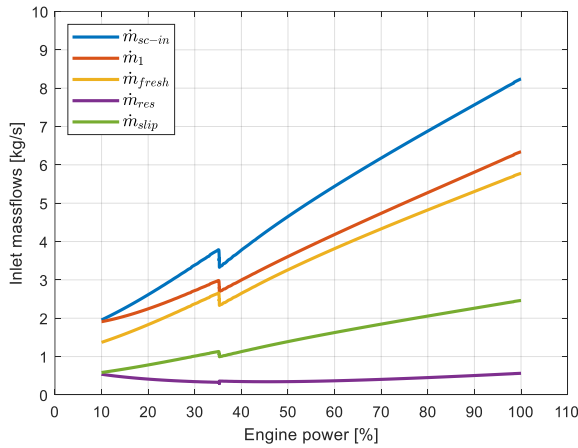
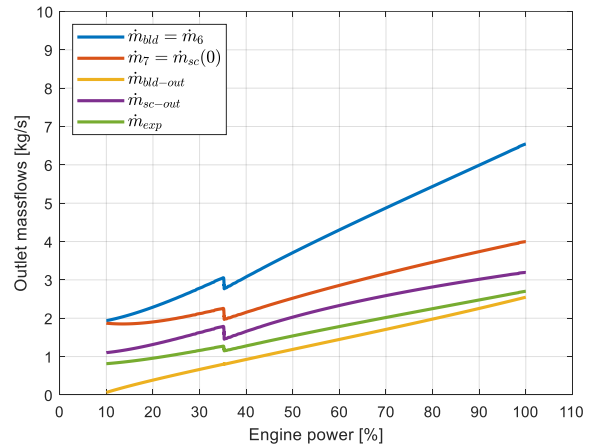


Figure 4.19: Scavenging mass flows



(a) Inlet mass flows



(b) Outlet mass flows

Figure 4.20: Inlet and outlet mass flows

The compositions (air mass ratio) of the gases in the gas exchange process is shown in Figure 4.21. The air mass ratios of the exhaust gases increase when the load decreases because of the decreasing fuel mass injected and burnt at low engine loads. The air mass ratio of the trapped mass in cylinder after gas exchange process  $x_1$  is as high as 0.96 at high engine loads

and decreases slightly at low engine loads due to the slight increase of the residual gas (Figure 4.20(a)) at low loads.

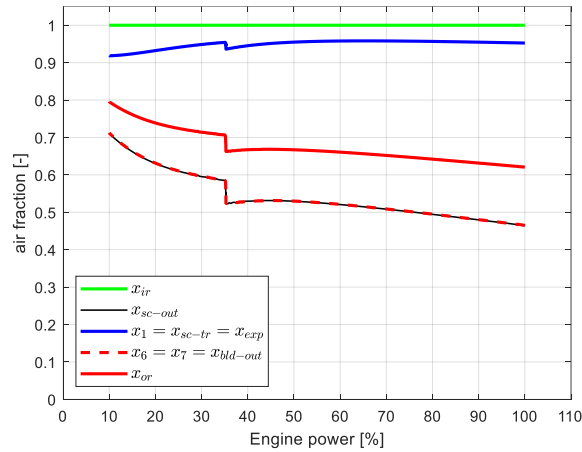
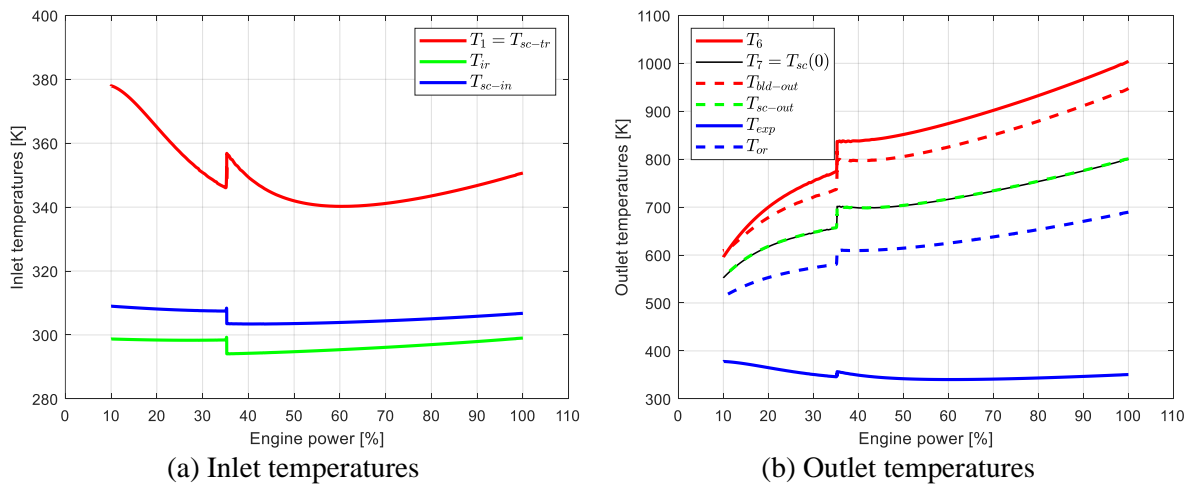


Figure 4.21: Compositions

According to equation (E. 26), the temperature of the mass trapped in the cylinder after scavenging  $T_{sc-tr}$  (Figure 4.22(a)) if still in stage I has an inverse trend as that of the relative scavenging time  $t_{sc,r}$  (Figure 4.18). The temperature of the trapped mass in the cylinder after EC (exhaust valve closed)  $T_1$ , which is the same as  $T_{sc-tr}$ , is higher than the temperature in the inlet receiver  $T_{ir}$  by as high as 50 °C at high loads and 80 °C at low loads. Due to the heat pickup during the inlet process, temperature of the ingoing scavenging air  $T_{sc-in}$  is higher than the temperature in the inlet receiver  $T_{ir}$  by around 10 °C. The average temperature of the outgoing scavenging flow  $T_{sc-out}$  Figure 4.22(b) is the same as the initial temperature of the exhaust gas in the cylinder  $T_{sc}(0)$  ( $=T_7$ ) as only gases from A zone are scavenged out of the cylinder and gases B zone remain in the cylinder till the end of the scavenging process. The temperature in the outlet receiver  $T_{or}$  is lower than those of the exhaust gases from blowdown  $T_{bld-out}$  and scavenging processes  $T_{sc-out}$  due to the expelled gases with much lower temperature  $T_{exp}$  from the expelling process.



(a) Inlet temperatures

(b) Outlet temperatures

Figure 4.22: Temperatures of gas exchange process

## 4.7 Summary and Conclusions

This chapter has introduced a mean value first principle parametric (MVFPP) engine model of the two-stroke marine uniflow diesel engine. In particular, a mean value first principle gas exchange model of the two-stroke uniflow marine diesel engines, including the two-zone scavenging model, blowdown model and the expelling process model, has been proposed. The mean value two-zone scavenging model is developed based on the basic physical laws, such as the mass balance, energy balance, composition balance and the idea gas law. The gas exchange model introduced in this chapter has been integrated into the mean value model of a two-stroke marine diesel engine, which also includes a mean value model for the closed-cylinder process and also other engine components models. The mean value model of the complete engine cycle has been calibrated and validated using the engine test data and a good consistency has been obtained. However, only (quasi-)static simulation results of the engine model along the generator law have been validated due to the limited engine test data.

Based on the simulation results the performance of the gas exchange process of the engine, such as the mass flows, temperatures, pressures, compositions and scavenging efficiency, under various engine loads has been discussed. According to the two-zone scavenging model, the initial size of A zone (exhaust gas zone)  $S_A(0)$ , which is the only empirical constant in the model, has a big influence on the scavenging performance. A larger  $S_A(0)$  is better for the scavenging performance, and in particular it will be a perfect displacement model if  $S_A(0)=1$  while a perfect mixing model if  $S_A(0)=0$ . For a two-stroke diesel engine with EC (Exhaust valve close) after IC (Inlet ports close) by a large crank angle, the fresh air loss in expelling process may be much larger than that in the scavenging process.

## **5 Integrated Ship Propulsion and Manoeuvring Model**

### **5.1 Introduction**

The MVFPP (Mean Value First Principle Parametric) two-stroke marine diesel engine model introduced in Chapter 4 has been integrated into the ship propulsion model of the benchmark chemical tanker. Consequently, the ship propulsion model used for investigating the ship transport performance in Chapter 2 and Chapter 3 has been updated, i.e., the engine model has been updated from a test-data-based fitting model to a thermodynamic-based mean value first principle model.

Another update of the propulsion system model is that the propeller model has been updated from considering only the propeller open water diagram of the first quadrant to taking the four quadrants open water characteristics into account. The four quadrants open water diagram is more convenient when investigating the whole field of operation for the propeller during ship manoeuvring, including running astern and dynamic behaviour such as stopping and acceleration (Klein Woud and Stapersma, 2002; Carlton, 2019). To update the propeller model, the original MAN Alpha propeller that is really installed on the chemical tanker has been replaced by a Wageningen C-series Controllable Pitch Propeller (CPP) (Dang et al., 2013), which is developed by MARIN (the Maritime Research Institute Netherlands). The Wageningen C-series CPP comprises 4- and 5-bladed propellers with blade area ratios of 0.40, 0.55, 0.60, 0.70 and 0.75. The 5-bladed C-series propeller is for naval applications. The 4-bladed C-series propellers including C4-40, C4-55 and C4-70 have four quadrants open water diagrams for nominal pitches of  $P/D=0.8$ , 1.0, 1.2 and 1.4. The C4-55 propeller with nominal pitch of  $P/D=0.8$  has been chosen for modelling the propeller, as it has closer blade area ratio (0.55) and design pitch to those of the MAN Alpha propeller installed in the benchmark ship, which has

blade ratio of 0.52 and design pitch of  $P/D=0.7075$ . However, to model the propeller of the benchmark ship using the data of C4-55, the open water characteristics of the chosen C4-55 propeller needs to be corrected to reduce the differences between the two different propellers as much as possible. However, only data of the open water diagram at design pitch in the first quadrant is available for the MAN Alpha propeller. So, the characteristics of the C4-55 propeller has been corrected based on the open water diagram of the original MAN Alpha propeller at design pitch ( $P/D=0.7075$ ), and the correction method has been introduced in Appendix G.

The updated ship propulsion model has been further integrated with the manoeuvring model of the benchmark chemical tanker. The components of ship propulsion model including sub-models of ship resistance, wake factor, thrust deduction factor and relative rotative efficiency, etc., have been introduced previously in Chapter 2. This chapter will thus mainly focus on the ship manoeuvring model.

There are different types of ship manoeuvring models for various applications. Taking different Degrees of Freedoms (DOF) of ship motions into consideration, the ship manoeuvring model can be categorised as: 3DOF models, such as horizontal plane models (surge, sway and yaw), longitudinal models (surge, heave and pitch) and lateral models (sway, roll and yaw); 4DOF models (surge, sway, yaw and roll); and 6DOF models (surge, sway, heave, roll, pitch and yaw), etc., (Fossen and Wiley, 2011). Depending on different manners that the components of external forces and moments acting on the ship are expressed and parametrised, the ship manoeuvring models can be divided as: the whole ship models and the modular models (Liu, 2017). The whole ship models, such as the Abkowitz model (Abkowitz, 1964), address the hull, propeller and the rudder together as a black box without considering the interactions between them; and the hydrodynamic forces and moments are expressed in Taylor series as functions of kinematic parameters and rudder angles without clear physical meanings. The modular models, such as the MMG model proposed and developed by the Mathematical Modeling Group of the Society of Naval Architects of Japan (Ogawa et al., 1977; Inoue et al., 1981; Kijima et al., 1990; Yasukawa and Yoshimura, 2015), consider the component hydrodynamic forces and moments caused by the hull, propeller, rudder and also the hull-propeller-rudder interactions. So, the modular manoeuvring models are first principle and have explicit physical meanings. Using the modular models, the effects of the physical components including the hull, propeller, rudder, the interactions between them and even the external disturbances (such as wind and waves) on the ship manoeuvring performance can be analysed separately and/or in combination, with the possibility of using different methods (experimental, numerical or empirical) (Zhang et al., 2019; Aung and Umeda, 2020; Yasukawa and Sakuno, 2020).

In this dissertation, when investigating the engine behaviour of the low-powered ocean-going cargo ship during various propulsion and manoeuvring operations in different sea conditions (normal and adverse), it is assumed that the ship sails at the design loading condition in open sea, and the ship heaving and pitching motions are left out of consideration. The rolling motion caused by ship turning in normal sea condition is considered negligible for the ocean-going cargo ship. Also, ship rolling caused by wind and waves in adverse sea conditions will be left out of consideration, as the impacts of rolling motion on the hydrodynamic manoeuvring forces and moments by the propeller, rudder and hull are assumed negligible for the ocean-

going cargo ship, which generally has single propeller and single rudder at the centreline of the ship. So, the 3DOF ship manoeuvring model (surge, sway and yaw) is considered sufficient and has been used in this dissertation for investigating the engine behaviour during ship operations in different sea conditions. The research in this dissertation intends to develop a modular and integrated first principle ship propulsion and manoeuvring model that is capable of estimating the impacts of different components on both the ship transport performance and operational safety. So, the modular and first principle MMG model, which can provide satisfactory insights of the physical phenomena of ship manoeuvring, has been used in this dissertation. To determine the hydrodynamic coefficients in the manoeuvring model, empirical methods based on a limited number of main particulars of the ship have been applied; while the expensive experimental methods and complicated numerical methods, which are out of scope of this research, have been avoided. The description, calibration and validation of the applied 3DOF MMG manoeuvring model will be presented in details in this chapter.

## 5.2 Coordinate system of 3DOF manoeuvring model

The manoeuvring model is developed based on the theory of ship's dynamics, which studies both the geometrical aspects of ship motion (kinematics) and the forces causing the motion (kinetics) (Fossen and Wiley, 2011). To express and analyse ship's motions and the hydrodynamic forces, a convenient coordinate system, including the earth-fixed and body-fixed coordinate systems, needs to be established first. The North-East-Down (NED) coordinate system ( $O_0, x_0, y_0, z_0$ ) has been used as the earth-fixed reference system, in which the  $x$  axis points towards the north, the  $y$  axis towards the east and the  $z$  axis downwards normal to the Earth's surface (Fossen and Wiley, 2011). The origin of the earth-fixed coordinate system ( $O_0$ ) could be located at the start point of the ship's operation. The Bow-Starboard-Down coordinate system ( $O, x, y, z$ ) with origin  $O$  fixed on the centre of gravity of the ship  $G$  is selected as the body-fixed reference system of the ship. The earth-fixed and body-fixed coordinate systems of MMG manoeuvring model are illustrated in Figure 5.1.

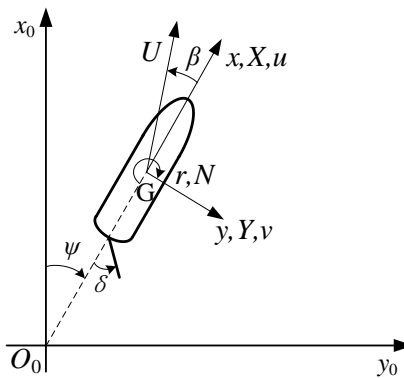


Figure 5.1: Coordinate system of MMG manoeuvring model

## 5.3 Equations of ship motions

According to (Kijima et al., 1990), the equations of the ship's 3DOF dynamic motions are expressed by equation (5.1).



$$\left. \begin{aligned} (m + m_x) \cdot \dot{u} - (m + m_y) \cdot v \cdot r &= X \\ (m + m_y) \cdot \dot{v} + (m + m_x) \cdot u \cdot r &= Y \\ (I_z + J_z) \cdot \dot{r} &= N \end{aligned} \right\} \quad (5.1)$$

where,  $m$ ,  $m_x$ , and  $m_y$  are the mass of the ship, the added mass of the entrained water in  $x$ -direction (kg) and  $y$ -direction (kg) respectively;  $I_z$  and  $J_z$  are the moment of inertia of the ship ( $\text{kg} \cdot \text{m}^2$ ) and the added moment of inertia of the entrained water ( $\text{kg} \cdot \text{m}^2$ ) respectively;  $v$ ,  $u$  and  $r$  are the ship velocity in  $x$ -axis direction (m/s), ship velocity in  $y$ -axis direction (m/s) and the yaw rate around the  $z$ -axis (rad/s) respectively;  $\dot{v}$ ,  $\dot{u}$  and  $\dot{r}$  are the accelerations of  $v$ ,  $u$  and  $r$  respectively;  $X$ ,  $Y$  and  $N$  are the external forces acting on ship in  $x$ -axis direction and  $y$ -axis direction (N) and the yaw moment around  $z$ -axis acting on ship (Nm) respectively.

## 5.4 Hydrodynamic forces and moments

The external forces and moments are divided according to the contributions of the hull, propeller and rudder components, which are denoted with the subscripts of  $H$ ,  $P$  and  $R$  respectively, as shown in equation (5.2). Note that in this chapter the calm sea condition is assumed, while the external environmental forces, including the wind- and waves-induced steady forces in adverse sea conditions, will be included and discussed in Chapter 7.

$$\left. \begin{aligned} X &= X_H + X_P + X_R \\ Y &= Y_H + Y_R \\ N &= N_H + N_R \end{aligned} \right\} \quad (5.2)$$

The prime symbols refer to the nondimensionalized quantities as follows:

$$X', Y' = \frac{X}{0.5 \cdot \rho \cdot L \cdot d \cdot U^2}, \frac{Y}{0.5 \cdot \rho \cdot L \cdot d \cdot U^2} \quad (5.3)$$

$$N' = \frac{N}{0.5 \cdot \rho \cdot L^2 \cdot d \cdot U^2} \quad (5.4)$$

$$v', u' = \frac{v}{U}, \frac{u}{U} \quad (5.5)$$

$$r' = \frac{rL}{U} \quad (5.6)$$

$$m', m'_x, m'_y = \frac{m}{0.5 \cdot \rho \cdot L^2 \cdot d}, \frac{m_x}{0.5 \cdot \rho \cdot L^2 \cdot d}, \frac{m_y}{0.5 \cdot \rho \cdot L^2 \cdot d} \quad (5.7)$$

$$I'_z, J'_z = \frac{I_z}{0.5 \cdot \rho \cdot L^4 \cdot d}, \frac{J_z}{0.5 \cdot \rho \cdot L^4 \cdot d} \quad (5.8)$$

where,  $L$  is the length of the ship;  $d$  is the ship draught,  $U$  is the ship absolute speed ( $U = \sqrt{u^2 + v^2}$ ) and  $\rho$  is the water density.

### 5.4.1 Forces and moment on hull

The hull force in  $x$ -axis direction  $X_H$  consists of two parts, which according to (Inoue et al., 1981) are the ship resistance depending on the ship longitudinal speed  $u$  in  $x$ -axis direction (the first term in equation (5.9)) and the force generated by the sway and yaw motions of the ship (the second term in equation (5.9)).

$$X'_H = X'(u) + X'_{vr} \cdot v' \cdot r' \quad (5.9)$$

where,  $X'(u)$  is the non-dimensional ship resistance as a function of the ship longitudinal speed  $u$ , and it is calculated using the ship resistance model introduced in Chapter 2;  $X'_{vr}$  is the hydrodynamic derivative of the coupled motions of sway and yaw in  $x$ -axis direction, which according to (Inoue et al., 1981) is calculated by equation (5.10).

$$X'_{vr} = (c_m - 1) \cdot m'_y \quad (5.10)$$

where,  $c_m$  is a constant that may have approximate values in the range of 0.5 – 0.75 for different ship types (Inoue et al., 1981). In (Yoshimura and Nomoto, 1978),  $c_m$  is set as 0.72 ~ 0.75 for tankers and 0.41 for container ships. In (Hasegawa, 1980) an estimation chart of  $c_m$  has been proposed as shown in Figure 5.2. A regression formula of the estimated linear relationship between  $c_m$  and the block coefficient  $C_b$  in Figure 5.2 has been made as shown in equation (5.11), and it is used to calculate  $c_m$  in the manoeuvring model of the benchmark chemical tanker.

$$c_m = 1.66 \cdot C_b - 0.49 \quad (5.11)$$

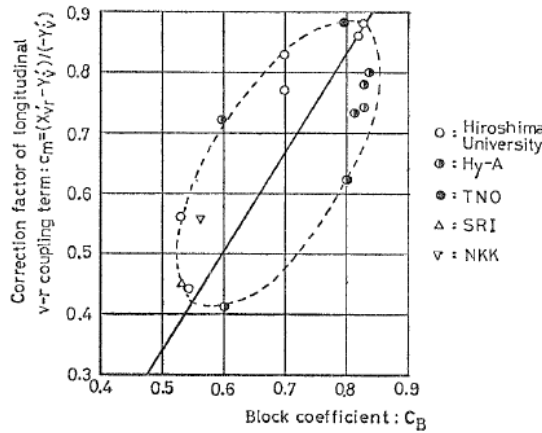


Figure 5.2: Estimation chart of longitudinal  $v$ - $r$  coupling term (Hasegawa, 1980)

In (Kijima et al., 1990), the hull force in  $x$ -axis direction  $X_H$  is expressed by equation (5.12). The formulas in equations (5.9) and (5.12) are essentially the same and  $X'_{\beta r} = -X'_{vr}$ ,  $X'_{uu} \cdot \cos^2 \beta = X'(u)$ .

$$X'_H = X'_{uu} \cdot \cos^2 \beta + X'_{\beta r} \cdot r' \cdot \sin \beta \quad (5.12)$$

where,  $X'_{uu}$  and  $X'_{\beta r}$  the hydrodynamic derivatives;  $\beta$  is the drift angle of the ship ( $\beta = \arctan(-v/u)$ ).

According to (Kijima et al., 1990), the nondimensionalized lateral force  $Y'_H$  and yaw moment  $N'_H$  acting on the ship hull are expressed by equation (5.13) and (5.14).

$$Y'_H = Y'_\beta \beta + Y'_r r' + Y'_{\beta\beta} \beta |\beta| + Y'_{rr} r' |r'| + (Y'_{\beta\beta r} \beta + Y'_{\beta rr} r') \beta r' \quad (5.13)$$

$$N'_H = N'_\beta \beta + N'_r r' + N'_{\beta\beta} \beta |\beta| + N'_{rr} r' |r'| + (N'_{\beta\beta r} \beta + N'_{\beta rr} r') \beta r' \quad (5.14)$$

where,  $Y'_\beta$ ,  $Y'_r$ , ...,  $N'_{\beta rr}$  are hydrodynamic derivatives;  $Y'_H$ ,  $N'_H$  and  $r'$  are the nondimensionalized lateral force, yaw moment and the yaw rate of the ship respectively as shown in equations (5.3) and (5.4).

In (Kijima et al., 1990), the approximate formulae for estimating the hydrodynamic derivatives ( $Y'_\beta$ ,  $Y'_r$ , ...,  $N'_{\beta rr}$ ) derived from model test results have been proposed for the manoeuvrability prediction of conventional ship at the initial design stage. The approximate formulae are functions of ship's main particulars including the ship length  $L$ , breadth  $B$ , draft  $d$ , block coefficient  $C_b$  and aspect ratio of the ship hull  $k = 2d/L$ . However, as it has been noted in both (Kijima et al., 1990) and (Kijima et al., 2000), the Kijima-1990 approximate formulae are effective to estimate the hydrodynamic derivatives for ships that have conventional body shape and inherently good course stability, while for unstable ships the accuracy of the estimation may deteriorate. The ship manoeuvring performance and the dynamic yaw stability is considerably influenced by the shape of the aft body of the hull (Kijima and Nakiri, 1999; Oltmann, 2003) and ships with full aft body may have worse course stability (Kijima et al., 2000). However, no parameters expressing the shape of the aft body of the ship hull has been included in Kijima-1990 method. In order to improve the accuracy of the estimations by taking influence of the aft body hull shape into consideration, in (Kijima et al., 2000) four parameters expressing the aft hull shape, namely  $e_a$ ,  $e'_a$ ,  $\sigma_a$  and  $K$  defined by equation (5.15), which are proposed by (Mori, 1995), have been introduced and included into the approximate formulae for estimating the hydrodynamic derivatives. In (Kijima and Nakiri, 2003) the approximate formulas of Kijima-2000 method (Kijima et al., 2000) have been further updated as shown in equations (5.16) to (5.27). The updated formulas in (Kijima and Nakiri, 2003) have been used in the manoeuvring model of the benchmark 13000 DWT chemical tanker.

$$\left. \begin{aligned} e_a &= \frac{L}{B} \cdot (1 - C_{pa}) \\ e'_a &= \frac{e_a}{\sqrt{\frac{1}{4} + \frac{1}{(B/d)^2}}} \\ \sigma_a &= \frac{1 - C_{wa}}{1 - C_{pa}} \\ K &= \left( \frac{1}{e'_a} + \frac{1.5}{L/B} - 0.33 \right) \cdot (0.95 \cdot \sigma_a + 0.40) \end{aligned} \right\} \quad (5.15)$$

where,  $C_{wa}$  and  $C_{pa}$  are the water plane coefficient and prismatic coefficient of the aft half hull respectively. When calibrating the manoeuvring model, it is found that both  $C_{wa}$  and  $C_{pa}$  are very sensitive parameters, which have an obvious influence on the simulation results of the manoeuvring operations. However, the real data of  $C_{wa}$  and  $C_{pa}$  of the chemical tanker are not

available, so they are estimated based on  $C_w$  and  $C_p$  as well as the available photos of the ship, which (roughly) show the aft body shape. In the model,  $C_{pa}$  and  $C_{wa}$  are set as 0.78 and 0.96 respectively.

$$Y'_{\beta} = \frac{1}{2} \cdot \pi \cdot k + 1.9257 \cdot C_b \cdot \frac{B}{L} \cdot \sigma_a \quad (5.16)$$

$$Y'_r = \frac{1}{4} \cdot \pi \cdot k + 0.052 \cdot e'_a - 0.457 + (m' + m'_x) \quad (5.17)$$

$$Y'_{\beta\beta} = \begin{cases} 52.9 \cdot (1 - C_b) \cdot \frac{d}{B} \cdot K - 0.12473 & \text{for } C_b \leq 0.6, \\ -0.170 \cdot e'_a \cdot K \cdot \frac{B}{d} + 1.08 & \text{for } 0.6 < C_b \leq 0.75, \\ 4.17 \cdot k \cdot C_b \cdot e'_a - 0.4475 & \text{for } 0.75 \leq C_b \text{ \& } K \leq 0.35, \\ -0.4784 \cdot \frac{B}{d} \cdot K + 1.3 & \text{otherwise} \end{cases} \quad (5.18)$$

$$Y'_{rr} = 0.24267 \cdot C_b \cdot \frac{d}{B} \cdot e'_a - 0.13108 \quad (5.19)$$

$$Y'_{\beta rr} = -1.38643 \cdot C_b \cdot e'_a \cdot K + 1.29 \quad (5.20)$$

$$Y'_{\beta\beta r} = \begin{cases} 306.52 \cdot C_b \cdot \frac{B}{L} \cdot K - 2.31454 & \text{for } C_b \leq 0.6 \text{ \& } C_b \cdot \frac{B}{L} \cdot K < 0.008, \\ -186.14 \cdot C_b \cdot \frac{B}{L} \cdot K + 0.902 & \text{for } C_b \leq 0.6 \text{ \& } 0.008 \leq C_b \cdot \frac{B}{L} \cdot K, \\ 13.018 \cdot C_b - 9.2775 & \text{for } 0.6 < C_b \leq 0.75, \\ -42.6537 \cdot C_b \cdot \frac{B}{L} + 5.9 & \text{for } 0.75 < C_b \text{ \& } K \leq 0.3, \\ 0.78145 \cdot e'_a \cdot K - 0.43232 & \text{otherwise} \end{cases} \quad (5.21)$$

$$N'_{\beta} = \begin{cases} k \cdot \left\{ 150.668 \cdot \left[ (1 - C_b) \cdot \frac{d}{B} \cdot e'_a \cdot K \right]^2 - 23.819 \cdot \left[ (1 - C_b) \cdot \frac{d}{B} \cdot e'_a \cdot K \right] + 1.976 \right\} \\ \quad \text{for } 0.0133 \leq (1 - C_b) \cdot \frac{d}{B} \cdot \sigma_a \cdot K \leq 0.0144, \\ k \cdot \left\{ 150.668 \cdot \left[ (1 - C_b) \cdot \frac{d}{B} \cdot e'_a \cdot K \right]^2 - 23.819 \cdot \left[ (1 - C_b) \cdot \frac{d}{B} \cdot e'_a \cdot K \right] + 1.802 \right\} \\ \quad \text{otherwise} \end{cases} \quad (5.22)$$

$$N'_r = -0.54 \cdot k + k^2 - 0.0477 \cdot e'_a \cdot K + 0.0368 \quad (5.23)$$

$$N'_{\beta\beta} = 43.857 \cdot \left[ (1 - C_b) \cdot \frac{d}{B} \cdot e'_a \cdot K \right]^2 - 3.671 \cdot \left[ (1 - C_b) \cdot \frac{d}{B} \cdot e'_a \cdot K \right] + 0.086 \quad (5.24)$$

$$N'_{rr} = 0.15 \cdot K - 0.068 \quad (5.25)$$

$$N'_{\beta rr} = -0.4086 \cdot C_b + 0.27 \quad (5.26)$$

$$N'_{\beta\beta r} = -0.826 \cdot (1 - C_b) \cdot \frac{d}{B} \cdot e'_a - 0.026 \quad (5.27)$$

### 5.4.2 Force by propeller

The propeller thrust is calculated by equation (5.29) using the non-dimensional propeller thrust coefficient  $C_T^*$ , which is defined in equation (5.28). The four-quadrant propeller diagram, in which the thrust coefficient  $C_T^*$ , torque coefficient  $C_Q^*$  are expressed versus the hydrodynamic pitch angle  $\beta_p^*$  and propeller pitch ratio  $P/D$ , is developed by MARIN (the Maritime Research Institute Netherlands) for describing the entire four quadrant operation of the propeller (Klein Woud and Stapersma, 2002). The thrust coefficient  $C_T^*$  is a function of the hydrodynamic pitch angle  $\beta_p^*$  and the propeller pitch ratio  $P/D$  as shown in equation (5.30). The hydrodynamic pitch angle  $\beta_p^*$  is calculated by equation (5.31). In the manoeuvring model of the chemical tanker, the propeller model based on the four-quadrant propeller open water diagram, which has been pre-defined in a lookup table, is used to calculate the propeller thrust coefficient  $C_T^*$ .

$$\left. \begin{aligned} C_T^* &= \frac{T_p}{\pi/8 \cdot \rho \cdot D_p^2 \cdot \left[ v_A^2 + (0.7 \cdot \pi \cdot n_p \cdot D_p)^2 \right]} \\ C_Q^* &= \frac{Q_p}{\pi/8 \cdot \rho \cdot D_p^3 \cdot \left[ v_A^2 + (0.7 \cdot \pi \cdot n_p \cdot D_p)^2 \right]} \end{aligned} \right\} \quad (5.28)$$

$$X_p = (1 - t_p) \cdot C_T^* \cdot \frac{\pi}{8} \cdot \rho \cdot D_p^2 \cdot \left[ v_A^2 + (0.7 \cdot \pi \cdot n_p \cdot D_p)^2 \right] \quad (5.29)$$

$$C_T^* = f(\beta_p^*, P/D) \quad (5.30)$$

$$\beta_p^* = \arctan\left(\frac{v_A}{0.7 \pi \cdot n_p \cdot D_p}\right) \quad (5.31)$$

The advance speed of the propeller  $v_A$  is calculated by equation (5.32).

$$v_A = u \cdot (1 - w_p) \quad (5.32)$$

The effective wake fraction  $w_p$  generally varies during manoeuvring motions from that in the straight forward motion  $w_{p0}$  (Inoue et al., 1981). Due to the effects of the drift angle, yaw rate, ship stern shape, propeller rotation, propeller working load and even the rudder, the variation of wake fraction during manoeuvring motions is complicated (Liu, 2017). The wake factor in manoeuvring in this thesis is estimated by equation (5.33) considering the geometrical inflow angle at the propeller position (Inoue et al., 1981; Kijima et al., 2000).

$$w_P = w_{P0} \cdot \exp(-4 \cdot \beta_P^2) \quad (5.33)$$

$$\beta_P = \beta - x'_P \cdot r' \quad (5.34)$$

$$x'_P = -(0.5 + x_G/L) \quad (5.35)$$

where,  $w_{P0}$  is the wake factor at propeller location in straight forward motion;  $\beta_P$  is the geometrical inflow angle to the propeller;  $x'_P (= x_P/L)$  is the relative longitudinal position of the propeller;  $x_G$  is the longitudinal distance between the centre of buoyancy and mid ship ( $L_{PP}/2$ ), which is positive when the centre of buoyancy is forward of mid ship, while negative when backward.  $t_P$  and  $w_{P0}$  are calculated using the models introduced in Chapter 2.

### 5.4.3 Forces and moment by rudder

According to (Kijima et al., 2000), the rudder forces and moment  $X_R$ ,  $Y_R$  and  $N_R$  are calculated by equation (5.36).

$$\left. \begin{aligned} X_R &= -(1-t_R) \cdot F_N \cdot \sin \delta \\ Y_R &= -(1+a_H) \cdot F_N \cdot \cos \delta \\ N_R &= -(x_R + a_H \cdot x_H) \cdot F_N \cdot \cos \delta \end{aligned} \right\} \quad (5.36)$$

$$F_N = 0.5 \cdot \rho \cdot A_R \cdot U_R^2 \cdot C_N \cdot \sin \alpha_R \quad (5.37)$$

$$C_N = \frac{6.13 \cdot \Lambda_R}{\Lambda_R + 2.25} \quad (5.38)$$

Where,  $F_N$  is the normal force acting on rudder;  $\delta$  is rudder angle;  $x_R$  is the longitudinal position of the rudder, and it is assumed that  $x'_R (= x_R/L) = x'_P$ ;  $a_H$  is the additional interaction coefficient (ratio of additional lateral force) indicating the interaction between rudder and hull;  $x_H$  is the longitudinal position of the additional lateral force;  $A_R$  is the rudder area;  $U_R$  is the effective rudder inflow speed;  $\alpha_R$  is the effective rudder inflow angle;  $\Lambda_R$  is aspect ratio of rudder, which is commonly expressed as span/mean chord ( $\Lambda_R = D_R/\bar{L}_R$ ), or square of the rudder span/rudder area ( $\Lambda_R = D_R^2/A_R$ ).

The real data of the rudder area  $A_R$  and the rudder aspect ratio  $\Lambda_R$  of the chemical tanker are not available, so they are estimated based on the data in literature (Barrass, 2004; Molland and Turnock, 2011; Papanikolaou, 2014) and the photo of the rudder of the ship, which shows that the rudder is a spade type of rectangular profile. In the model of the chemical tanker, the rudder area  $A_R$  is set as 1.7% of the ship lateral underwater area, i.e.,  $A_R/(L \cdot d) = 1.7\%$ , and the rudder aspect ratio  $\Lambda_R$  is set as 1.5.

#### (1) Rudder inflow velocity and angle

The effective rudder inflow velocity  $U_R$  and the effective rudder inflow angle  $\alpha_R$  illustrated in Figure 5.3 are calculated by equations (5.39) and (5.40) respectively (Yasukawa and Yoshimura, 2015).

$$U_R = \sqrt{u_R^2 + v_R^2} \quad (5.39)$$

$$\alpha_R = \delta - \arctan(v_R/u_R) \quad (5.40)$$

where,  $u_R$  is the longitudinal component of the rudder inflow velocity and  $v_R$  is the lateral component of the rudder inflow velocity as illustrated in Figure 5.3.

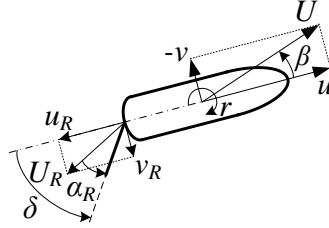


Figure 5.3: Rudder inflow velocity and angle

According to (Yasukawa and Yoshimura, 2015), the longitudinal component of the rudder inflow velocity is calculated by equation (5.41).

$$u_R = u \cdot (1 - w_R) \cdot \sqrt{\eta_R \cdot \left[ 1 + \kappa_R \left( \sqrt{1 + C_T} - 1 \right) \right]^2 + (1 - \eta_R)} \quad (5.41)$$

where,  $C_T$  is the non-dimensional propeller thrust loading coefficient, which is defined by equation (5.42);  $\eta_R$  is the ratio of propeller diameter  $D_P$  to rudder span  $D_R$  ( $\eta_R = D_P/D_R$ );  $w_R$  is the wake factor at rudder location, which according to (Kijima et al., 2000) is calculated by equation (5.43);  $\kappa_R$  is a constant and according to the actuator disc theory it is a function of the distance from the rudder to the propeller plane (Dirix, 2002). Following (Yasukawa and Yoshimura, 2015)  $\kappa_R$  is set as 0.5 in the model.

$$C_T \stackrel{\text{def}}{=} \frac{T_P}{0.5 \cdot \rho \cdot v_a^2 \cdot \pi/4 \cdot D_P^2} = \frac{8 \cdot K_T}{\pi \cdot J_P^2} \quad (5.42)$$

$$w_R = w_{R0} \cdot \frac{w_P}{w_{P0}} \quad (5.43)$$

$$\varepsilon = \frac{1 - w_{R0}}{1 - w_{P0}} \quad (5.44)$$

where,  $w_{R0}$  is the wake factor at rudder location in straight forward motion;  $\varepsilon$  is the wake fraction ratio. In the model according to (Kijima et al., 1990)  $\varepsilon$  is calculated by equation (5.45).

$$\varepsilon = -156.2 \cdot \left( C_b \cdot \frac{B}{L} \right)^2 + 41.6 \cdot C_b \cdot \frac{B}{L} - 1.76 \quad (5.45)$$

The lateral component of the rudder inflow velocity  $v_R$  is calculated by equation (5.46).

$$v_R = -\gamma_R \cdot (v + r \cdot \ell_R) \quad (5.46)$$

where,  $\gamma_R$  is the flow straightening coefficient indicating the flow straightening phenomena at the rudder, which is caused by the presence of hull and propeller slip stream.  $\gamma_R$  is usually smaller than 1.0 (Yasukawa and Yoshimura, 2015) and the possible range of the value is 0.35 to 0.65.  $\ell_R$  is the effective longitudinal coordinate of rudder position, which represents the effect of yaw rate on the lateral inflow velocity to the rudder.  $\ell_R/L$  is close to -1.0 (Yasukawa

and Yoshimura, 2015) and according to (Kijima et al., 1990)  $\ell_R/L = 2x'_R \approx -1.0$ . In the manoeuvring model of the benchmark ship,  $\gamma_R$  and  $\ell_R/L$  are set as 0.6 and -1.0 respectively.

## (2) Interaction between rudder and hull

### *Steering resistance deduction factor*

The steering resistance deduction factor  $t_R$ , which is actually the coefficient for additional rudder drag, is calculated using the following formula in (Kijima et al., 1990).

$$t_R = -0.28 \cdot C_b + 0.45 \quad (5.47)$$

### *Rudder force increase factor*

The rudder force increase factor  $a_H$ , which indicates the additional lateral force acting on the ship by steering due to the interaction between rudder and hull, is calculated using the following formula in (Dirix, 2002). The formula in equation (5.48) is actually a regression polynomial of the curve (Figure 5.4) in (Kijima et al., 1990) expressing the relation between  $a_H$  and the ship block coefficient  $C_b$ .

$$a_H = 2.75 \cdot C_b^2 - 1.485 \cdot C_b + 0.2115 \quad (5.48)$$

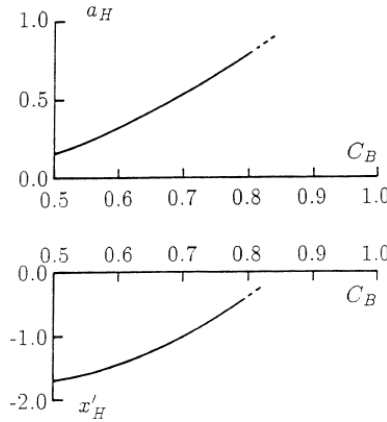


Figure 5.4: The interaction force coefficients (Kijima et al., 1990)

### *Position of the additional lateral rudder force*

The non-dimensional longitudinal position  $x'_H (= x_H/L)$  of the addition lateral rudder force is calculated using the regression formula in (Dirix, 2002) of the curve in Figure 5.4 (Kijima et al., 1990) expressing the relation between  $x'_H$  and  $C_b$ .

$$x'_H = 7.5 \cdot C_b^2 - 5.05 \cdot C_b - 1.155 \quad (5.49)$$

## 5.4.4 Hydrodynamic mass and moment of inertia

### (1) Mass and moment of inertia of the ship

The ship mass and moment of inertia are calculated by equation (5.50) and (5.51) respectively.

$$m = \rho \cdot \nabla \quad (5.50)$$



$$I_z = m \cdot r_{gyr}^2 \quad (5.51)$$

where,  $\nabla$  is the ship displacement volume ( $m^3$ );  $r_{gyr}$  is the gyration radius (m) ( $r_{gyr} = k_{gyr} \cdot L$ );  $k_{gyr}$  is the coefficient, which varies from 0.18 to 0.25 for most ships according to (Dirix, 2002), in which  $k_{gyr}$  is set as 0.225. In (Liu, 2017)  $k_{gyr}$  is set as 0.2536, while in (Yasukawa and Yoshimura, 2015) it is set as 0.25. In the model of the chemical tanker,  $k_{gyr}$  is set as 0.25.

## (2) Added mass and added moment of inertia

The added mass at x-axis direction is calculated by the following formula in (Dirix, 2002).

$$m_x = \frac{m_{ship}}{\pi \sqrt{L^3 / \nabla - 14}} \quad (5.52)$$

The added mass at y-axis direction and the added moment of inertia are calculated by the following formulas in (Clarke, 1983).

$$m_y = \frac{\pi}{2} \cdot \rho \cdot d^2 \cdot L \cdot \left[ 1 + 0.16 \cdot C_b \cdot \frac{B}{d} - 5.1 \cdot \left( \frac{B}{L} \right)^2 \right] \quad (5.53)$$

$$J_z = \frac{\pi}{2} \cdot \rho \cdot d^2 \cdot L^3 \cdot \left( \frac{1}{12} + 0.017 \cdot C_b \cdot \frac{B}{d} - 0.33 \cdot \frac{B}{L} \right) \quad (5.54)$$

In the model the added masses at both x-axis and y-axis directions have been corrected by multiplying the correction factors  $C_{mx}$  (=0.5) and  $C_{my}$  (=0.5) to the results calculated by equations (5.52) and (5.53).

### 5.4.5 Calibrating parameters

For calibrating the manoeuvring model of the benchmark chemical tanker (Castillo de Tebra), the main particulars of the ship and the estimated model parameters are summarized in Table 5.1, Table 5.2 and Table 5.3.

Table 5.1: Main Particulars of Castillo de Tebra (at design loading condition)

| Main particulars                         | Symbol   | Unit              | Value  |
|--|----------|-------------------|--------|
| Length between Perpendiculars            | $L_{pp}$ | [m]               | 113.80 |
| Length on load water line                | $L_{wl}$ | [m]               | 116.60 |
| Breath                                   | $B$      | [m]               | 22.00  |
| Draft                                    | $d$      | [m]               | 8.50   |
| Displacement                             | $\nabla$ | [m <sup>3</sup> ] | 16988  |
| Midship coefficient                      | $C_m$    | [-]               | 0.991  |
| Waterline coefficient                    | $C_w$    | [-]               | 0.897  |
| Block coefficient                        | $C_b$    | [-]               | 0.7791 |
| Prismatic coefficient                    | $C_p$    | [-]               | 0.7862 |
| Centre of buoyancy forward of $L_{pp}/2$ | $x_G$    | [m]               | 1.698  |

Table 5.2: Parameters set as constants

| Parameters | Value | Parameters        | Value |
|------------|-------|-------------------|-------|
| $C_{mx}$   | 0.5   | $A_R/(L \cdot d)$ | 1.7%  |
| $C_{my}$   | 0.5   | $\Lambda_R$       | 1.5   |
| $k_{gyr}$  | 0.25  | $\kappa_R$        | 0.5   |
| $C_{wa}$   | 0.96  | $\ell_R/L$        | -1.0  |
| $C_{pa}$   | 0.78  | $\gamma_R$        | 0.6   |

Table 5.3: Parameters calculated by approximate formulas

| Parameters        | Equations | Value      | Parameters          | Equations | Value   |
|-------------------|-----------|------------|---------------------|-----------|---------|
| $m'$              | (5.7)     | 0.3087     | $Y'_{\beta\beta r}$ | (5.21)    | -0.5247 |
| $m'_x$            | (5.7)     | 0.0099     | $N'_\beta$          | (5.22)    | 0.1541  |
| $m'_y$            | (5.7)     | 0.1328     | $N'_r$              | (5.23)    | -0.0469 |
| $I'_z$            | (5.8)     | 0.0193     | $N'_{\beta\beta}$   | (5.24)    | 0.0097  |
| $J'_z$            | (5.8)     | 0.0126     | $N'_{rr}$           | (5.25)    | -0.0237 |
| $c_m$             | (5.11)    | 0.8034     | $N'_{\beta rr}$     | (5.26)    | -0.0484 |
| $X'_{vr}$         | (5.10)    | -0.0274    | $N'_{\beta\beta r}$ | (5.27)    | -0.1529 |
| $\sigma_a$        | (5.15)    | 0.1818     | $\varepsilon$       | (5.45)    | 0.9622  |
| $K$               | (5.15)    | 0.2951     | $t_R$               | (5.47)    | 0.2318  |
| $Y'_\beta$        | (5.16)    | 0.2874     | $a_H$               | (5.48)    | 0.7239  |
| $Y'_r$            | (5.17)    | 0.0725     | $x'_H$              | (5.49)    | -0.5367 |
| $Y'_{\beta\beta}$ | (5.18)    | 0.4266     | $x'_P$              | (5.35)    | -0.5149 |
| $Y'_{rr}$         | (5.19)    | 4.8210e-04 | $x'_R$              | (5.35)    | -0.5149 |
| $Y'_{\beta rr}$   | (5.20)    | 0.7159     |                     |           |         |

## 5.5 Model validation and verification

The integrated ship propulsion and manoeuvring model has been validated using the sea trial test data of the benchmark chemical tanker. The ship draft and environmental condition during the sea trial test have been shown in Table 5.4. In this thesis, the service margin or sea margin (SM) is assumed to be zero (SM=0) during the sea trial test, despite of the fact that the wind force was actually Beaufort 3-4 and the sea state was Douglas 2-3 rather than a very calm sea. So, when validating the ship propulsion and manoeuvring model, in the simulation model the sea margin is set at zero and the ship draft is set at design draft (8.50 m).

Table 5.4: Sea trial condition

|                     |                |                |             |          |        |
|---------------------|----------------|----------------|-------------|----------|--------|
| Geographic position | East China Sea | Wind scale     | 3-4 Bft.    | Draft TF | 8.50 m |
| Weather             | Cloudy         | Wind Direction | NE          | Draft TM | 8.55 m |
| Depth of Water      | 75 m           | Sea state      | Douglas 2-3 | Draft TA | 8.60 m |

According to the sea trial report, only limited data of ship behaviour during sea trial test

have been measured and recorded. For instance, during the inertia and crash stop test, turning circle test and Zigzag test, only ship speed, position and heading, etc., have been measured, while the data of propeller thrust, propeller torque, ship yaw rate, drift angle, engine power and fuel rack, etc., have not been measured or recorded. So, with the limited test data the ship manoeuvring model has been partly validated. However, for model verification, some important simulation results will still be presented although there is no test data for validating them.

### 5.5.1 Propulsion validation

The ship propulsion model has been validated using the sea trial measurement data and the model test results as shown in Figure 5.5. Note that, the simulation results are generated by running the ship propulsion model under constant propeller pitch control mode (see Section 2.5.1 of Chapter 2), where the propeller pitch is kept constant (at design pitch  $P/D=0.7075$ ) until the engine revolution reaches the minimum speed limit (81.83 rpm, 49% of the engine nominal revolution) that is set in the combinator curve. So, the simulation results show that the ship velocity and shaft power (Figure 5.5(b)) will increase at constant shaft revolution in the beginning when it is at low ship velocities. A good consistency between the propulsion simulation results and the ship propulsion model test results as well as the sea trial test data has been shown in Figure 5.5.

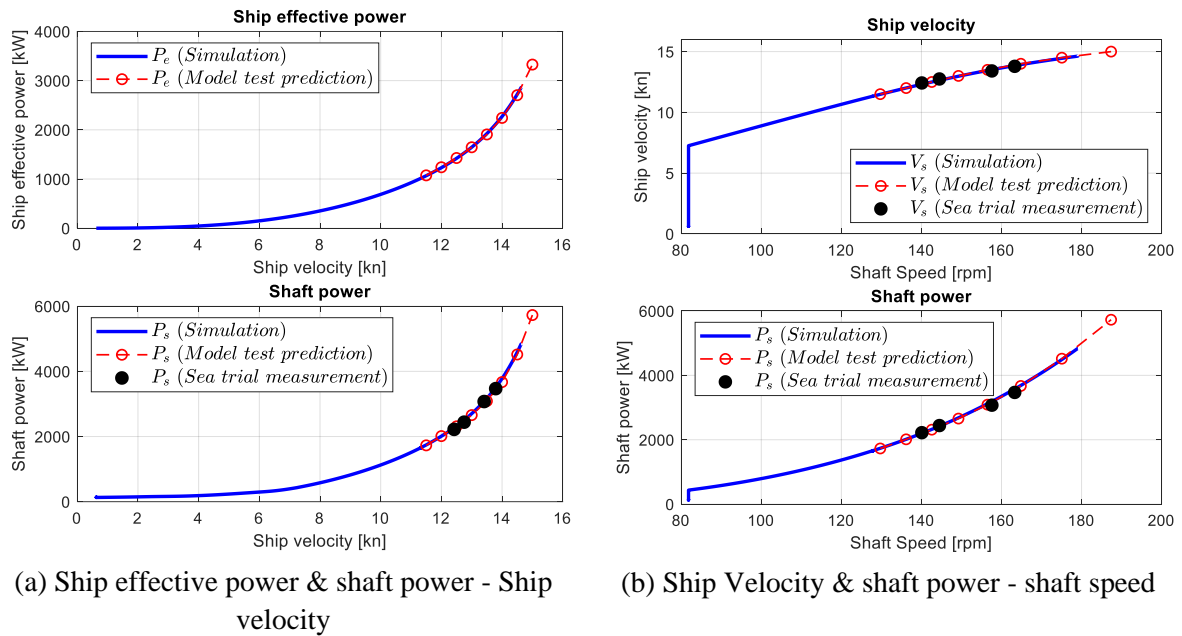


Figure 5.5: Ship propulsion validation results

### 5.5.2 Turning circle validation and verification

During the turning circle sea trial test, according to the sea trial report, the engine rotational speed is kept constant at 163.7 rpm, but the propeller pitch is not recorded. However, in the simulation both the engine rotational speed and the propeller pitch are kept as constant, which are 163.7 rpm and  $P/D=0.6022$  respectively. The ship start speed is thus 12.8 kn. For the portside turning circle test, the rudder angle is set as -35 degree, while for the starboard turning circle

rudder angle is set as 35 degrees.

In reality the behaviour of the portside and starboard turning operations may be somewhat asymmetrical especially for the ship with single propeller; however, in the model all the constants are set as the same for both portside steering and starboard steering as shown in Table 5.2. So, symmetrical simulation results for portside and starboard turning are shown in the following.

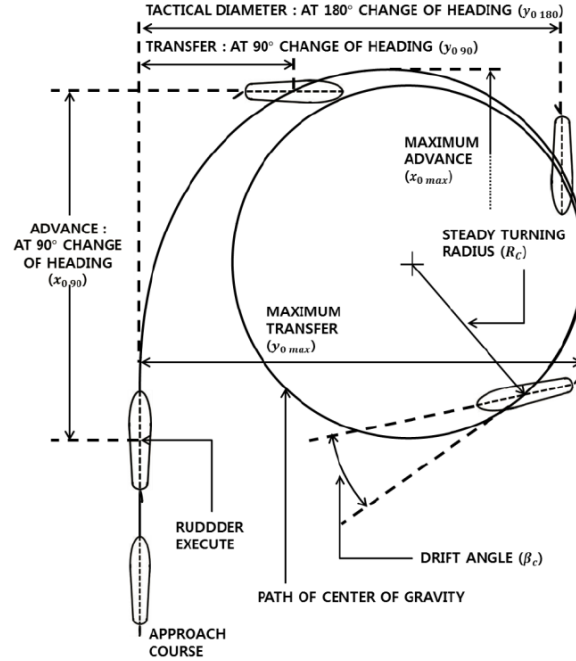


Figure 5.6: Turning circle definitions (ITTC, 2017)

To quantify the accuracy of the simulation results of the turning circle, the average relative deviation  $\bar{\sigma}_T$  between the simulation results and test data are calculated as the following:

$$\bar{\sigma}_T = 100\% \times \left( \left| \frac{x_{0max}^{Sim} - x_{0max}^{Test}}{x_{0max}^{Test}} \right| + \left| \frac{y_{0max}^{Sim} - y_{0max}^{Test}}{y_{0max}^{Test}} \right| + \left| \frac{R_C^{Sim} - R_C^{Test}}{R_C^{Test}} \right| + \left| \frac{V_C^{Sim} - V_C^{Test}}{V_C^{Test}} \right| \right) / 4 \quad (5.55)$$

Where,  $x_{0max}$  is the maximum advance (m);  $y_{0max}$  is the maximum transfer (m);  $R_C$  is the steady turning radius (m);  $V_C$  is the ship speed in steady turn (kn). The maximum advance  $x_{0max}$ , maximum transfer  $y_{0max}$  and the steady turning radius  $R_C$  are defined and illustrated in Figure 5.6.

### (1) Portside turning

The validation results of portside turning circle test with a rudder angle of -35 degree are shown in Figure 5.7 and Table 5.5. The average relative deviation  $\bar{\sigma}_T$  between the simulation results and the sea trial test data of portside turning circle is 7.70%. The uncertainties of the validation results will be analysed later in the following section.

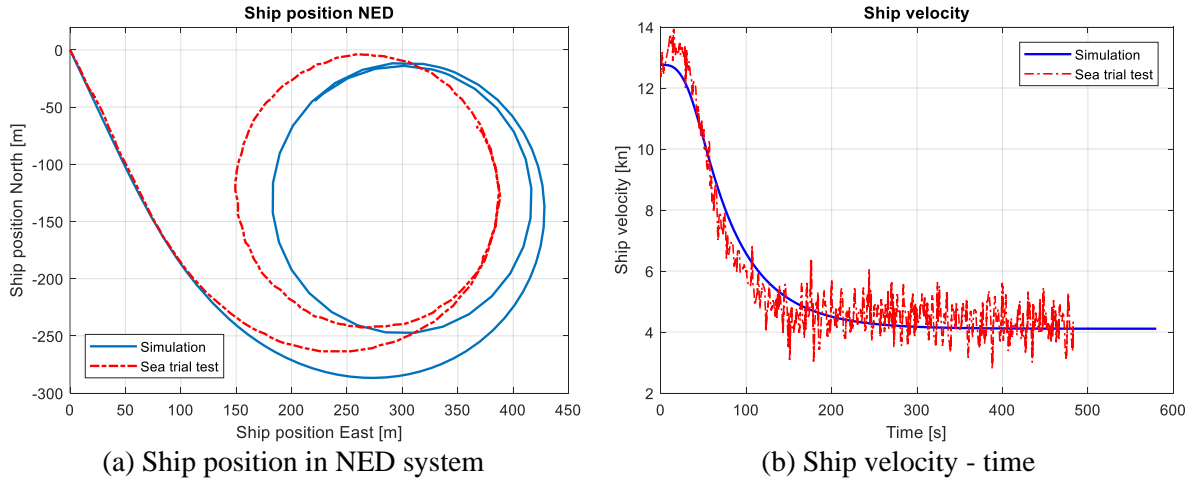
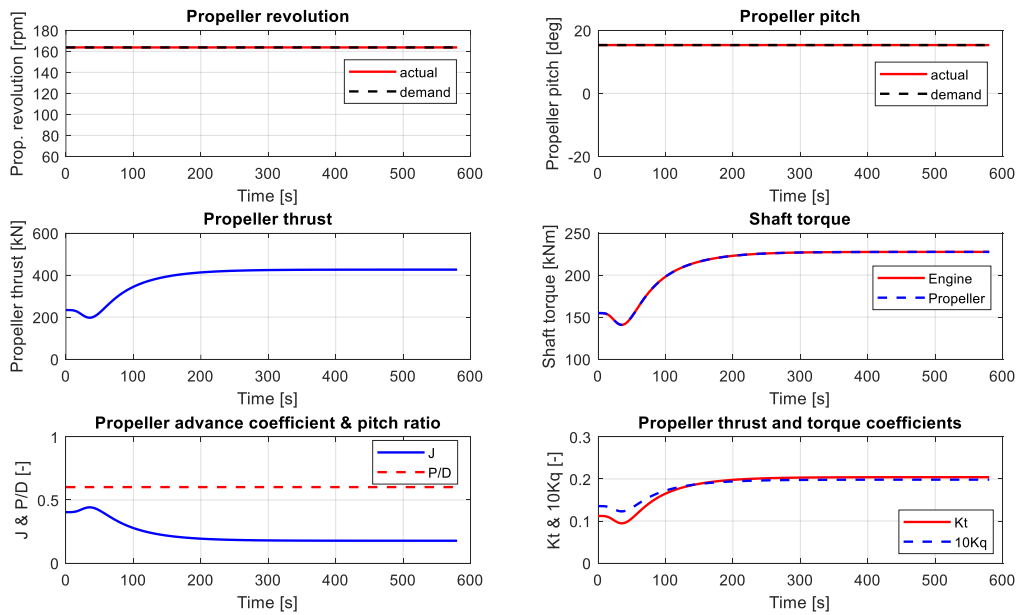


Figure 5.7: Validation results of turning circle trial (Portside with rudder angle: -35 deg.)

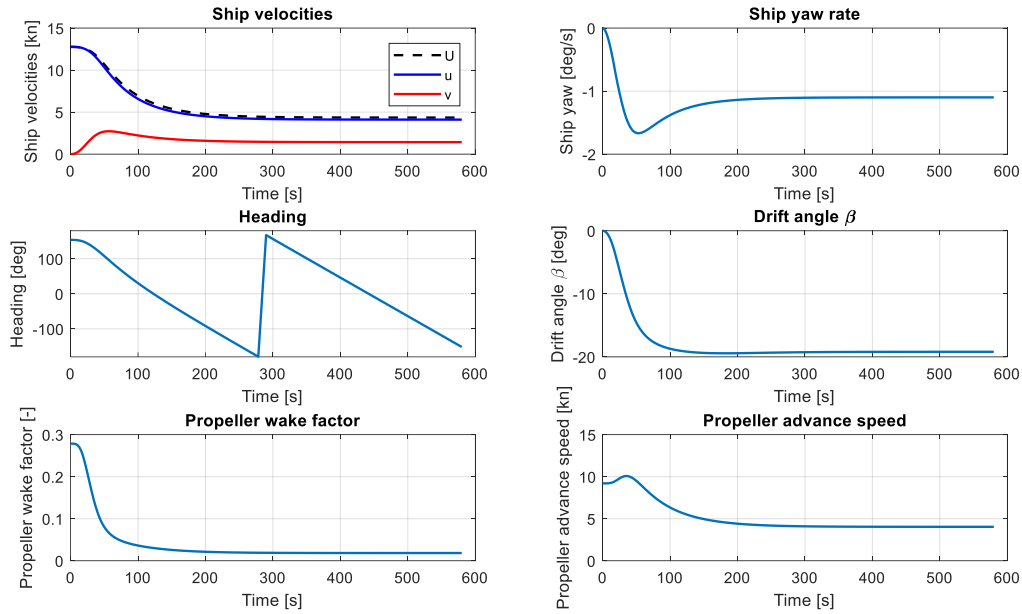
Table 5.5: Deviation between simulation results and test data of turning circle (Portside with rudder angle: -35 deg.)

| Turning Criteria | Test   | Sim.   | Relative Deviation $\sigma_T$ (%) | Average Relative Deviation $\bar{\sigma}_T$ (%) |
|------------------|--------|--------|-----------------------------------|---|
| $x_{0\max}$ (m)  | 358.60 | 392.50 | 9.45                              | 7.70  |
| $y_{0\max}$ (m)  | 304.10 | 335.40 | 10.29                             |   |
| $R_C$ (m)        | 120.40 | 116.25 | 3.45                              |   |
| $V_C$ (kn)       | 4.47   | 4.13   | 7.61                              |   |

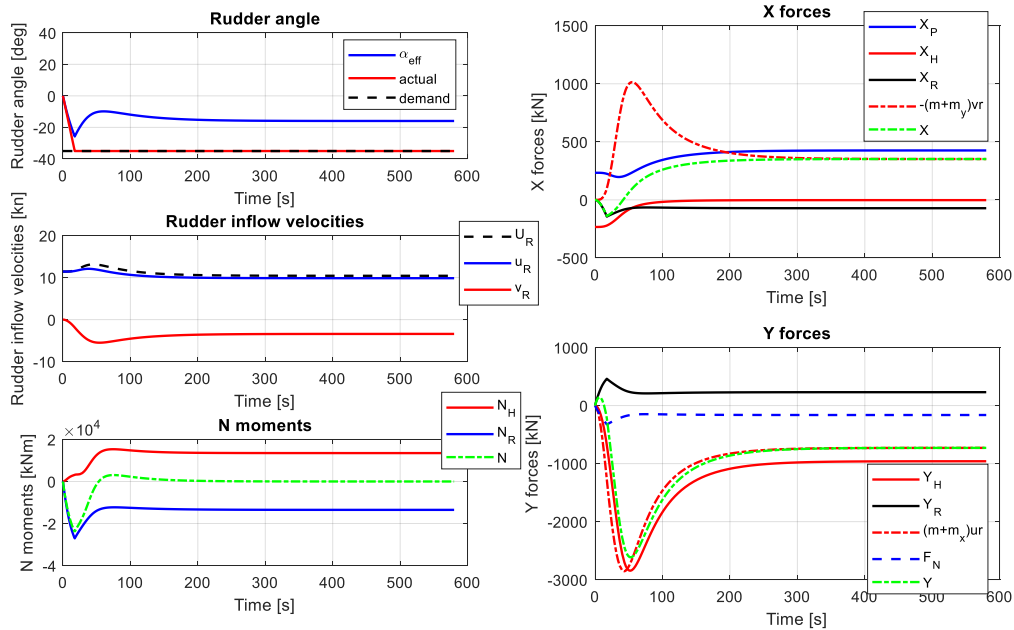
For model verification, the simulation results of the propeller, ship, and rudder behaviour during the portside turning of the ship have been shown in Figure 5.8 (a) – (c).



(a) Simulation results of propeller



(b) Simulation results of ship



(c) Simulation results of Rudder and Forces

Figure 5.8: Simulation results of turning circle trial (Portside with rudder angle: -35 deg.)

## (2) Starboard turning

The validation results of starboard turning circle test with a rudder angle of 35 degrees are shown in Figure 5.9 and Table 5.6. The average relative deviation  $\bar{\sigma}_T$  between the simulation results and the sea trial test data of starboard turning circle is 8.18%. The uncertainties of the validation results will be analysed later in the following section.

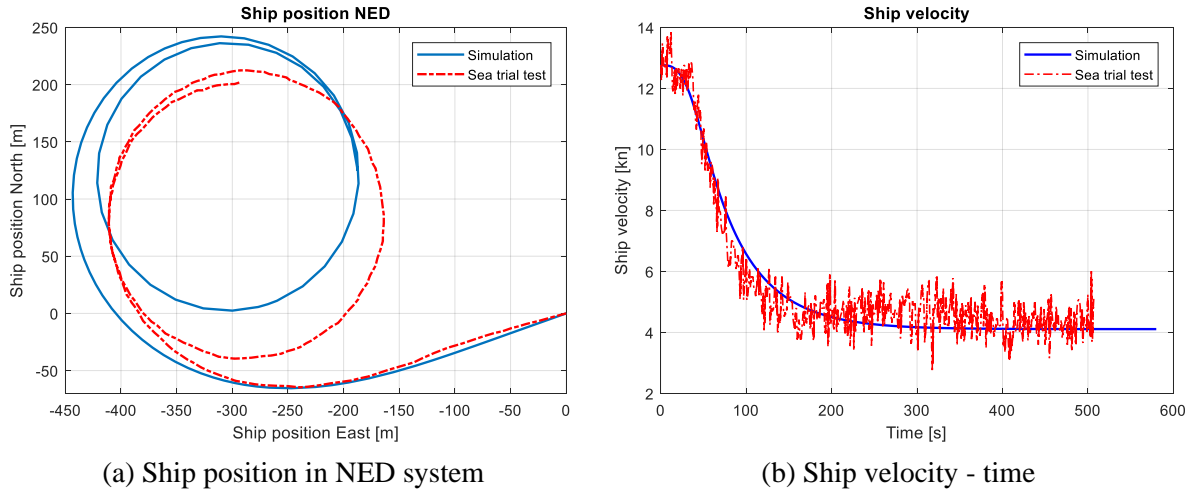
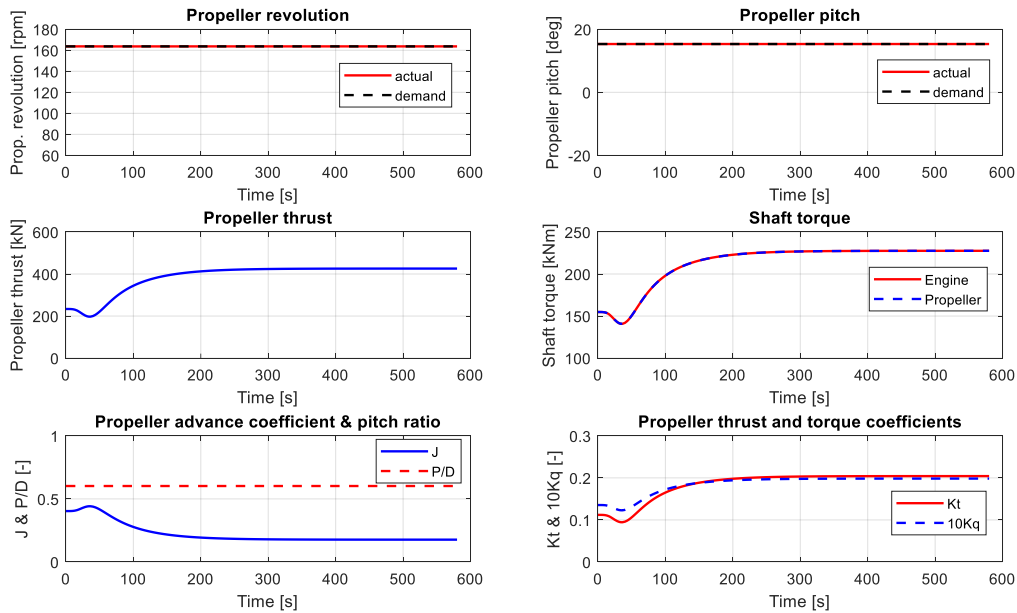


Figure 5.9: Validation results of turning circle trial (Starboard with rudder angle: 35 deg.)

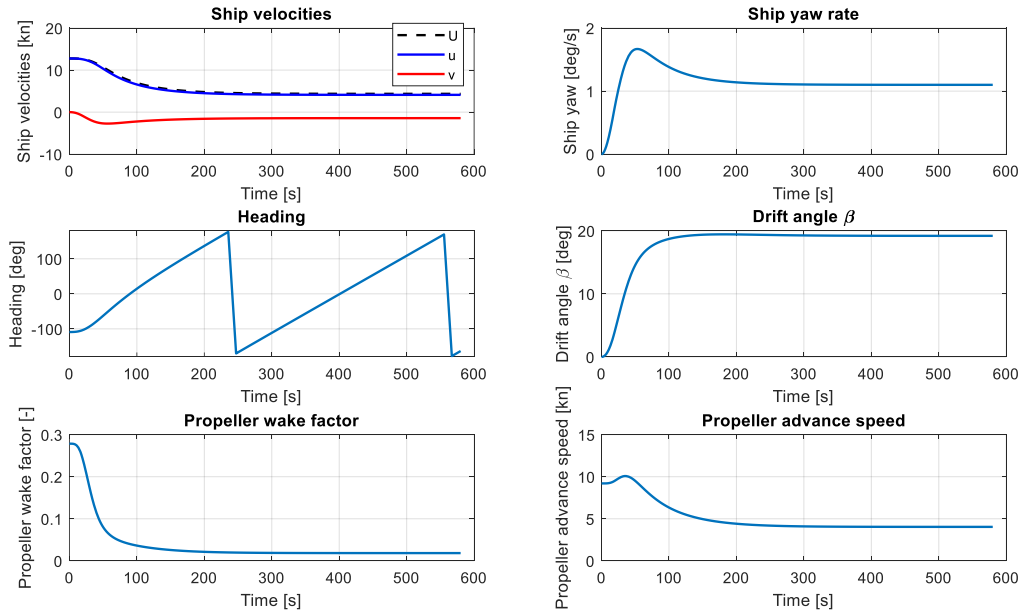
Table 5.6: Deviation between simulation results and test data of turning circle (Starboard with rudder angle: 35 deg.)

| Turning Criteria | Test   | Sim.   | Relative Deviation $\sigma_T$ (%) | Average Relative Deviation $\bar{\sigma}_T$ (%) |
|------------------|--------|--------|-----------------------------------|---|
| $x_{0\max}$ (m)  | 368.40 | 392.50 | 6.54                              | 8.18  |
| $y_{0\max}$ (m)  | 300.00 | 335.40 | 11.80                             |   |
| $R_C$ (m)        | 123.85 | 116.25 | 6.14                              |   |
| $V_C$ (kn)       | 4.50   | 4.13   | 8.22                              |   |

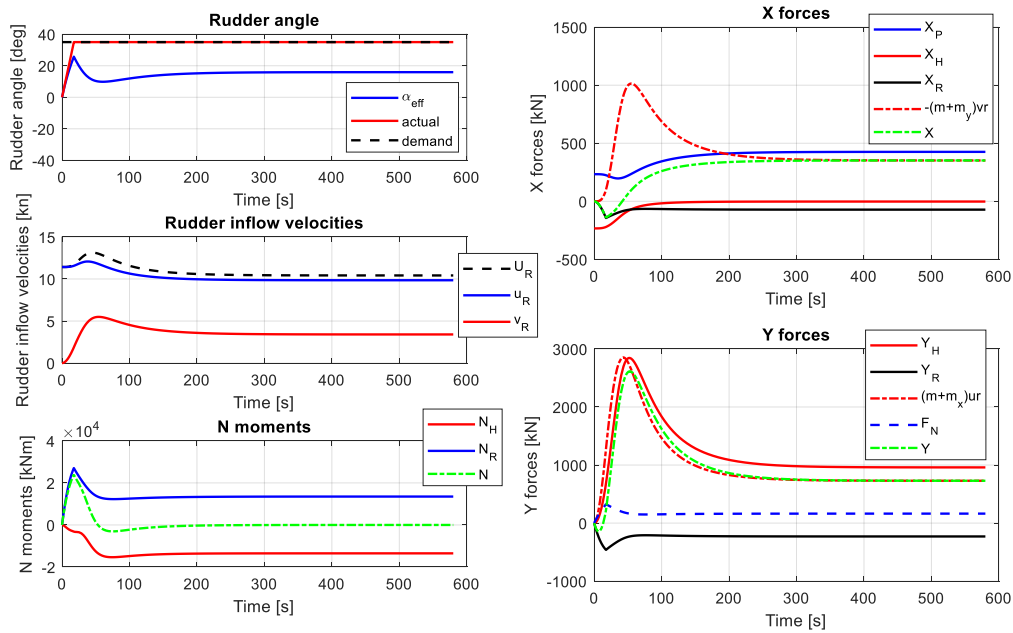
For model verification, the simulation results of the propeller, ship, and rudder behaviour during the starboard turning of the ship have been shown in Figure 5.10 (a) – (c).



(a) Simulation results of propeller



(b) Simulation results of ship



(c) Simulation results of Rudder and Forces

Figure 5.10: Simulation results of turning circle trial (Starboard with rudder angle 35 deg.)

### 5.5.3 Zigzag validation and verification

During the Zigzag test, the engine rotational speed is kept as constant while the propeller pitch is unknown. However, in the simulation of Zigzag operation both the engine speed and the propeller pitch are set as constant, which are 163.7 rpm and  $P/D=0.5661$  respectively. The ship start speed is thus 12.3 knots according to the sea trial report.



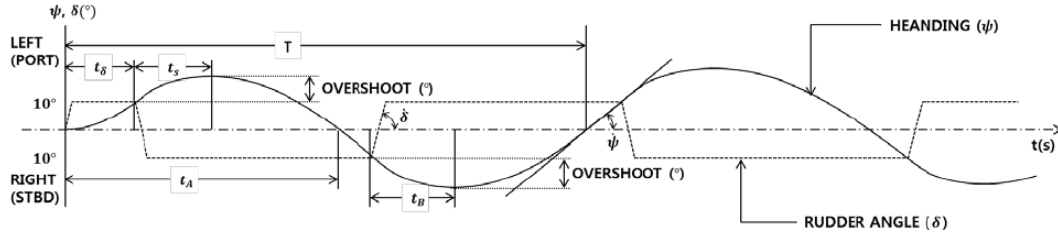


Figure 5.11: Time trace of Zigzag manoeuvre parameters (ITTC, 2017)

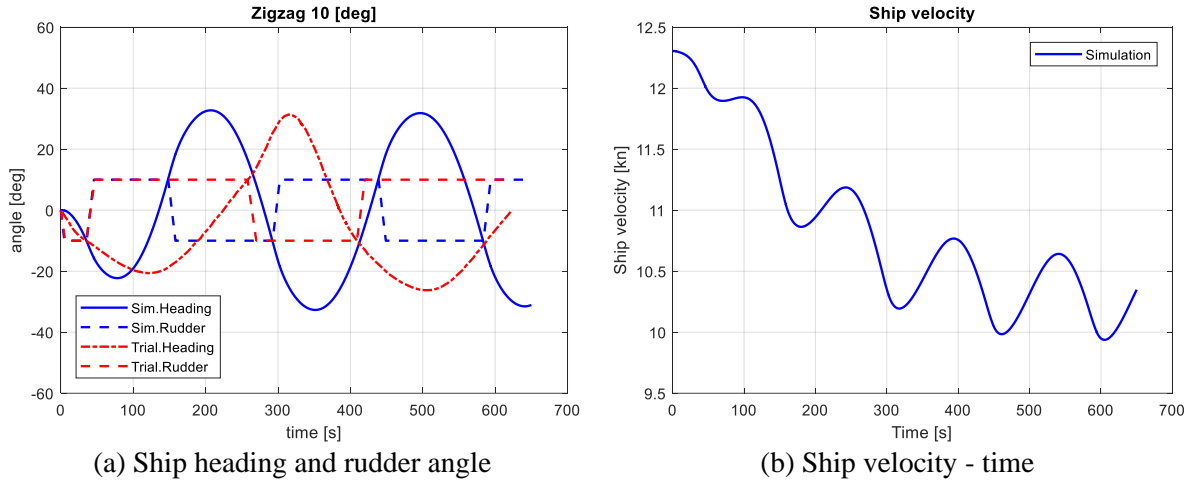
To quantify the accuracy of the simulation results of the Zigzag test, the average relative deviation  $\bar{\sigma}_Z$  between the simulation results and test data are calculated as following (Liu, 2017):

$$\bar{\sigma}_Z = 100\% \times \left( \left| \frac{\psi_{O1}^{Sim} - \psi_{O1}^{Test}}{\psi_{O1}^{Test}} \right| + \left| \frac{\psi_{O2}^{Sim} - \psi_{O2}^{Test}}{\psi_{O2}^{Test}} \right| + \left| \frac{t_{O1}^{Sim} - t_{O1}^{Test}}{t_{O1}^{Test}} \right| + \left| \frac{t_{O2}^{Sim} - t_{O2}^{Test}}{t_{O2}^{Test}} \right| \right) / 4 \quad (5.56)$$

Where,  $\psi_{O1}$  is the first overshoot angle (deg.) at time  $t_{O1}$  (s);  $\psi_{O2}$  is the second overshoot angle (deg.) at time  $t_{O2}$  (s).

### (1) Rudder: 10 deg.

The validation results of the Zigzag operation with rudder angle of 10 degrees are shown in Figure 5.12 (a) and Table 5.7. The data of ship velocity during Zigzag tests has not been recorded in the sea trial report, so, the test data of ship velocity is not available for validating the simulation results. An obvious inconsistency between the simulation results and the sea trial data has been shown (Figure 5.12(a)), and the average relative deviation  $\bar{\sigma}_Z$  is 23.25% (Table 5.7). The uncertainties of the validation results will be analysed later.



(a) Ship heading and rudder angle

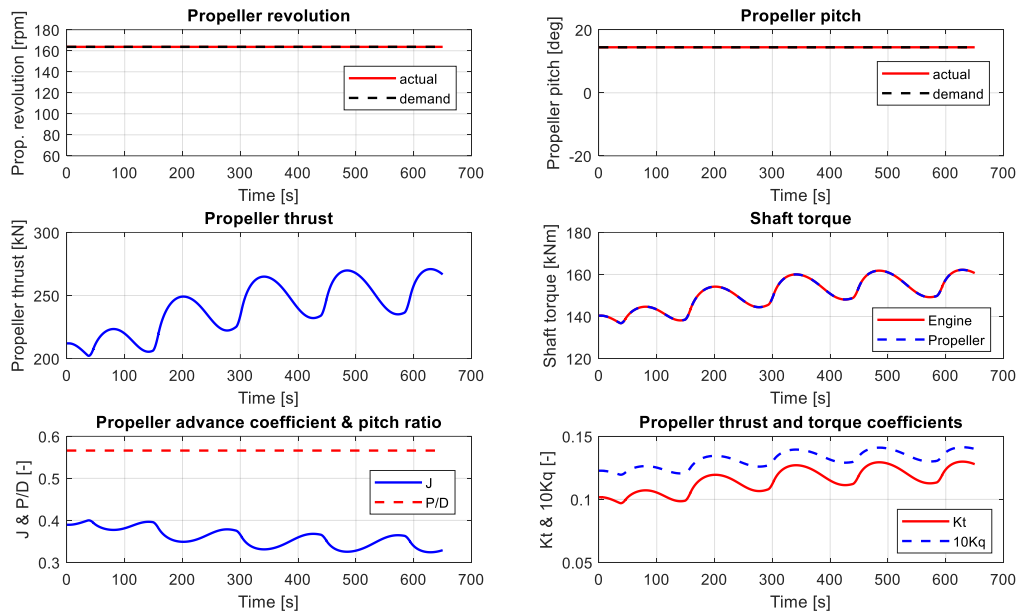
(b) Ship velocity - time

Figure 5.12: Validation results of Zigzag test (Rudder angle: 10 deg.)

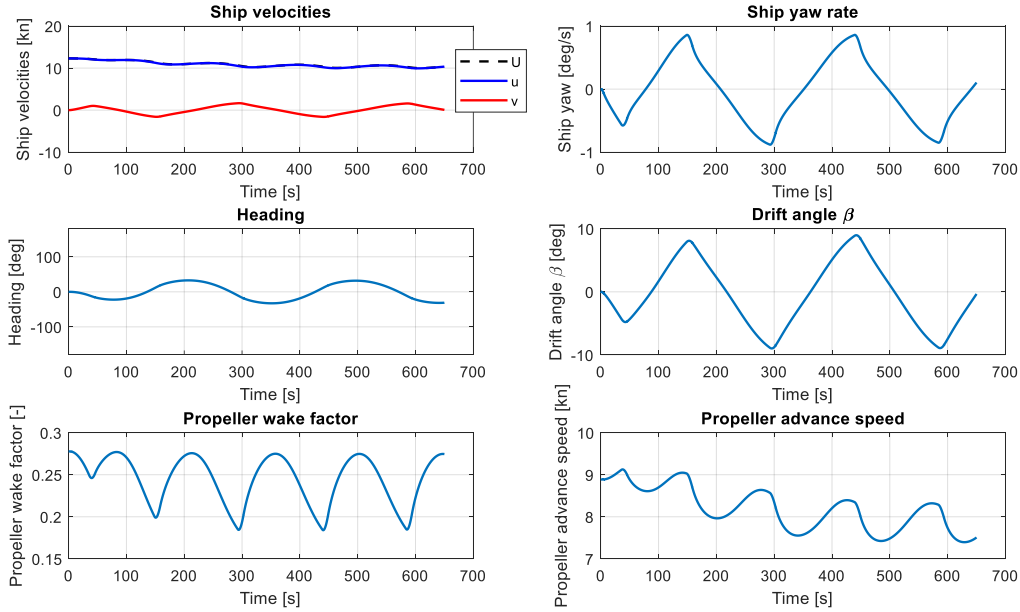
Table 5.7: Deviation between simulation results and test data of Zigzag  
(Zigzag with rudder angle: 10 deg.)

| Turning Criteria   | Test   | Sim.   | Relative Deviation $\sigma_z$ (%) | Average Relative Deviation $\bar{\sigma}_z$ (%) |
|--------------------|--------|--------|-----------------------------------|---|
| $\psi_{01}$ (deg.) | 10.65  | 12.27  | 15.21                             | 23.25   |
| $\psi_{02}$ (deg.) | 21.37  | 22.73  | 6.36                              |   |
| $t_{01}$ (s)       | 124.10 | 78.00  | 37.15                             |   |
| $t_{02}$ (s)       | 315.10 | 207.10 | 34.27                             |   |

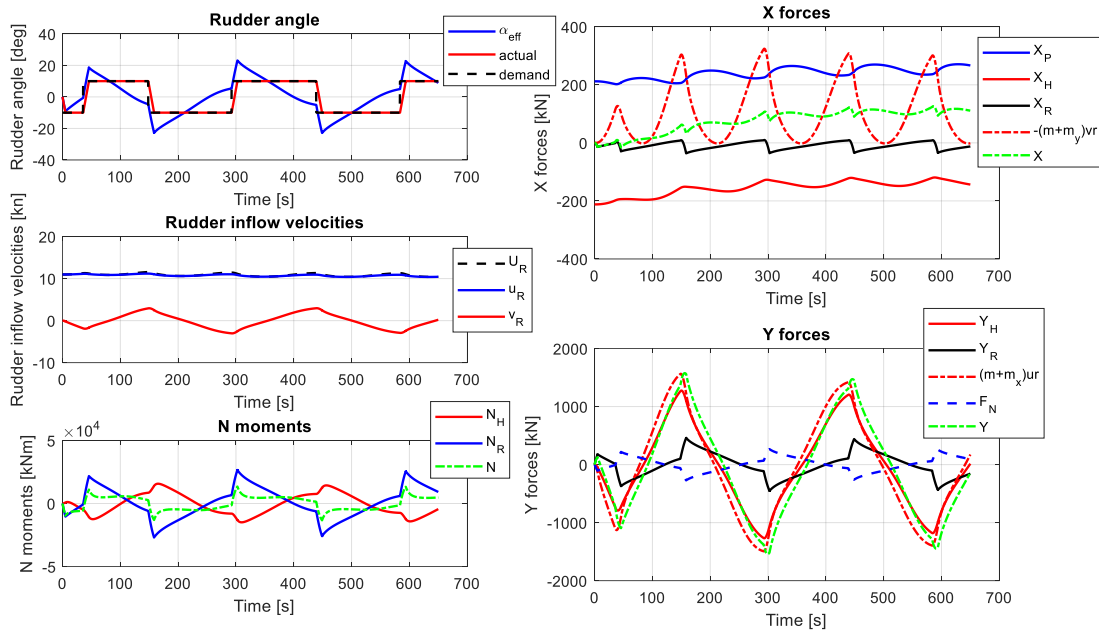
For model verification, the simulation results of the propeller, ship and rudder behaviour during the Zigzag with rudder angle of 10 degrees have been shown in Figure 5.13 (a) – (c).



(a) Simulation results of propeller



(b) Simulation results of ship



(c) Simulation results of Rudder and Forces

Figure 5.13: Simulation results of Zigzag test (Rudder angle: 10 deg.)

## (2) Rudder: 20 deg.

The validation results of the Zigzag test with rudder angle of 20 degrees are shown in Figure 5.14(a) and Table 5.8. A good consistency between the simulations results and the sea trial data has been shown, and the average relative deviation  $\bar{\sigma}_Z$  is 2.19%.

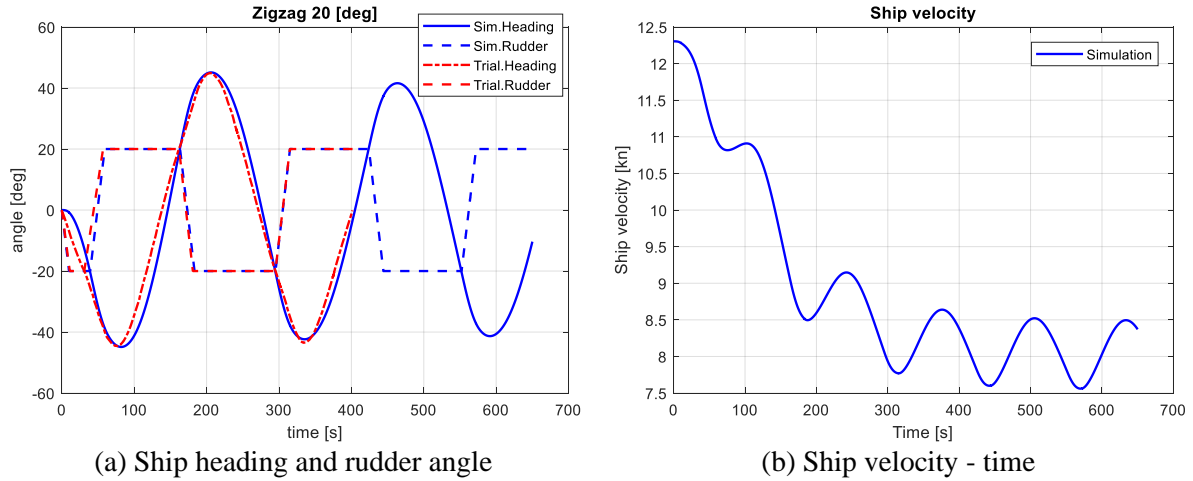
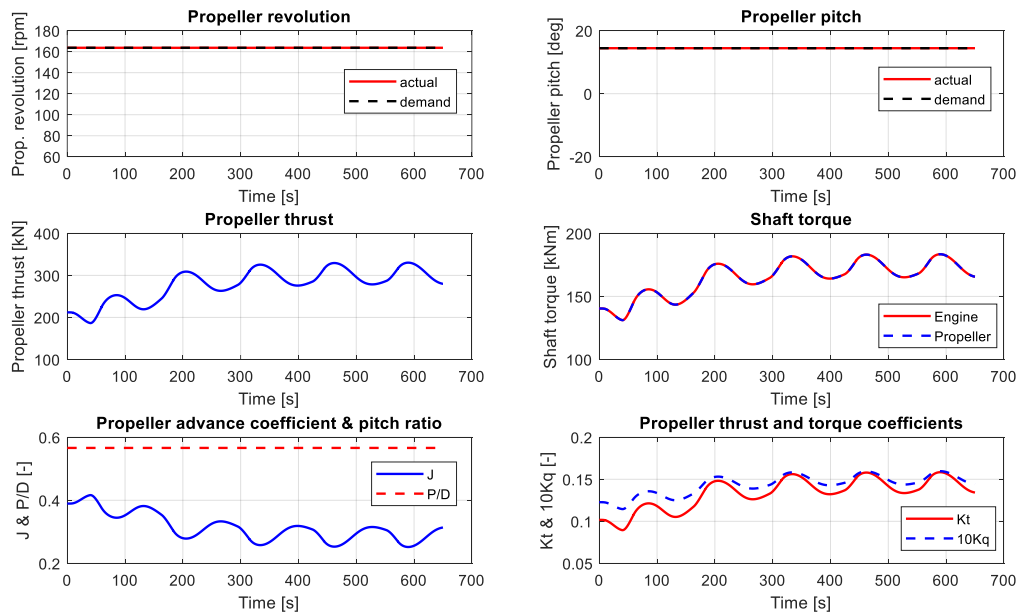


Figure 5.14: Validation results of Zigzag test (Rudder angle: 20 deg.)

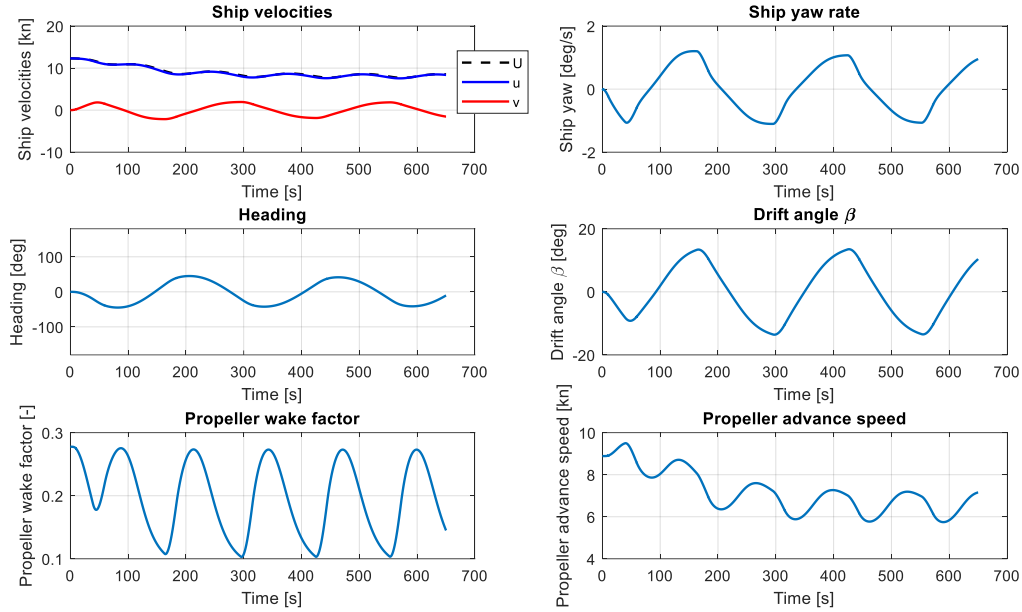
Table 5.8: Deviation between simulation results and test data of Zigzag (Zigzag with rudder angle: 20 deg.)

| Turning Criteria   | Test   | Sim.   | Relative Deviation $\sigma_Z$ (%) | Average Relative Deviation $\bar{\sigma}_Z$ (%) |
|--------------------|--------|--------|-----------------------------------|---|
| $\psi_{01}$ (deg.) | 24.59  | 24.88  | 1.18                              | 2.19  |
| $\psi_{02}$ (deg.) | 24.92  | 25.11  | 0.76                              |   |
| $t_{01}$ (s)       | 77.32  | 82.05  | 6.12                              |   |
| $t_{02}$ (s)       | 204.60 | 206.00 | 0.68                              |   |

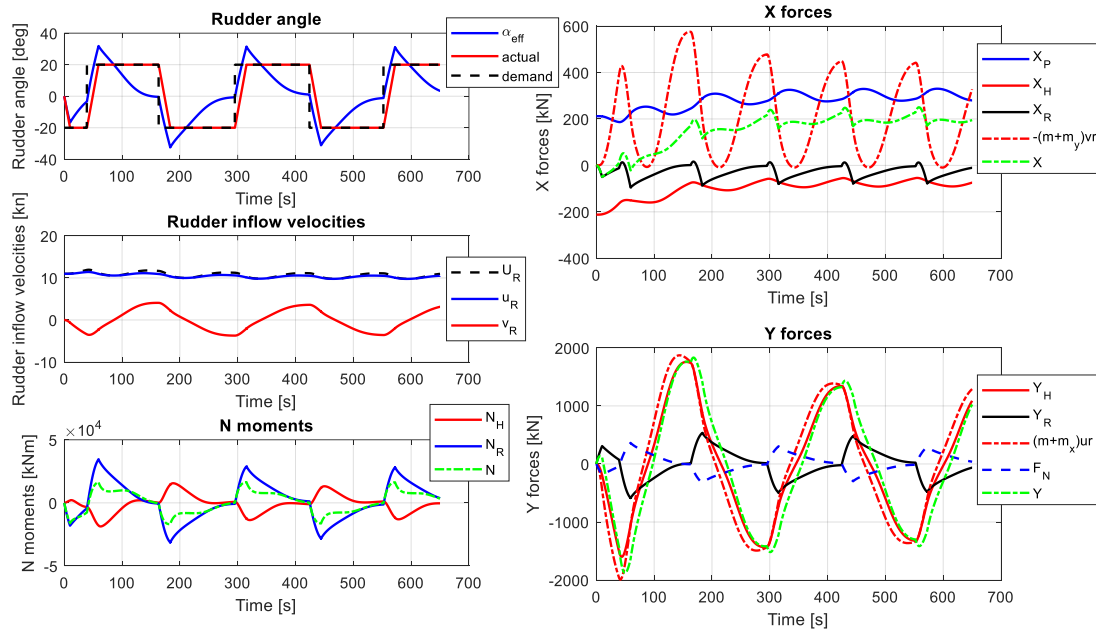
For model verification, the simulation results of the propeller, ship and rudder behaviour during the Zigzag with rudder angle of 20 degrees have been shown in Figure 5.15 (a) – (c).



(a) Simulation results of propeller



(b) Simulation results of ship



(c) Simulation results of Rudder and Forces

Figure 5.15: Simulation results of Zigzag test (Rudder angle: 20 deg.)

### 5.5.4 Inertia and crash stop validation and verification

During stopping inertia test, the rudder can be maintained at midships throughout the trial (“free stop”) or moved to 35 degrees port or starboard (“IMO stop”) (ITTC, 1999). The “Full Ahead => Stop” and “Full Ahead => Full Astern” tests results have shown that the ship headings have been noticeably changed during the tests and the trajectory of the ship courses have been significantly curved to port side or starboard. So, it is inferred that the rudder angle throughout the tests is set as 35 degrees portside for “Full Ahead => Stop” and 35 degrees starboard for

“Full Ahead => Full Astern” although there is no rudder angle recording in the sea trial report. The rudder angle in the simulation of stopping inertia test is also set at 35 degrees portside or starboard accordingly.

The test data of propeller rotational speed, propeller pitch and engine power are not available, however, following the test data in turning circle and Zigzag tests, the propeller rotational speed is also set as 163.7 rpm in the simulation. The full ahead propeller pitch (“100% Ahead Pitch”) is set as  $P/D = 0.6553$  (92.6% of the design pitch), so, the ship start speed is then 13.30 knots, which has been recorded in the sea trial report. The full astern pitch (“-100% Astern Pitch”) is set as  $P/D = -0.4501$  (-63.6% of the design pitch) to protect the engine from overloading during “Full Ahead => Full Astern”. The propeller pitch rate of change is set as 3.9 (%/s), so that the time from “100% Ahead Pitch” to “-100% Astern Pitch” is 37 seconds as recorded in the sea trial report.

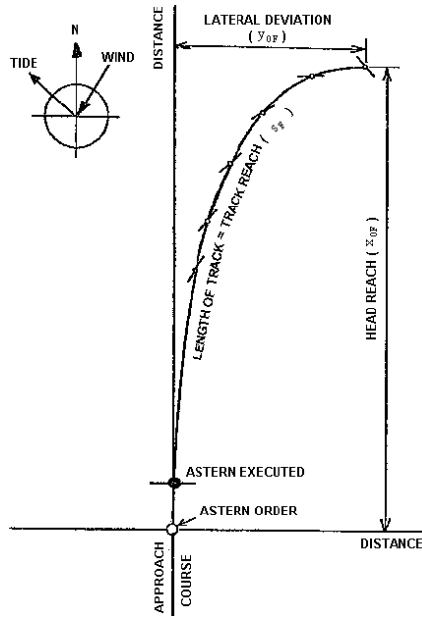


Figure 5.16: Definitions used in stopping trials (ITTC, 2017)

To quantify the accuracy of the simulation results of the stopping trial test, the average relative deviation  $\bar{\sigma}_s$  between the simulation results and test data are calculated as the following:

$$\bar{\sigma}_s = 100\% \times \left( \left| \frac{x_{0F}^{Sim} - x_{0F}^{Test}}{x_{0F}^{Test}} \right| + \left| \frac{y_{0F}^{Sim} - y_{0F}^{Test}}{y_{0F}^{Test}} \right| + \left| \frac{S_F^{Sim} - S_F^{Test}}{S_F^{Test}} \right| + \left| \frac{V_D^{Sim} - V_D^{Test}}{V_D^{Test}} \right| \right) / 4 \quad (5.57)$$

Where,  $x_{0F}$  is the head reach (or offset advance) defined as the distance travelled in the direction of the ship's initial course (m) (Figure 5.16);  $y_{0F}$  is the lateral deviation (or offset transfer) defined as the distance to port or starboard measured normal to ship's initial course (m);  $S_F$  is the track reach (length of track) defined as the total distance travelled along the ship's path (m);  $V_D$  is the ship speed drop (kn).

### (1) Full Ahead => Stop

During the full ahead to stop test the propeller pitch has been reduced from 100% full ahead pitch to zero (thrust) pitch. The validation results of “Full Ahead => Stop” are shown in Figure 5.17 and Table 5.9. Deviations between the simulation results and sea trial test data for the ship stopping distance and ship velocity have been found, and the average relative deviation  $\bar{\sigma}_s$  calculated by equation (5.57) is 14.29%. The uncertainties of the validation results will be analysed later in the following section.

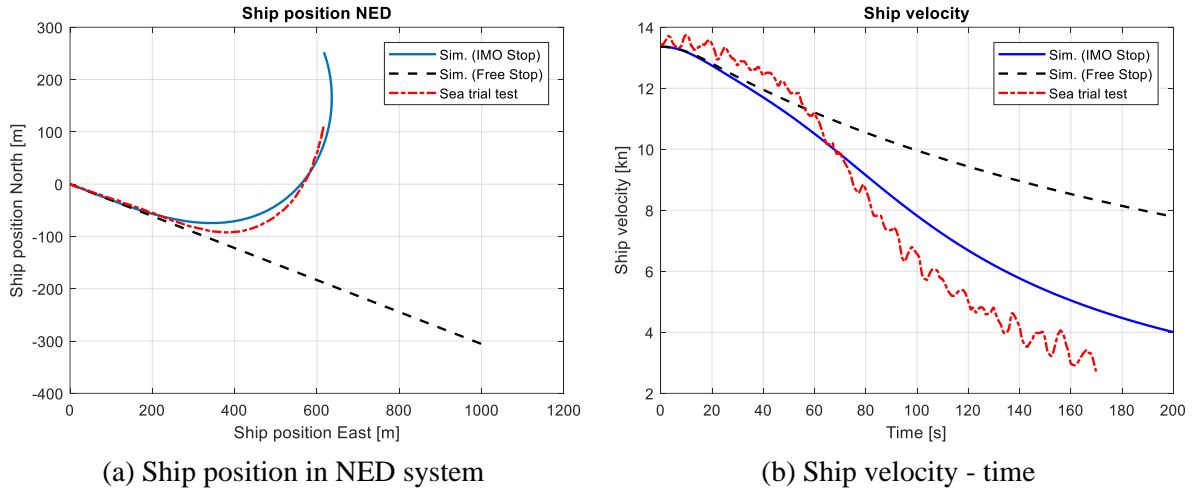
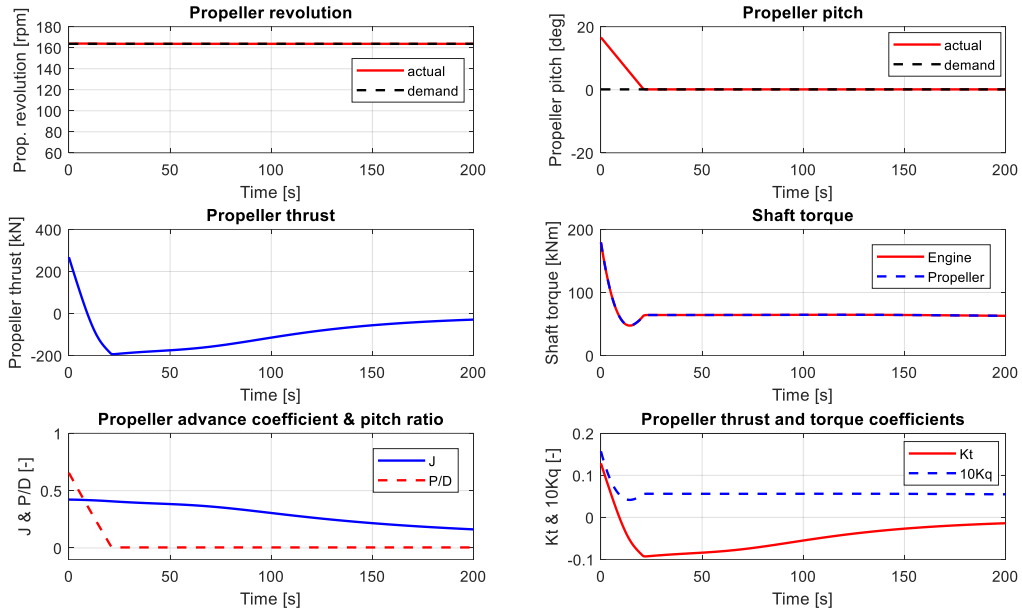


Figure 5.17: Validation results of Inertial Trial (FULL AH. – STOP)

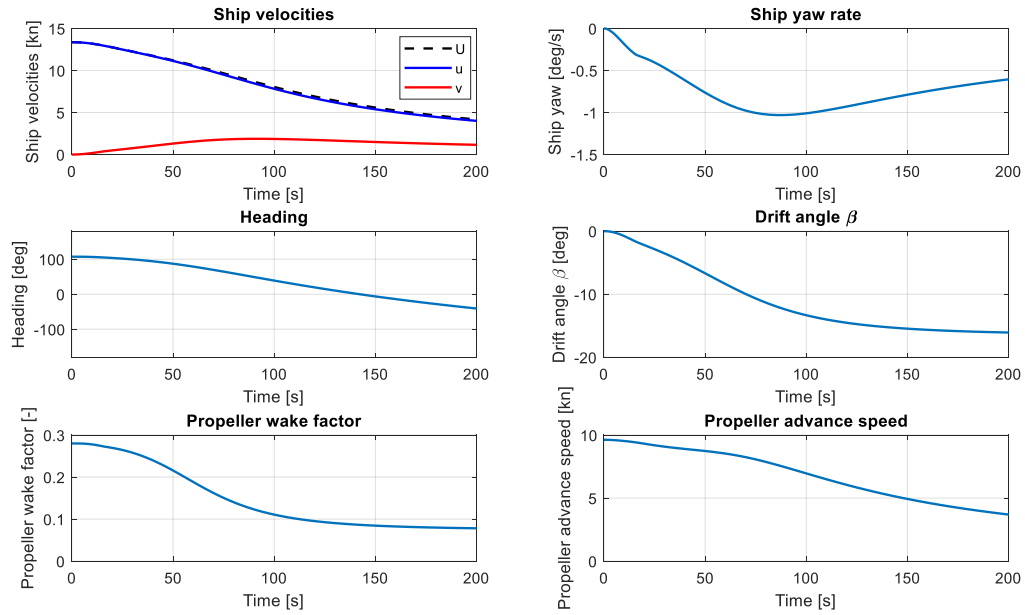
Table 5.9: Deviation between simulation results and test data of stopping trial  
(FULL AH. - STOP with rudder angle: -35 deg.)

| Turning Criteria | Test   | Sim.   | Relative Deviation $\sigma_s$ (%) | Average Relative Deviation $\bar{\sigma}_s$ (%) |
|------------------|--------|--------|-----------------------------------|---|
| $x_{0F}$ (m)     | 556.50 | 551.80 | 0.84                              | 14.29   |
| $y_{0F}$ (m)     | 285.00 | 363.10 | 27.40                             |   |
| $S_F$ (m)        | 732.17 | 794.19 | 8.47                              |   |
| $V_D$ (kn)       | 10.77  | 8.57   | 20.43                             |   |

For model verification, the simulation results of the propeller, ship and rudder behaviour during the “Full Ahead => Stop” operation of the ship have been shown in Figure 5.18 (a) – (c).

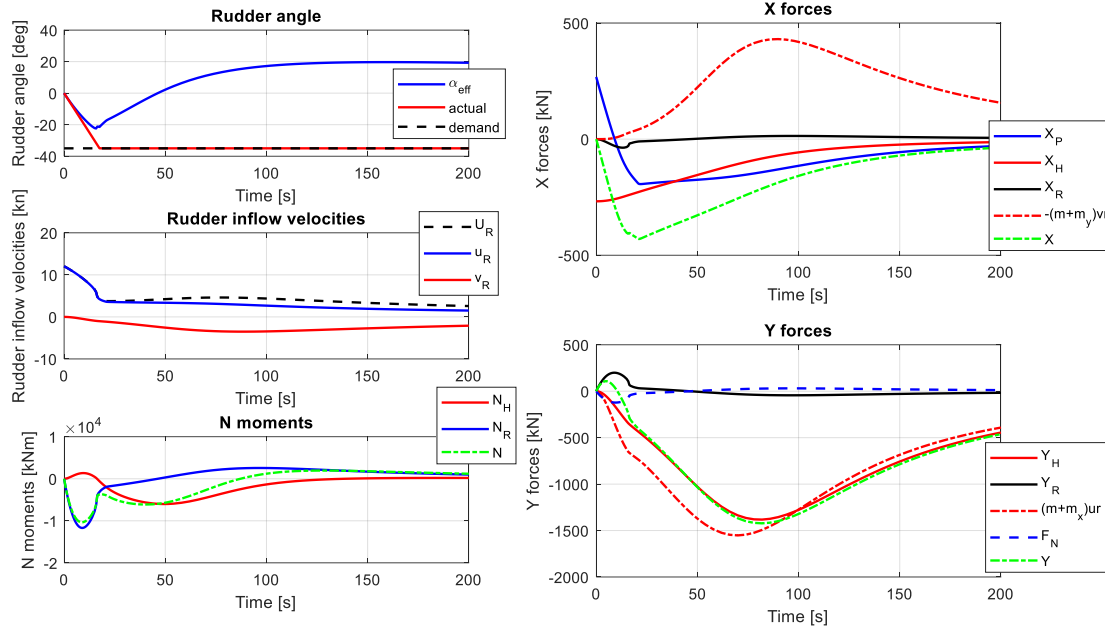


(a) Simulation results of Propeller (“IMO Stop”)



(b) Simulation results of ship (“IMO Stop”)



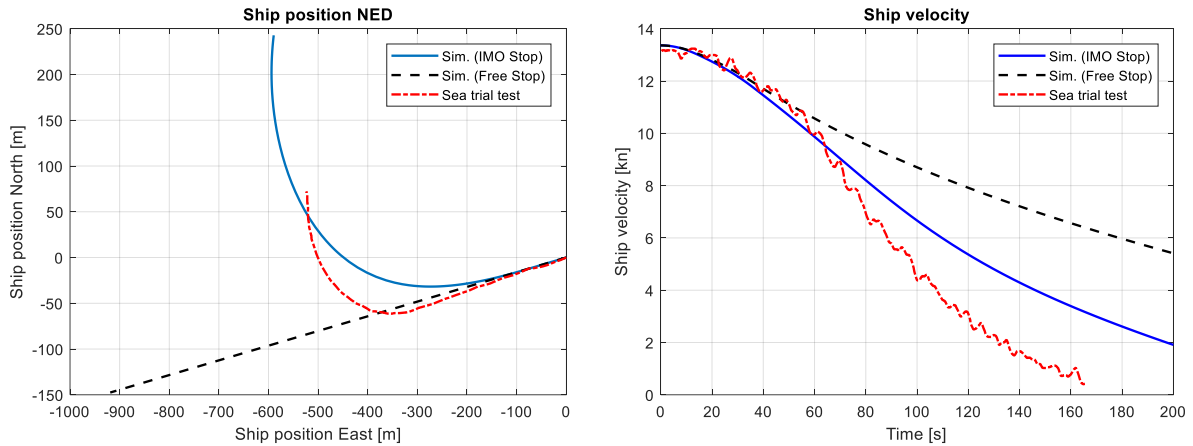


(c) Simulation results of Rudder and Forces (“IMO Stop”)

Figure 5.18: Simulation results of Inertial Trial (FULL AH. – STOP)

## (2) Full Ahead => Full Astern

During the full ahead to full astern test the propeller pitch has been reduced from 100% Ahead pitch to -100% Astern pitch. The validation results of FULL AH. – FULL AST. test has been shown in Figure 5.19 and Table 5.10. Obvious inconsistency between the simulation results and the sea trial data has been found, and the average relative deviation  $\bar{\sigma}_s$  is 33.39%. The uncertainties of the validation results will be analysed later in the following section.



(a) Ship position in NED system

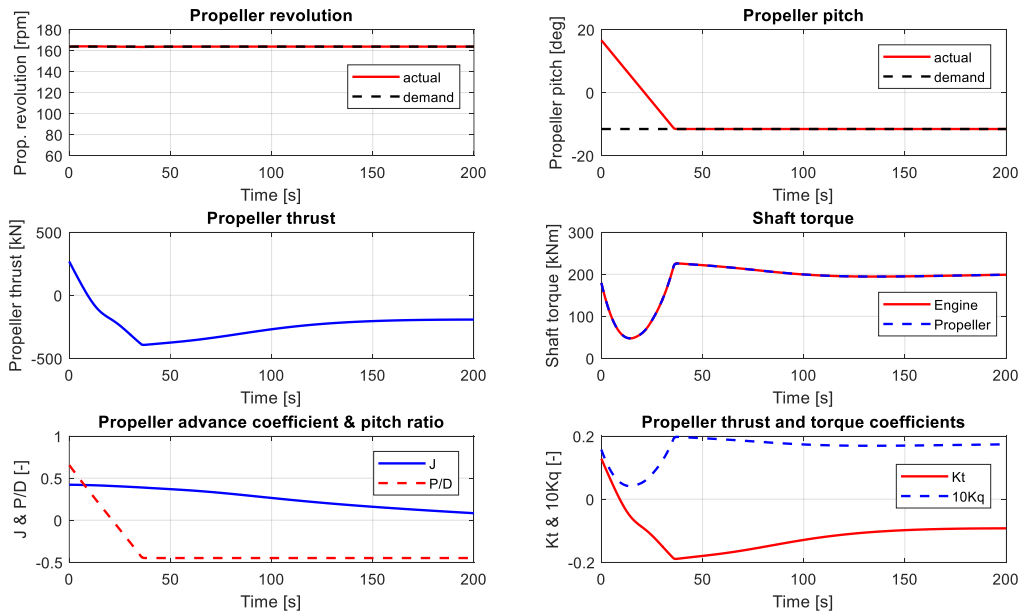
(b) Ship velocity - time

Figure 5.19: Validation results of Inertial Trial (FULL AH. – FULL AST.)

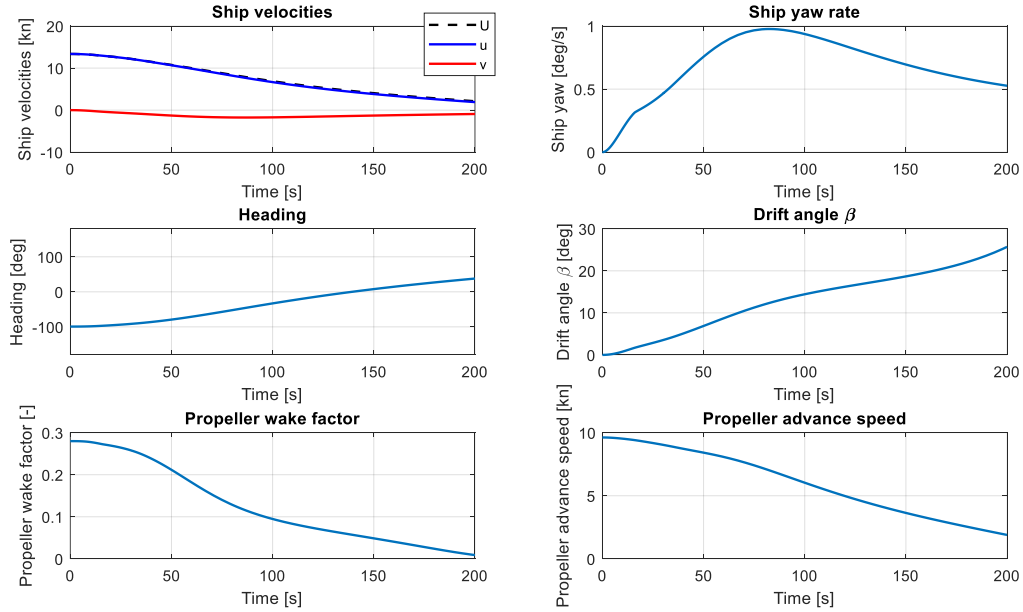
Table 5.10: Deviation between simulation results and test data of stopping trial  
(FULL AH. – FULL AST. with rudder angle: 35 deg.)

| Turning Criteria | Test   | Sim.   | Relative Deviation $\sigma_s$ (%) | Average Relative Deviation $\bar{\sigma}_s$ (%) |
|------------------|--------|--------|-----------------------------------|---|
| $x_{0F}$ (m)     | 505.70 | 554.20 | 9.59                              | 33.39   |
| $y_{0F}$ (m)     | 154.50 | 287.60 | 86.15                             |   |
| $S_F$ (m)        | 605.27 | 711.32 | 17.52                             |   |
| $V_D$ (kn)       | 12.75  | 10.16  | 20.31                             |   |

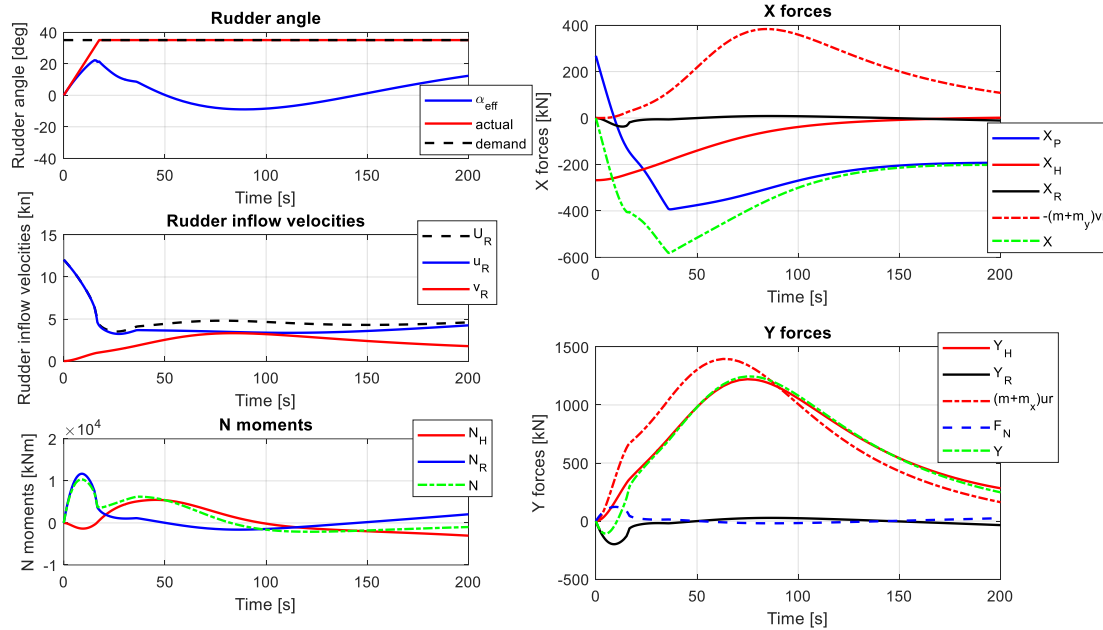
For model verification, the simulation results of the propeller, ship and rudder behaviour during the “Full Ahead => Full Astern” operation of the ship have been shown in Figure 5.20 (a) – (c).



(a) Simulation results of propeller (“IMO Stop”)



(b) Simulation results of ship ("IMO Stop")



(c) Simulation results of Rudder and Forces ("IMO Stop")

Figure 5.20: Simulation results of Inertial Trial (FULL AH. – FULL AST.)

### 5.5.5 Uncertainty and sensitivity analysis

From the validation results shown above, differences between the simulation results and the sea trial test data have been found. The uncertainties causing the differences could exist in the model, the simulation process, and also the sea trial test data.

In the manoeuvring model, some hydrodynamic coefficients for calculating the manoeuvring forces and moments are calculated (using empirical formulas) or estimated as constants (Table 5.2 and Table 5.3), while in reality they could change due to the changes of ship motions and rudder angles. Apart from the parameters calculated using the approximate

empirical formulas, the most uncertain parameters that are set as constants in the model are  $C_{my}$ ,  $C_{wa}$ ,  $C_{pa}$ ,  $A_R/(L \cdot T)$ ,  $\ell_R/L$  and  $\gamma_R$  as listed in Table 5.11. These parameters are estimated according to data from literature as well as trial-and-error during model calibration process. The uncertainties of the model parameters  $U$  are quantified as following (Schulten, 2005):

$$U = \left| \frac{(R_{\max} - R_{\min}) / 2}{R_{sel}} \cdot 100\% \right| \quad (5.58)$$

Where,  $R_{sel}$  is the selected value for a certain model parameter;  $R_{\min}$  is the minimum value of the possible range for the model parameter;  $R_{\max}$  is the maximum value of the possible range for the model parameter;  $R_{mid}$  is the middle value of the possible range for the model parameter  $R_{mid} = (R_{\min} + R_{\max}) / 2$ .

In order to have an insight into the sensitivity of the simulation results to the uncertainties of the model parameters, the influences of the uncertain model parameters listed in Table 5.11 on the turning circle behaviour have been shown in Figure 5.21 - Figure 5.26.

Table 5.11: Uncertain model parameters

| Parameters           | Selected value<br>$R_{sel}$ | Possible range<br>$[R_{\min} \ R_{\max}]$ | Middle value<br>$R_{mid}$ | Uncertainty<br>$U$ |
|----------------------|-----------------------------|---|---------------------------|--------------------|
| $C_{my}$             | 0.50                        | [0.10 1.00]                               | 0.55                      | 90.00%             |
| $C_{wa}$             | 0.96                        | [0.90 0.98]                               | 0.94                      | 4.17%              |
| $C_{pa}$             | 0.78                        | [0.75 0.85]                               | 0.80                      | 6.41%              |
| $100A_R/(L \cdot d)$ | 1.70                        | [1.30 1.90]                               | 1.60                      | 17.65%             |
| $\ell_R/L$           | -1.00                       | [-1.00 -0.70]                             | -0.85                     | 15.00%             |
| $\gamma_R$           | 0.60                        | [0.35 0.65]                               | 0.50                      | 25.00%             |

As mentioned previously, the applied propeller model is based on the corrected open water characteristics of Wageningen C4-55 propeller rather than the real propeller that is installed in the benchmark chemical tanker. Although the data of C4-55 open water characteristics has been corrected based on the data of the real propeller at design pitch in the first quadrant, there are still uncertainties in the propeller model at off-design pitches as well as in the other operating quadrants, especially in the fourth quadrant. For instance, during both “Full Ahead => Stop” and “Full Ahead => Full Astern”, the propeller will mainly operate in the fourth quadrant until the ship velocity drops to zero, as can be seen from the simulation results of propeller advance coefficient and thrust coefficient in Figure 5.18 (a) and Figure 5.20 (a). It is possible that the real propeller installed in the ship is able to produce larger negative thrust than the corrected C4-55 propeller in the fourth quadrant.

Uncertainties could also exist in the sea trial test data. For instance, the sea trial data of Zigzag with rudder angle of 10 degrees is somewhat questionable or wrong. The larger rudder angle (20 deg.) Zigzag test has shown a logical, stable and symmetrical behaviour. A similarly stable behaviour is expected when the excitation is less, i.e., a smaller rudder angle (10 deg.).

The ship behaviour with smaller rudder angle (10 deg.) to portside is different when the ship has rudder angle to starboard, the rotation in one direction takes longer and changes much slower than in the other direction. However, even unstable ships should have a more or less symmetrical response to the same input signal, i.e., the rudder angle. Although in general the oscillation periods of ship heading of Zigzag with smaller rudder angle are longer, the sea trial test data of this benchmark ship has shown a much longer period of Zigzag with rudder angle of 10 degrees than that of 20 degrees when comparing it with the results from literature (Kijima and Nakiri, 2002; Aoki et al., 2006; Yasukawa and Yoshimura, 2015; Liu, 2017; Zaky et al., 2018).

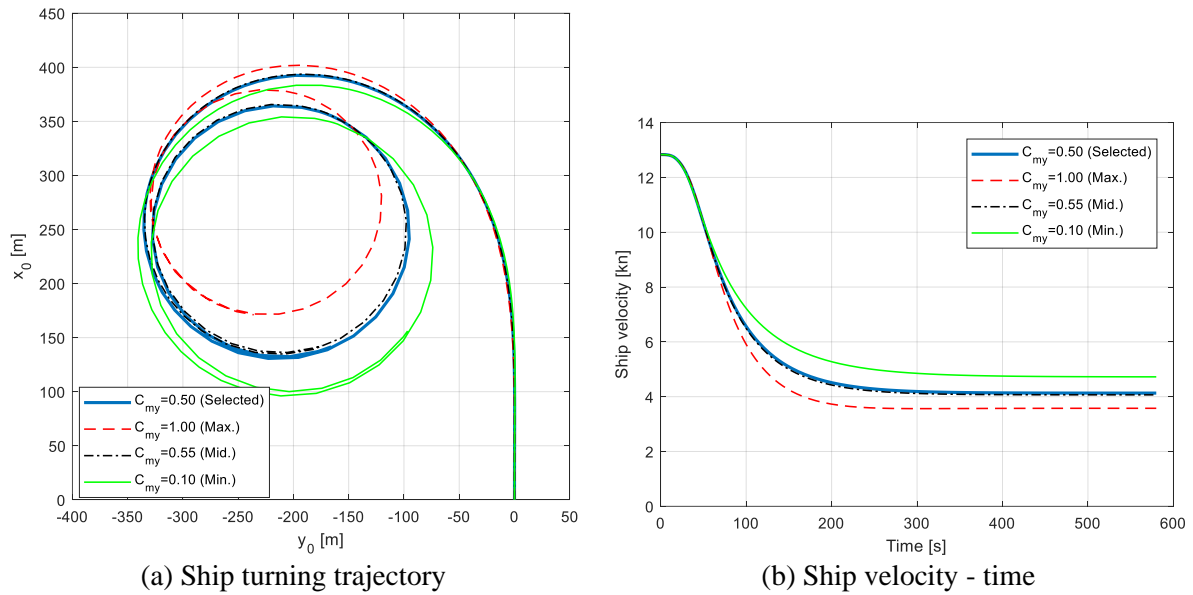


Figure 5.21: Influence of  $C_{my}$  on turning manoeuvre (Portside with rudder angle: -35 deg.)

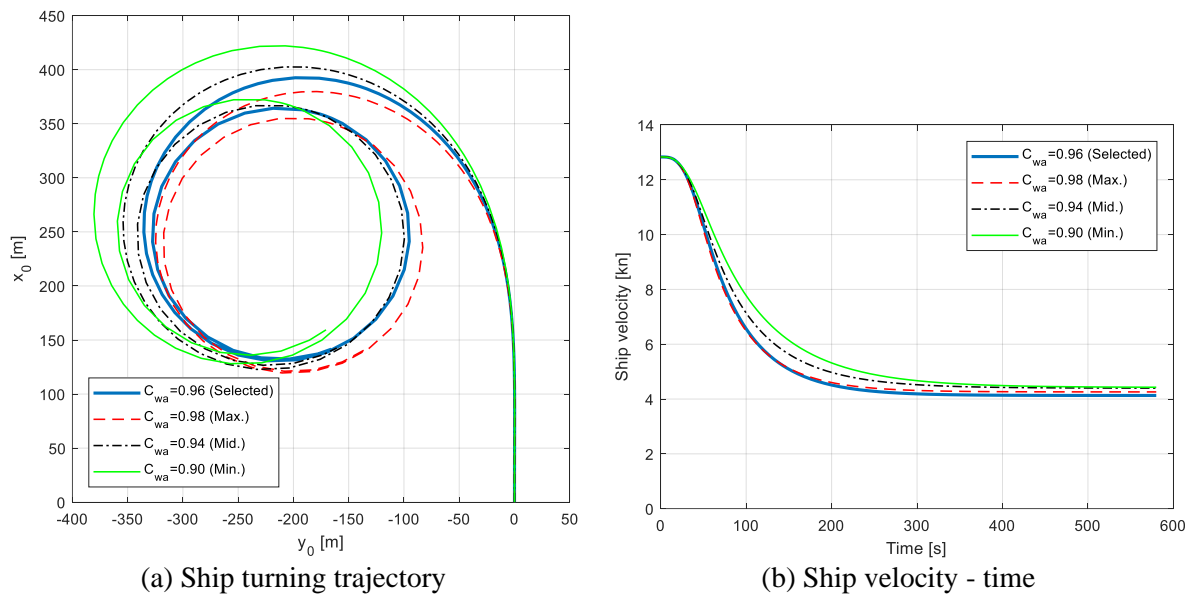
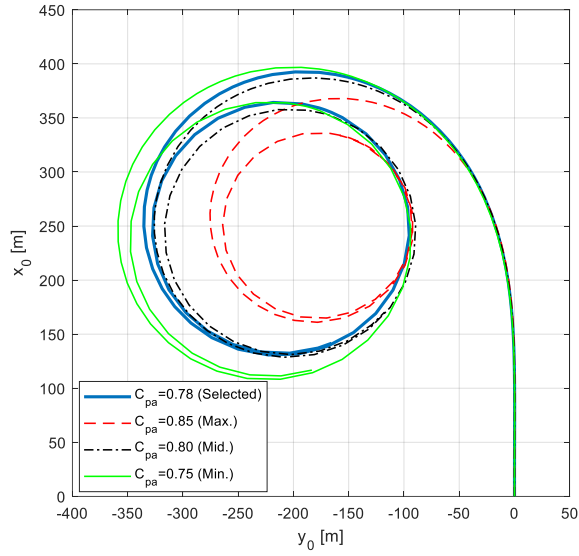
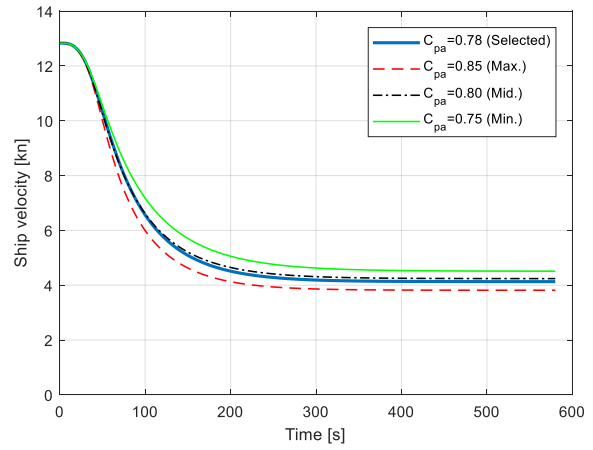


Figure 5.22: Influence of  $C_{wa}$  on turning manoeuvre (Portside with rudder angle: -35 deg.)

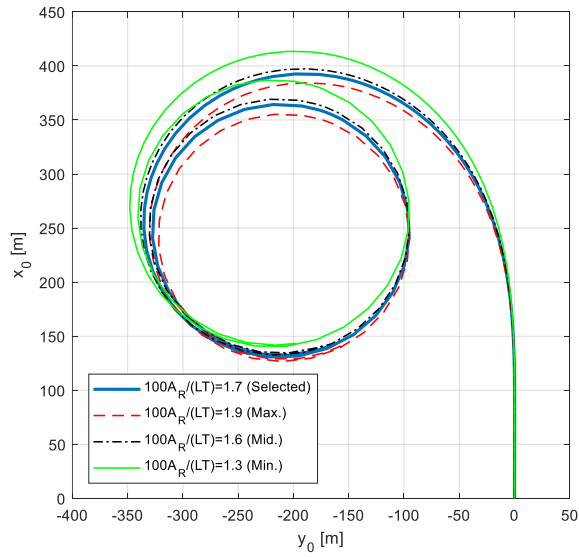


(a) Ship turning trajectory

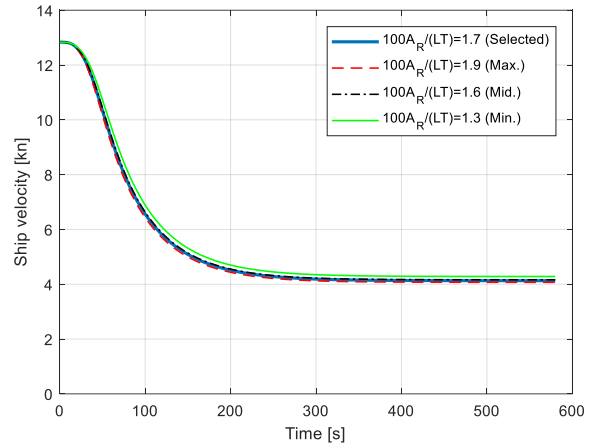


(b) Ship velocity - time

Figure 5.23: Influence of  $C_{pa}$  on turning manoeuvre (Portside with rudder angle: -35 deg.)



(a) Ship turning trajectory



(b) Ship velocity - time

Figure 5.24: Influence of  $100A_R/(L \cdot d)$  on turning manoeuvre (Portside with rudder angle: -35 deg.)

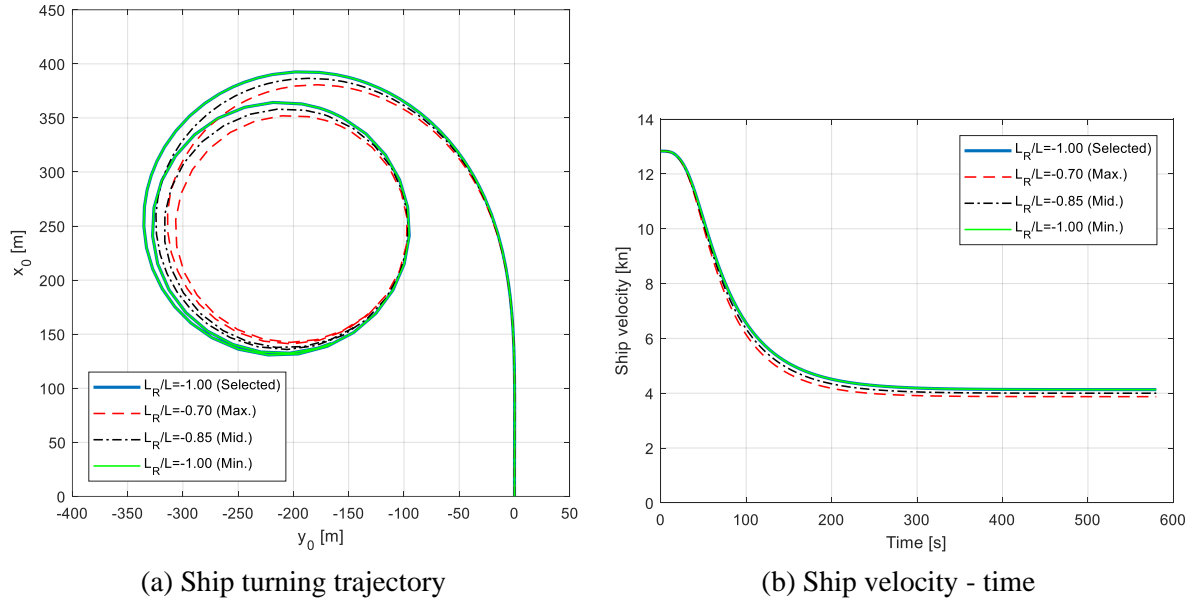


Figure 5.25: Influence of  $\ell_R/L$  on turning manoeuvre (Portside with rudder angle:  $-35$  deg.)

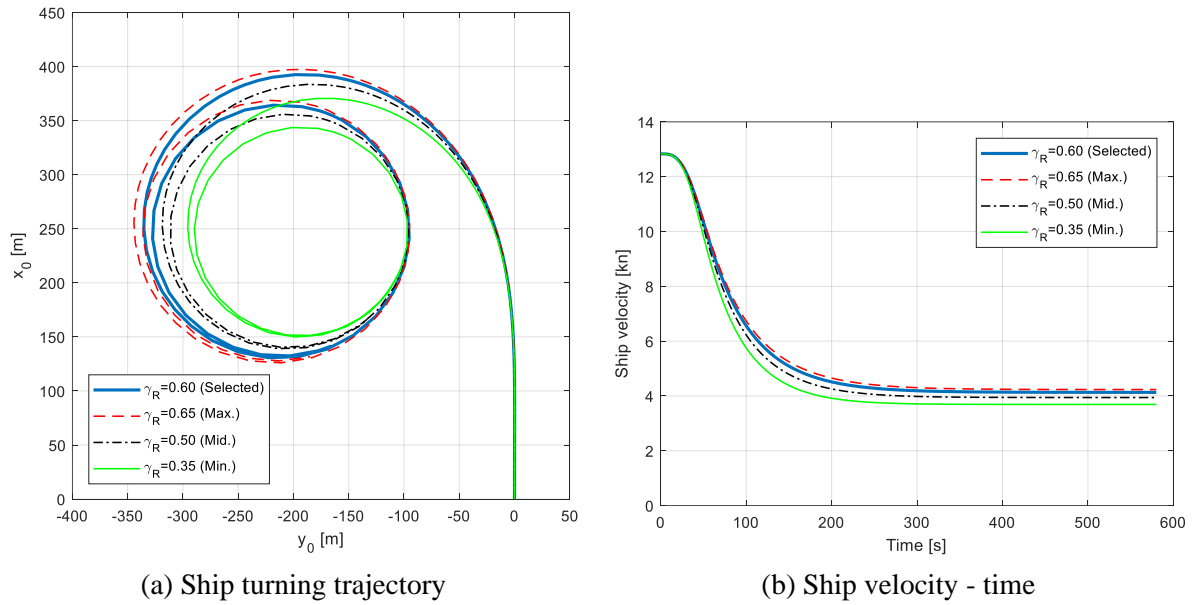


Figure 5.26: Influence of  $\gamma_R$  on turning manoeuvre (Portside with rudder angle:  $-35$  deg.)

## 5.6 Summary and Conclusions

In this chapter, the integrated first principle ship propulsion and manoeuvring model has been introduced. The ship propulsion model introduced in Chapter 2 has been updated by: firstly, updating the engine model from a test-data-based fitting model to a thermodynamic-based mean value first principle model; secondly, updating the propeller model from considering only the propeller open water characteristics in the first quadrant to taking the four quadrants open water characteristics into account, and the corrected Wageningen propeller C4-55 data has been used.

A 3DOF (Degree of Freedom) MMG manoeuvring model (surge, sway and yaw) has been applied and described. The manoeuvring model has been calibrated, verified and validated using the real ship data and sea trial test data of propulsion (speed trial), inertia and crash stop, turning circle and Zigzag operations. The uncertainties of both the ship trial test data and the manoeuvring model have been discussed, and the sensitivities of the simulation results to some uncertain model parameters has been presented.

The first principle ship propulsion and manoeuvring model is capable of providing sufficient information on the dynamic interactions between different components during various ship manoeuvres, and the simulation results have shown the right trends. Based on the verification and validation results, and the analyses on the uncertainties in both the simulation model and the ship trial test data, it is considered that the calibrated 3DOF MMG manoeuvring model of the benchmark chemical tanker is sufficiently accurate for the research in this dissertation. The integrated ship propulsion and manoeuvring model will be used to investigate the engine dynamic behaviour during different ship operations in normal sea condition in Chapter 6.





## **6 Engine Behaviour of Low-Powered Ocean-Going Cargo Ship under Various Propulsion and Manoeuvring Operations**

### **6.1 Introduction**

Under the current regulations by IMO (International Maritime Organization), new ships strive to achieve a small EEDI (Energy Efficiency Design Index). However, reducing EEDI by simple reduction of installed engine power may lead to underpowered ships, which could have insufficient power for propulsion and manoeuvring in adverse sea conditions. Due to the serious safety concerns on the underpowered ships that have small installed engine power, it is of high importance to evaluate the ship's operational safety, in particular the engine's behaviour in various operating conditions.

The engine thermal loading, mechanical loading and compressor surge limits are the important features in relation to the engine and ship operational safety. The engine operating envelope in particular the torque/speed limit of a turbocharged diesel engine is shaped mainly by the engine thermal loading limit (MAN, 2018). During engine operations, to protect the engine from being overloaded, the engine is not allowed to operate outside the engine envelope, which is specified by the engine manufacturer, and this is normally controlled by the engine governor with a fuel rack limiter (Grimmelius and Stapersma, 2000; Schulten, 2005). In case of an underpowered ship, when the ship is sailing and manoeuvring in adverse weather conditions, the engine could automatically shut down as it cannot provide the required power within the envelope and the ship could lose her power for propulsion and steering in that dangerous situation.

In order to investigate the influence of various operating conditions on the thermal loading

of the engine, quantitative thermal loading indicators need to be defined. To define and quantify the engine thermal loading, a number of thermal loading indicators have been introduced in (Grimmelius and Stapersma, 2000) when investigating the influence of irregular waves as well as different control strategies on the thermal loading of a turbocharged diesel engine. These thermal loading indicators includes the air excess ratio, charge pressure, engine slip factor, maximum in-cylinder temperature, cylinder temperature just before exhaust valve opening (EO), gas temperature directly after exhaust valve, exhaust receiver temperature and gas exhaust temperature (after turbine), etc. Among others, the air excess ratio can be used as the indicator of both engine smoke-limit and thermal loading (Stapersma, 2010b). Visible (black) smoke in the engine exhaust will be observed when the air excess ratio is lower than the smoke-limit as the combustion is incomplete due to the insufficient air. A low air excess ratio will also cause high surface temperature of engine components that could lead to an operation life reduction or catastrophic failure of the components (Nanda et al., 2017).

In this chapter, the above-mentioned thermal loading indicators will be used to investigate the operational safety of the two-stroke marine diesel engine of a possibly low-powered or even underpowered 13,000 DWT ocean-going chemical tanker under various operating conditions in normal sea condition (15% Sea Margin). It will be explained why the benchmark chemical tanker could be a low-powered or even underpowered ship (Section 6.2). Based on the mean value first principle parametric (MVFP) model, the detailed static engine performance across the entire engine envelope will be investigated (Section 6.3). Based on the integrated ship propulsion and manoeuvring model, the dynamic engine behaviour during ship acceleration, deceleration, crash stop and turning will be investigated (Section 6.4). The engine operational limits (envelope) will be finally transformed into the ship thrust limit (envelope), which is the real limiting factor of ship operational safety in adverse conditions (Section 6.5).

## 6.2 Low-powered ocean-going chemical tanker

The 13,000 DWT benchmark chemical tanker, which has a small EEDI of 9.92 gCO<sub>2</sub>/ton-mile, meets the EEDI requirement (10.59 gCO<sub>2</sub>/ton-mile) of phase 2 (1 Jan 2020 - 31 Dec 2024) and is very close to the EEDI requirement (9.91 gCO<sub>2</sub>/ton-mile) of phase 3 (1 Jan 2025 and onwards). According to the EEDI technical file of the benchmark chemical tanker, which is submitted to class for final verification for the attained EEDI at the delivery stage, the 2013 interim minimum power guidelines (RESOLUTION MEPC.232(65)) (MEPC, 2013) has been applied for assessing whether the ship has sufficient power to maintain the manoeuvrability in adverse conditions. However, currently there is in fact no minimum power guidelines applicable for ships with capacity less than 20,000 DWT including the benchmark chemical tanker. If applicable, according to the level 1 assessment of 2013 interim guidelines, i.e., the minimum power lines assessment, the installed MCR of the main engine of the benchmark chemical tanker should not be less than 4148.7 kW, so, the installed engine power (4170 kW) on the ship meets this minimum power requirement.

However, according to the latest amended guidelines (MEPC.1/Circ.850/Rev.2) (MEPC, 2017), the minimum installed engine power of the chemical tanker is 6807.8 kW, which is much higher than the MCR power (4170 kW) of the main engine installed on the ship. So, if applicable,

according to the amended 2013 guidelines, the benchmark chemical tanker would be a low-powered or even underpowered ship as it cannot meet the latest minimum power requirement. On the other hand, if the installed engine on the same ship is replaced by a larger engine with power of 6810 kW, the ship design speed will then increase from 13.30 knots to 15.80 knots, and as a result the EEDI of the ship will increase from 9.92 to as high as 14.00, which cannot meet the EEDI requirement even for phase 0 (11.97 gCO<sub>2</sub>/ton-mile) anymore.

### 6.3 Engine static behaviour and operational limits

Based on the MVFPP engine model, static operating points covering the entire engine envelope (Figure 6.1) specified by the engine manufacturer (MAN, 2014; 2018) have been simulated to investigate the engine static behaviour. In particular the engine mechanical loading, thermal loading and compressor surge across the whole engine operating envelope will be investigated. In the simulation model the fuel rack limiter is switched off so that the engine can also run outside the envelope to reveal both the causes and consequences of engine overloading. It can also provide an insight on how the engine operating limits are specified. For these purposes, the contour plots of the indicators of the engine mechanical loading, thermal loading and compressor surge across the entire engine operating envelope have been presented in Figure 6.2 to Figure 6.12. Note that, the ‘dense belts’ in the contour plots are caused by the operation of the auxiliary blower, which has been mentioned in Chapter 4 and explained in Appendix F.3.

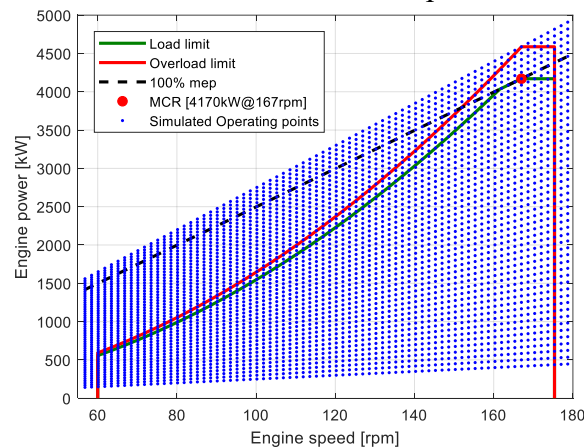


Figure 6.1: Simulated operating points cross the engine envelope

#### 6.3.1 Engine mechanical loading

The engine torque (or the mean effective pressure, mep) and the maximum in-cylinder pressure have been selected as the indicators of the engine mechanical loading. The engine torque is almost proportional to the injected fuel per cycle that is proportionally determined by the fuel rack position (Figure 6.2), which is controlled by the engine governor. According to the simulation results, the highest maximum in-cylinder pressure happens in high engine speed and load area (Figure 6.3) and the maximum in-cylinder pressure will drop when the engine speed and engine torque decrease. So, the engine mechanical overloading is not the limiting factor of the engine torque and power when operating (statically) in low speed and/or low power area, where the engine thermal overloading is the real limiting factor.

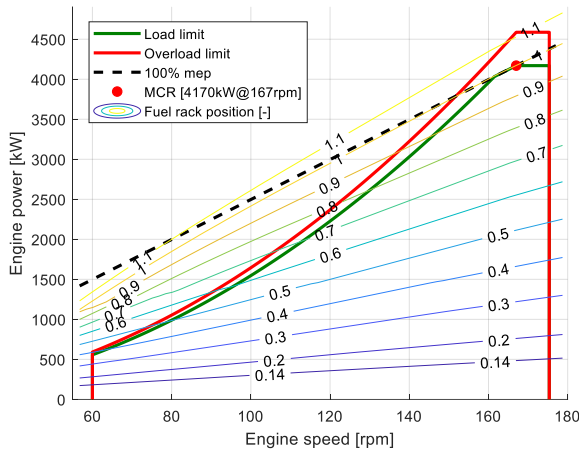
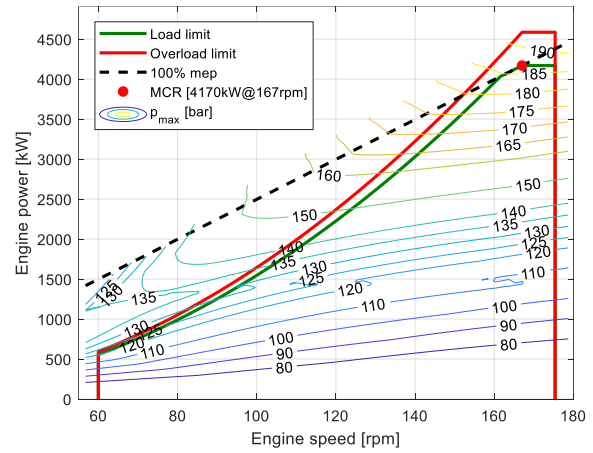
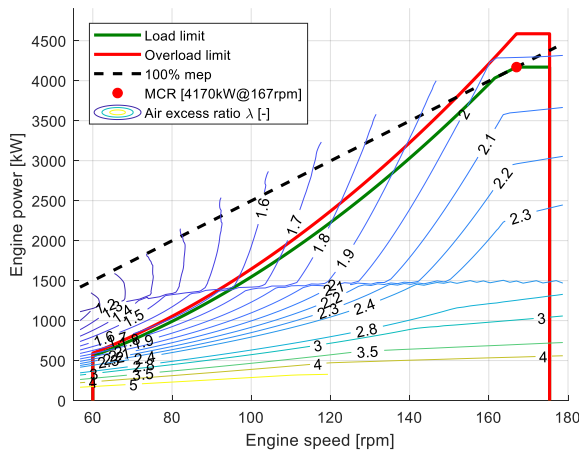
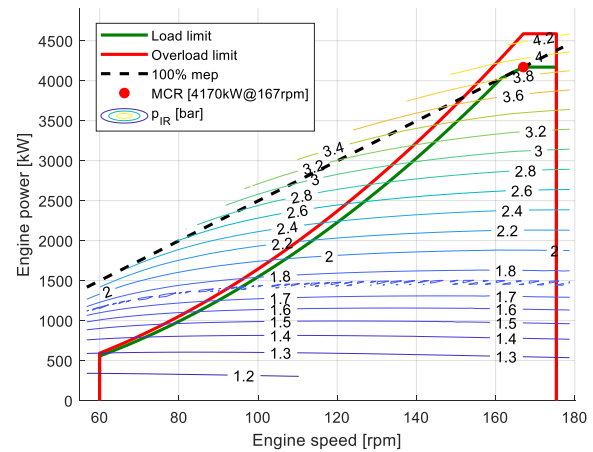


Figure 6.2: Fuel rack position

Figure 6.3: Maximum in-cylinder pressure  $p_{max}$ 

### 6.3.2 Engine thermal loading

The air excess ratio  $\lambda$ , inlet receiver pressure  $p_{IR}$ , maximum in-cylinder temperature  $T_{max}$ , in-cylinder temperature just before opening of the exhaust valve (EO)  $T_{EO}$ , exhaust valve temperature  $T_{EV}$ , temperature in outlet receiver  $T_{OR}$  and temperature after turbine  $T_{TUR}$  have been selected as the thermal loading indicators for investigating the engine thermal load limit. The air excess ratio (Figure 6.4), which is the indicator of both engine thermal loading and black-smoke, will decrease when the engine operates at low speeds with high engine torque. For the same engine torque and thus the same injected fuel mass, the inlet receiver pressure (charge pressure) (Figure 6.5) will decrease at lower engine speeds and consequently the available combustion air mass for the engine will drop. According to the simulation results in Figure 6.4 to Figure 6.7, the operating areas of the highest maximum in-cylinder temperature and highest in-cylinder temperature just before EO coincide with that of the lowest air excess ratio. When the air excess ratio decreases, the maximum in-cylinder temperature (Figure 6.6) and in-cylinder temperature just before EO (Figure 6.7) will increase and could exceed the allowable high temperature limit if the engine runs outside the operating envelope especially at low speeds.

Figure 6.4: Air excess ratio  $\lambda$ Figure 6.5: Inlet receiver pressure  $p_{IR}$

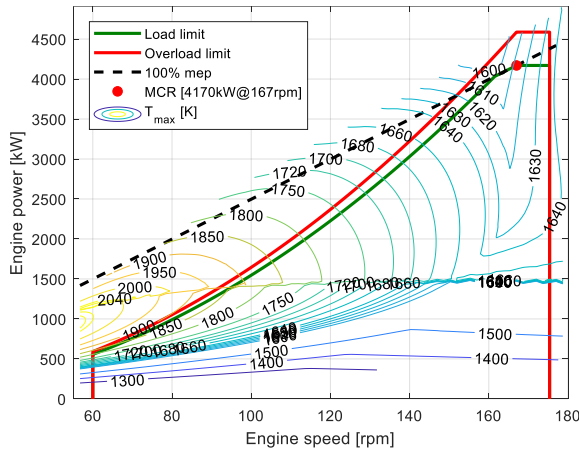


Figure 6.6: Maximum in-cylinder temperature  $T_{max}$

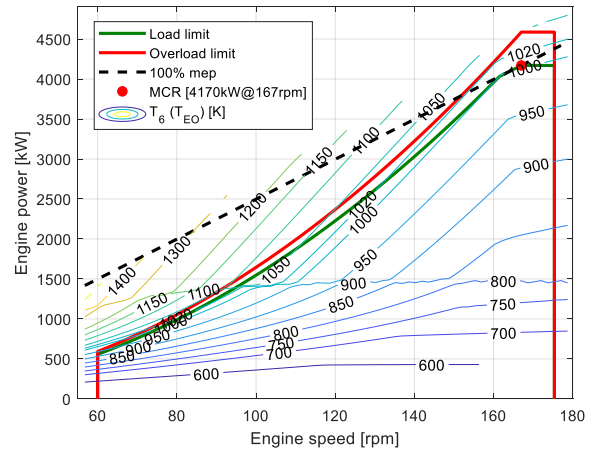


Figure 6.7: In-cylinder temperature just before EO  $T_{EO}$

The (average) exhaust valve temperature (Figure 6.8) and the temperature in the outlet receiver (Figure 6.9) have different trends from that of the in-cylinder temperature just before EO  $T_{EO}$  due to the cooling effect of the slipping charged air during the gas exchange process, which is indicated by the engine slip factor (Figure 6.11). The slip factor is the highest when the engine runs in the operating area where the air excess ratio is the lowest, and the possible highest exhaust valve temperature and outlet receiver temperature have been cooled down due to the high slip factor in that area. As a result, the highest exhaust valve temperature and outlet receiver temperature happen in the area that is close to MCR. Due to the influence of the turbine pressure ratio and turbine efficiency, the trend of the temperature after turbine (Figure 6.10) is different from that of the temperature before the turbine (the outlet receiver temperature). When the engine power drops, the temperature after turbine will first slightly drop and then go up until the auxiliary blower starts operating.

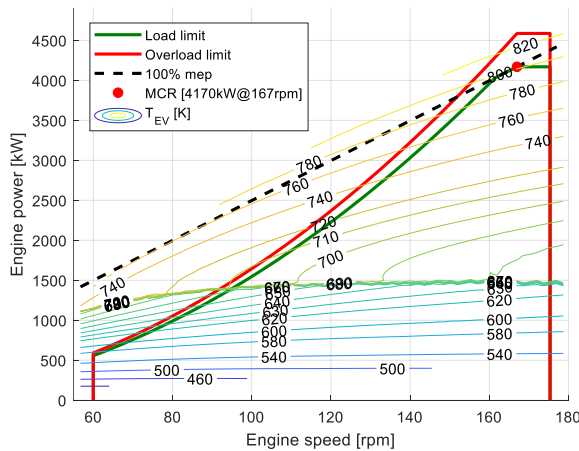


Figure 6.8: Exhaust valve temperature  $T_{EV}$

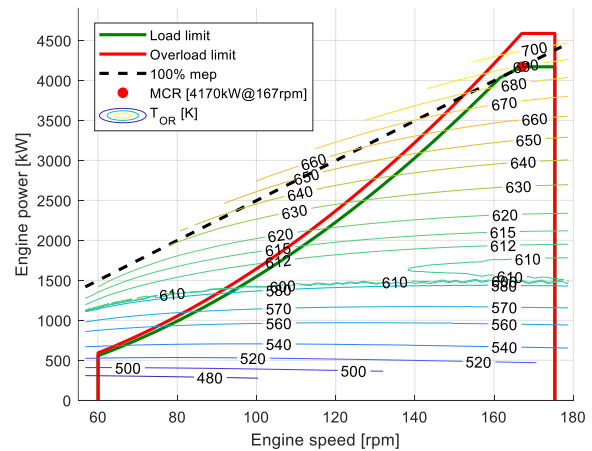
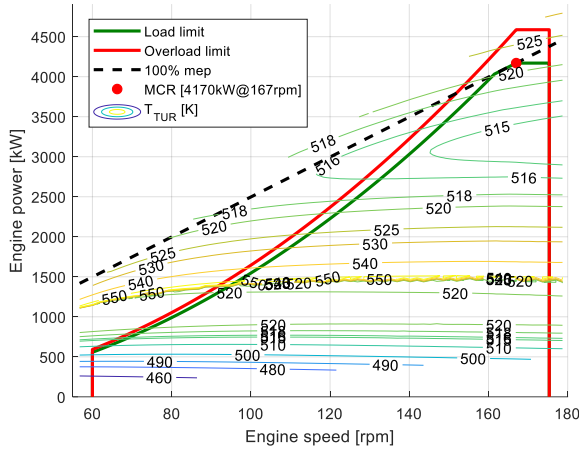
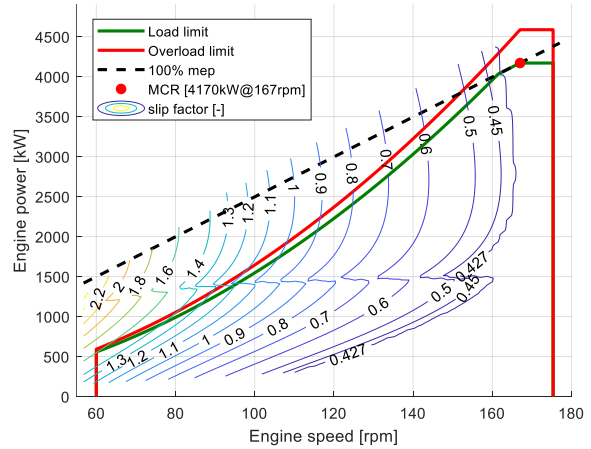


Figure 6.9: Outlet receiver temperature  $T_{OR}$

Figure 6.10: Temperature after turbine  $T_{TUR}$ Figure 6.11: Slip factor  $s$ 

### 6.3.3 Compressor surge

The engine operations could also be limited by the compressor surge, especially for four-stroke diesel engines operating along the propeller law (constant propeller pitch) (Stapersma, 2010c). However, for the two-stroke marine diesel engine investigated in this thesis, the compressor surge index\* is negative across the entire engine operating envelope (Figure 6.12) indicating that in static operations the compressor will not surge. The constant surge index lines are almost parallel to the constant power lines and the surge index decreases (the compressor operating point gets closer to the surge line) when the engine power reduces until the auxiliary blower starts operating. It indicates that the compressor surge is influenced almost equally by the engine torque and the engine speed, and the operation of the auxiliary blower helps to prevent the compressor from surging when the engine is running at low engine speed and/or torque. Without the auxiliary blower, the engine will surge when operating below certain power and the surge limit line locates somewhere below the ‘dense belt’ and is parallel with the constant surge index lines.

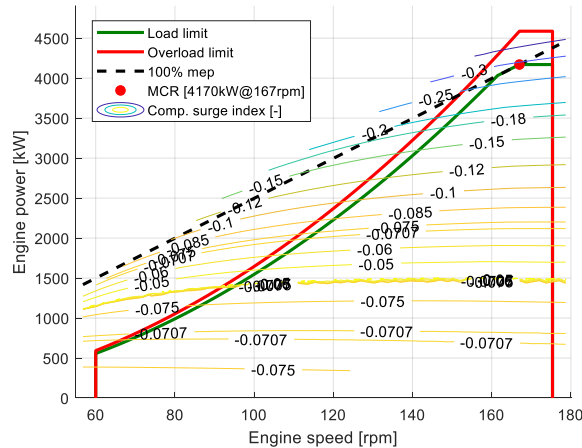


Figure 6.12: Compressor surge index

\* The compressor surge index is the nondimensional distance between the compressor operating point and the surge line (Appendix F.1); a negative surge index indicates the compressor is safe from surge.



## 6.4 Engine dynamic behaviour in different ship operations

In this chapter, the dynamic engine behaviour during ship acceleration, deceleration, crash stop, and turning will be investigated based on the integrated ship propulsion and manoeuvring model. The ship operations are implemented by controlling the engine (propeller) revolution, propeller pitch and rudder angle. As explained previously in Chapter 2, the engine revolution and propeller pitch are controlled by the single lever command (SLC) using the pre-defined combinator curve, and the SLC has a range from -100 (full astern) to 100 (full ahead). In the simulations of the above-mentioned ship operations, the actual sea condition is set as normal, i.e., with 15% of sea margin, and the shaft generator (PTO) is switched on, and the PTO power is set as constant, i.e., 350 kW.

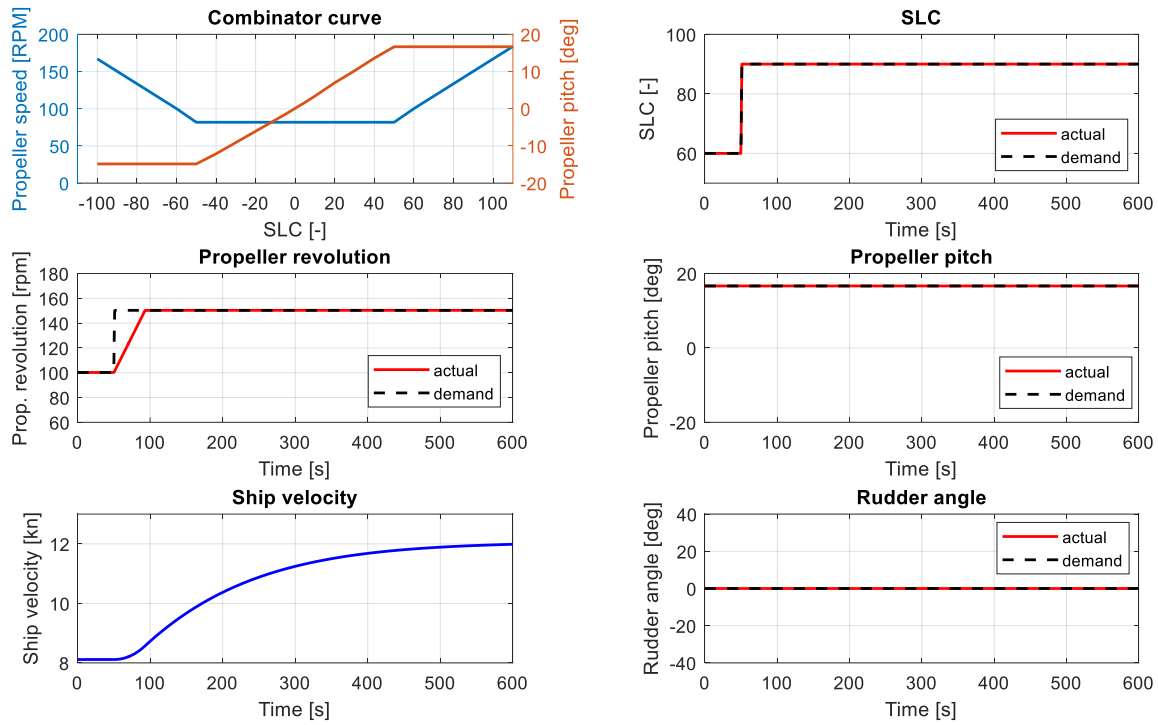
### 6.4.1 Ship acceleration

In the simulations of ship acceleration and deceleration, the constant pitch propulsion control mode has been applied. The propeller pitch (angle) is set at 16.6 degrees, which is 93% of the design pitch (17.83 degrees or equivalently  $P/D = 0.7075$ ), and the ship acceleration and deceleration are implemented by changing the propeller revolution through SLC.

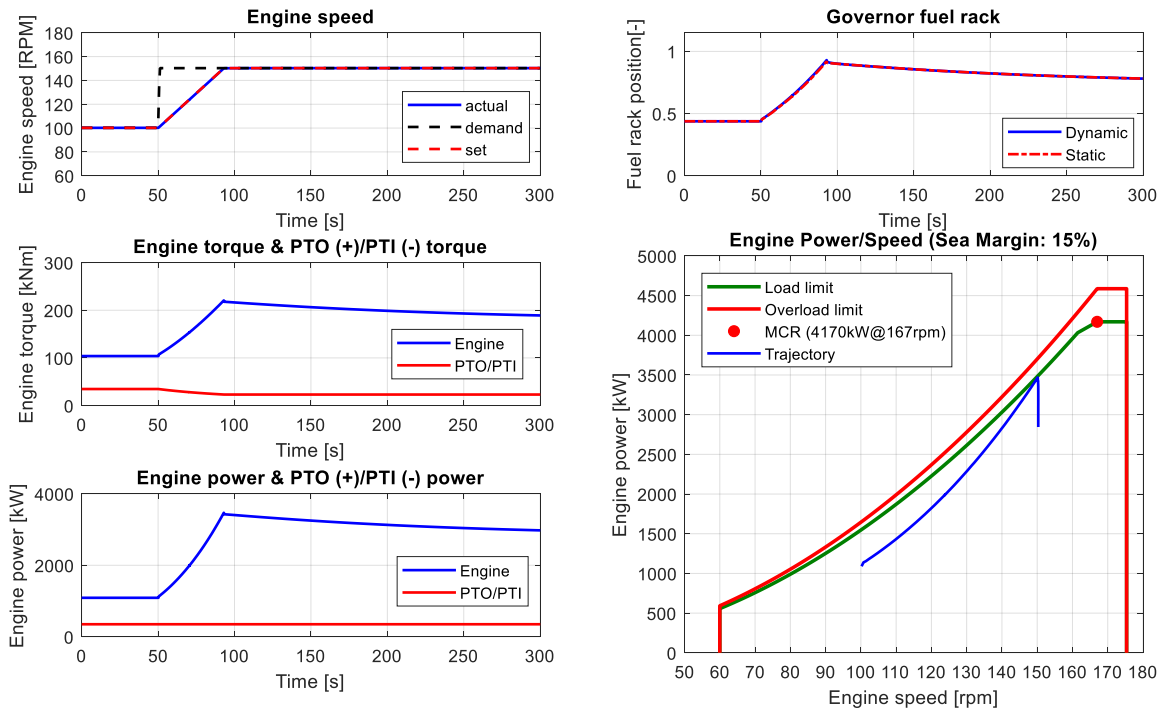
To accelerate the ship, the SLC command is increased from 60 to 90 and the corresponding propeller revolution is increased from 100 rpm to 150 rpm (Figure 6.13(a)). The ship speed will be consequently increased from 8.1 knots to 12 knots finally. The engine brake performance including the engine speed, torque, power and fuel rack behaviour during the ship acceleration is shown in Figure 6.13(b). The engine power trajectory during ship acceleration is inside the engine operating envelope during the dynamic process. The dynamic behaviour of the engine thermal loading during ship acceleration are compared with the corresponding static results (Figure 6.13(c)), which are read (interpolated) directly from the static engine performance maps (Figure 6.4 to Figure 6.12) according to the engine power trajectory.

From the comparison, obvious differences between the dynamic and static results are observed especially during the transient process, while they coincide with each other when the process becomes steady. During the transient process of ship acceleration, the air excess ratio drops from 2 to the lowest 1.7 and exceeds the air excess ratio limit assumed in the model, which is 1.7. The dynamic value of the air excess ratio is much lower than the static value read from the static map (Figure 6.4). The maximum in-cylinder temperature  $T_{max}$  and in-cylinder temperature just before EO  $T_{EO}$ , exhaust valve temperature  $T_{EV}$ , outlet receiver temperature  $T_{OR}$  and temperature after turbine  $T_{TUR}$  will all first increase to the highest values during the transient process before dropping to the steady (static) values. The dynamic increases of the temperatures are higher than the static values. For instance, the in-cylinder OE temperature is higher than the static value by 82 K reaching as high as 1072 K and it could exceed the thermal load limit of the engine, which is assumed to be 1050 K according to Figure 6.7. The turbocharger speed, air mass flow, compressor pressure ratio, and consequently the inlet receiver pressure and the maximum in-cylinder pressure will increase during ship acceleration. The (negative) compressor surge index will drop, indicating that the compressor operating points are moving away from the surge line, so the compressor will not surge during ship acceleration.

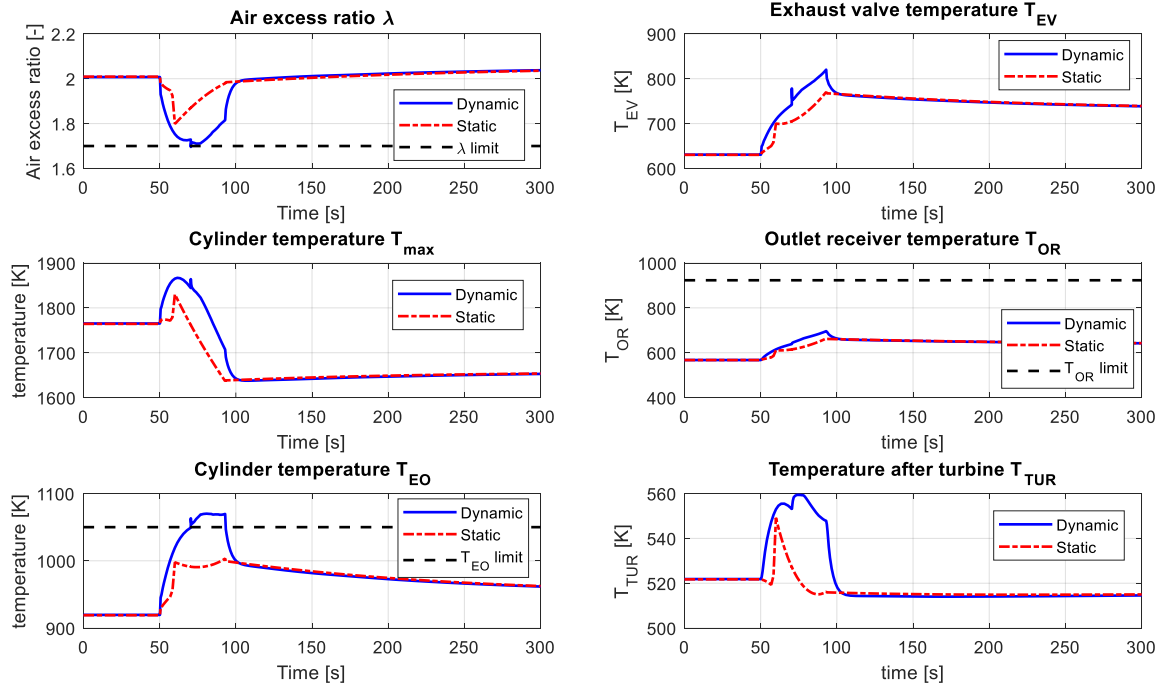




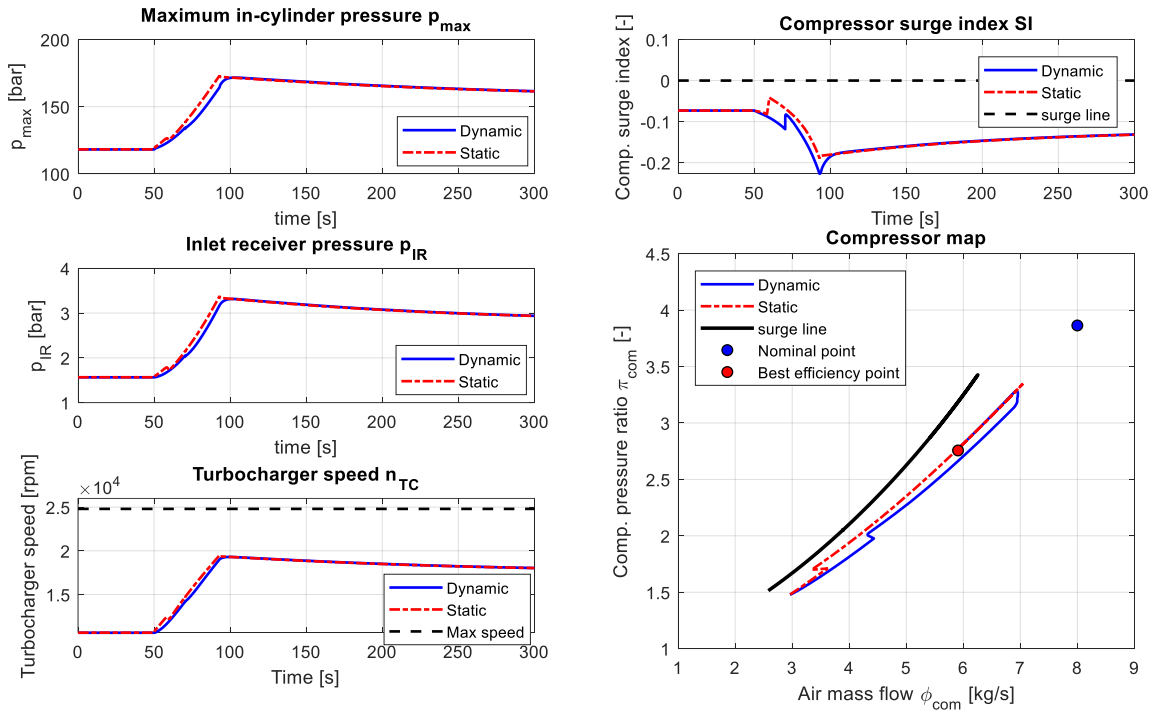
(a) Control setting of ship acceleration



(b) Engine speed, fuel rack, torque and power during ship acceleration



(c) Engine thermal loading during ship acceleration

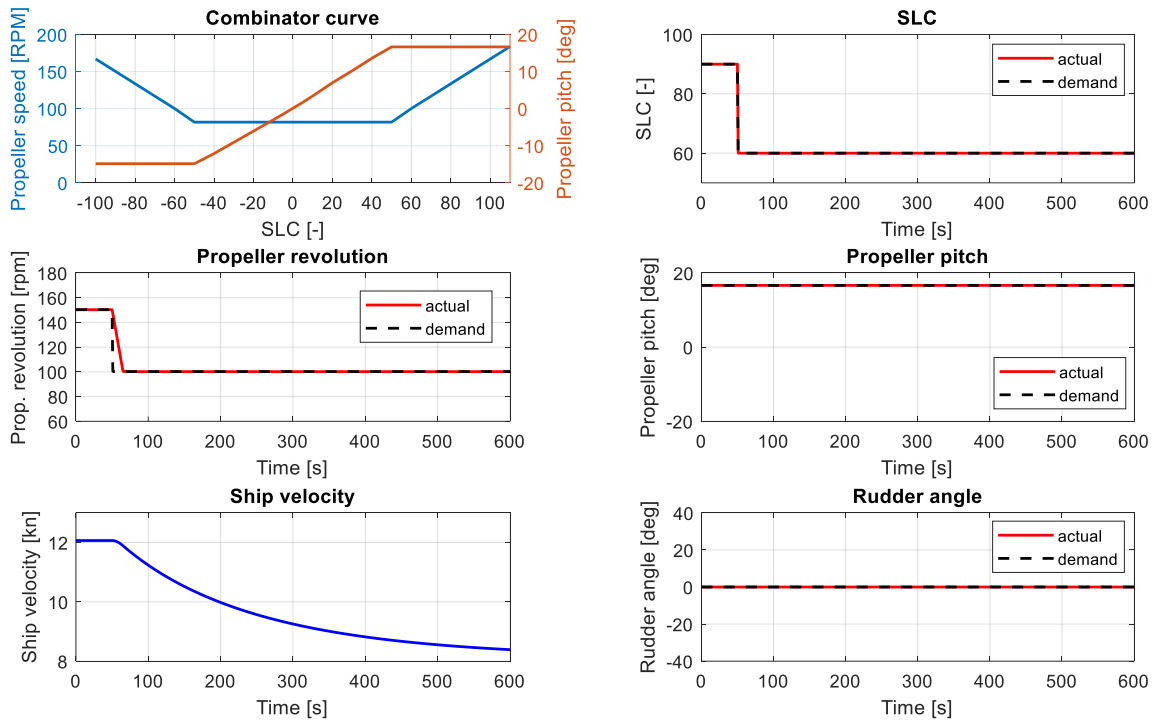


(d) Maximum in-cylinder pressure and compressor behaviour during ship acceleration

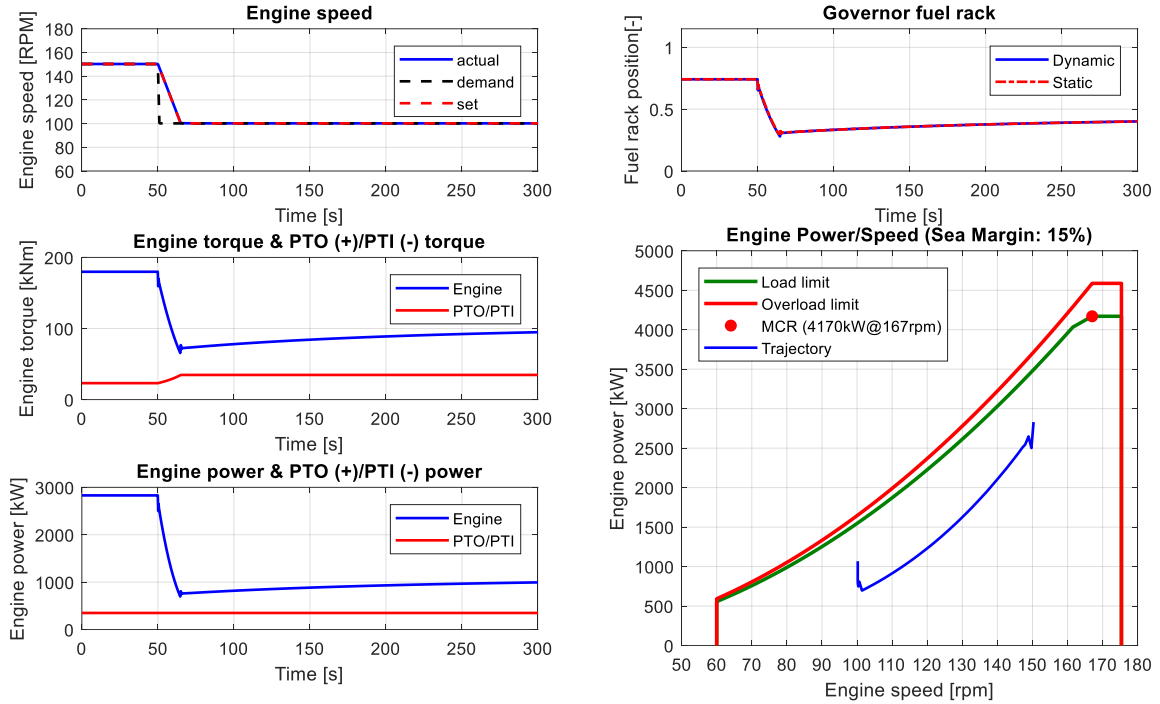
Figure 6.13: Simulation results of ship acceleration

### 6.4.2 Ship deceleration

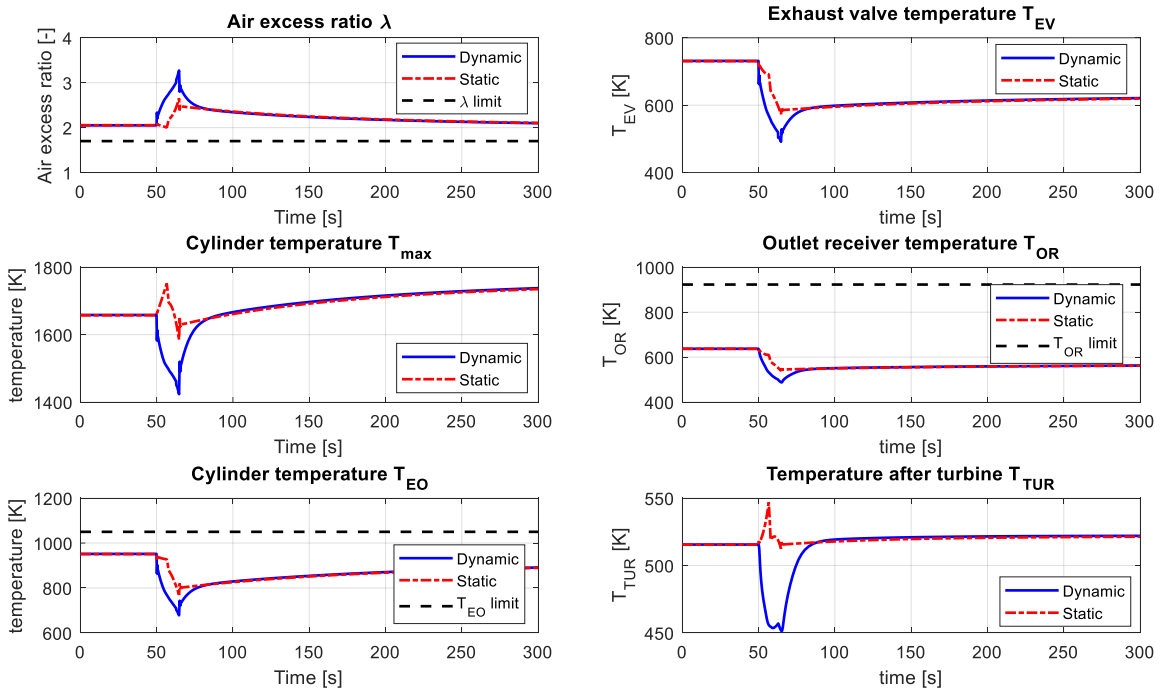
To decelerate the ship, the SLC is reduced from 90 to 60 and the corresponding propeller revolution is increased from 150 rpm to 100 rpm (Figure 6.14(a)). Again, obvious differences between the dynamic simulation results and the static results interpolated from the static engine performance maps can be found (Figure 6.14(c) and (d)). During the transient process of the ship deceleration, the air excess ratio will go up as high as 3.3 before drop back to around 2; the maximum in-cylinder temperature, in-cylinder temperature just before EO, exhaust valve temperature, outlet receiver temperature and temperature after turbine will first drop before gradually going up to a steady value (Figure 6.14 (c)). During ship deceleration, although the engine will be neither mechanically nor thermally overloaded (Figure 6.14(b) and (c)), the compressor can surge, i.e., the compressor surge index becomes positive (Figure 6.14(d)). A positive compressor surge index indicates that the compressor operating line has crossed the surge line and runs in the unstable surge area as can be seen in the compressor map (Figure 6.14(d)).



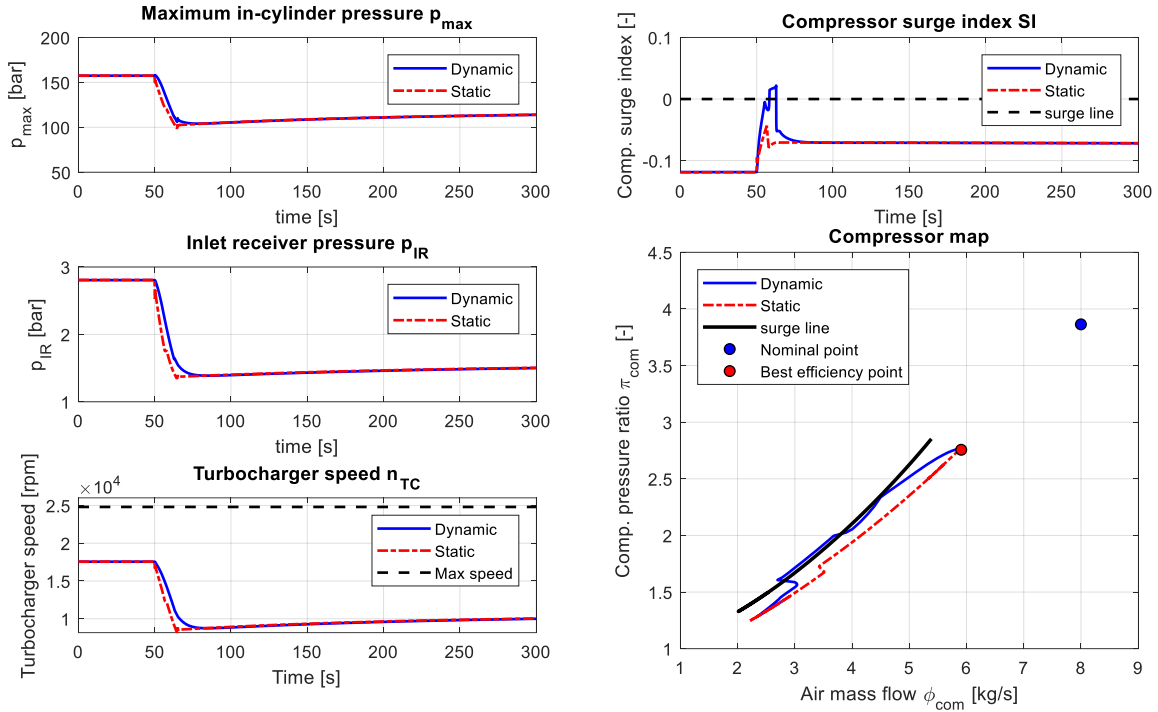
(a) Control setting of ship deceleration



(b) Engine speed, fuel rack, torque and power during ship deceleration



(c) Engine thermal loading during ship deceleration



(d) Maximum in-cylinder pressure and compressor behaviour during ship deceleration

Figure 6.14: Simulation results of ship deceleration

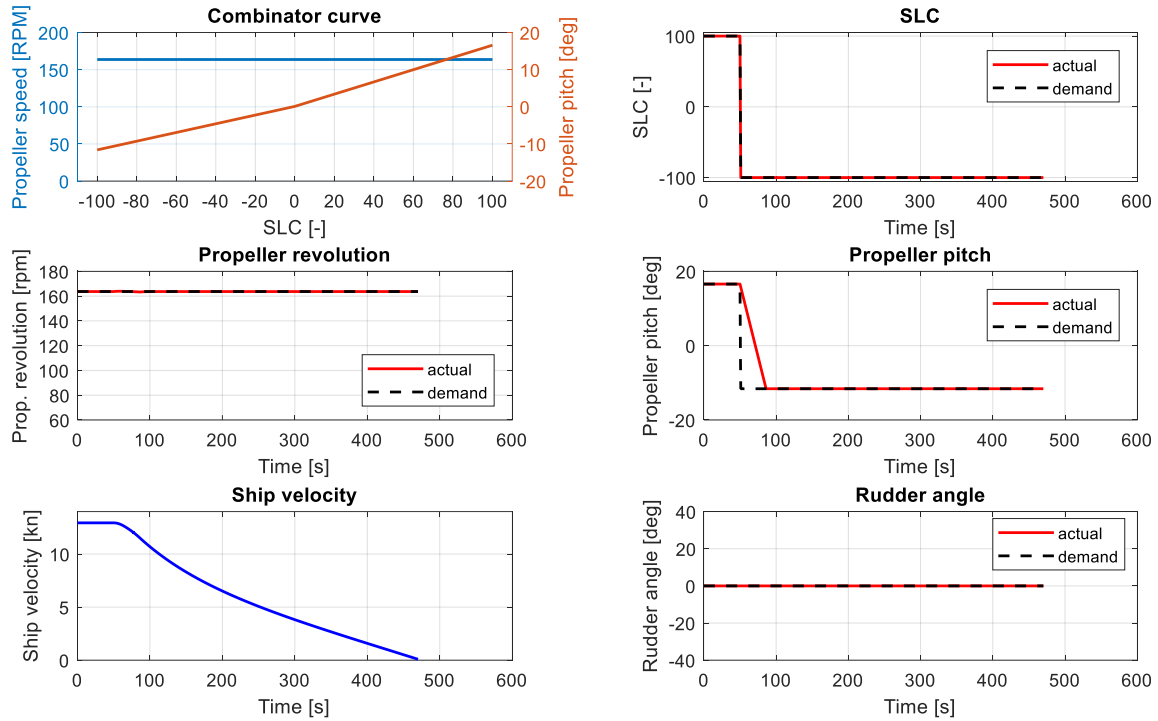
### 6.4.3 Ship crash stop

In the simulations of ship crash stop, the constant revolution propulsion control mode has been applied. The propeller revolution is set at 163.7 rpm and kept constant. The full ahead (SLC = 100) propeller pitch angle is set at 16.6 degrees, which is 93% of the design pitch (17.83 degrees or equivalently  $P/D = 0.7075$ ); while the full astern (SLC = -100) propeller pitch is set at -11.6 degrees, which is -65% of the design pitch.

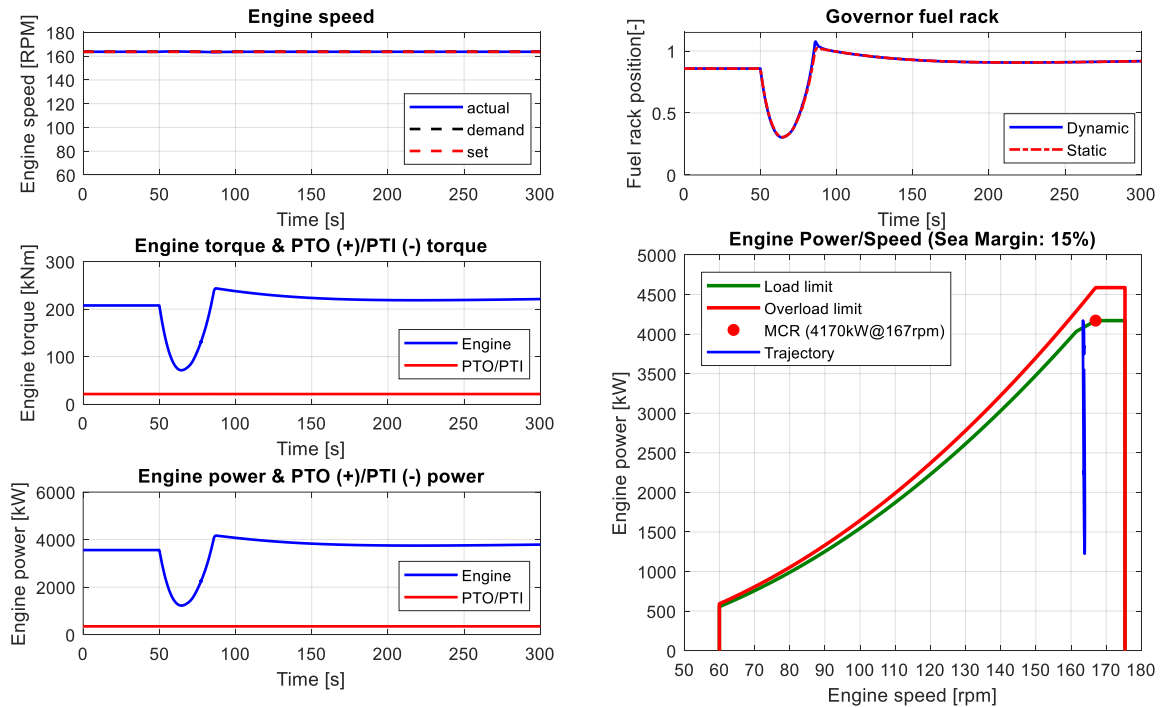
The ship crash stop is implemented by reducing SLC from 100 to -100 (full ahead to full astern), so the propeller pitch will consequently change from 16.6 degrees to -11.6 degrees (Figure 6.15(a)). During ship crash stop, the engine mechanical load (torque and maximum in-cylinder pressure) will first drop due the decreasing positive propeller pitch; and then increase again (slightly overloaded) due to the increasing negative pitch (Figure 6.15(b) and (d)). The engine thermal load will also first drop and then go up again during the transient process of ship crash stop (Figure 6.15(c)). In particular, when the engine load goes up, the air excess ratio drops below the limit as low as 1.47, and the engine could black-smoke and be thermally overloaded. However, before the engine is thermally overloaded, the compressor will surge first when the engine load drops, making the engine dynamic behaviour even worse during the ship crash stop.

From the simulation results of ship acceleration, deceleration and crash stop, it is learnt that when the engine is under dynamic operations, although the engine power is within the (static) operating envelope, the engine could still exceed the operating limits, especially the thermal overloading limit, black-smoke limit and compressor surge limit. To protect the engine from overloading, black smoking and compressor surge during ship acceleration, deceleration and

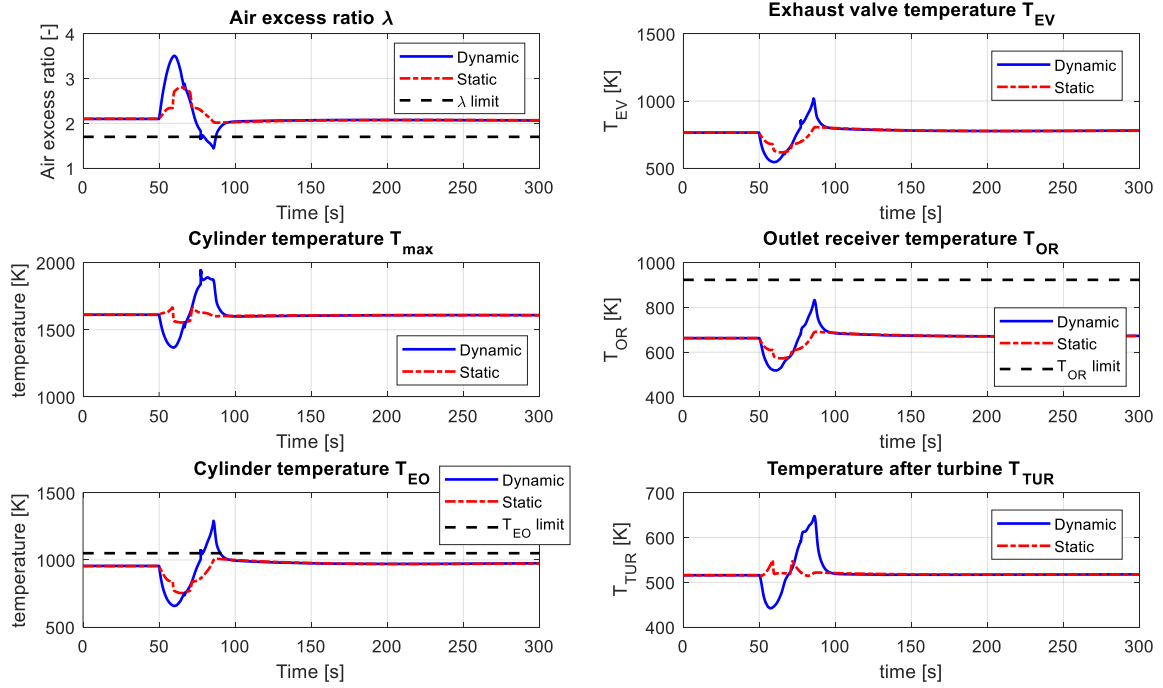
(crash) stop, the changing rates of propeller revolution and pitch should be carefully controlled.



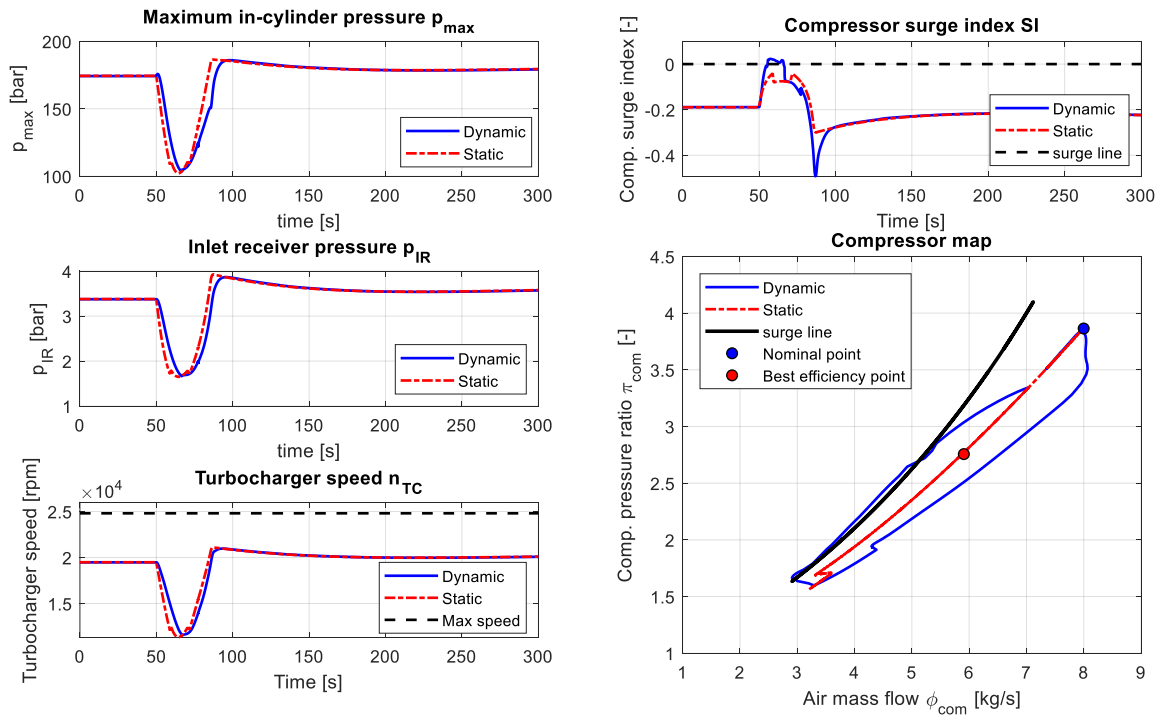
(a) Control setting of ship crash stop



(b) Engine speed, fuel rack, torque and power during ship crash stop



(c) Engine thermal loading during ship crash stop



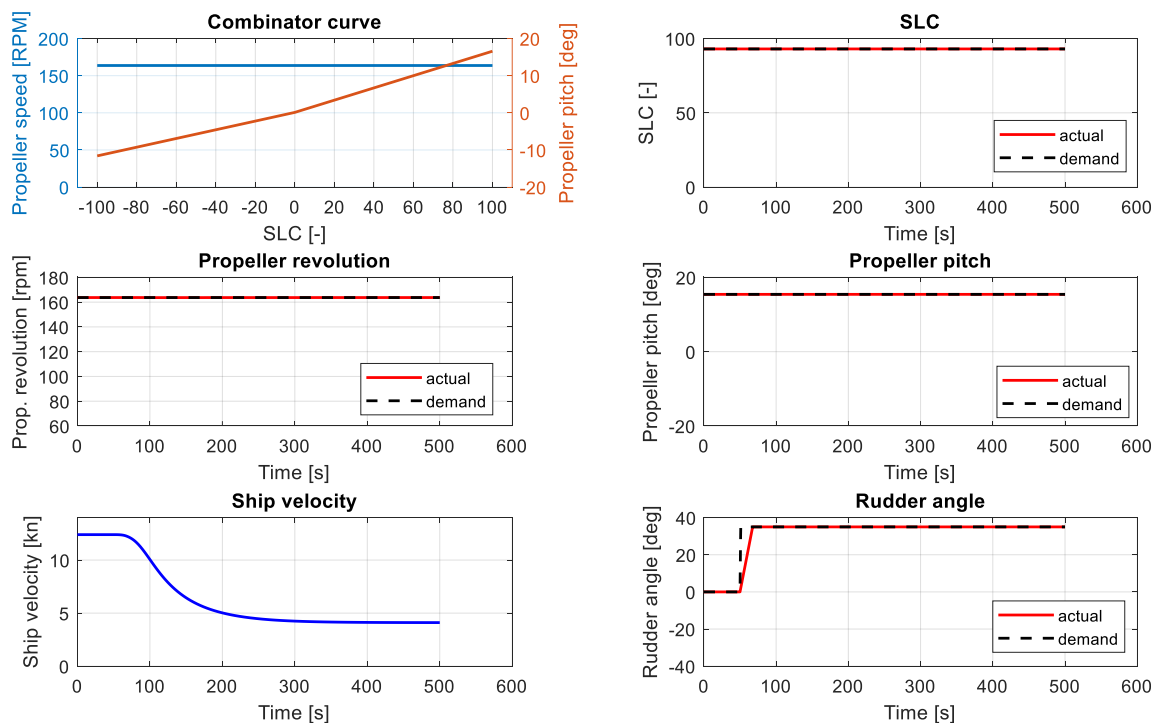
(d) Maximum in-cylinder pressure and compressor behaviour during ship crash stop

Figure 6.15: Simulation results of ship crash stop

### 6.4.4 Ship turning

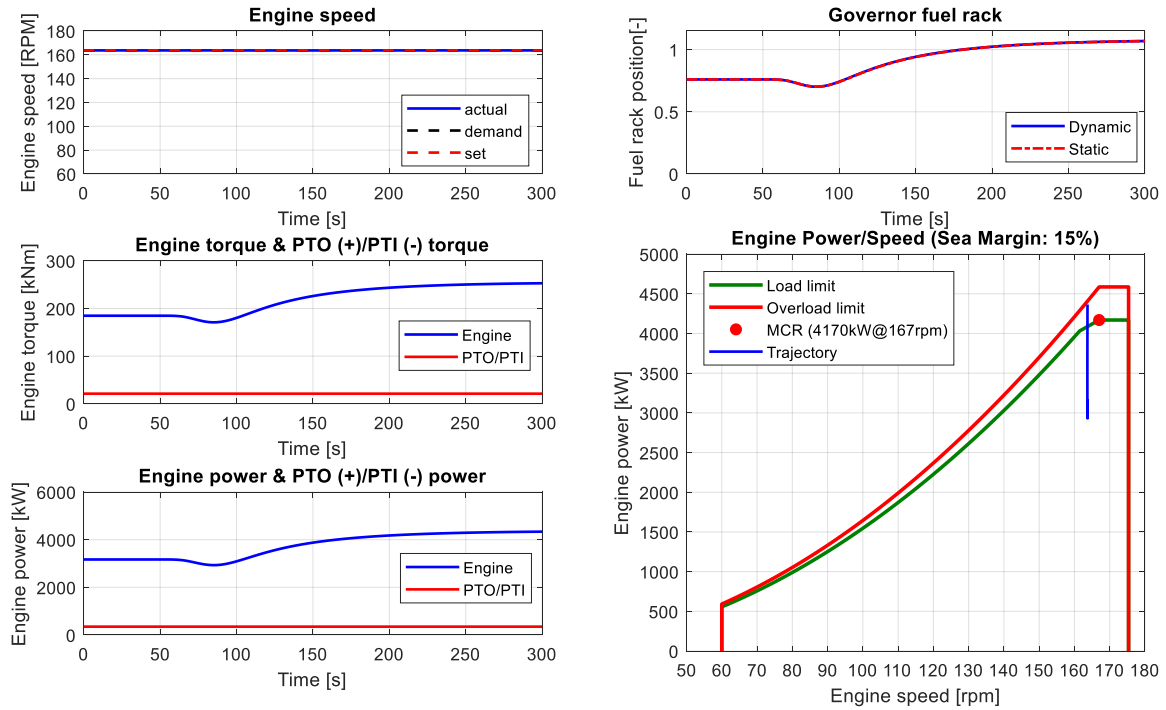
In the simulation of ship turning, the same propulsion control mode and combinator curve for that of ship crash stop has been used. During ship turning, the SLC is set and kept at 93 and the corresponding propeller pitch and propeller revolution are 15.43 degrees and 163.7 rpm respectively. The start ship speed is 12.4 knots and will drop during the ship turning (Figure 6.16(a)). To turn the ship to starboard, the rudder angle is set at 35 degrees. During ship turning, both the engine mechanical and thermal loads will increase (Figure 6.16(b) and (c)), in particular, the engine will be heavily overloaded mechanically. The engine load increases relatively slower during ship turning than that during ship acceleration and crash stop, so the engine is not thermally overloaded although it is heavily mechanically overloaded. To protect the engine from overloading during ship turning, the following solutions could be considered: reducing the rudder angle, reducing the propeller pitch (thus the ship start velocity and velocity during the dynamic process) and switching off the shaft generator (PTO), etc.

Note that, when simulating ship turning in normal sea conditions, only the disturbances of the actual sea state on the ship resistance (x-direction) have been considered, which is indicated by the 15% sea margin, while the disturbance on sway forces (y-direction) and yaw moments (around z axis) on the hull have not been considered. The main reason for the neglect is that the disturbances on the sway forces and yaw moments on the ship in the normal sea condition as well as in the sea trial condition are small and negligible. However, when investigating ship turning in adverse weather conditions, the disturbances especially the waves- and wind-induced steady forces and moments on the ship hull should be taken into account.

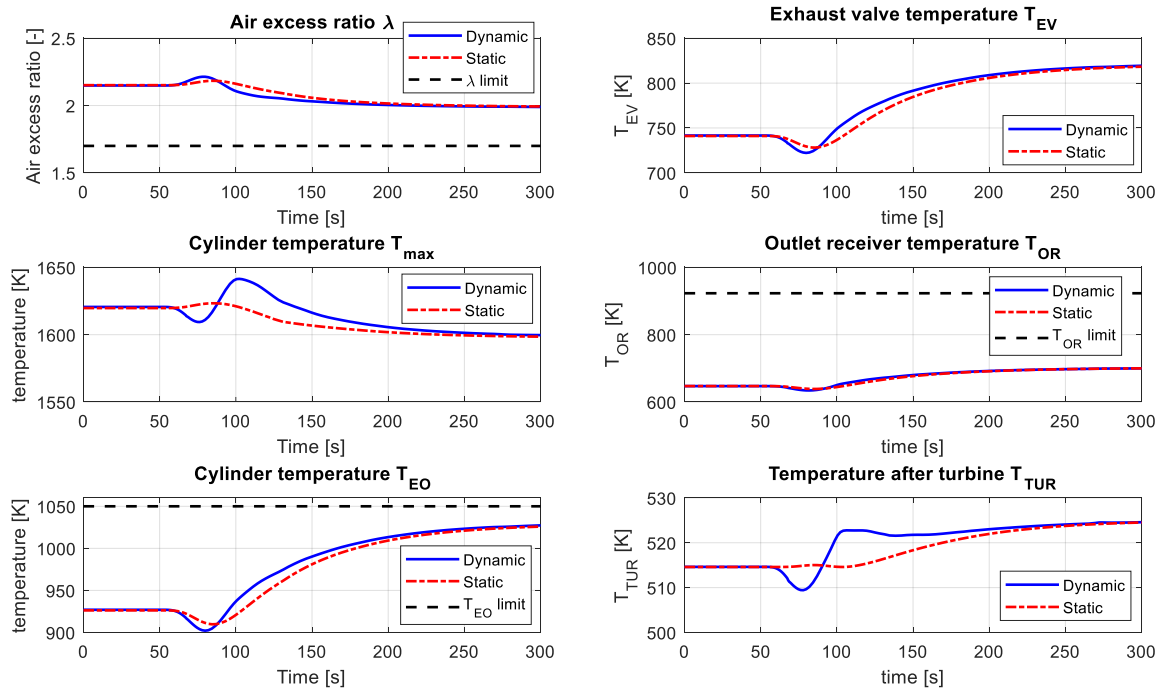


(a) Control setting of ship turning

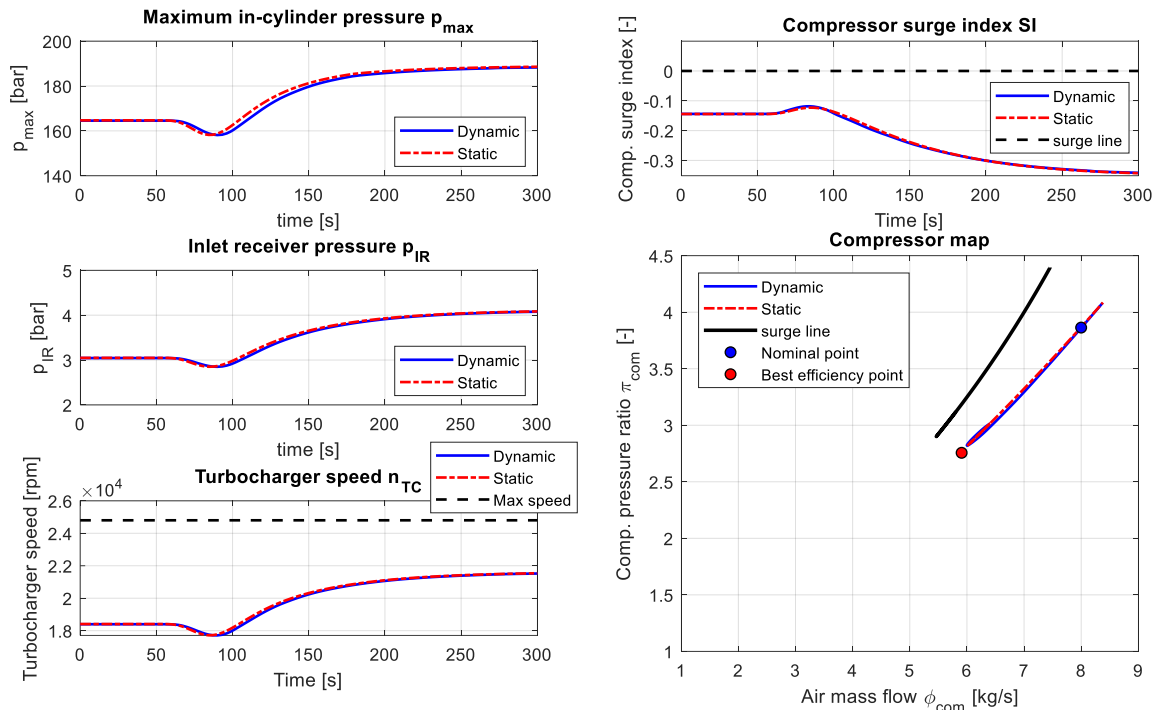




(b) Engine speed, fuel rack, torque and power during ship turning



(c) Engine thermal loading during ship turning



(d) Maximum in-cylinder pressure and compressor behaviour during ship turning

Figure 6.16: Simulation results of ship turning

## 6.5 Engine operational limits and ship thrust limit

The available engine power is actually dependent on the available engine torque, which is the mechanical load that the engine can directly ‘feel’ and also the driving force that the engine needs to provide. The engine torque is almost proportionately determined by the injected fuel per cycle, which is controlled by the governor. And the engine torque is the real force that drives the propeller rotating in water. So, the real limiting factor is the actually the engine torque rather than engine power, although in fact the engine operating envelope specified by the manufacturer is most of the time expressed by the engine power and speed (Figure 6.17(a)). The engine operating envelope specified by the manufacturer is defined by the following limits (MAN, 2014; 2018).

- 1) Minimum speed limit:  
The engine speed should be no less than the minimum speed limit, otherwise the engine is not able to run smoothly or stop completely due to the too low engine compression for good combustion (Schulten, 2005).
- 2) Reduced torque (or fuel injection) limit:  
The reduced torque limit is the speed-dependent torque limit of the engine, which is mainly limited by the thermal load as discussed in previous section. During operation, the torque at low engine speeds is reduced by reducing the fuel injection controlled by the governor.
- 3) Constant torque (mean effective pressure, mep) limit:  
The constant torque (mean effective pressure) limit represents the maximum torque

(engine mechanical load) for continuous operation, which is only a limit at high loads and engine speeds, where the thermal load is not the limiting factor.

- 4) Constant (or continuous) power limit:

The constant power limit represents the maximum power for continuous operation. When the engine speed is higher than a certain value (nominal speed at MCR), the maximum fuel injection and consequently the engine torque should be reduced.

- 5) Maximum speed limit:

The engine has a maximum speed limit controlled by the governor to protect the engine from over-speeding, which could cause disastrous damage to the engine. If the maximum speed limit is reached, the governor stops the fuel injection and the engine is shut down completely.

- 6) Overload limit:

Overload limit represents the overload operation limit of the engine. Due the high resulting thermal load, overload operating is possible only for limited periods in certain situations.

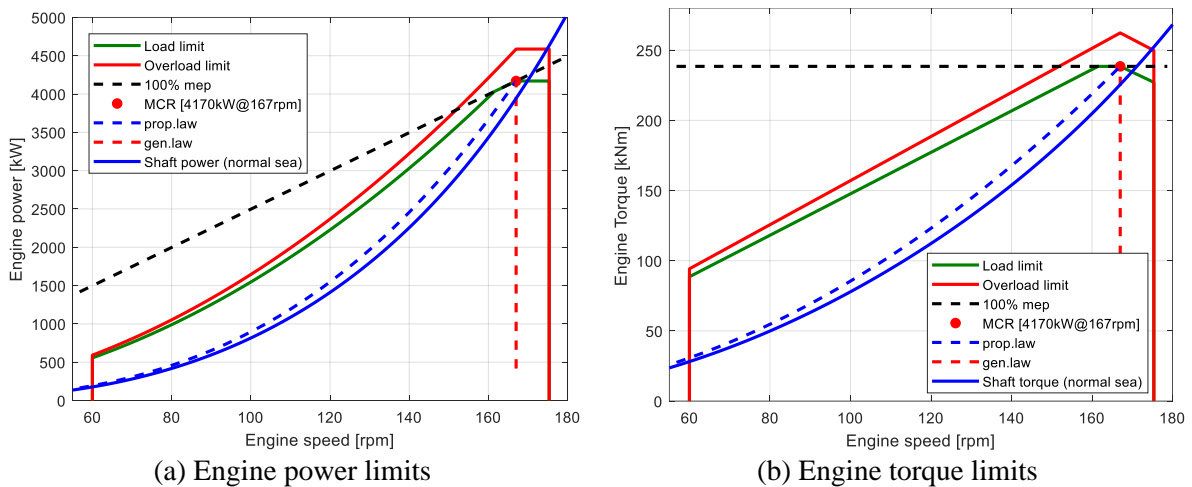


Figure 6.17: Engine operating envelope

For a ship sailing and manoeuvring in adverse sea conditions, it is not the available engine power but the available ship thrust that drives the ship sailing at the sustained speed and turning the bow of the ship towards the head waves (Dallinga et al., 2020). So, it is important to know whether the propeller is able to provide sufficient thrust to the ship for operating in dynamic and/or adverse sea conditions without overloading the engine. The engine power limit and torque limit (Figure 6.17) can be transformed into the ship thrust limit (Figure 6.18) using the propeller characteristics at design pitch without PTO/PTI operation. However, if the ship is installed with a controllable pitch propeller and/or a PTO/PTI system, for instance the updated benchmark chemical tanker, the ship thrust envelope will be different with a different propeller pitch and/or a different PTO/PTI operation, and this will be elaborated in next chapter.

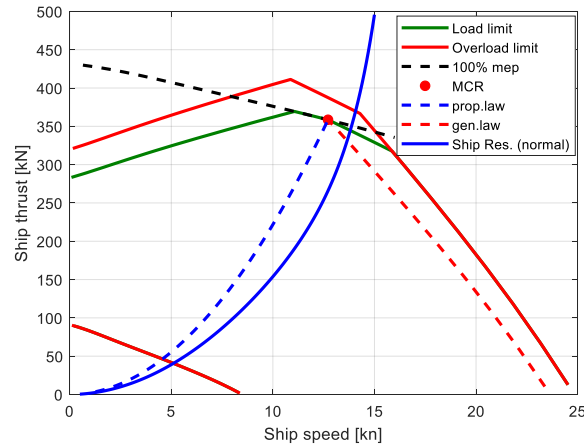


Figure 6.18: Ship thrust limits

## 6.6 Summary and Conclusions

Based on the mean value first principle parametric (MVFP) engine model and the integrated ship propulsion and manoeuvring model, the engine behaviour including mechanical loading, thermal loading and compressor surge of the low-powered benchmark chemical tanker under both static and dynamic operating conditions has been investigated in details. The relationship between the engine power limits and the ship thrust limits has also been investigated.

For the two-stroke marine diesel engine, the torque/speed limit is mainly limited by the engine thermal load at lower engine speeds and mechanical load at high speeds. The air excess ratio, the maximum in-cylinder temperature, and especially the in-cylinder temperature just before exhaust valve opening (EO) are the effective indicators for engine thermal loading. A large slip factor of the two-stroke diesel engine helps cooling the exhaust valve temperature and the temperature in the outlet receiver before the turbine. Compressor surge is not a limiting factor of the operations of the two-stroke engine under static conditions even at low loads, especially for two-stroke marine diesel engines installed with auxiliary blowers. During transient process of dynamic operations, the engine behaviour cannot be directly read (interpolated) from the static engine behaviour maps (the static performance plotted in engine power/revolution envelope). The engine could be still thermally overloaded during for instance ship acceleration, while the compressor could surge during deceleration even if the engine power trajectory is still inside the static engine power/revolution envelope during the dynamic process.

When investigating the dynamic engine behaviour during ship acceleration, deceleration, crash stop and turning, only normal sea condition has been considered in this chapter. The sea condition is simply modelled by the sea margin (SM), which indicates the increase of ship resistance due to actual sea conditions compared to the sea trial condition (calm sea). In Chapter 7, a more detailed sea state model especially the wind and waves models will be applied and integrated into the ship propulsion and manoeuvring model. Based on the model, the investigation on the effects of adverse sea conditions on the ship propulsion and manoeuvring performance as well as the engine behaviour will be elaborated in following chapter.



## **7 Effects of Adverse Sea Conditions on Propulsion and Manoeuvring Performance of Low-Powered Ocean-Going Cargo Ship**

### **7.1 Introduction**

According to the statistical analysis of marine accidents (Ventikos et al., 2015; Shigunov et al., 2019a), it is believed that a quite number of underpowered ships are currently sailing at sea worldwide, especially the ships with small EEDI that is achieved by simply reducing the installed engine power. To prevent the irrational reduction of the installed engine power, the 2013 interim guidelines for the minimum installed propulsion power to maintain the manoeuvrability of ship in adverse conditions have been adopted by IMO in 2013 (MEPC, 2013) and further updated (strengthened) in 2015 (MEPC, 2015). The consolidated version of the 2013 interim guidelines (MEPC, 2017) is the only regulatory requirement that addresses the ships minimum propulsion power issues in adverse sea conditions. Tankers, bulk carriers and combination carriers, which are considered the most critical ship types concerning the power sufficiency for steering in adverse weather conditions (Psaraftis, 2019a), have been addressed in the 2013 interim minimum power guidelines. The current guidelines apply to the above-mentioned ships with a capacity of equal or above 20,000 DWT. Due to the disputed sufficiency of the 2013 interim guidelines, among several others two large research projects, i.e., SHOPERA (Energy Efficient Safe Ship OPERations) and JASNAOE (Japan Society of Naval Architects and Ocean Engineers), have been conducted trying to revise and improve the minimum power guidelines (Papanikolaou et al., 2016; IMO, 2016a; 2016b; Shigunov, 2018). However, the conclusions of the research projects are considered not mature enough to revised the guidelines, for example, among others the agreement on the definition of adverse sea states

where the ship needs to maintain safe operation could not be made; so, the guidelines has not been finalized to date (IMO, 2019; Psaraftis, 2019a). Moreover, currently there is no minimum power guidelines applicable for ships with capacity less than 20,000 DWT and studies in this regard for these ships are still ongoing.

As it has raised serious safety concerns on the underpowered ships, many researches have been conducted to assess ship safety in adverse sea conditions. In (Shigunov, 2018), the required criteria, measures and standards of manoeuvrability of ships in adverse weather conditions have been addressed and a practical assessment procedure has been proposed. In (Shigunov, 2020), the practical assessment of ship manoeuvrability in adverse sea conditions and the availability of experimental, numerical and empirical methods for evaluating the time-average wind and waves induced forces and moments, etc., have been discussed. Shigunov's work is part of the previously mentioned project of SHOPERA, of which the goal is trying to revise the current minimum propulsion power guideline and the assessment procedure of ship manoeuvrability in adverse weather conditions. Nevertheless, they mainly consider what is happening outside of the ship hull in adverse sea conditions, while this research mainly focuses on what is happening inside the ship, especially the dynamic behaviour of the engine. When sailing in adverse weather conditions, the ship propulsion and manoeuvring behaviour will be influenced by not only the wind and waves induced steady forces but also the dynamic propeller wake variation and even propeller ventilation and emergence in harsher weather. Consequently, the interactions between the ship propulsion system, the ship, and the waves and winds, etc., in high sea states are very complex and highly dynamic. Having a detailed insight of these complex and highly dynamic interactions between the inside and outside of the ship is the crux of the evaluation of ship operational safety in adverse sea conditions. In (Taskar et al., 2016), the effects of propeller wake variation and emergence on the engine-propeller dynamics and ship propulsion performance when sailing in waves have been investigated. In (Yum et al., 2017), the simulation of a two-stroke marine diesel engine for ship propulsion in waves has been conducted based on a propulsion system model in waves; and the effects of propeller inflow velocity variations and propeller emergence on the transient performance of the engine have been investigated. A detailed crank-angle engine model has been used in (Taskar et al., 2016) and (Yum et al., 2017) to investigated the waves effects on the engine dynamics, however, only ship propulsion in waves has been considered, while ship manoeuvring in wind and waves (such as turning into head waves) in adverse sea conditions has not been taken into account. In (Aung and Umeda, 2020), based on the simulation model for ship manoeuvring in adverse weather conditions, the effects of different sea states (indicated by Beaufort No.), ship initial forward speed and engine SMCR power on ship manoeuvring behaviour in adverse weather conditions have been investigated; the influence of the emergence of propeller and rudder has been considered. However, in (Aung and Umeda, 2020), a simplified engine model neglecting the engine thermodynamics process has been used. In their engine model, only engine torque has been modelled and it is assumed to be linearly proportional to the amount of the injected fuel into the engine, with the consideration of the static engine load limits. So, the work in (Aung and Umeda, 2020) mainly focuses on the ship manoeuvrability and seakeeping in wind and waves; while it hasn't provided the detailed insight of the engine dynamic behaviour when

ships are manoeuvring in adverse sea conditions. Since the ship safety in adverse weather conditions is highly related to the engine operational safety, a detailed and systematic investigation on the engine behaviour (including both static and dynamic behaviour) under various operating conditions is important and necessary, however, the research in this respect is still limited.

There are many challenges in the study of ship operational safety in adverse sea conditions, especially when taking the engine behaviour, ship manoeuvrability and seakeeping into account as a whole system. Normally, a collaboration of experimental and simulation methods is needed, especially when investigating the ship manoeuvring and seakeeping in waves, which is a difficult hydrodynamic problem (Shigunov, 2019b). In this research, the needed experimental data are obtained from our cooperation partners, including the engine manufacturer and the shipyard; while the numerical calculation data of waves induced steady forces in different sea states are obtained from the published literatures. The research in this thesis aims to develop an integrated first principle and modular simulation model that is capable of providing detailed insights of the complicated and dynamic interactions between the engine, the propeller, the ship and the wind and waves, etc., when the ship is sailing and manoeuvring in adverse sea conditions. The model is first principle at different levels as much as possible, so, it is able to predict the ship behaviour with right trends. With the model calibration using real ship data, adequate and reasonable model verification, and model validation using experimental and trial test data, the model is sufficiently accurate. Moreover, the model is easy to use and is able to run on a normal PC with an acceptable calculation speed (running time within several minutes), without the need of high-performance computer.

To provide the detailed insights of the engine dynamic behaviour in various operating conditions, a Mean Value First Principle Parametric engine model has been developed and applied (Chapter 4). To investigate ship manoeuvrability in adverse sea, an empirical 3DOF ship manoeuvring model has been applied (Chapter 5), and in this chapter the wind and waves model will be presented and applied. When taking the influences of wind and waves in adverse sea conditions into account, only wind- and waves-induced steady forces, including ship resistance increase, wind- and waves-induced steady lateral forces and yaw moments, and waves-induced propeller wake fluctuations will be considered, while the influences of possible propeller ventilation and propeller emergence will be left out of scope. Currently there is no well-established empirical formulae for estimating the waves-induced steady forces, especially the waves-induced lateral force and yaw moment, so, the experimental and numerical results from literature in this regard will be used in this thesis.

The main goals and outline of this chapter are:

- 1) The definition of adverse sea conditions and the safety criteria of ship propulsion and manoeuvring in adverse sea for the benchmark chemical tanker according to the current 2013 interim minimum power guidelines will be introduced (Section 7.2);
- 2) The model of wind- and waves-induced steady forces and moments will be presented (Section 7.3);
- 3) The model of propeller wake fluctuation in waves will be presented (Section 7.4);



- 4) The model of wind and waves will be verified by simulating ship turning in different sea state with different initial velocities (Section 7.5);
- 5) Based on the integrated ship propulsion, manoeuvring and sea state model, the ship propulsion and manoeuvring performance when sailing in head sea and turning to head sea will be investigated in details (Section 7.6);
- 6) The influence of the operational measures, such as changing propeller pitch and PTO/PTI, on the ship thrust envelope will also be investigated (Section 7.7);
- 7) Summary and conclusions of this chapter will be provided (Section 7.8).

## 7.2 Definition of adverse sea conditions and safety criteria

According to the current 2013 interim minimum power guidelines (MEPC, 2017), the adverse sea conditions for different ship sizes are defined by the corresponding wind speed and the significant wave height as shown in Table 7.1. For ships having length shorter than 200 meters, the adverse sea condition is defined with the wind speed of 15.7 m/s and significant wave height of 4.0 m, and the corresponding Beaufort number (BF) is 7 according to the World Meteorological Organization (WMO, 2019). For ships having length longer than 250 meters, the adverse sea condition is defined with the wind speed of 19.0 m/s and significant wave height of 5.5 m, and the corresponding Beaufort number (BF) is 8. For ships having length between 200 and 250 meters, the corresponding wind speed and significant wave height are linearly interpolated according to the ship's length.

Table 7.1: Adverse sea conditions defined for different ship sizes by existing guidelines (MEPC, 2017)

| Ship's length $L_{PP}$<br>(m) | Wind speed<br>(m/s)  | Peak wave<br>period $T_P$ (s) | Significant wave<br>height $H_S$ (m) | Beaufort<br>number (BF) |
|-------------------------------|--|-------------------------------|--------------------------------------|-------------------------|
| $L_{PP} < 200$                | 15.7   | 7.0 to 15.0                   | 4.0                                  | 7                       |
| $200 \leq L_{PP} \leq 250$    | Parameters linearly interpolated according to ship's length $L_{PP}$ |                               |                                      |                         |
| $L_{PP} > 250$                | 19.0   | 7.0 to 15.0                   | 5.5                                  | 8                       |

According to level 2 assessment of the current guidelines for minimum propulsion power, i.e., the simplified assessment, the safety assessment criteria is based on the principle that, '*if the ship has sufficient installed power to move with a certain advance speed in head waves and wind, the ship will also be able to keep course in waves and wind from any other direction*' (MEPC, 2017). The required ship advance speed sailing in head wind and waves should be the larger of: minimum navigational speed or the minimum course-keeping speed. In the current guidelines, the minimum navigational speed is set to 4.0 knots, with which the ship is considered to be able to leave coastal area within sufficient time before the storm escalates. The minimum course-keeping speed is selected based on ship design parameters, such as the rudder area and lateral windage area, etc., which have significant impacts on the course-keeping performance of the ship in adverse sea conditions. For details of the estimation procedure of the minimum course-keeping speed, please refer to (MEPC, 2017).

Note that, the above definition of adverse conditions in the current guidelines are applicable

to ships (bulk carriers, tankers and combination carriers) with the size of equal to or more than 20,000 DWT. However, in this thesis, for the moment it is assumed that the guidelines are also applicable to the benchmark chemical tanker, which has the capacity of 13,000 DWT. The specified adverse condition for the benchmark chemical tanker is the sea condition with Beaufort number of 7. The required advance speed of the benchmark chemical tanker in head wind and waves according to the current guidelines is 6.4 knots.

### 7.3 Wind- and waves-induced steady forces and moments

When taking the influences of wind and waves in adverse sea conditions into account, only time-averaged steady wind- and waves-induced forces and moments acting on the ship hull will be considered, while the time-varying oscillatory forces and moments will be neglected assuming that the time scale is shorter than that of the ship motions (Shigunov, 2019b). The equations of ship motions and hydrodynamic forces and moments when including the wind- and waves-induced steady forces and moments are shown in equation (7.1). The structure of the integrated ship propulsion, manoeuvring and sea state model is illustrated in Figure 7.1.

$$\left. \begin{aligned} (m + m_x) \cdot \dot{u} - (m + m_y) \cdot v \cdot r &= X_H + X_P + X_R + X_A + X_W \\ (m + m_y) \cdot \dot{v} + (m + m_x) \cdot u \cdot r &= Y_H + Y_R + Y_A + Y_W \\ (I_z + J_z) \cdot \dot{r} &= N_H + N_R + N_A + N_W \end{aligned} \right\} \quad (7.1)$$

Where,  $X_A$ ,  $Y_A$  and  $N_A$  are the wind-induced steady longitudinal force, lateral force and moment respectively;  $X_W$ ,  $Y_W$  and  $N_W$  are the waves-induced steady longitudinal force, lateral force and moment respectively.

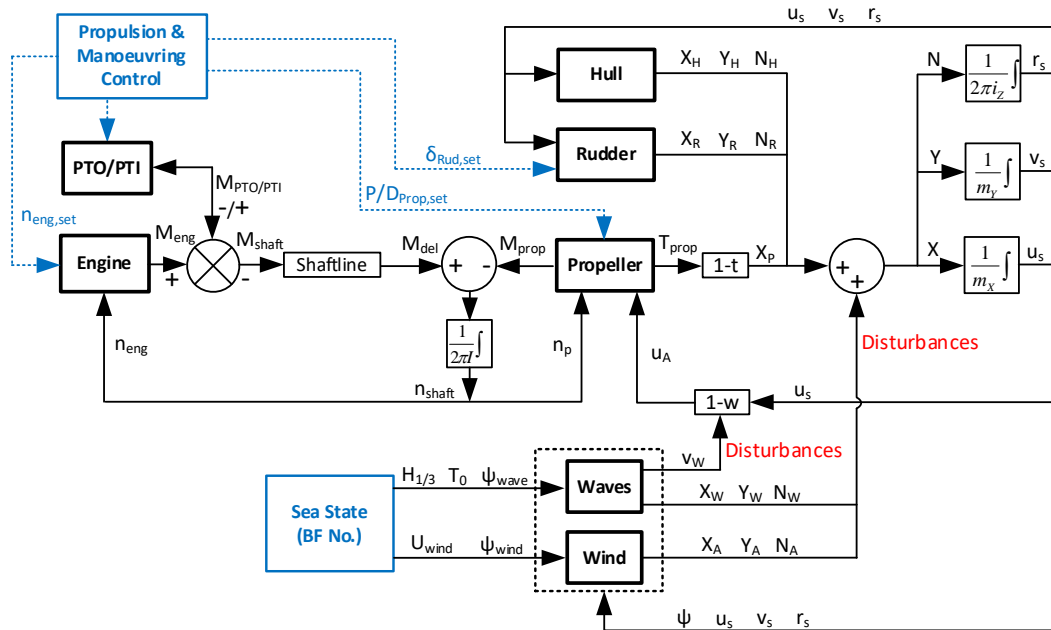


Figure 7.1: Integrated ship propulsion, manoeuvring and sea state model

The coordinate system of the wind and waves is illustrated in Figure 7.2. It is assumed that the wind and waves come from the same direction.

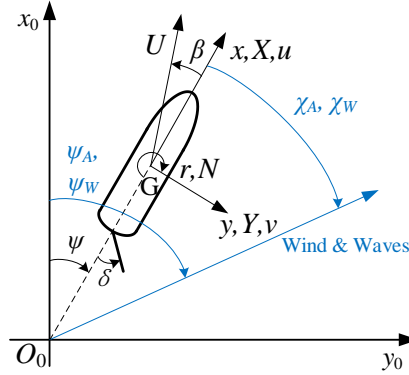


Figure 7.2: Coordinate system of wind and waves

### 7.3.1 Wind-induced steady forces and moment

The wind-induced external steady forces ( $X_A$ ,  $Y_A$ ) and moment ( $N_A$ ) acting on the ship are estimated using Fujiwara's empirical wind model (Fujiwara et al., 2006; Kitamura et al., 2017). According to (Fujiwara et al., 2006) the wind forces and moment in the constant and uniform wind are expressed as:

$$\left. \begin{aligned} X_A &= 1/2 \cdot \rho_a \cdot U_A^2 \cdot C_{XA}(\chi_A) \cdot A_X \\ Y_A &= 1/2 \cdot \rho_a \cdot U_A^2 \cdot C_{YA}(\chi_A) \cdot A_Y \\ N_A &= 1/2 \cdot \rho_a \cdot U_A^2 \cdot C_{NA}(\chi_A) \cdot A_Y \cdot L_{OA} \end{aligned} \right\} \quad (7.2)$$

Where,  $\rho_a$  is the air density;  $U_A$  is the relative wind velocity;  $C_{XA}$ ,  $C_{YA}$  and  $C_{NA}$  are the wind forces and moment coefficients;  $\chi_A$  is the relative wind direction;  $A_X$  and  $A_Y$  are the frontal and lateral projected areas of the ship above water respectively;  $L_{OA}$  is the overall ship length.

For estimating the wind forces and moment coefficients,  $C_{XA}$ ,  $C_{YA}$  and  $C_{NA}$ , when using the method in (Fujiwara et al., 2006), eight basic hull form parameters representing the above water structural shape of ships are needed. However, some of the needed above water structural parameters of the benchmark chemical tanker are not available, so, they are estimated using the regression formulae in (Kitamura et al., 2017). The calculated wind forces and moment coefficients of the benchmark chemical tanker for different wind directions using the method in (Fujiwara et al., 2006; Kitamura et al., 2017) have been shown in Figure 7.3.

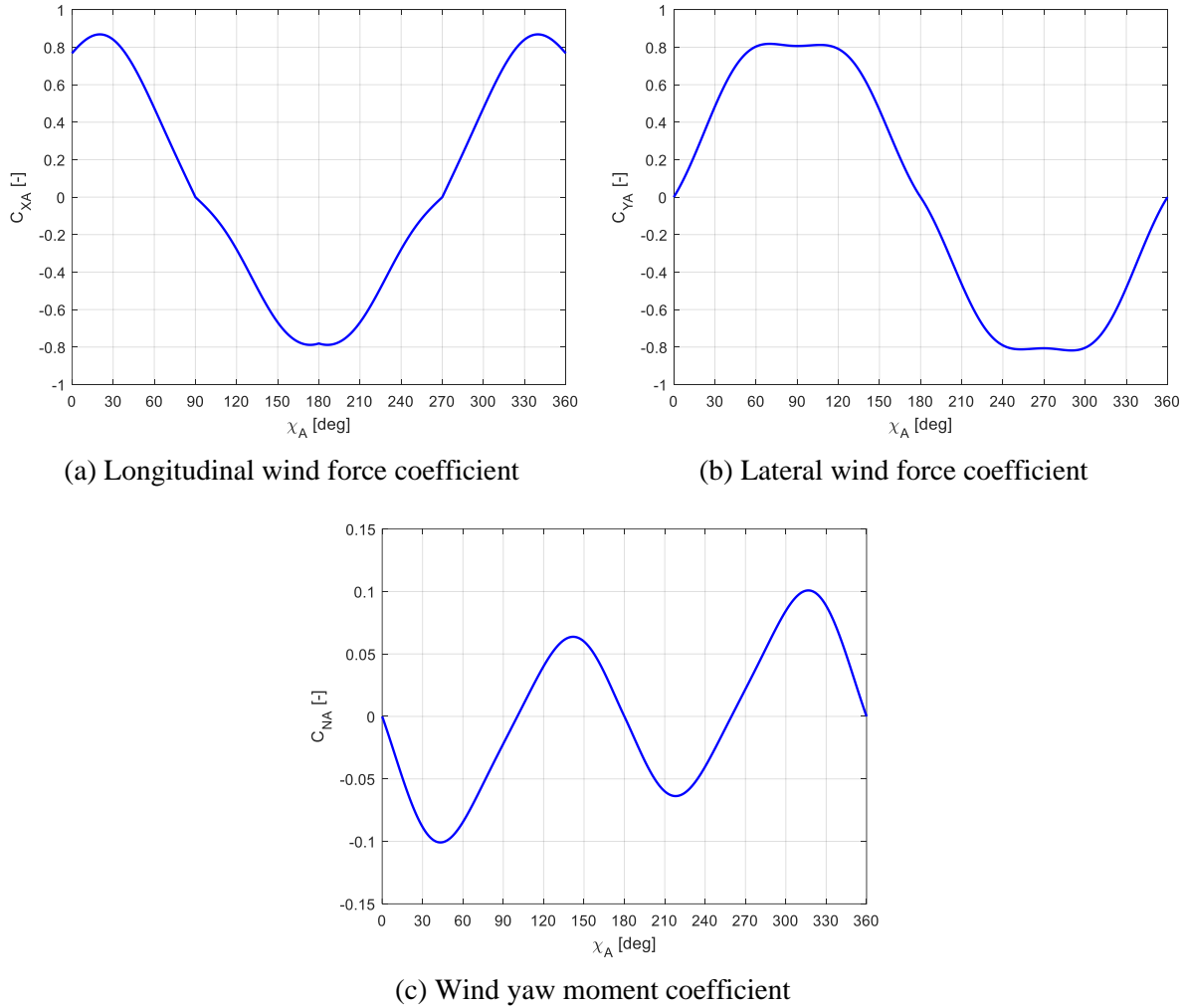


Figure 7.3: Wind-induced steady forces and moment coefficients

### 7.3.2 Waves-induced steady forces and moments

According to (Yasukawa et al., 2019), the averaged waves-induced steady forces ( $X_W$ ,  $Y_W$ ) and moment ( $N_W$ ) in irregular waves are expressed as:

$$\left. \begin{aligned} X_W &= \rho_w \cdot g \cdot H_{1/3}^2 \cdot (B^2/L) \cdot C_{XW}(U, T_v, \chi_w) \\ Y_W &= \rho_w \cdot g \cdot H_{1/3}^2 \cdot (B^2/L) \cdot C_{YW}(U, T_v, \chi_w) \\ N_W &= \rho_w \cdot g \cdot H_{1/3}^2 \cdot B^2 \cdot C_{NW}(U, T_v, \chi_w) \end{aligned} \right\} \quad (7.3)$$

Where,  $\rho_w$  is the sea water density;  $g$  is the gravity acceleration;  $H_{1/3}$  is the significant wave height;  $T_v$  is the averaged wave period;  $\chi_w$  is the relative wave direction;  $B$  and  $L$  are the ship width and length respectively;  $C_{XW}$ ,  $C_{YW}$  and  $C_{NW}$  are the averaged steady forces and moment coefficients in irregular waves.

For estimating the averaged waves-induced steady forces coefficients of the benchmark chemical tanker, the numerical calculation results of those coefficients of a full hull ship S-Cb84 (Figure 7.4) published in (Yasukawa et al., 2019) have been used. The S-Cb84 is a bulk

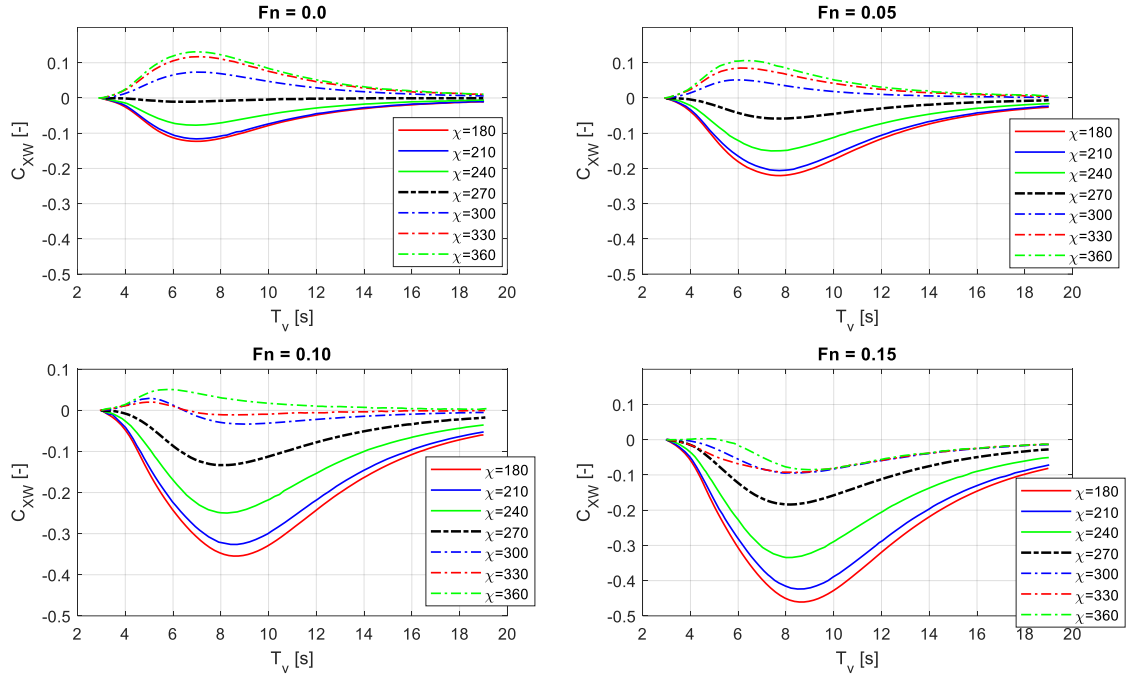
carrier, which originally was a VLCC (Very Large Crude Carrier) tanker. The principal particulars of S-Cb84 are shown in Table 7.2. The averaged steady forces and moments coefficients of S-Cb84 in irregular waves shown in Figure 7.4 are calculated by using the strip theory-based Kochin-function method (SKFM) assuming a slender ship; the ITTC (International Towing Tank Conference) wave spectrum, and  $\cos^2$  wave direction distribution function have been used (Yasukawa et al., 2019). The applicability of the numerical calculation results using SKFM method to the manoeuvring problems in irregular waves has been validated by the free-running model test results, and it is concluded that the accuracy is acceptable for practical purposes, even though the calculation accuracy of the steady yaw moment is insufficient as mentioned in (Yasukawa et al., 2019).

In the simulation model of the benchmark chemical tanker, the waves-induced forces coefficients are stored in look-up tables as functions of ship speeds, averaged wave period and wave encounter headings. During simulation, under the quasi-static assumption the coefficients in different operating conditions are estimated by using interpolation method. Although there will be some extra uncertainties when using these numerical calculation results to a different ship, i.e., the benchmark chemical tanker for this research, it is assumed that the uncertainties in this regard are acceptable for this research. And the reasons for this assumption are as follows: firstly, both the two ships are tankers, so, they have similar hull shape although with different sizes; secondly, the numerical calculation results for the waves induced steady forces are nondimensional; thirdly, the simulation results of the benchmark chemical tanker turning in different sea states with different ship speeds have been verified (in section 7.5), and the model verification shows reasonable results comparing to the simulation and model test results in (Yasukawa et al., 2019).

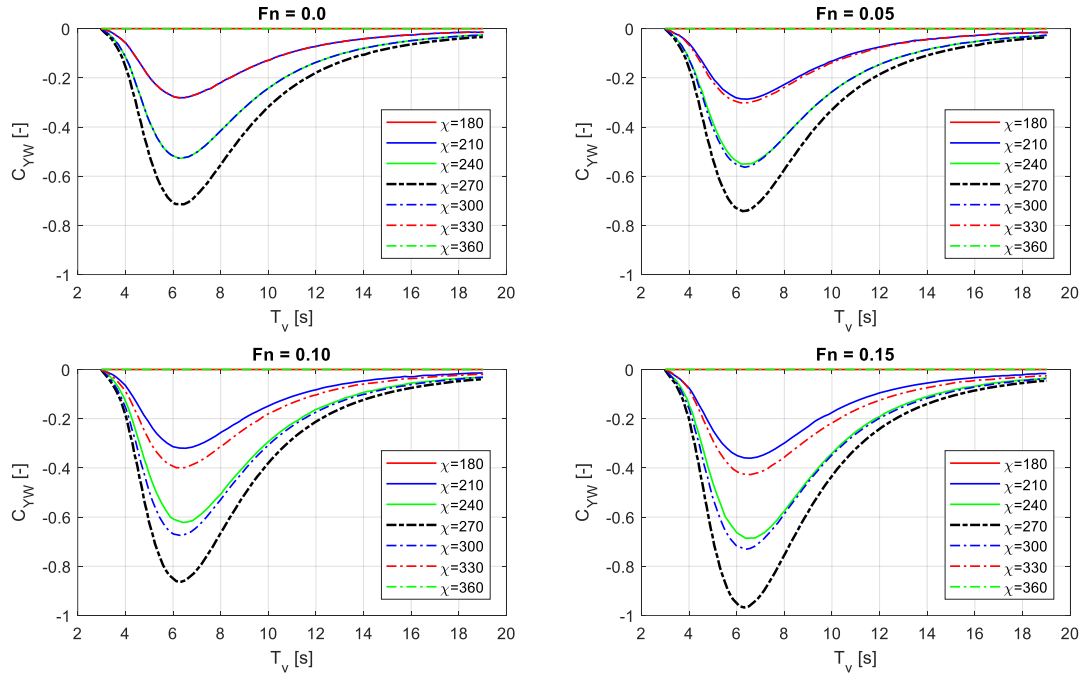
Table 7.2: Principal particulars of S-Cb84 (Yasukawa et al., 2019)

|  |        |
|--|--------|
| Ship Length between perpendiculars $L$ (m)                 | 178.00 |
| Breadth $B$ (m)  | 32.26  |
| Depth $D$ (m)  | 14.46  |
| Draught $d$ (m)  | 11.57  |
| Displacement volume $\nabla$ (m <sup>3</sup> )             | 55810  |
| Longitudinal position of the centre of gravity $x_G$ (m) * | 5.33   |
| Block coefficient $C_b$ (-)                                | 0.84   |

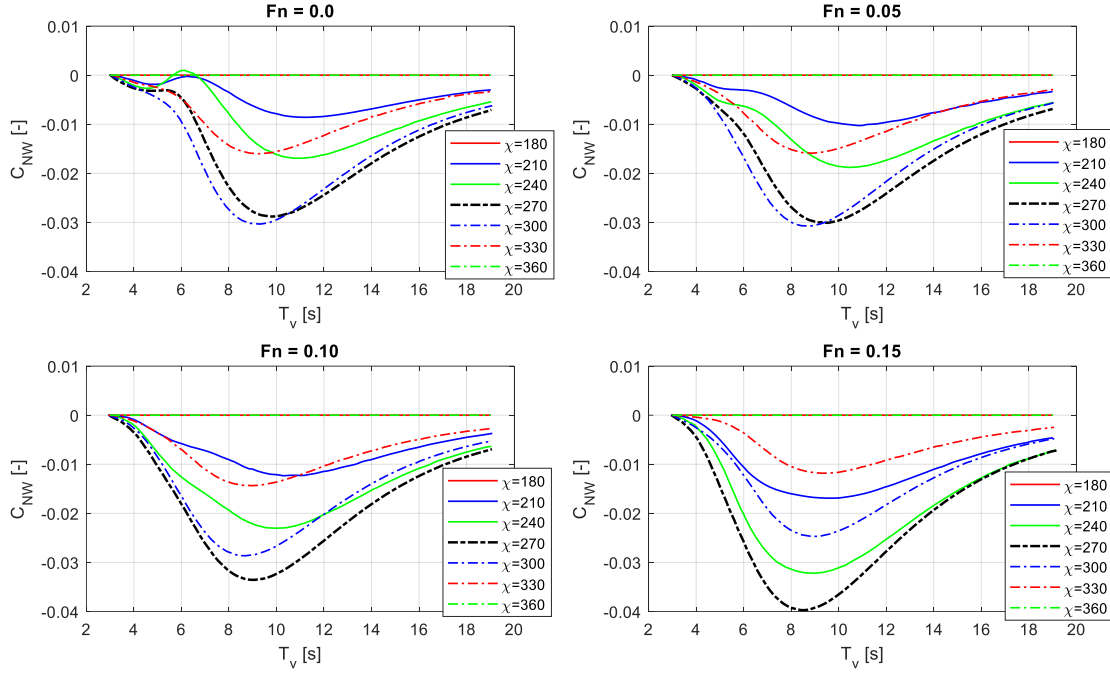
\*  $x_G$  is defined based on the midship and is positive when locating forward of midship. \*



(a) Steady longitudinal force coefficients



(b) Steady lateral force coefficients



(c) Steady yaw moment coefficients

Figure 7.4: Averaged steady forces and moments coefficients of S-Cb84 in irregular waves calculated using SKFM (Yasukawa et al., 2019)

## 7.4 Propeller wake fluctuation in waves

The effective inflow velocity to the propeller in waves is determined by the average ship speed, ship motion and wave induced orbital motion of water particles (Ueno et al., 2013). The variation of effective wake fraction during ship manoeuvring motions in calm water considering the geometrical inflow angle at the propeller position has been discussed in Chapter 5. According to (Ueno et al., 2013) the fluctuating propeller inflow velocities in waves are caused by the surge oscillation effect and the orbital motion of water particles. In this thesis, the effect of ship manoeuvring motions on the average propeller inflow velocity and the effect of the water orbital movement on the oscillating inflow velocity in regular waves will be considered; while the effects of surge oscillation and the interaction between the ship manoeuvring motions and the water orbital movement will be left out of account. So, the propeller inflow velocity  $v_A$  in regular waves is expressed as:

$$v_A = u \cdot (1 - w_p) + \alpha \cdot \omega \cdot h_a \cdot \exp(-k \cdot z_p) \cdot \cos \chi_w \cdot \cos(\omega_e \cdot t - k \cdot x_p \cdot \cos \chi_w) \quad (7.4)$$

$$\alpha = \begin{cases} 0.2 \cdot \left( \frac{\lambda}{L \cdot |\cos \chi_w|} \right) + 0.5, & \text{for } \frac{\lambda}{L \cdot |\cos \chi_w|} \leq 2.5 \\ 1, & \text{for } \frac{\lambda}{L \cdot |\cos \chi_w|} > 2.5 \end{cases} \quad (7.5)$$

Where,  $u$  is the ship longitudinal velocity;  $w_p$  is the effective wake fraction including the effect of ship manoeuvring motions;  $\alpha$  is the coefficient representing the effect of wave

amplitude decrease at the stern in case of head and bow-quartering waves due to the influence of the hull (calculated by equation (7.5)) (Ueno et al., 2013);  $\omega$  is the wave circular frequency;  $\omega_e$  is the wave encounter circular frequency defined by  $\omega_e = \omega - k \cdot u \cdot \cos \chi_w$ ;  $h_a$  is the wave amplitude;  $k$  is the wave number;  $x_P$  and  $z_P$  are the longitudinal and vertical positions of the propeller in the ship-fixed coordinate system;  $\chi_w$  is the wave encounter angle;  $t$  is time;  $\lambda$  is the wave length and  $L$  is the ship length between perpendiculars.

## 7.5 Verification of wind and waves model

As there is no test data for validating the wind and waves model of the benchmark chemical tanker, only verification results of the ship turning in wind and waves are provided as shown in Figure 7.5. The average waves period of 8 seconds ( $T_v = 8$  s) has been applied. The ship turning trajectories, including both starboard and portside turning with rudder angle of 35 degrees, in sea states of BF6 and BF7 have been compared with those in calm sea (BF0). The influences of different initial ship speed, i.e., 12 knots, 8 knots and 4 knots, on turning in wind and waves have also been presented. During the turning the propeller pitch is set and kept at the design pitch (pitch angle = 17.83 degrees or equivalently P/D = 0.7075), and the propeller revolution is set and kept at the MCR engine revolution (167 rpm). The ship velocities during the turning are shown in Figure 7.6. According to the results shown in Figure 7.5, the ship drifts more significantly in higher sea state, and in the same sea state the ship drifts more significantly with a lower ship speed. It is caused by the relatively large effect of the wave-induced steady forces on the ship when turning with a lower speed and/or in a higher sea state (Yasukawa et al., 2019).

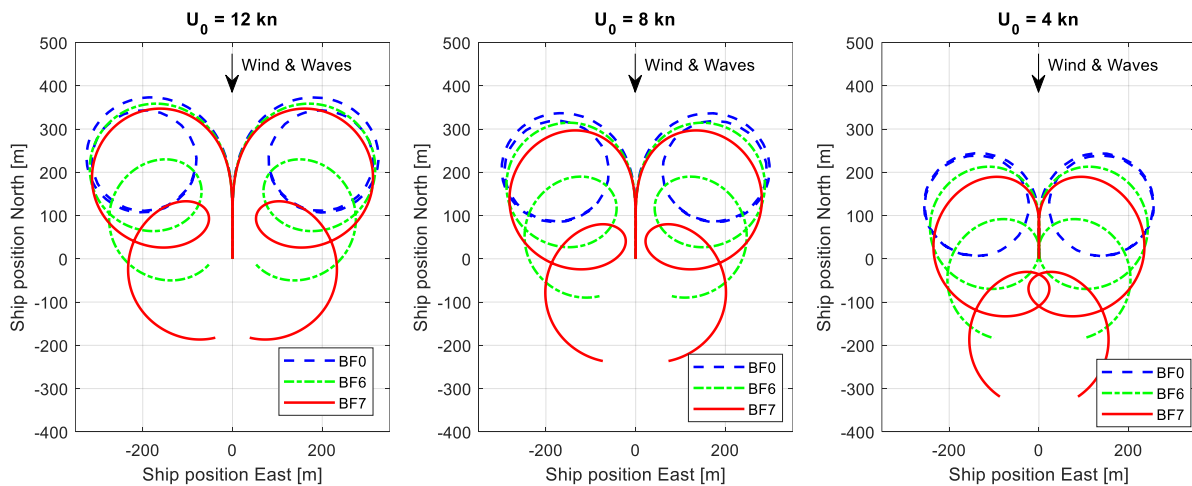


Figure 7.5: Ship turning trajectories in wind and waves (rudder angle: 35 deg.)



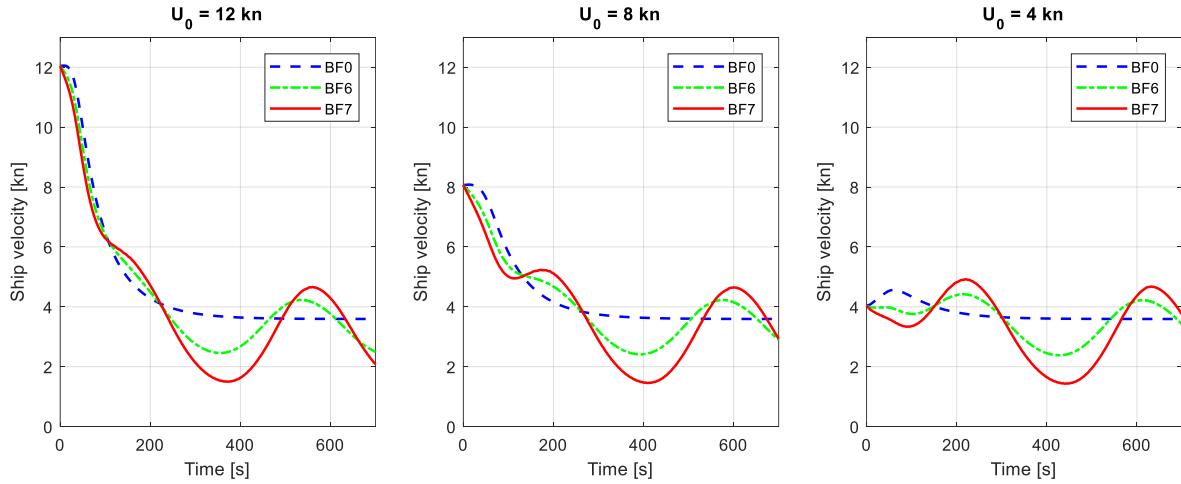


Figure 7.6: Ship velocity during turning in wind and waves (rudder angle: 35 deg.)

## 7.6 Ship propulsion and manoeuvring performance in adverse sea

In this section, based on the integrated ship propulsion, manoeuvring and sea state model, the ship propulsion and manoeuvring performance of the benchmark chemical tanker in adverse sea conditions (sea states of BF7 and BF8) will be investigated. In particular, the three most important scenarios when the ship operates in adverse sea, i.e., sailing in head sea, accelerating in head sea, and turning to head sea, will be studied in details. So, the abilities of the ship to keep a certain advance speed, to accelerate, and to keep and change heading in adverse sea will be investigated. During the simulation of ship sailing and manoeuvring in adverse sea, the shaft generator (PTO) has been shut off, so, the main engine only provides power to the propeller and the onboard electric power is supplied by the auxiliary generators. As the fixed pitch propellers (FPP) are most commonly installed on the ocean-going cargo ships, to have a generic study, the constant pitch propulsion control mode has been applied in this investigation. The propeller pitch is set and kept at the design pitch (pitch angle = 17.83 degrees or equivalently  $P/D = 0.7075$ ). So, the ship speed will be controlled by changing the propeller revolution and thus the engine revolution. The fuel rack limiter of the engine is switched on so that the engine can only run inside its specified operating envelope and it will not be mechanically overloaded.

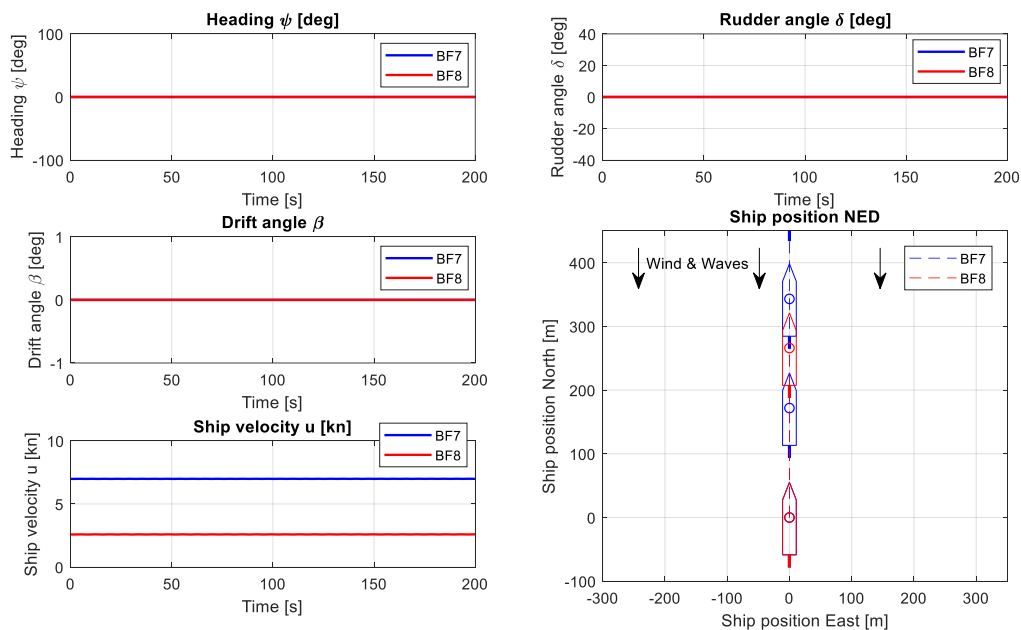
### 7.6.1 Ship sailing in head sea

The ship heads to North ( $\psi = 0$  deg.) and the head wind and waves come from the North ( $\psi_A = \psi_W = 180$  deg.) as shown in Figure 7.7 (a). The propeller revolution is set and kept at the MCR engine revolution (167 rpm) as shown in Figure 7.7 (b). The simulation results of ship sailing in head sea are shown in Figure 7.7 (a) to (f).

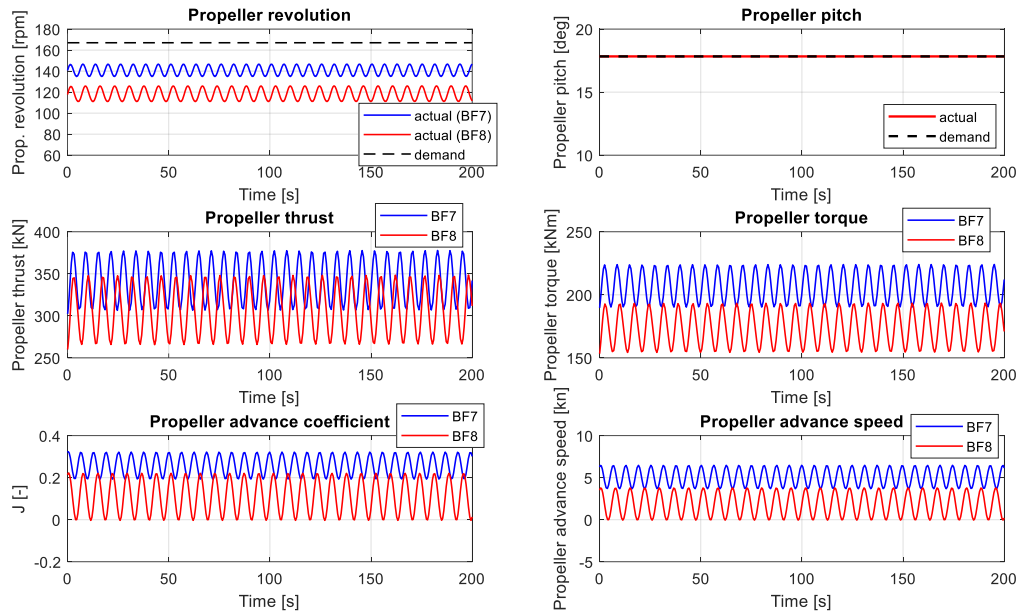
Due to the wake fluctuation caused by the waves, the propeller advance speed and advance coefficient fluctuates and consequently the propeller torque, thrust and revolution also oscillates (Figure 7.7 (b)). However, the ship velocity hardly fluctuates due to the big inertia of the ship surge motion. The maximum available ship thrusts in different sea conditions oscillate around the static thrust limit as shown in Figure 7.7 (c), and the equilibrium point of the oscillation locates on the static thrust limit. So, the waves-induced wake fluctuation and the resulting ship

thrust fluctuation on average do not have an influence on the ship speed. But the ship speed is highly influenced by the added ship resistance in adverse sea conditions. The maximum ship advance speed sailing in head sea of BF7 is 7.0 knots, while in head sea of BF8 the maximum speed is only 2.6 knots. In head sea of BF9, the ship is not able to move forward at all as the ship resistance completely exceeds the ship thrust limit (Figure 7.7 (c)).

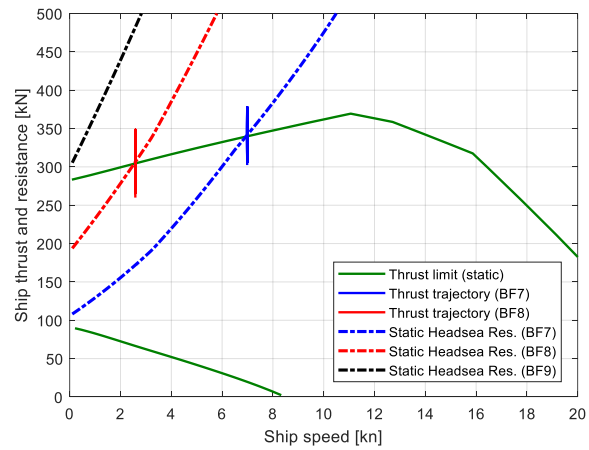
The engine behaviour also fluctuates because of the fluctuating loads, i.e., the propeller torque (Figure 7.7 (d) to (f)). The engine is not able to run at the demanded revolution because the fuel rack and consequently the engine torque are limited to protect the engine from overloading as shown in Figure 7.7 (d). The engine runs on its limit but still not exceeding the (static) operating envelope. However, dynamically the engine could have already been thermally overloaded especially in BF8 sea condition as shown in Figure 7.7 (e). The air excess ratio and the cylinder temperature just before EO exceeds their limits in sea state of BF8. Without reducing the propeller pitch, the engine is forced to operate at low-speed area in adverse sea condition, and this is the case for most of the ocean-going cargo ships that have fixed pitch propeller. In particular, the engine speed in BF8 is lower than that in BF7, and consequently the turbocharger speed, the charging pressure and the air mass flow in BF8 are lower as well. Although the compressor does not surge in both BF7 and BF8, the compressor operating point in BF8 is closer to the surge line than that in BF7.



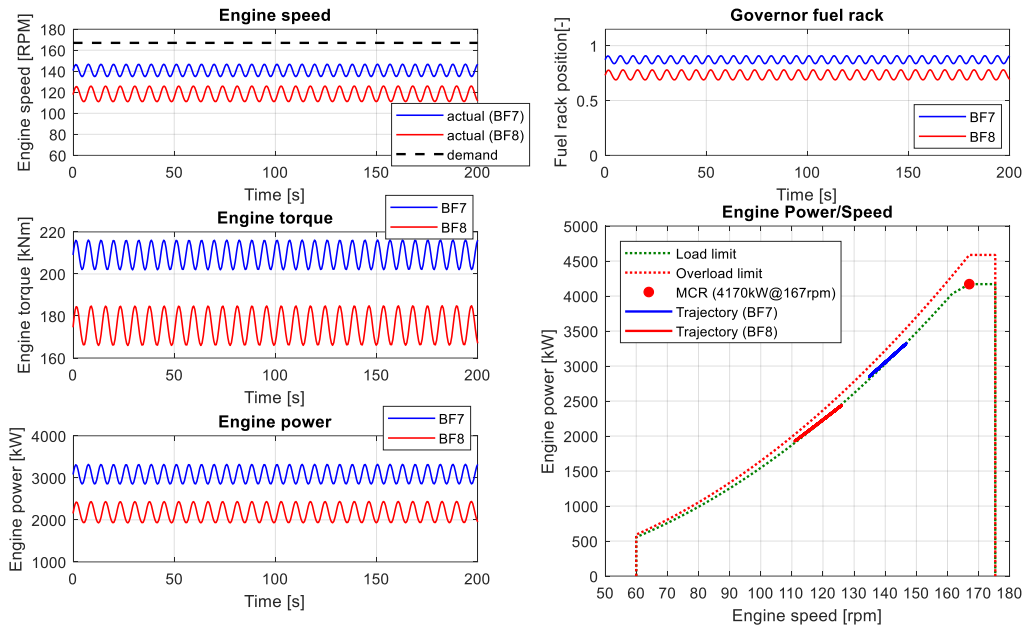
(a) Simulation results of ship



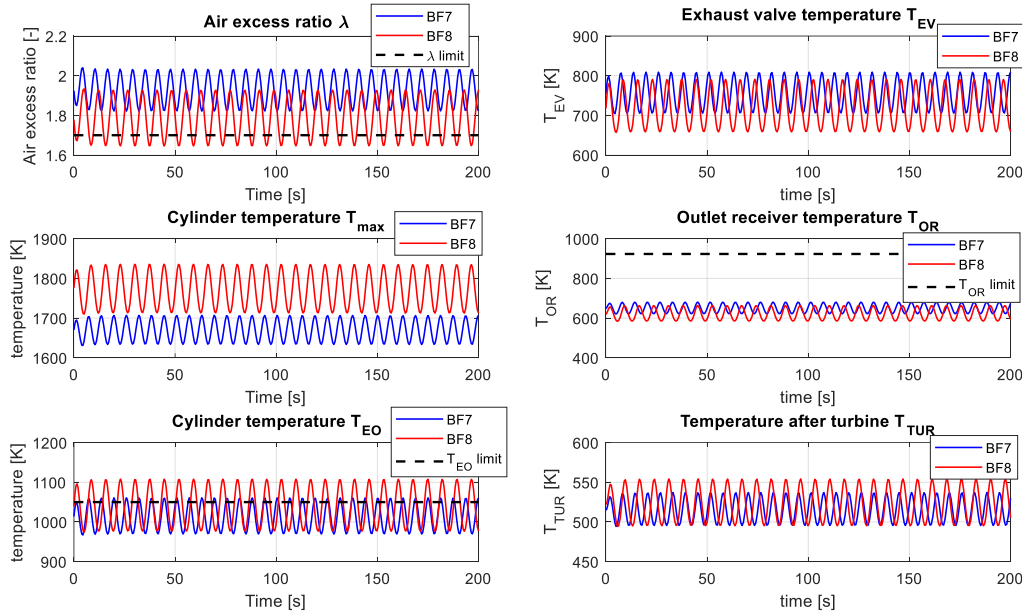
(b) Simulation results of propeller



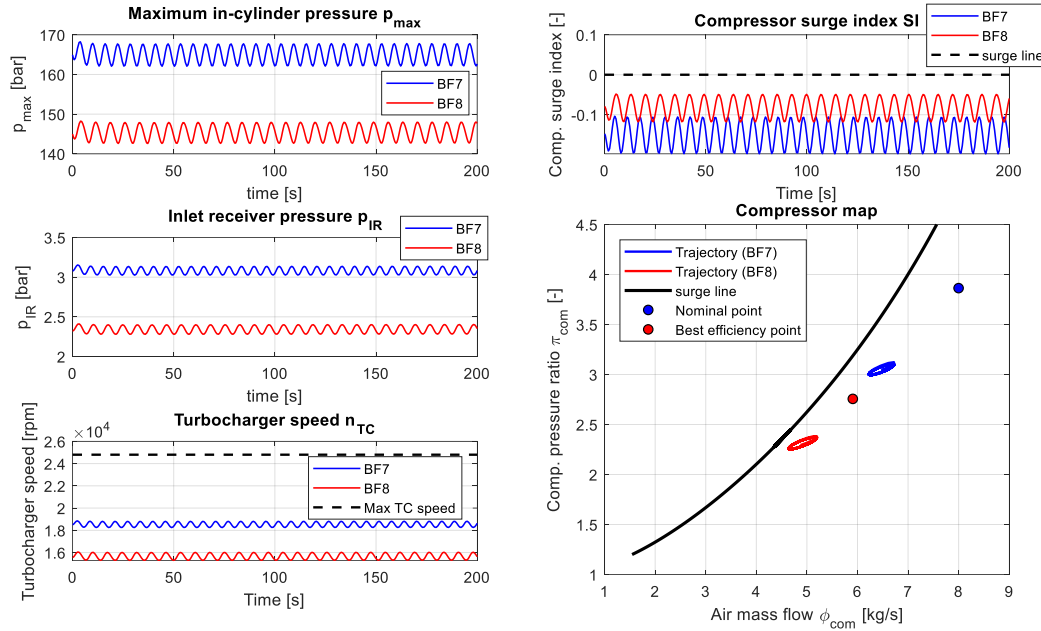
(c) Ship thrust and resistance



(d) Engine speed, fuel rack, torque and power



(e) Engine thermal loading



(f) Maximum in-cylinder pressure and compressor behaviour

Figure 7.7: Simulation results of ship sailing in head sea

### 7.6.2 Ship acceleration in head sea

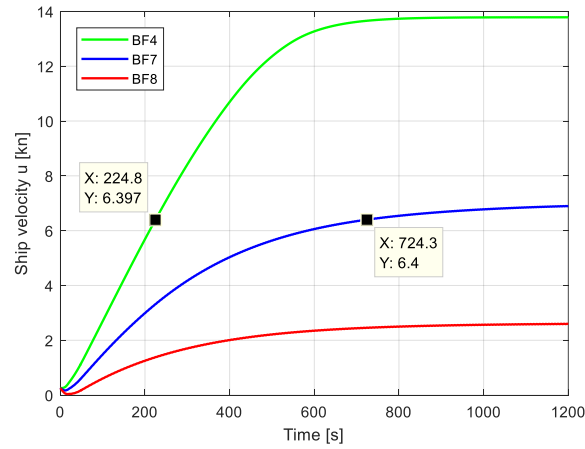
In previous section, only ship propulsion performance in stationary operating conditions, i.e., ship sailing at stationary maximum forward speeds, when sailing in head sea in adverse sea conditions (BF7, BF8) has been investigated. Only influences of the increased ship resistance and wake fluctuations due to high sea states on the propulsion performance of the ship have been investigated in previous section. In adverse sea conditions and/or in increasing high sea states, the capability of the ship propulsion plant to accelerate the ship to reach a certain speed, for instance the required advance speed in head wind and waves, in a certain short time is very crucial to ship's safety. To have an insight of the combined influence of ship acceleration and increased ship resistance as well as propeller wake fluctuation in adverse weather conditions, ship acceleration in head sea in sea states of BF7 and BF8 will be investigated in this section. The ship acceleration performance in adverse sea conditions has been compared with that in normal sea condition (BF4, corresponding to the 15% sea margin) as presented in Figure 7.8(a)-(f). The stationary end of the acceleration processes, when equilibrium states have been reached, will be exactly the same stationary operating conditions discussed in the previous section. Only time trajectory of the simulation results in the time period from 0s to 700s of the acceleration process (before stationary states have been reached) have been shown in Figure 7.8 (b)-(f).

As mentioned earlier, the constant pitch propulsion control mode (see section 2.5.1 in Chapter 2) has been applied in this Chapter. The stationary initial condition of the ship acceleration is set as following: the initial SLC (single lever command) is set at zero; the corresponding initial propeller (and engine) revolution is 82 rpm; the initial propeller pitch is nearly zero; and consequently, the initial ship speed in normal sea condition (BF4) is nearly zero (Figure 7.8 (a)). During the simulation, when the ship starts acceleration (at 0s), the sea condition is switched to sea states of BF7 or BF8 and kept unchanged throughout the whole

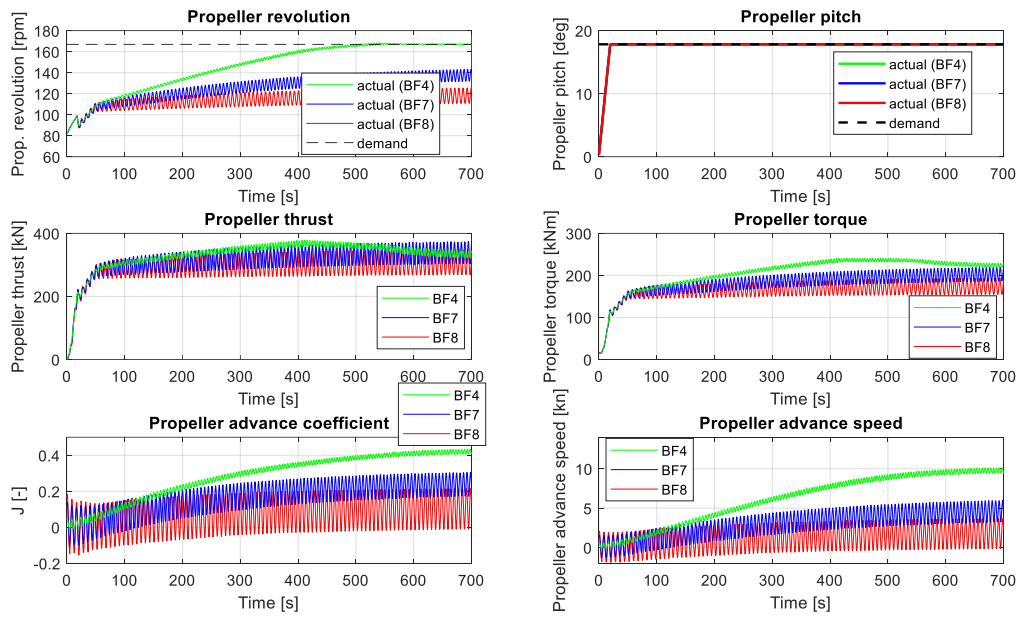
acceleration process; the propeller (and engine) revolution demand is set and kept at the MCR engine revolution (167 rpm); and the propeller pitch demand is set and kept at the design pitch (Figure 7.8 (b)). Note that, for ships that have installed fixed pitch propeller, the propeller (and engine) revolution will increase from zero when the ship starts acceleration.

As explained in the previous section, the maximum forward speed the ship can reach in head sea in higher sea states are lower than that in lower sea states. Also, the ship acceleration in higher sea states is slower than in lower sea states as shown Figure 7.8 (a) due to the larger increased ship resistance in higher sea states, which is shown in Figure 7.8 (c). It takes more than 12 minutes (724 seconds) for the ship to reach the speed at 6.4 knots, which is the required advance speed of the benchmark chemical tanker in head wind and waves, in sea state of BF7; while it only takes less than 4 minutes (225 seconds) to reach the same speed in sea state of BF4 (normal sea condition). For both adverse sea conditions (BF7 and BF8) and normal sea condition (BF4), in the first 20 seconds of the acceleration process, the fast increase of the propeller thrust and torque is mainly caused by the increase of the propeller pitch (from zero to design pitch) implemented by the pitch actuator (Figure 7.8 (b)). Consequently, the engine torque, power and fuel rack position increase quickly as well (Figure 7.8 (d)). This causes a sharp increase of the engine thermal loads as shown in Figure 7.8 (e). In particular, the air excess ratio  $\lambda$  and the cylinder temperature just before EO  $T_{EO}$  exceeds their limits in both adverse and normal sea conditions.

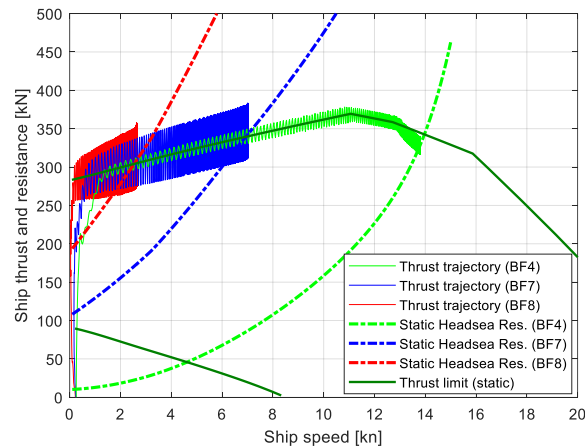
Another notable turning point during the ship acceleration process is the time at around 50s, from where the torque-speed limit of the engine comes into force (through the action of the governor fuel rack limiter). Before this point, there is hardly any differences between time trajectories of the simulation results in different sea states. The reason for this is that, in both adverse and normal sea conditions, it is still in the very early stage of the acceleration process. The ship speeds and propeller advance coefficients increase slightly (from zero). Consequently, the loads ‘felt’ by the engine are almost the same. At the same time, the engine torque is not yet limited by the torque-speed limit, so, the acceleration processes in the early 50 seconds in different sea states are almost the same. However, after this point, when the differences in the engine loads side become obviously larger in different sea states, and the engine torque-limit starts to take effect, the differences of the acceleration processes in different sea states will become more obvious. The differences after this point can then be explained using the analysis made in the previous section.



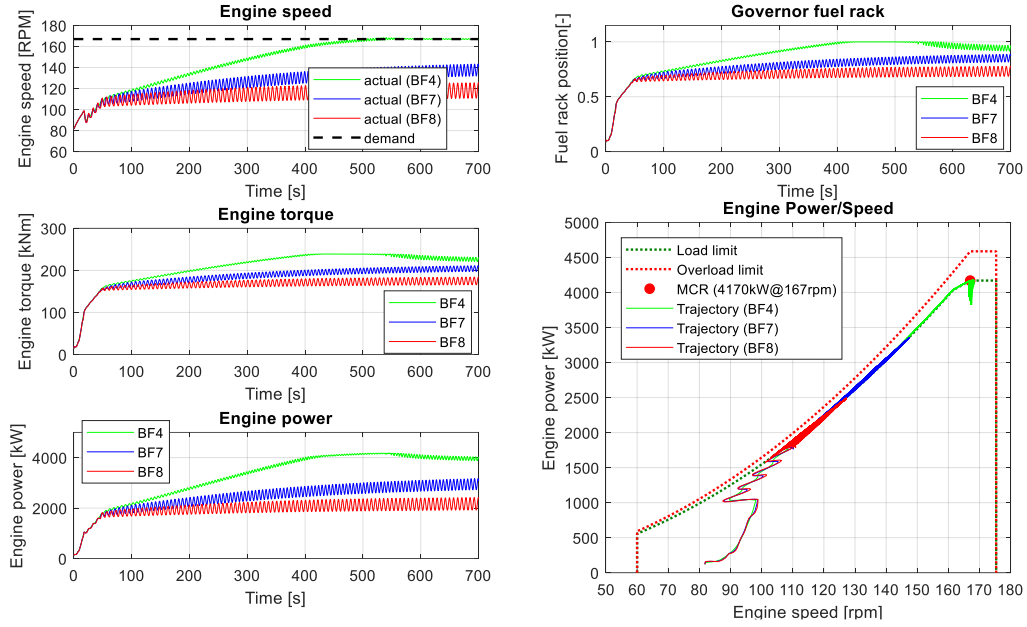
(a) Ship speed



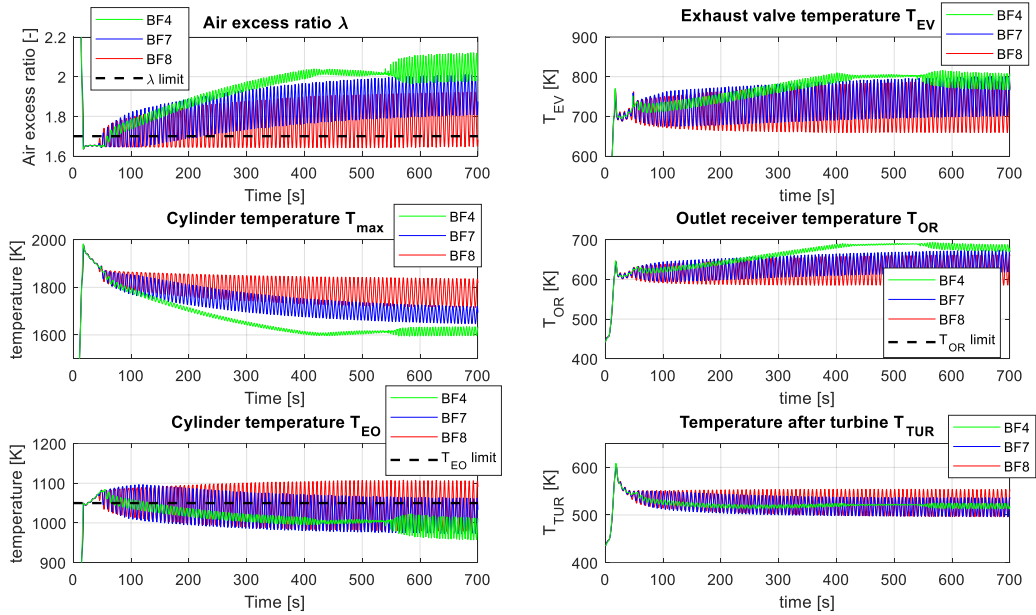
(b) Simulation results of propeller



(c) Ship thrust and resistance

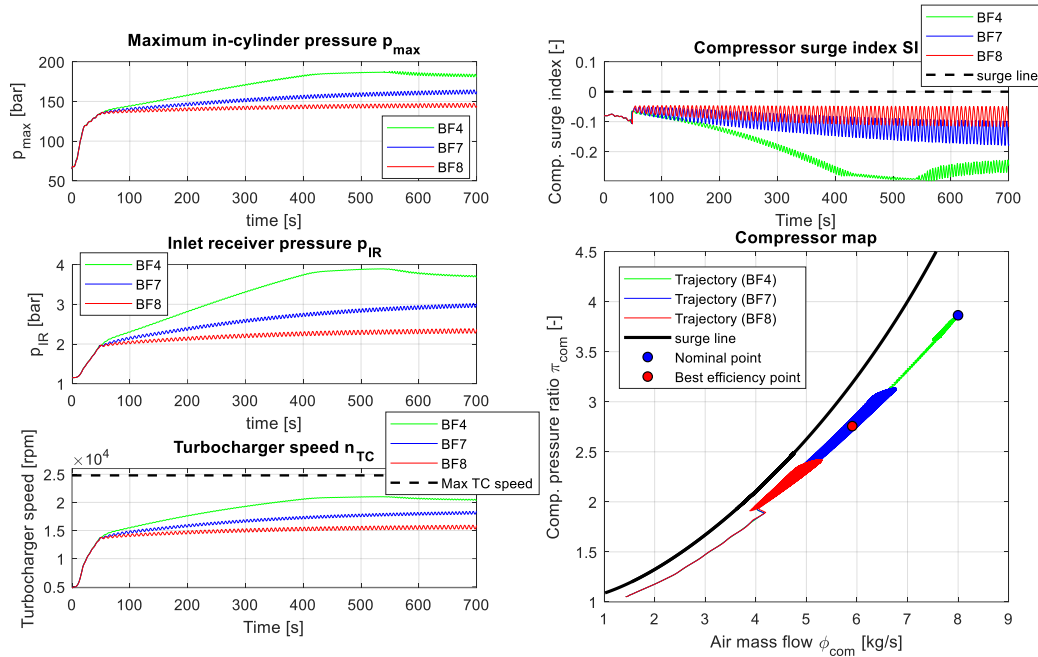


(d) Engine speed, fuel rack, torque and power



(e) Engine thermal loading





(f) Maximum in-cylinder pressure and compressor behaviour

Figure 7.8: Simulation results of ship acceleration in head sea

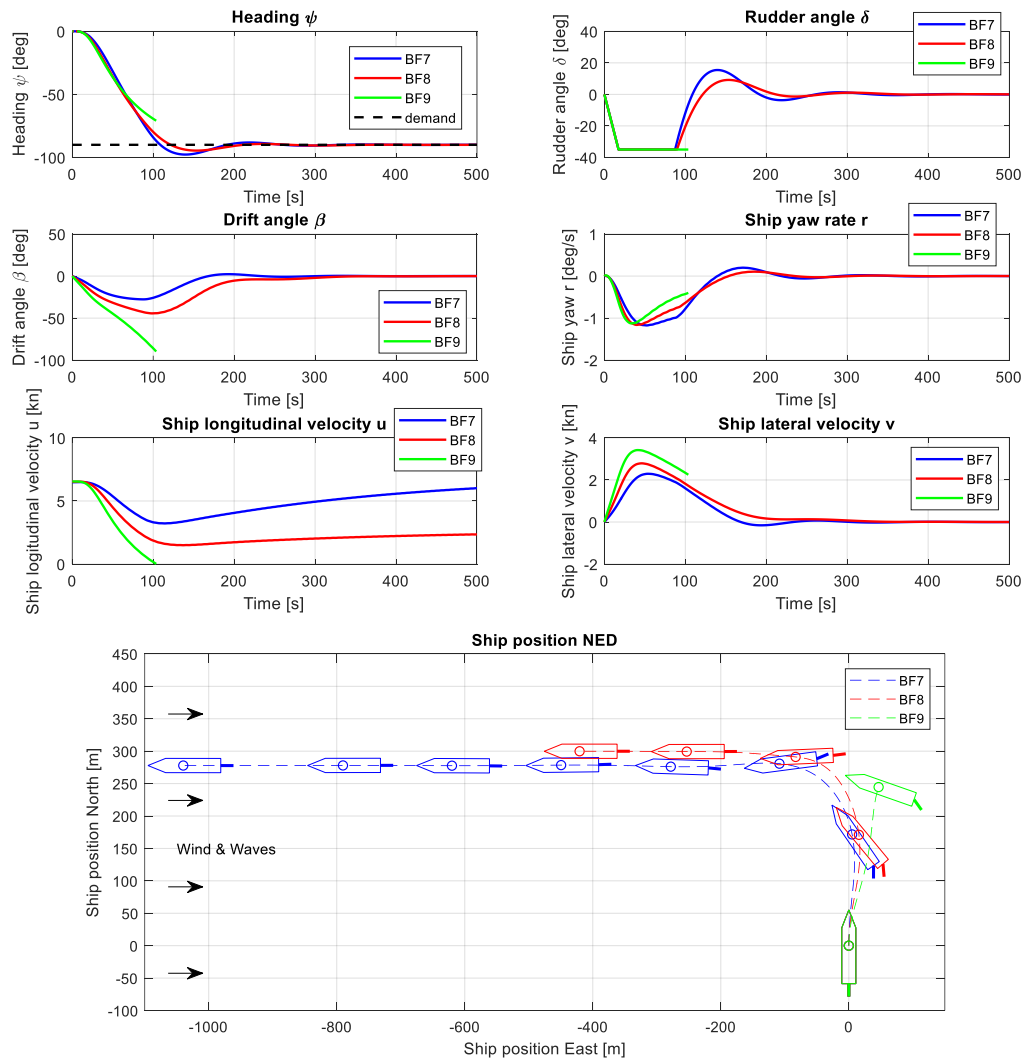
### 7.6.3 Ship turning to head sea

The initial ship forward speed is set at  $u = 6.5$  knots and the initial ship heading is set at  $\psi = 0$  degree (heading towards North). The wind and waves come from West ( $\psi_A = \psi_W = 90$  degrees) towards the portside of the ship. The ship tries to turn its bow to head wind and waves for weather-vanning. Same as sailing in head sea, during ship turning to head sea the propeller revolution is set and kept at the MCR engine revolution (167 rpm). The ship heading is controlled in autopilot mode, where the rudder angle is controlled by a PID heading controller based on the demanded ship heading and actual heading feedback. The simulation results of ship turning to head sea are shown in Figure 7.9 (a) to (f).

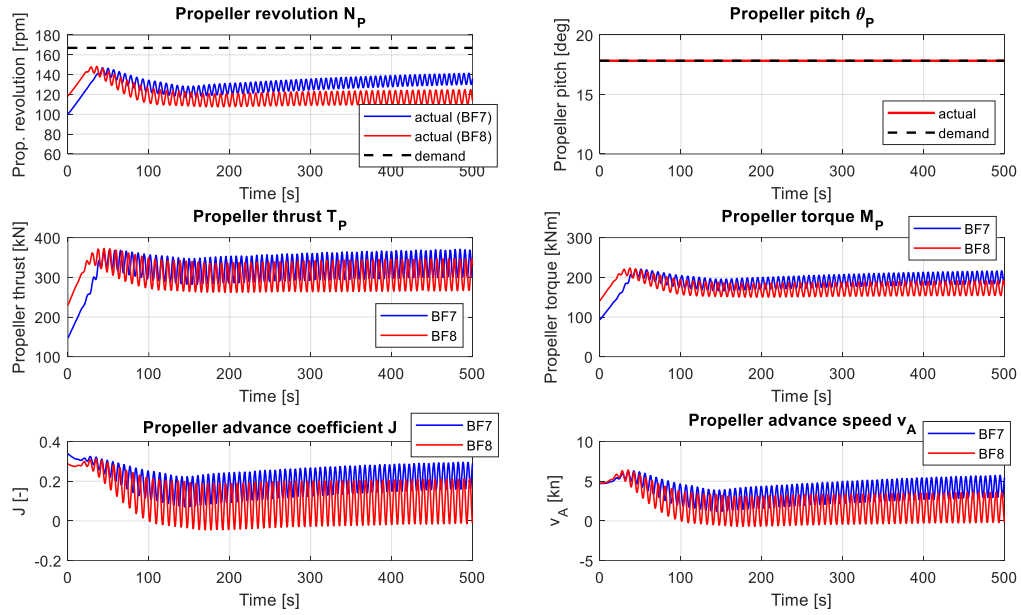
According to the simulation results, the ship is able to turn its bow to head sea in both sea states of BF7 and BF8, while in BF9 the ship is not able to make it before the forward speed drops to zero as shown in Figure 7.9 (a). Note that the ship initial forward speed has an influence on the ship turning behaviour. If the ship speed is too slow, the ship will not be able to turn its bow to head waves even in sea state of BF7. Although the ship with initial speed of 6.5 knots is able to turn to head waves in BF8, it cannot make it with a lower speed, for instance 2.6 knots, which is the maximum speed the ship can reach in head sea condition in BF8.

When the turning to head sea starts, the propeller revolution, thrust and torque will increase from the initial values (Figure 7.9 (b)), while the ship longitudinal velocity will drop due to the dominating increasing ship resistance (Figure 7.9 (c)). Both the engine mechanical and thermal loads will increase during ship turning to head sea (Figure 7.9 (d) to (f)), and the engine is thermally overloaded especially in BF8, while due to the fuel rack limiter the engine is not mechanically overloaded. When the ship has turned its bow to head waves, the ship velocity will increase again trying to accelerate slowly in head sea. The propeller load and engine load will

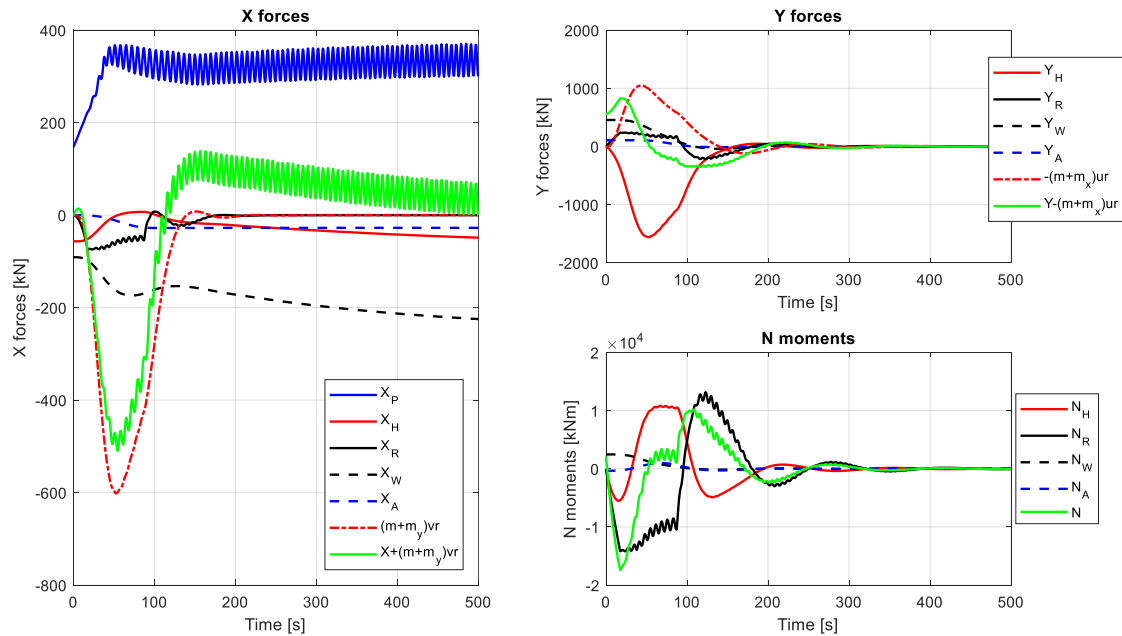
drop slightly and increase again slowly until reaching a stable condition sailing in head waves, which has been discussed in previous section.



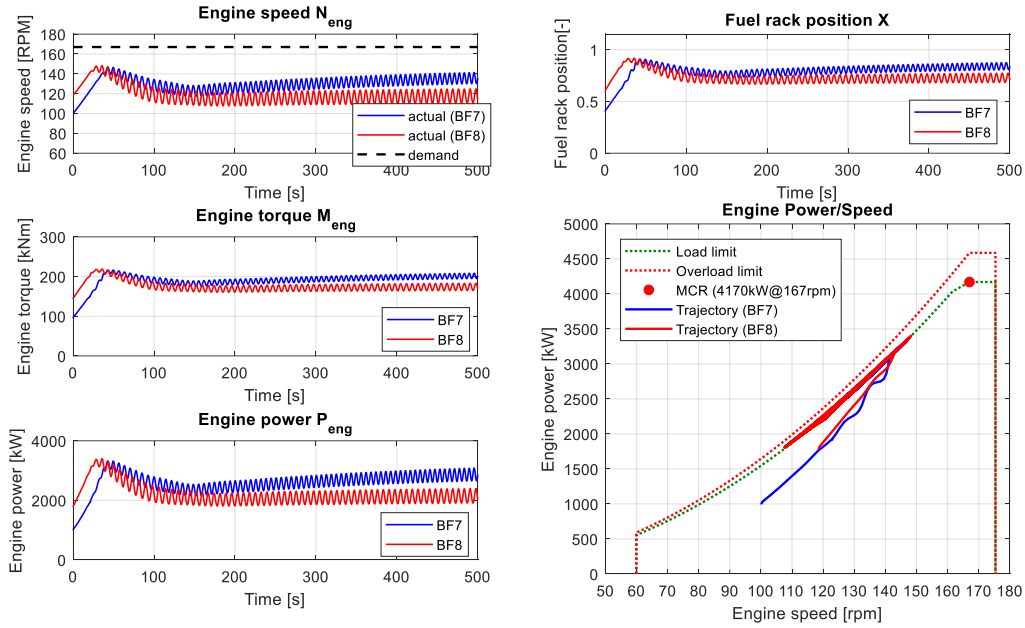
(a) Simulation results of ship



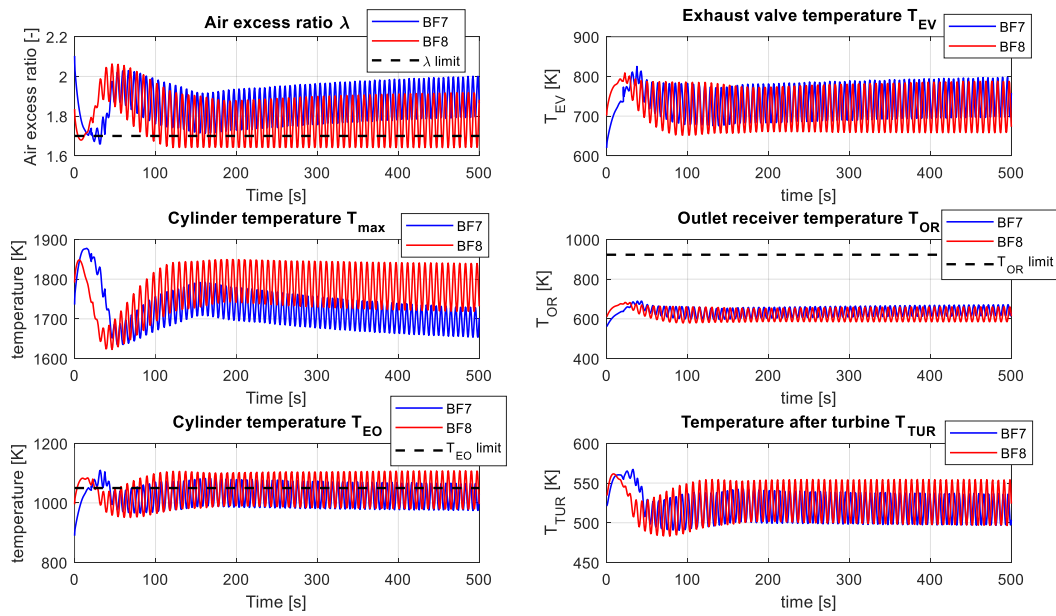
(b) Simulation results of propeller



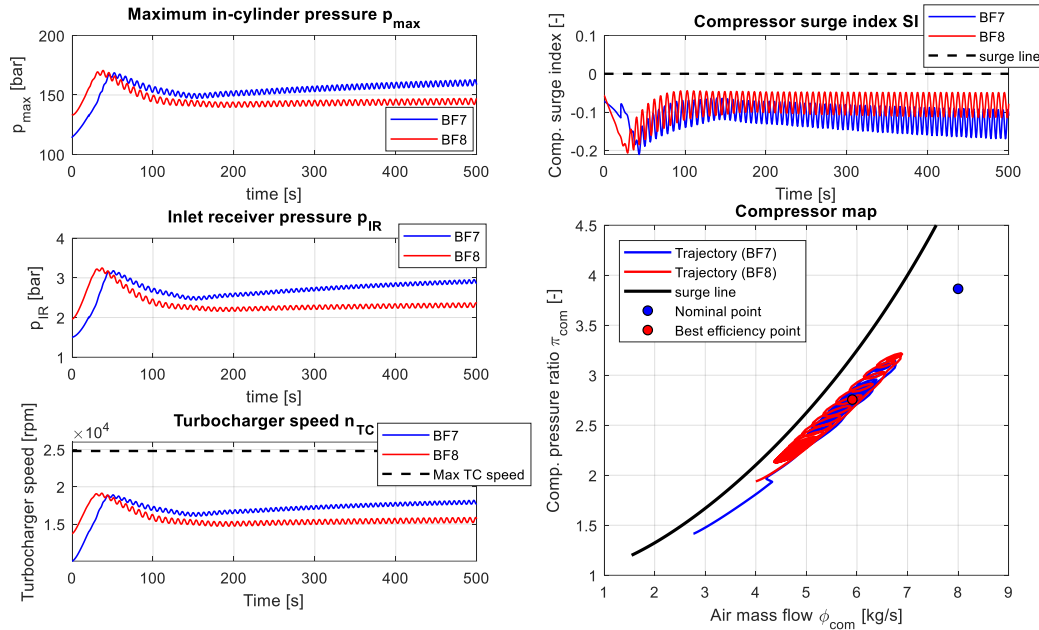
(c) Forces and moments during turning to head sea in BF7



(d) Engine speed, fuel rack, torque and power



(e) Engine thermal loading



(f) Maximum in-cylinder pressure and compressor behaviour  
Figure 7.9: Simulation results of ship turning to head sea

## 7.7 Influence of operational measures

### 7.7.1 Propeller pitch

For a controllable pitch propeller, the ship thrust limit will be different at different propeller pitches even if for the same engine power limit (Figure 7.10). The ship thrust envelopes with propeller pitches of 60%, 80% and 100% of the design pitch have been shown in Figure 7.10. When the ship is sailing in adverse weather conditions, due to the significant ship resistance increase caused by the wind and waves, the ship resistance curves will shift to the upper left side of the ship thrust envelope (Figure 7.10). In sea state of BF9, the ship head sea resistance is completely outside the thrust envelope when 100% design pitch has been applied. Taking sea state of BF8 for instance, in order to sail the ship at sustained speed of 5 knots without overloading the engine, the propeller pitch should be reduced accordingly to 80% design pitch, otherwise the ship can only sail at a maximum velocity of 2.6 knots. When the propeller pitch has been reduced, the engine can consequently run at a higher speed, which helps to reduce the engine thermal loading (Figure 7.11). However, reducing the propeller pitch should be careful, otherwise the engine could be more likely to encounter over-speeding, which could cause the engine shutting down.

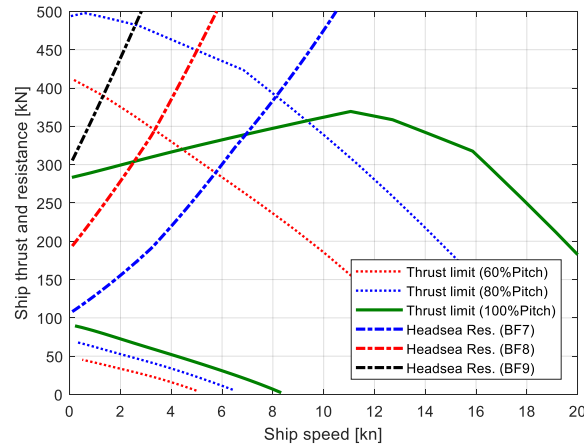


Figure 7.10: Ship thrust envelope with different propeller pitches

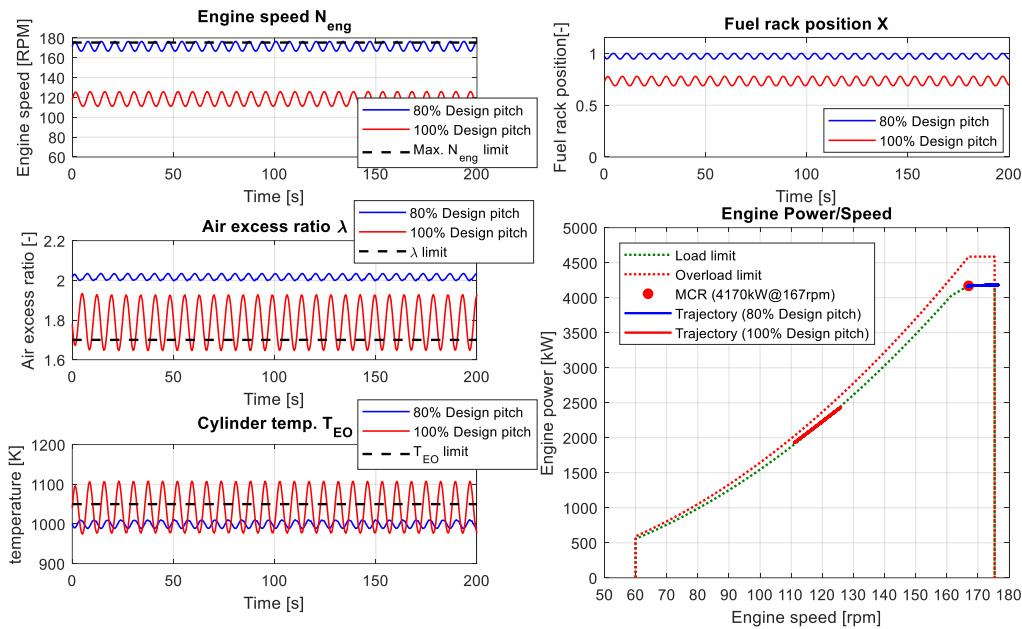


Figure 7.11: Influence of reducing propeller pitch on engine performance when ship sailing in head sea in BF8

## 7.7.2 Power-take-in (PTI)

If the main engine also provides power to a shaft generator (PTO, power-take-off), the ship thrust envelope will become smaller; while the thrust envelope will be enlarged if a shaft motor (if any) (PTI, power-take-in) also provides power to the propeller (Figure 7.12). The ship thrust envelope with PTO power of 350 kW, and PTI power of 500 kW and 1000 kW are shown in Figure 7.12. Still taking sea state of BF8 for instance, with a PTI power of 1000 kW, the ship is able to sail at maximum speed of 6 knots (at design propeller pitch) in head sea condition, otherwise the ship can only sail at a maximum speed of 2.6 knots without PTI. The operation of PTI also helps to increase the engine operating speed and thus to reduce the engine thermal loading (Figure 7.13).

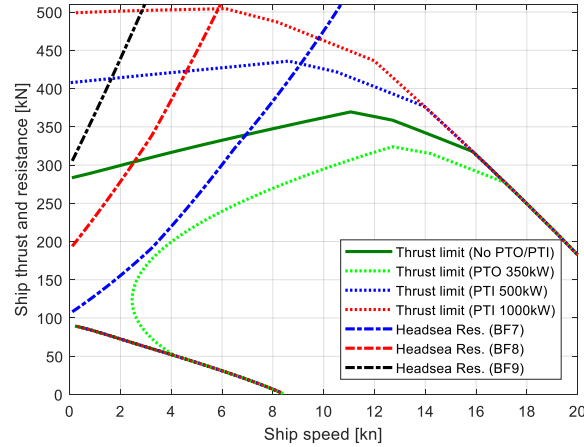


Figure 7.12: Ship thrust envelope with PTO/PTI

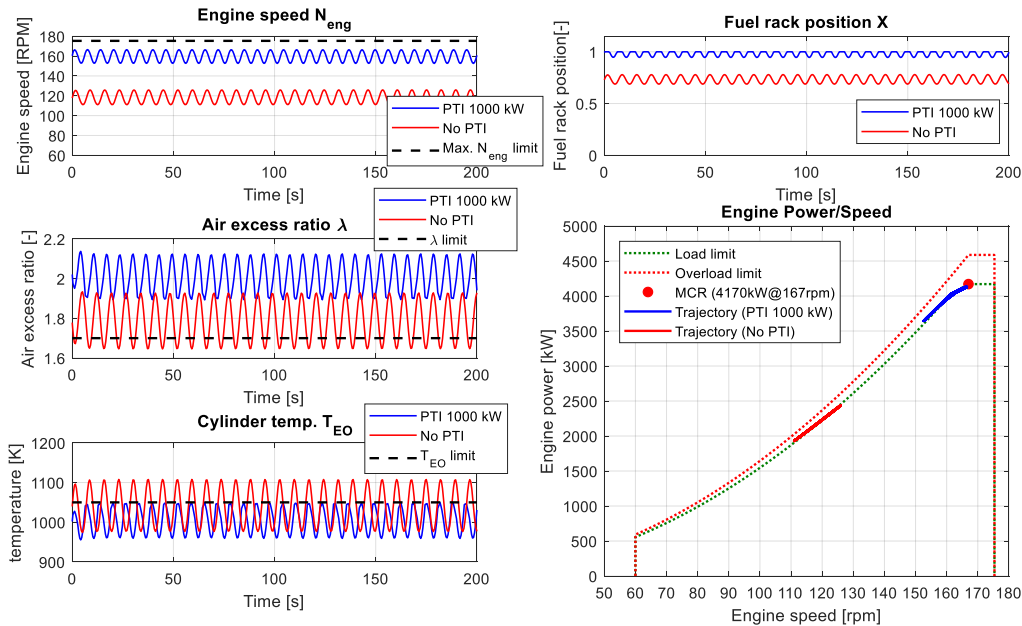


Figure 7.13: Influence of PTI on engine performance when ship sailing in head sea in BF8

## 7.8 Summary and Conclusions

The models of disturbances of wind and waves have been integrated in the ship propulsion and manoeuvring model. In particular, the wind and waves induced steady forces, which include the ship added resistance, steady lateral force and steady yaw moment, and the waves induced propeller wake variation have been taken into account. Based on the integrated ship propulsion, manoeuvring and sea state model, the ship propulsion and manoeuvring performance in adverse sea conditions (BF7 and BF8) has been investigated. The influences of the propeller pitch and the PTO/PTI on the ship thrust envelope have also been investigated.

According to the simulation results, the maximum advance speed the benchmark chemical tanker is able to sail in head sea in sea state of BF7 is 7 knots, while in BF8 the maximum advance speed is 2.6 knots (but the engine will be highly thermally overloaded), and in BF9 the

ship is not able to move forward at all. With an initial ship speed of 6.5 knots, the ship is able to turn to head wind and waves in both sea states of BF7 and BF8, while it cannot turn to head sea in BF9 before the ship speed drops to zero. According to the current 2013 interim minimum power guidelines, the specified adverse sea condition for the benchmark ship is sea state of BF7; and according to the level 2 assessment of the guidelines, the required ship advance speed is 6.4 knots. So, the benchmark ship meets the requirement of the level 2 assessment of the current guidelines, although it is an underpowered ship according to the level 1 assessment of the guidelines as explained in Chapter 6. Note that, as mentioned previously both the level 1 and level 2 assessments of the current guidelines are only applicable for ships with capacity over 20,000 DWT, although in this thesis for the moment it is assumed that the guidelines are also applicable for the benchmark chemical tanker that has a capacity of 13,000 DWT. However, the contradictory results of the assessments of level 1 and level 2 for the benchmark chemical tanker shows the necessity of a proper minimum power guidelines for ships with capacity less than 20,000 DWT.

The wake fluctuation due to waves will cause fluctuations in propeller torque and thrust. Although the oscillating propeller thrust hardly has any influence on the ship motions due to the relatively large ship inertia, the fluctuating propeller torque does have notable impacts on the engine behaviour. The fluctuating propeller wake will finally cause the fluctuations in engine speed, torque and thermal loading. Due to high sea states, for instance BF8, the engine could be thermally overloaded by the combined effects of the increasing steady loads and the fluctuating loads, even though the engine power or torque trajectories are still within the static operating envelope.

When transforming the engine power/revolution envelope to ship thrust/velocity envelope, for the same engine envelope, using different propeller or different propeller pitch will lead to a different ship thrust envelope. For the same ship velocity, the engine could more easily exceed the thermal loading limit at high propeller pitches and overspeed at low pitches. That is why a good matching between the engine and propeller, and a good control of the engine and propeller especially under dynamic operations and/or in adverse weather conditions are very important from the operational safety point of view. A shaft generator (power-take-off, PTO) will narrow the ship thrust/velocity envelope; however, if the shaft generator can also work as a shaft motor (power-take-in, PTI) the ship thrust envelope can be widened. So, the shaft generator/motor can work as a generator in PTO mode when the ship sails in normal sea conditions for a better energy efficiency, while work as a motor in PTI mode when the ship needs more propulsion power especially in adverse weather conditions for a better operational safety of both the engine and the ship.





## 8 Suggestions on Amendments of IMO's EEDI

### 8.1 Introduction

The intent of EEDI (Energy Efficiency Design Index) is to stimulate innovation and technical development of all the components, including well-designed hull forms, engines, propellers, etc., that can contribute to more energy efficient ship designs. Nevertheless, recognising its usefulness of increasing the awareness of energy efficient ship designs, the weaknesses of the current EEDI regulations could have been undermining the expected effects, i.e., reducing CO<sub>2</sub> emissions from ships. At the same time, it has caused the safety concerns with respect to leading to possible underpower ships in adverse weather. So, many suggestions for amending the current EEDI regulations from various aspects have been proposed by different researchers. In (Lindstad et al., 2019), it is suggested that a threshold of EEDI for realistic sea conditions ('weather EEDI') should be included in addition to the current requirement on EEDI for only calm water conditions. According to this suggestion, ship designs must satisfy criteria for both calm water and real sea conditions, otherwise, ship designers could be tempted to improve the ship performance in only calm water rather than in real sea conditions. In (Psaraftis, 2019b), it is proposed that the reference ship speed should also be introduced into the EEDI reference line formula, which currently includes only ship size (DWT) and is independent of ship speed. According to this proposal, simply reducing the ship design speed (thus installed engine power) to comply with the EEDI requirements will not be that easy any more, as the required EEDI will also decrease when reducing the ship design speed. In (Trivyza et al., 2020), the following recommendations are proposed to improve the current EEDI: (1) a more realistic (ship) operating profile and more than one operating points of the engine should be considered to express the ship performance more realistically; (2) all the ship energy systems should be included; (3) the (ultimate) greenhouse warming impacts of ships should be

considered, so, not only CO<sub>2</sub> emissions but also methane and other equivalent carbon emissions should be taken into account.

In this chapter, reflecting on the research that has been done in this dissertation as well as those from literature that are reviewed above, some suggestions on amendments of IMO's current EEDI regulations will be proposed.

## 8.2 Recommended EEDI formula

The current formula calculating the attained EEDI of ships (IMO, 2018) is shown in equation (8.1). However, in this thesis, to explain the idea of the suggestions to improve the current EEDI formula in a simple way, the simplest form of the EEDI formula will be used.

$$\frac{\left( \prod_{j=1}^n f_j \right) \left( \sum_{i=1}^{nME} P_{ME(i)} \cdot sfc_{ME(i)} \cdot C_{FME(i)} \right) + \left( P_{AE} \cdot sfc_{AE} \cdot C_{FAE} \right) + \left( \left( \prod_{j=1}^n f_j \right) \cdot \sum_{i=1}^{nPTI} P_{PTI(i)} - \sum_{i=1}^{neff} f_{eff(i)} \cdot P_{AE_{eff(i)}} \right) \cdot sfc_{AE} \cdot C_{FAE} - \left( \sum_{i=1}^{neff} f_{eff(i)} \cdot P_{eff(i)} \cdot sfc_{ME(i)} \cdot C_{FME(i)} \right)}{f_i \cdot f_c \cdot Capacity \cdot f_w \cdot V_{ref}} \quad (8.1)$$

The simplest form of the current EEDI formula is as following:

$$EEDI = \frac{P_{ME} \cdot sfc \cdot C_F}{DWT \cdot V_{ref}} \quad (8.2)$$

Where,  $P_{ME}$  is the main engine power at 75% MCR, (kW);  $sfc$  is the specific fuel consumption of the engine at 75% MCR power, (g/kWh);  $C_F$  is the nondimensional conversion factor between fuel consumption and CO<sub>2</sub> emission, (-);  $DWT$  is the ship deadweight tonnage representing the capacity of the ship, (ton);  $V_{ref}$  is the reference ship velocity corresponding to the engine power at 75% MCR in calm water condition, (kn).

According to the current EEDI, the engine power  $P_{ME}$  in the numerator in equation (8.2) is determined by the rated installed power  $P_{MCR}$  of the main engine, i.e.,  $P_{ME} = 75\% P_{MCR}$ . Then, the reference ship speed  $V_{ref}$  can be determined from the 'Main Engine Power – Ship Velocity' curve in calm water condition as illustrated in Figure 8.1. When the engine power and the corresponding reference ship speed are determined, they are used to calculate the attained EEDI of the ship by equation (8.2), or actually equation (8.1) in its expended form.

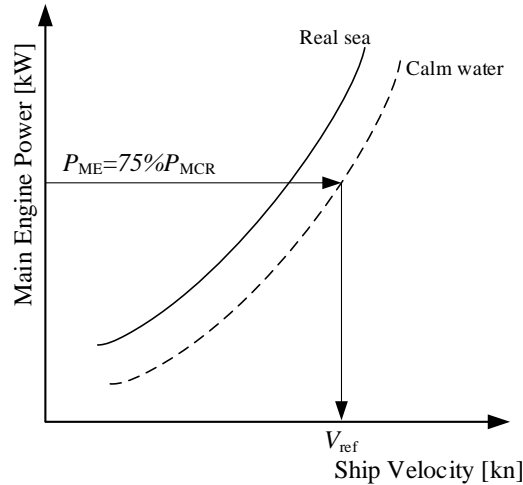


Figure 8.1: Current EEDI (from installed engine power to design ship speed)

Nevertheless, as explained previously, a representative ship operating profile (containing multiple weighted ship velocities) and multiple weighted engine operating points should be included when calculating EEDI in a more realistic way. So, in this thesis, the recommended EEDI formula in its simplified form is as following:

$$EEDI = \frac{C_F \cdot \sum_i P_{ME,i} \cdot sfc_i \cdot wf_i}{DWT \cdot \sum_i V_{ref,i} \cdot wf_i} \quad (8.3)$$

Where,  $V_{ref,i}$  are the reference ship operational speeds (in real sea conditions) that are determined by the ship design speed and the predetermined standardised operational profile for certain ship types (to be elaborated later), (kn);  $wf_i$  are the corresponding weighting factors for different reference ship operational speeds, (-);  $P_{ME,i}$  are the engine powers corresponding to the reference ship operational speeds (in real sea conditions), (kW);  $sfc_i$  are the engine specific fuel consumption corresponding to the engine powers at different operating points, (g/kWh).

The weighting factors  $wf_i$  should be determined by the running time  $\Delta t_i$  for each operating condition as a percentage of the total running time  $\Delta t_{total}$  of the engine and ship based on a predetermined operating profile for a certain ship type.

$$wf_i = \frac{\Delta t_i}{\Delta t_{total}} = \frac{\Delta t_i}{\sum_i \Delta t_i} \quad (8.4)$$

The idea for this proposal is that the attained EEDI of the ship is calculated using the engine powers and ship reference speeds, etc., that are determined from the load side (ship operational profile and ship-propeller-engine matching characteristics in real sea conditions) rather than the engine capacity (installed maximum engine power, MCR)\*. According to the proposal, the ship could be designed with a high design speed under service conditions, but the attained EEDI of the ship is calculated using lower representative operational speeds with higher weighting factors. So, to reduce the attained EEDI, the ship is allowed to have a lower design speed and lower operational speeds, but no necessarily a lower installed engine MCR power. In other words, the ship designer is able to select a sufficiently large engine margin and thus a large engine MCR power to guarantee that the engine is able to provide sufficient power for ship propulsion and manoeuvring in adverse sea conditions, without worrying about a high EEDI the ship may get due to the large installed engine MCR power. Note that, the important assumption of this proposal is that the ship operators will not purposefully use the reserved engine margin (“safety margin”) in normal operations. There are multiple ways to prevent the possible “bad behaviour” of the ship operators to ensure the additional engine power is not used to sail the ship too fast. For instance, according to the idea proposed in (Mundt et al., 2019), some technical measures could be adopted on the engine to limit the engine power in normal operations, while pressing an “emergency button” to use the reserved power only in emergency

---

\* This idea is contributed by Professor Douwe Stapersma (retired), who is the former supervisor of this PhD research project.

situations, such as in adverse sea conditions.

According to the proposed amendments, the calculation procedure of the attained EEDI of ships is explained as follows:

**Step 0:** Standardising ship operational profile;

The standardised representative ship operational profile for certain ship types operating in certain sea areas (with possibly different dominant sea states) should be defined by IMO, as what has been done in the car industry (Lindstad et al., 2019). In the proposed standardised ship operational profile shown in Table 8.1, the representative ship operational speeds are normalised by the slow steaming factor  $x_i$ , which are the ratios between the operational speeds and the design ship speed. The running times that the ship sails at certain speeds are normalised by the weighting factor  $wf_i$ , which are the percentages of time the ship running at certain speeds over the total time of the ship voyage. The real sea conditions (service conditions) where the ships operate in certain sea areas are normalised by the sea margins  $SM$ .

Table 8.1: Standardised ship operational profile for certain ship types operating in certain sea areas (proposed to be defined by IMO)

| Operating Points | Slow steaming factor<br>$x_i = \frac{V_{operation}}{V_{design}} \cdot 100\%$ | Weighting factor<br>$wf_i = \frac{\Delta t_i}{\Delta t_{total}} \cdot 100\%$ | Sea Margin<br>$SM = \frac{P_{service} - P_{trial}}{P_{trial}} \cdot 100\%$ |
|------------------|--|--|--|
| 1                | $x_1$  | $wf_1$   | $SM$   |
| 2                | $x_2$  | $wf_2$   |  |
| ...              | ...  | ...  |  |
| i                | $x_i$  | $wf_i$   |  |

**Step 1:** Determining the design ship speed  $V_{design}$ ;

The design ship speed  $V_{design}$  is determined by the engine power at CSR (continuous service rating)  $P_{CSR}$  using the ‘Main Engine Power – Ship Velocity’ curve under service condition, i.e., real sea condition, as illustrated in Figure 8.2.

**Step 2:** Determining the representative operational ship speeds  $V_{ref,i}$ ;

The representative operational ship speeds  $V_{ref,i}$  are calculated from the maximum (or design) ship speed  $V_{design}$  by multiplying different ‘slow steaming factors’  $x_i$  ( $x_i \leq 100\%$ ), i.e.,  $V_{ref,i} = x_i \cdot V_{design}$ , based on the predetermined operational profile for the certain ship types.

**Step 3:** Calculating the engine powers  $P_{ME,i}$  from the operational ship speeds;

The corresponding engine powers  $P_{ME,i}$  are determined by the operational ship speeds  $V_{ref,i}$  using the ‘Main Engine Power – Ship Velocity’ curve in real sea condition as illustrated in Figure 8.2.

**Step 4:** Determining the weighting factors  $wf_i$ ;

The weighting factors  $wf_i$  for different operational ship speeds  $V_{ref,i}$  and consequently for different engine operating points ( $P_{ME,i}$ ,  $sfc_i$ ) are determined by the time percentages of the ship running at certain speeds over the total time of the ship voyage based on the predetermined ship

operational profile.

**Step 5:** Calculating the attained EEDI of the ship;

The attained EEDI of the ship for real sea conditions is calculated using the representative operational ship speeds  $V_{ref,i}$  and the corresponding engine powers  $P_{ME,i}$ , specific fuel consumption  $sfc_i$  and the weighting factors  $wf_i$  by equation (8.3), which should be expanded to a detailed form like equation (8.1).

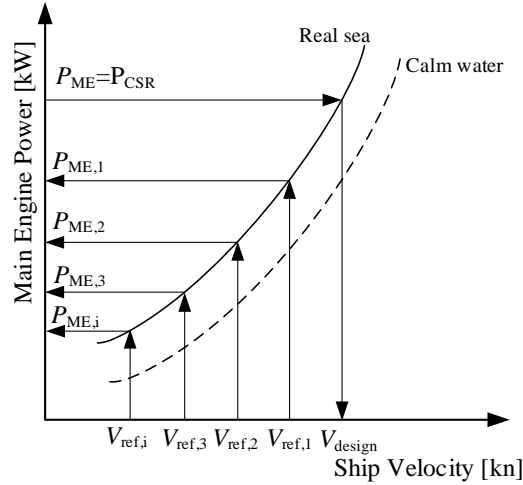


Figure 8.2: Recommended EEDI (from operational ship speeds to operational engine powers)

Note that, this thesis only provides a general idea on how to improve the current EEDI formula as explained above. The details of, for example, how to determine the representative operational profile for certain ship types; how to choose the representative ship operational speeds; and how to determine the weighting factors; etc., are left out of scope of this dissertation.

### 8.3 Minimum propulsion power guidelines

The above introduced proposal for amending the current EEDI formula tries to make the EEDI calculation more realistic and representative when estimating ship performance at the design stage. Moreover, it can also partly solve the current EEDI weakness with respect to the issues of underpowered ships, because the ship designer is able to select a sufficiently large engine margin according to the proposal. However, with the introduced proposal, ship owners and designers could still choose to reduce the installed engine power thus the ship design speed and consequently the reference ship operational speeds, to reduce the EEDI. To really prevent ship designers to take this easy solution instead of innovative measures, the proposal to reduce the required EEDI for ships having low design speed as recommend in (Psaraftis, 2019b) could be considered. However, reducing the ship design speed should be allowed as an option to reduce EEDI, as long as the installed engine power meets the minimum propulsion power requirements. So, the minimum propulsion power guidelines are still necessary and important, despite of the fact that the current minimum power guidelines have not yet been finalized to date and the guideline for ships having capacity less than 20,000 DWT is still not introduced.

According to the current minimum power guidelines, the level 1 assessment ('minimum

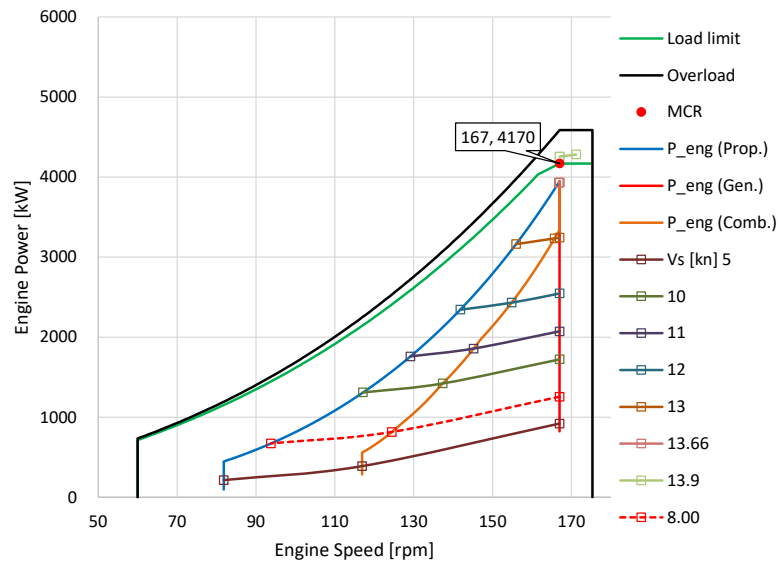
power lines assessment’) considers only the minimum installed propulsion power (MEPC, 2017). It is required that the total installed MCR power of all main propulsion engines should not be less than the minimum power line value. Although level 1 assessment is easy to apply, it has no requirements on minimum ship thrust and minimum ship speed in adverse sea conditions. The available propeller thrust and the attainable ship speed, which have the direct and dominant impact on ship operational safety in adverse weather conditions, are in fact limited by the available torque that the engine is able to deliver at low engine speeds due to the torque-speed limit (Reduced torque limit), rather than the installed maximum engine power (MCR). The level 2 assessment (‘simplified assessment’) has considered the available propeller thrust and the minimum ship speed that the ship needs to maintain in adverse sea conditions. In level 2 assessment, the torque-speed limit of the engine is taken into account when estimating the available propeller thrust in adverse weather. However, only static engine load limits rather than dynamic load limits have been considered in the present level 2 assessment. According to the research in this dissertation especially in Chapter 7, even though the engine power or torque are still within the static load limits, the engine could still be thermally overloaded due to the dynamic loads caused by the waves and/or ship manoeuvring. So, it is proposed that the engine dynamic load limits should be considered when evaluating the engine and ship operational safety in adverse sea conditions, or at least an extra and reasonable margin for the engine dynamic overloading limits should be introduced in the assessment. This extra engine margin for dynamic overloading limits should be considered when selecting the total engine margin and thus the installed maximum engine power, of which more freedom now is given to the ship owners and designers by the proposed EEDI calculation as introduced previously.

## **8.4 Installing a larger engine on the benchmark ship**

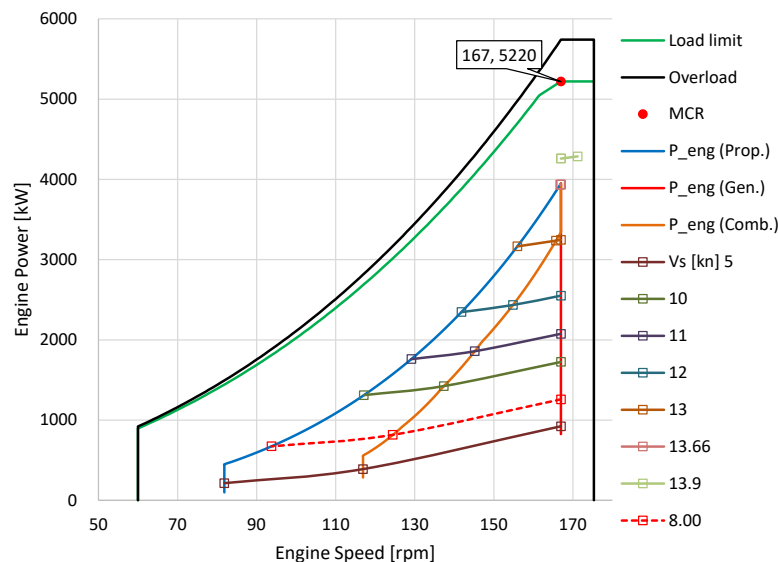
The benchmark 13000DWT chemical tanker will be used as an example to further (better) explain the advantages of the proposed amendments of EEDI. As introduced in previous chapters, the benchmark ship has installed a low speed 2-stroke diesel engine with MCR of 4170kW@167rpm (Engine 1) working as the main engine driving a controllable pitch propeller and a shaft generator. In this section, the propulsion system of the chemical tanker will be upgraded by installing a larger engine with MCR of 5220kW@167rpm (Engine 2, which comes from the same engine family) driving the same CP propeller and the same shaft generator.

The operation results in terms of engine power and engine speed under different propulsion control modes at various ship speeds when matching the propulsion system with different engines (Engine 1 and Engine 2) are presented in Figure 8.3(a) and Figure 8.3(b). Note that, the sea condition for the operation is set as normal, i.e., with 15% of sea margin; and the PTO is switched off, so, the engine only provides power to the propeller.

According to the results shown in Figure 8.3, the two engines provide the same operational power at the same engine speed when the ship sails at the same ship speeds under the same propulsion control modes. In other words, if the ship mission profile is the same, the engine operational power will be the same. However, Engine 2 has a larger reserved power for ship acceleration and operation in heavy loading conditions.



(a) Matching the propulsion system with Engine 1 (MCR: 4170kW@167rpm)



(b) Matching the propulsion system with Engine 2 (MCR: 5220kW@167rpm)

Figure 8.3: Matching the propulsion system of chemical tanker with different engines

#### 8.4.1 EEDI of the ship with larger engine

Assume that the two engines have the same specific fuel consumption at nominal operating point (MCR). Further assume that the trends of specific fuel consumption of the two engines are the same; in other words, the percentages of the specific fuel consumption (ratios of values at part loads to that at nominal loads) at different percentages of load are the same for the two engines as shown in Table 8.2, Table 8.3 and Figure 8.4. In addition, the two engines use the same type of fuel.

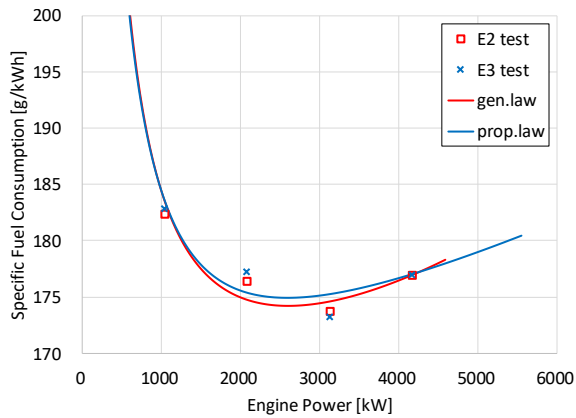


Table 8.2: Fuel consumption of Engine 1 at different operating points

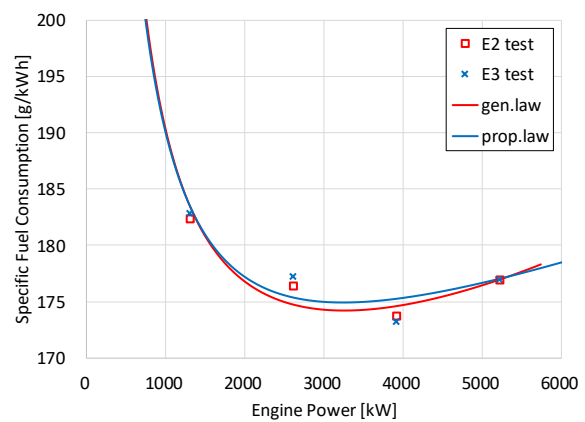
| Engine 1                   | Test Cycles | Power [%] | sfc [%] | sfc [g/kWh] | Power [kW] | fc [kg/h] |
|----------------------------|-------------|-----------|---------|-------------|------------|-----------|
| MCR:<br>4170kW@167rpm      | E2          | 100%      | 100.00% | 177.00      | 4170       | 738.09    |
|                            |             | 75%       | 98.17%  | 173.76      | 3127.5     | 543.44    |
|                            |             | 50%       | 99.68%  | 176.43      | 2085       | 367.86    |
|                            |             | 25%       | 103.05% | 182.40      | 1042.5     | 190.15    |
| $sfc_{nom}$ :<br>177 g/kWh | E3          | 100%      | 100.00% | 177.00      | 4170       | 738.09    |
|                            |             | 75%       | 97.86%  | 173.21      | 3127.5     | 541.72    |
|                            |             | 50%       | 100.14% | 177.25      | 2085       | 369.56    |
|                            |             | 25%       | 103.28% | 182.81      | 1042.5     | 190.57    |

Table 8.3: Fuel consumption of Engine 2 at different operating points

| Engine 2                   | Test Cycles | Power [%] | sfc [%] | sfc [g/kWh] | Power [kW] | fc [kg/h] |
|----------------------------|-------------|-----------|---------|-------------|------------|-----------|
| MCR:<br>5220kW@167rpm      | E2          | 100%      | 100.00% | 177.00      | 5220       | 923.94    |
|                            |             | 75%       | 98.17%  | 173.76      | 3915       | 680.27    |
|                            |             | 50%       | 99.68%  | 176.43      | 2610       | 460.49    |
|                            |             | 25%       | 103.05% | 182.40      | 1305       | 238.03    |
| $sfc_{nom}$ :<br>177 g/kWh | E3          | 100%      | 100.00% | 177.00      | 5220       | 923.94    |
|                            |             | 75%       | 97.86%  | 173.21      | 3915       | 678.13    |
|                            |             | 50%       | 100.14% | 177.25      | 2610       | 462.67    |
|                            |             | 25%       | 103.28% | 182.81      | 1305       | 238.56    |



(a) Specific fuel consumption of Engine 1



(b) Specific fuel consumption of Engine 2

Figure 8.4: Specific fuel consumption of the two engines

With the current EEDI regulation, if the installed engine (Engine 1) on the benchmark chemical tanker is replaced by the larger engine (Engine 2), the ship design speed (reference speed) will then increase from 13.30 knots to 14.40 knots, and as a result the attained EEDI of the ship will increase from 9.92 to 11.62, which cannot meet the EEDI requirement even for

phase 1 (11.28 gCO<sub>2</sub>/ton-mile) anymore. However, with the proposed amendments of EEDI calculation, the attained EEDI of the ship calculated based on the engine operational power and the corresponding ship operational speed (reference speed) in service conditions will be the same for the two cases, i.e., installing Engine 1 or Engine 2, if the defined ship operational profile remains unchanged. The reason for this is actually the same for the unchanged ship fuel consumption and energy effectiveness during actual ship operations as will be explained in the following section.

#### 8.4.2 Ship fuel consumption and energy effectiveness with larger engine

The fuel consumption and emissions performance of the chemical tanker installing different engines (Engine 1 or Engine 2) during actual operations, when sailing in normal sea condition (SM=15%), are compared with each other and presented in Figure 8.5-Figure 8.9. The fuel used by the main engine is heavy fuel oil (HFO) and the fuel for auxiliary engines is the marine diesel fuel (MDF). The operation setting is shown in Table 8.4.

Table 8.4: Operation setting at normal sea margin

| Propulsion Control<br>Modes | Generator Switch [On/Off] |            |
|-----------------------------|---------------------------|------------|
|                             | PTO                       | Aux.GenSet |
| Constant Speed              | On                        | Off        |
| Constant Pitch              | Off                       | On         |
| Combinator                  | Off                       | On         |

According to the results, the ship driven by Engine 2 has almost the same fuel index, CO<sub>2</sub> emission index, and energy conversion effectiveness compared to Engine 1, as shown in Figure 8.7, Figure 8.8 and Figure 8.9. Although the specific fuel consumption and specific CO<sub>2</sub> emission of Engine 2 are slightly higher especially at low ship speeds compared to Engine 1 (Figure 8.5 and Figure 8.6), the effects of those differences in specific fuel consumption and specific emissions on the overall performance of the whole power chain are nearly nothing if the ship operations keep the same. If the 'point value' of fuel index, emission indices and energy conversion effectiveness are the same, the 'mean value' indicators weighted over the ship operational profile will also be the same.

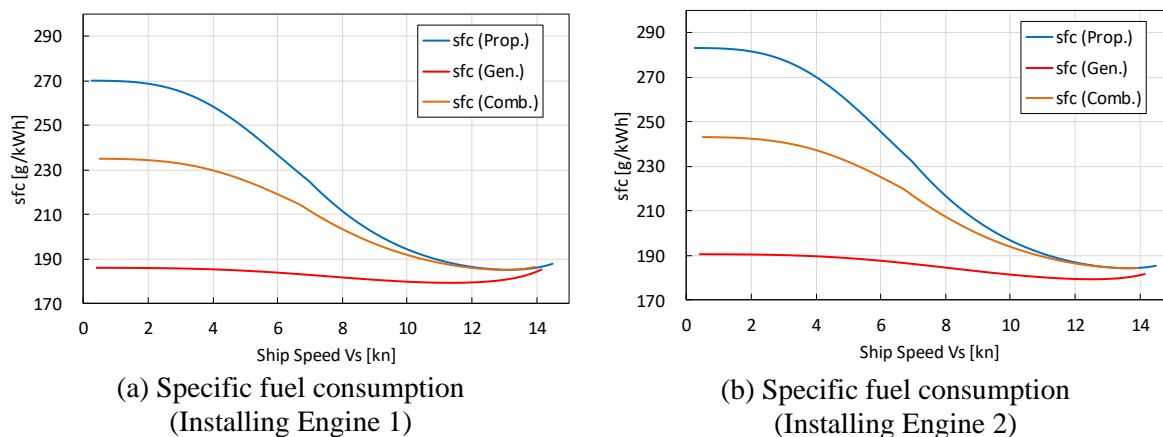
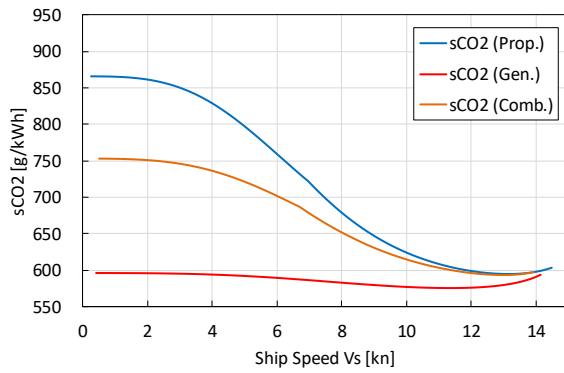
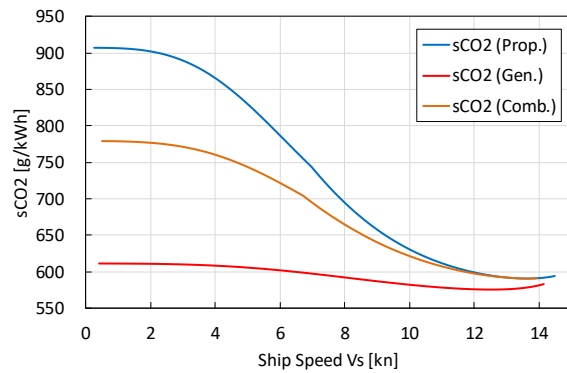


Figure 8.5: Specific fuel consumption (Operational results, SM=15%)

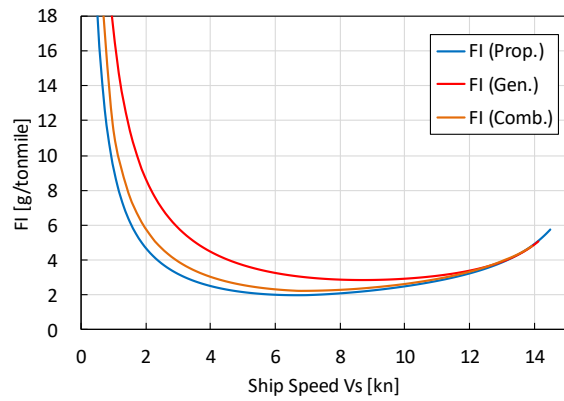


(a) Specific CO<sub>2</sub> emission  
(Installing Engine 1)

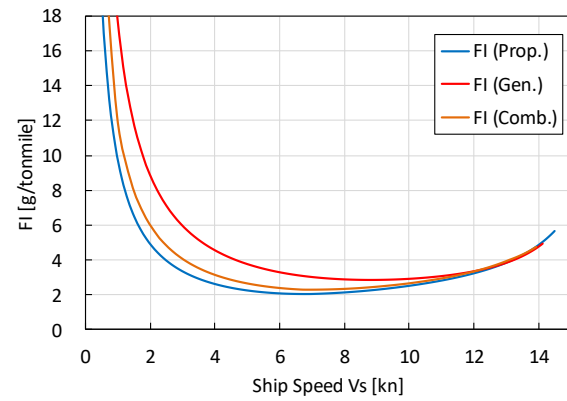


(b) Specific CO<sub>2</sub> emission  
(Installing Engine 2)

Figure 8.6: Specific CO<sub>2</sub> emission (Operational results, SM=15%)

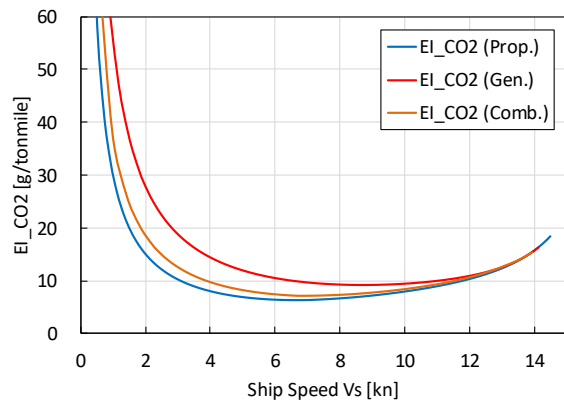


(a) Fuel index (Installing Engine 1)

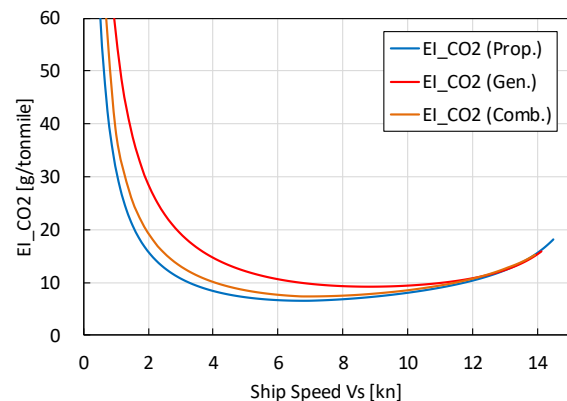


(b) Fuel index (Installing Engine 2)

Figure 8.7: Fuel index (Operational results, SM=15%)

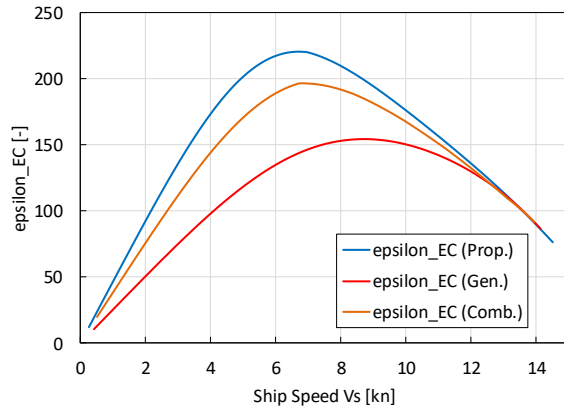


(a) CO<sub>2</sub> emission index (Installing Engine 1)

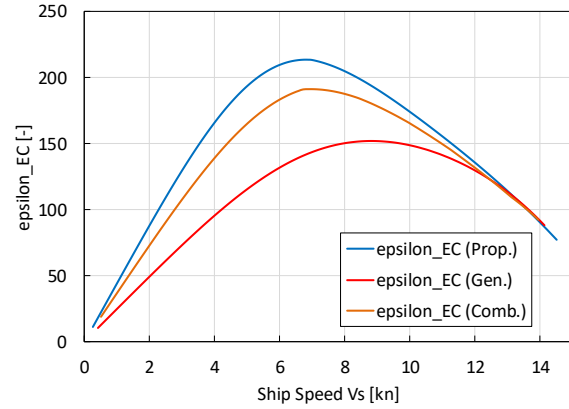


(b) CO<sub>2</sub> emission index (Installing Engine 2)

Figure 8.8: CO<sub>2</sub> emission index (Operational results, SM=15%)



(a) Energy conversion effectiveness  
(Installing Engine 1)

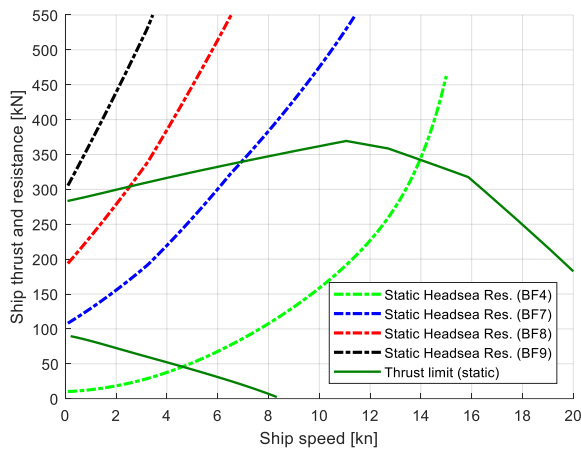


(b) Energy conversion effectiveness  
(Installing Engine 2)

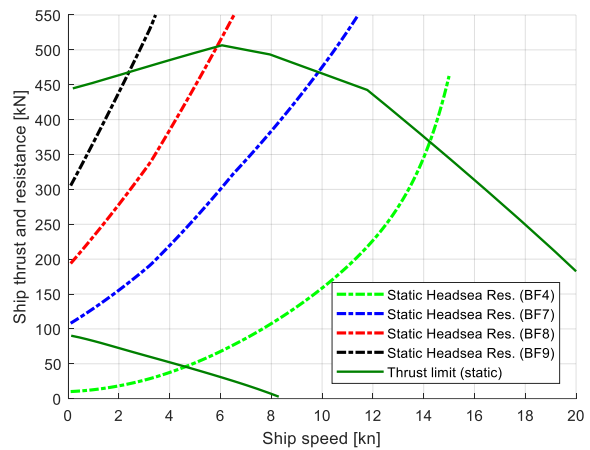
Figure 8.9: Energy conversion effectiveness (Operational results, SM=15%)

### 8.4.3 Ship propulsion capability in adverse sea with larger engine

The ship now has a larger thrust envelope when installing a larger engine as shown in Figure 8.10. Installing the larger engine (Engine 2), the maximum forward speed the ship is able to sail in head waves and wind is 10 knots in sea state of BF7 and 6 knots in BF8; while installing the smaller engine (Engine 1) the maximum forward ship speed is 7 knots in BF7 and 2.6 knots in BF8 as explained in Chapter 7. So, with the larger engine, the ship's propulsion capability and thus the ship operational safety especially in adverse sea conditions is improved.



(a) Ship thrust envelope  
(Installing Engine 1)



(b) Ship thrust envelope  
(Installing Engine 2)

Figure 8.10: Ship thrust envelope when installing different engines

## 8.5 Summary and Conclusions

As a reflection of the research in this dissertation, suggestions on amendments of IMO's current EEDI has been provided in this chapter. A proposal has been made on the formula calculating the attained EEDI of ships in a more realistic way, in which a representative ship

operating profile and multiple engine operating points are considered. The proposal for amending the current EEDI formula tries to make the EEDI calculation more realistic and representative when evaluating ship transport performance at the design stage. Moreover, it can also partly solve another weakness of the current EEDI with respect to the issues of underpowered ships, because the ship designer is able to install a larger engine by selecting a sufficiently large engine margin according to the proposal.

The concerns that, with the proposed EEDI regulation, the ship is able to install a larger engine with a larger engine margin so that it could sail at higher speeds (by using part of the reserved engine power) in actual operations (than the claimed design ship speed) thus producing more emissions over time, has also been addressed in this chapter.

The benchmark chemical tanker has been used as an example to further (better) explain the proposed idea for EEDI amendments. Through the example of the benchmark ship, two points are supposed to have been explained clearly. Firstly, with the proposed new EEDI formula, the ship is able to install an engine with a larger engine margin (thus a larger MCR power) but it will not produce more emissions during actual operation over time if the ship operational profile keeps the same (using theory from chapters 2 and 3). Secondly, installing an engine with a larger engine margin (thus a larger reserved engine power) will make the ship safer when operating in adverse sea conditions (using theory of chapter 7).

## 9 Conclusions and Recommendations

### 9.1 Addressing the research questions

In this thesis, the following main research question is addressed: *What is the transport performance of ocean-going cargo ships with small EEDI when sailing in realistic operating conditions; are these ships safe when sailing in heavy operating conditions; and, how to improve both the transport performance and operational safety of ocean-going cargo ships by using the short-term applicable ship propulsion options?*

To answer the main research question, the following sub-questions have been addressed.

#### **Q1. How to define and quantify the transport performance of cargo ships?**

The ship transport performance investigated in this thesis includes the energy conversion performance, fuel consumption performance and emission performance, which have been defined and quantified by three indicators, i.e., energy conversion effectiveness, fuel index, and emissions index (Chapter 2 and Chapter 3). The three indicators of ship transport performance are defined based on the analysis of energy conversion, fuel consumption and exhaust emissions processes in the ‘tank to wheel’ power chain of the ship propulsion and electric generation systems. The energy conversion effectiveness (nondimensional) is defined as a ratio of the fuel energy flow into the engines (J/s) and the ship mobility power indicating the ship deadweight transported at certain ship speeds (N·m/s). The fuel index (g/(ton·mile)) is defined as a ratio of the fuel consumption flow consumed by the engines (g/h) and the ship deadweight tonnage transported as certain ship speeds (ton·mile/h). The emission index (g/(ton·mile)) is defined as a ratio of the emissions flow emitted by the engines (g/h) and the ship deadweight tonnage transported as certain ship speeds (ton·mile/h). So, the energy conversion effectiveness is actually a benefit/cost ratio, while the fuel index and emission index are cost/benefit ratio. When taking the ship mission profiles into account, the mean energy conversion effectiveness, fuel index and emissions index, which are averaged over the whole voyage of the ship, are defined.

#### **Q2. What is the influence of various short-term applicable technical and operational**

***measures on the transport performance of cargo ships?***

The influences of the operational ship speed reduction, propulsion control, power-take-in/power-take-off, and using LNG as the fuel as well as the combination of these measures on the ship transport performance over the whole voyage have been systematically investigated in this thesis (Chapter 3). Reducing the ship average operational speed will effectively reduce both the fuel consumption and emissions of the ship over the voyage. Reducing the propeller revolution rather than the propeller pitch is more preferable for the operational ship speed reduction, as pitch reduction will reduce the propeller efficiency and consequently increase the fuel consumption. Generating the electric power by the shaft generator (PTO mode) rather than the auxiliary generator (Aux mode) will further reduce the fuel consumption while the NO<sub>x</sub> and HC emissions could increase. However, compared to the propulsion control modes, the electric generation modes have relatively minor influence on fuel consumption and emissions of the ship.

When the ship is sailing and manoeuvring in the coastal and port areas, providing the power for ship propulsion (PTI mode) and onboard electric loads by the auxiliary engines and shutting down the main engine will reduce the local NO<sub>x</sub> and HC emissions significantly while the fuel consumption and CO<sub>2</sub> emission will increase notably mainly due to the lower engine efficiency of the auxiliary engines. Using LNG (liquefied natural gas) as the fuel for both the main and auxiliary engines will reduce the NO<sub>x</sub> emission significantly compared to using HFO (heavy fuel oil) or MDF (marine diesel fuel). So, sailing the ship on LNG in close-to-port areas will produce much less local pollutant emissions. In particular, sailing the ship in PTI mode on LNG will further reduce the local pollutant emissions in coastal and port areas. The fuel consumption and CO<sub>2</sub> emission of the ship will also decrease notably over the whole voyage when sailing on LNG instead of HFO and MDF. However, the hydrocarbon (HC) emission is much higher when using LNG as a marine fuel than traditional diesel fuel due to the methane (CH<sub>4</sub>) slip and unburnt methane during engine operations.

***Q3. How to improve ship transport performance by using the short-term applicable ship propulsion options?***

To effectively reduce the fuel consumption and greenhouse gas emissions, the operational ship speed reduction and optimisation of the ship mission profiles over the voyage should still be the primary measures for the ocean-going cargo ships in short term. Although using LNG as the marine fuel helps to reduce the CO<sub>2</sub> emissions and especially pollutant emissions (such as NO<sub>x</sub>), it may have a worse impact on climate change (global warming) when taking the life-cycle emissions of natural gas, which is actually a more potent greenhouse gas than CO<sub>2</sub>, into consideration. In order to reduce the ship emissions significantly when manoeuvring in close-to-port areas, the ship should be driven by the auxiliary engines through PTI mode. As the methane emissions of LNG have no direct health effects on humans, from reducing the local pollutions point of view, driving the ship in PTI mode and using LNG as the fuel when manoeuvring in close-to-port areas is a better choice. It is clear either way that methane emissions from LNG engines should be minimised as much as possible.

***Q4. How to define and quantify ship operational safety?***

The Operational safety investigated in this thesis includes both engine operational safety and ship operational safety. The engine operational safety is indicated by the engine thermal loading, mechanical loading, compressor surge and engine over-speeding, which could lead to engine failure. The ship operational safety is indicated by the ship thrust availability especially when operating in adverse sea conditions. Based on the analysis of the engine and ship operational limits, the ship operational safety has been defined and quantified using the engine mechanical and thermal loading limits, engine maximum speed limits, compressor surge limit and ship thrust limit (Chapter 6). The engine torque (or mean effective pressure) and the maximum in-cylinder pressure are selected as the indicators of engine mechanical loading. The air excess ratio, the maximum in-cylinder temperature, and especially the in-cylinder temperature just before exhaust valve opening (EO) are the effective indicators for engine thermal loading. The compressor surge index, which is the nondimensional distance between the compressor operating point and the surge line, has been defined as the indicator of compressor surge. Although the engine operational limits have the dominate impacts, the available ship thrust is in the end the real limiting factor of the ship operational safety in adverse sea conditions.

***Q5. What is the influence of various ship operations and adverse sea conditions on ship operational safety?***

The engine dynamic behaviour during ship acceleration, deceleration, crash stop, and turning in normal sea condition (15% sea margin) has been investigated in this thesis (Chapter 6). The ship propulsion and manoeuvring performance when sailing in head sea and turning to head sea in adverse sea conditions (BF7 and BF8) has been investigated (Chapter 7). The influences of propeller pitch and PTO/PTI on the ship thrust limit and engine behaviour have also been investigated.

During the transient process of ship acceleration, the air excess ratio will drop, and the maximum in-cylinder temperature and in-cylinder temperature just before EO (exhaust valve open) will go up; while the (negative) compressor index will drop, i.e., the compressor operating point moves away from the surge line. So, during ship acceleration the engine could be thermally overloaded, but the compressor will not surge. During the transient process of ship deceleration, contrary to that of the ship acceleration, the air excess ratio will increase, and the maximum in-cylinder temperature and in-cylinder temperature just before EO (exhaust valve open) will drop; while the (negative) compressor index will go up. So, during ship deceleration the engine will not be thermally overloaded, but the compressor could surge. During the transient process of ship crash stop, the engine mechanical and thermal loads will first drop and then go up again. However, before the engine is thermally overloaded, the compressor will surge first when the engine load drops, making the engine dynamic behaviour during the ship crash stop even worse. During ship turning, similar to that in ship acceleration, both the mechanical and thermal loads will increase, while the compressor surge index will drop. So, the engine could be mechanically and/or thermally overloaded, but the compressor will not surge.

In high sea state, for instance BF8, the engine could be thermally overloaded by the combined effects of the increasing steady loads and the fluctuating loads. The increasing steady



loads are caused by the wind and waves induced steady forces on the ship, while the fluctuating engine loads are caused the propeller wake variation due to waves. Although the oscillating propeller thrust hardly has any influence on the ship motions due to the relatively big ship inertia, the fluctuating propeller torque does have notable impacts on the engine behaviour, i.e., engine speed, torque and thermal loading.

For the same engine operational limits, using different propeller or different propeller pitch will lead to a different ship thrust limit. When the propeller pitch has been reduced, the engine can consequently run at a higher speed, which helps to reduce the engine thermal loading. However, when reducing the propeller pitch the engine could be more likely to encounter over-speeding, which could cause the engine shutting down. A shaft generator (power-take-off, PTO) will narrow the ship thrust envelope, while a shaft motor (power-take-in, PTI) will widen the ship thrust envelop. The operation of PTI also helps to increase the engine operating speed and thus to reduce the engine thermal loading.

***Q6. How to improve ship operational safety by using the short-term applicable ship propulsion options?***

To protect the engine from overloading, compressor surge and over-speeding during dynamic ship operations and/or in high sea states, the engine and propeller should be carefully controlled. The shaft generator/motor can work as a motor in PTI mode when the ship needs more propulsion power especially in (heavy) adverse weather conditions for a better operational safety of both the engine and ship.

**A brief answer to the main research question:**

When assessing the ship transport performance, the ship's representative and realistic operation profile over the actual voyage as well as the 'tank to wheel' power chain of the ship should be taken into account. When assessing the ship operational safety in adverse sea, the dynamic engine behaviour, which is the most influencing limiting factor of the available ship thrust, should be taken into account. The influence of PTO/PTI and propeller should also be considered as in the end it is the ship thrust rather than the engine power that drives the ship sailing and manoeuvring in adverse sea condition. In the short-term future, a PTO/PTI system together with using LNG as the fuel for the engines, which forms a hybrid electric power generation system and a hybrid propulsion system, will help improve both the ship transport performance in normal sea and the ship operational safety in (heavy) adverse sea conditions.

## **9.2 Recommendations for future research**

The hybrid propulsion and using LNG as the marine fuel have been considered as the promising short-term applicable measures for improving both the transport performance and the operational safety of the ocean-going cargo ships. The following topics relating to the hybrid propulsion and using LNG as the fuel are recommended for future research:

- **Control and energy management of hybrid propulsion and power systems**

When the system becomes more complicated, the control and energy management will become more important and also more difficult. In different operating conditions and for different mission profiles, the control and energy management system should provide the

optimal control and management solutions for the right operations of the ship. For instance, when the ship sails and manoeuvres in adverse sea and the ship propulsion operates in PTI mode, the load sharing between the main engine and the shaft motor, and at the same time the shaft speed and the propeller pitch should be properly controlled; and in this case the top priority of the control and energy management should be the operational safety of the ship and engine. When the ship sails in normal sea conditions, the control and energy management system should put the ship transport performance at a higher priority, i.e., reduce the fuel consumption, emissions and operating cost over the whole voyage.

- **Dynamic behaviour of Gas engine and/or Dual fuel engine when ships sail and manoeuvre in adverse sea conditions**

The dynamic behaviour of a gas engine or a dual fuel engine in gas mode is worse compared to that of a diesel engine or dual fuel engine in diesel mode. Consequently, an ocean-going cargo ship powered by a gas engine would have more serious challenges when sailing and manoeuvring in adverse weather conditions. In addition to solving the methane slip problem of the marine gas engines, the operational safety issues in dynamic and heavy operation conditions should also be addressed before the gas engines are widely applied on the ocean-going cargo ships. So, the dynamic behaviour of gas engine and/or dual fuel engine when ships sail and manoeuvre in adverse sea conditions are recommended for future research. Then the control of the (gas) engine, the PTI and the propeller, etc., also needs to be well addressed.

- **Influence of the hybrid propulsion and alternative fuels on the capital expenditure (CAPEX) and operating expenditure (OPEX) of the ship**

In addition to the fuel consumption and emissions, the influence of the application of hybrid propulsion and alternative fuels on the capital expenditure (CAPEX) and operating expenditure (OPEX) of the ship in the lifetime cycle needs be investigated. The trade-off relationships between the ship CAPEX and OPEX, and between the energy effectiveness of the ship and the operational safety, need to be investigated.

Future research with respect to predicting ship propulsion, manoeuvring and seakeeping performance:

- **More accurate integrated modelling of ship propulsion, manoeuvring and seakeeping**

To improve the accuracy of the predictions of the interactions between the ship propulsion plant, the ship and waves, etc., in high sea states, more accurate modelling of ship propulsion, manoeuvring and seakeeping is needed. For instance, the ship manoeuvring model used in this thesis can be improved. To better capture ship behaviour in adverse sea conditions in a more realistic way, a 4 DOF or even 6DOF ship manoeuvring model could be used. The hydrodynamic coefficients in the manoeuvring and seakeeping models could be determined by experimental and advanced numerical methods.

- **Empirical formulas estimating the wave-induced steady forces, including the added wave resistance, the steady lateral force and the steady yaw moment**

Although experimental and advanced numerical methods could be more accurate when estimating the wave-induced steady forces, a well-established and simple-to-use empirical method is of great usefulness for practical applications. For instance, when the detailed information of the hull form is not available, which is the case in this study, or at the early design stage, where the detailed hull form is still under development, an empirical method using a limited number of main ship particulars to satisfactorily capture the physical phenomena is preferred.

Future work with respect to EEDI amendments:

- **Standardised representative operational profiles of ships**

According to the proposal in this thesis and many others in literature, to calculate the attained EEDI of ships reflecting ship performance in realistic operating conditions, standardised representative operational profiles for different ship types should be defined, and this work is recommended to be done by IMO.

## **A. Calibration and validation of ship propulsion system model**

### **A.1 Correction of towing tank measurement data**

At first the results data of model test of ship resistance and propeller open water characteristics were directly used in calibrating the ship resistance and the propeller open water characteristics models. However, there were discrepancies between the original model test prediction results of the delivered power and propeller speed at various ship speeds and the results of the real ship sea trial test. During the sea trial test, the shaft power was measured, from which the delivered power can be deduced assuming a transmission efficiency for the shaftline. Further propeller speed at various ship speeds was measured. Based on this, the original model test results of the chemical tanker have been corrected according to the sea trial test data as illustrated in Figure A. 1. The correction procedure will be briefly introduced in the following.

To compare the sea trial test results and the model prediction results and get the multiplicative correction factors for the model test results, ratios of relevant parameters of the sea trial test to those of the model prediction results are formed as shown in equation (A. 1). Note that the mathematical technique used here for relating sea trial to model test prediction is the same as relating the off-design condition variables to the corresponding variables of a known nominal condition as is done to normalised variables.

$$X^* = \frac{X_{trial}}{X_{prediction}} \quad (\text{A. 1})$$

The ratios according to equation (A. 1) can be derived from relevant variables with the added advantage that constant quantities (such as sea water density and propeller diameter) are removed from the considerations. Note that ship speed is dropping out since all comparisons are made for the same ship speed. For all other quantities it is assumed that there can be a

difference between the sea trial test and model prediction results. The correction factors for delivered power  $P_D^*$  and propeller speed  $n^*$  were determined using the sea trial results. These are the basis and final criterion for correction of the other parameters. Actually, there are many different solutions to correct the model prediction results by choosing different combinations of parameters having uncertainties that could be corrected.

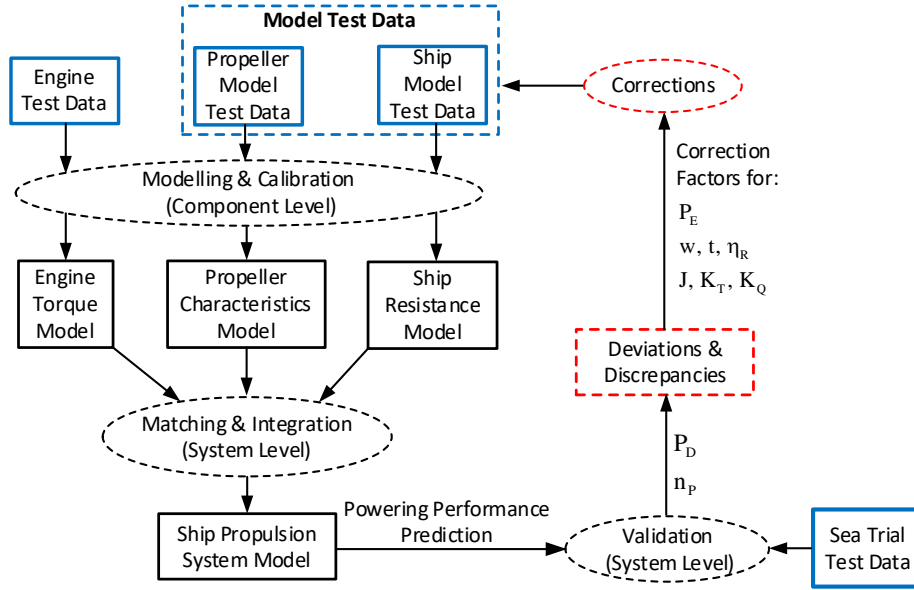


Figure A. 1: Correction of towing tank measurement data

It is assumed that the ship effective power and propeller characteristic rather than the relative rotation efficiency, thrust deduction fraction and wake fraction are the most uncertain factors. Therefore, the relative rotation efficiency, thrust deduction fraction and wake fraction are left out of the correction, in other words, they remain the same as the original model test data. Further assume that the propulsive efficiency which is the ratio of the ship effective power to the delivered power remains the same as the original model test prediction resulting in the same correction factor for the ship effective power and delivered power as shown in equation (A. 2).

$$P_E^* = P_D^* \quad (\text{A. 2})$$

Then the correction factors for the propeller open water characteristics can be derived from those for the delivered power, propeller speed and ship effective power as shown in equations (A. 3), (A. 4) and (A. 5).

$$K_Q^* = \frac{P_D^* \cdot \eta_R^*}{(n^*)^3} = \frac{P_D^* \cdot 1}{(n^*)^3} = \frac{P_D^*}{(n^*)^3} \quad (\text{A. 3})$$

$$J^* = \frac{(1-w)^*}{n^*} = \frac{1}{n^*} \quad (\text{A. 4})$$

$$K_T^* = \frac{P_E^*}{(n^*)^2 \cdot (1-t)^*} = \frac{P_E^*}{(n^*)^2 \cdot 1} = \frac{P_E^*}{(n^*)^2} \quad (\text{A. 5})$$

$$\eta_0^* = \frac{K_T^* \cdot J^*}{K_Q^*} = \frac{P_E^*}{(n^*)^2} \cdot \frac{1}{n^*} \cdot \frac{(n^*)^3}{P_D^*} = \frac{P_E^*}{P_D^*} = 1 \quad (\text{A. 6})$$

Where  $P_D^*$  is the ratio of delivered power,  $n^*$  is the ratio of propeller speed,  $K_Q^*$  is the ratio of propeller torque coefficient,  $\eta_R^*$  is the ratio of relative rotation efficiency,  $(1-w)^*$  is the ratio of wake fraction defect,  $J^*$  is the ratio of propeller advance coefficient,  $P_E^*$  is the ratio of the ship effective power,  $(1-t)^*$  is the ratio of thrust deduction fraction defect,  $K_T^*$  is the ratio of propeller thrust coefficient,  $\eta_D^*$  is the ratio of propulsive efficiency and  $\eta_0^*$  is the ratio of propeller open water efficiency.

As argued, the result presented in equation (A. 6) implies that the propeller open water efficiency at the same ship speed will remain the same as the original model test data as a result of the chosen solution for the corrections. Finally, the values of the correction factors deduced with the procedure above are presented in Table A. 1.

Table A. 1: Correction factors of ship model test data

(a) Required correction factors for propeller speed, delivered power and ship effective power as concluded from sea trials

| Correction factors | $n^*$  | $P_D^* = P_E^*$ |
|--------------------|--------|-----------------|
| Value              | 0.9824 | 0.8580          |

(b) Applied correction factors for specific resistance, wake factor, thrust deduction factor and relative rotative efficiency (chosen)

| Correction factors | $C_E^*$ | $(1-w)^*$ | $(1-t)^*$ | $\eta_R^*$ |
|--------------------|---------|-----------|-----------|------------|
| Value              | 0.8580  | 1         | 1         | 1          |

(c) Applied correction factors for propeller characteristics (derived)

| Correction factors | $J^*$  | $K_T^*$ | $K_Q^*$ | $\eta_0^*$ |
|--------------------|--------|---------|---------|------------|
| Value              | 1.0179 | 0.8890  | 0.9049  | 1          |

The model test results corrected using the above-mentioned method have been applied in developing and calibrating the models of propeller and ship resistance.

## A.2 Calibration of component models to testbed and towing tank measurements

### A.2.1 Fuel consumption and emissions of diesel engines

For the main engine, the test data provided in the technical file of the engine EIAPP (Engine International Air Pollution Prevention) certificate has been used for modelling the NO<sub>x</sub> and HC emissions as well as the fuel consumption. When calibrating the engine fuel consumption model

and emissions model, the engine test data come from the same operating points (i.e., 25%, 50%, 75%, 100% of rated engine load), which are selected along both the generator curve (E2 cycle) and the propeller curve (E3 cycle). However, the engine installed on the benchmark chemical tanker has been tested only for E2 cycle rather than E3 cycle due to the installed controllable pitch propeller. So, the test data for E3 cycle is obtained based on the mean value of the E3 cycle test data of the other four engines from the same engine family as shown in Table A. 2. The mean value of data of different engines is taken in the following way, firstly, the mean value of data of different engines at nominal points are taken as the new nominal value of the engine; secondly, the mean values of part load percentages, i.e., the ratios of part load value to nominal value, along generator curve (E2 cycle) and propeller curve (E3 cycle) of different engines are taken as the part load percentages of the engine along generator curve and propeller curve respectively.

Table A. 2: Available EIAPP test data of MAN6S35ME engines from the same engine family

| Test cycle        | E2   | E3   | E3   | E3   | E3   |
|-------------------|------|------|------|------|------|
| Rated Power (kW)  | 4170 | 5220 | 4500 | 4050 | 3320 |
| Rated speed (rpm) | 167  | 167  | 144  | 142  | 132  |

For the auxiliary engines, as the test data of the auxiliary engines installed in the benchmark ship is not available, the fuel consumption and emissions models of the auxiliary engines are calibrated using the average data of (a small number of) similar engines that are available in the internal dataset.

### (1) Fuel consumption

The calibration results of fuel consumption models of the main engine and auxiliary engines are shown in Table A. 3, Table A. 4, Figure A.2, Figure A.3 and Figure A. 4.

Table A. 3: Coefficients of engine torque model of main engine

| Nominal Parameters     |                              |                        | Coefficients |         |        |         |        |
|------------------------|------------------------------|------------------------|--------------|---------|--------|---------|--------|
| $M_{eng,nom}$<br>(kNm) | $m_{f,nom}$<br>(g/cyl/cycle) | $n_{eng,nom}$<br>(rpm) | $a$          | $b$     | $c$    | $d$     | $e$    |
| 238.4465               | 12.2769                      | 167                    | -0.0099      | -0.2046 | 0.9342 | -0.1056 | 0.0179 |

Table A. 4: Coefficients of engine torque model of auxiliary engine.

| Nominal Parameters     |                              |                        | Coefficients |         |        |         |        |
|------------------------|------------------------------|------------------------|--------------|---------|--------|---------|--------|
| $M_{eng,nom}$<br>(kNm) | $m_{f,nom}$<br>(g/cyl/cycle) | $n_{eng,nom}$<br>(rpm) | $a$          | $b$     | $c$    | $d$     | $e$    |
| 7.9577                 | 1.0417                       | 900                    | -0.0558      | -0.6022 | 0.9446 | -0.1548 | 0.1567 |

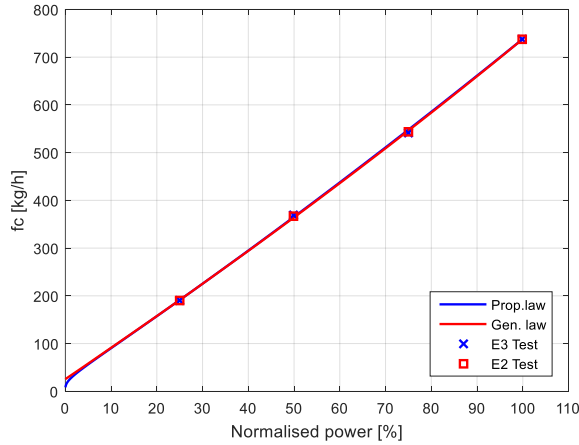


Figure A.2: Fuel Consumption Flow (Main engine)

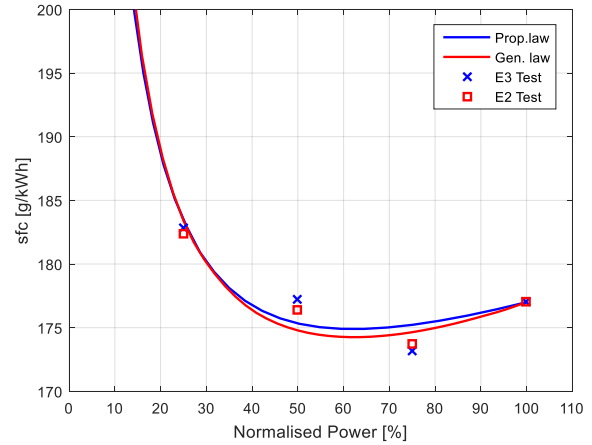


Figure A.3: Specific Fuel Consumption (Main engine)

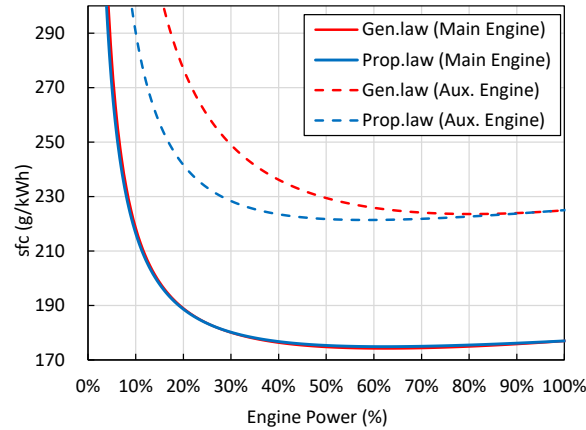


Figure A. 4: Specific fuel consumption of main engine and auxiliary engines.

From the above model results it is found that the fuel consumption performance of a 2-stroke diesel engine is different from that of a 4-stroke diesel engine. The specific fuel consumption of 4-stroke diesel engines is better (lower) when the engine is operating under the propeller law than under the generator law (Klein Woud and Stapersma, 2002). However, the 2-stroke diesel engine investigated in this thesis has better specific fuel consumption when operating under generator law than the propeller law, although in fact there is hardly any difference as shown in Figure A.3 and Figure A. 4, which is also different from 4-stroke diesel engine. But, very few data in this regard are found in the open literature and currently we have limitations to prove the accuracy of our model results. More data and research results in this regard are expected and encouraged to be published by the other researchers.

## (2) Emissions

Note that the specific HC emission data of the main engine at the point of 75% nominal power of the E2 cycle is believed too high (0.42g/kWh) to be reasonable compared to the data of the other points and there is no physical explanation for the measurement that lies so far outside the line that connects the other data points. Therefore, it is corrected (as a rule of thumb) to a lower value (0.30g/kWh) as shown in Figure A. 6(b) to make the trend smoother and the



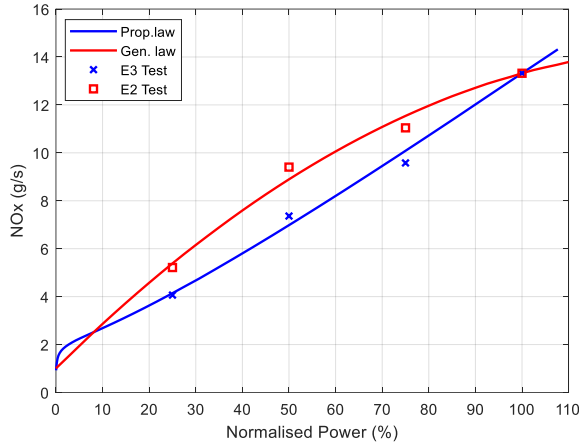
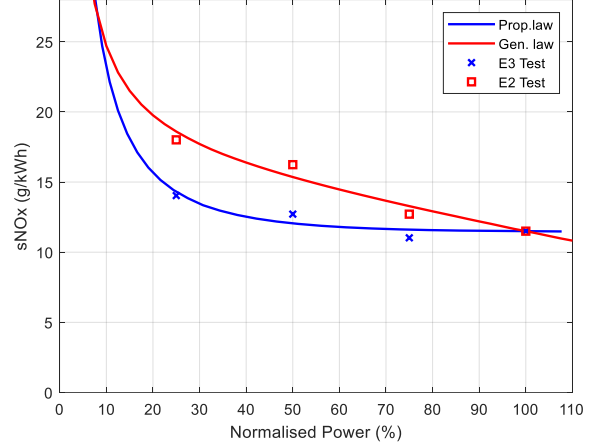
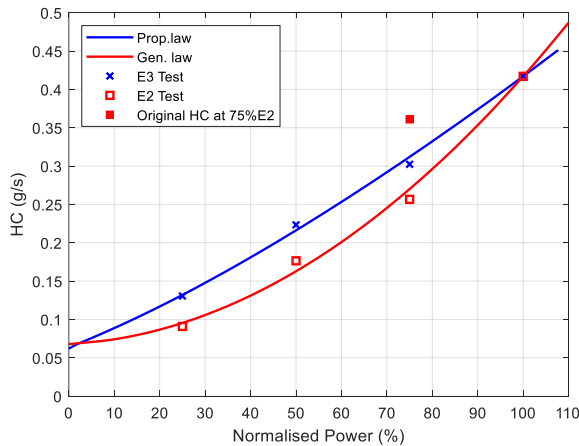
fitting results more acceptable in spite of the fact that we only have E2 cycle data of one two-stroke diesel engine. The modelling result of the NO<sub>x</sub> and HC emissions of the main engine and auxiliary engines are shown in Table A. 5 to Table A. 8, and Figure A. 5 to Figure A. 7.

Table A. 5: Coefficients of NO<sub>x</sub> emission model of main engine.

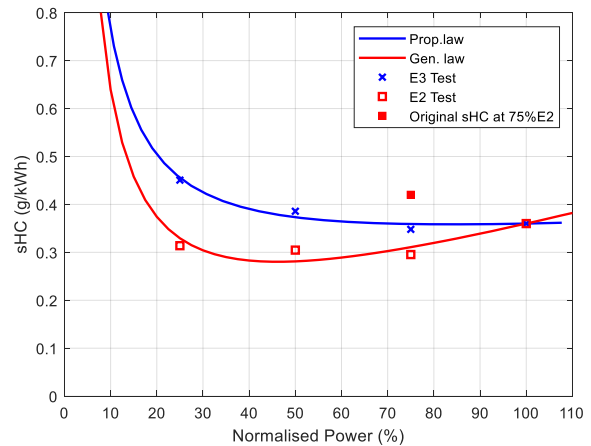
| Nominal Parameters        |                        |                        | Coefficients |           |           |           |           |
|---------------------------|------------------------|------------------------|--------------|-----------|-----------|-----------|-----------|
| $\Phi_{NOx,nom}$<br>(g/s) | $M_{eng,nom}$<br>(kNm) | $n_{eng,nom}$<br>(rpm) | $a_{NOx}$    | $b_{NOx}$ | $c_{NOx}$ | $d_{NOx}$ | $e_{NOx}$ |
| 13.3208                   | 238.4465               | 167                    | 2.1463       | -0.8538   | 0.4046    | -0.5199   | 1.4678    |

Table A. 6: Coefficients of HC emission model of main engine.

| Nominal Parameters       |                        |                        | Coefficients |          |          |          |          |
|--------------------------|------------------------|------------------------|--------------|----------|----------|----------|----------|
| $\Phi_{HC,nom}$<br>(g/s) | $M_{eng,nom}$<br>(kNm) | $n_{eng,nom}$<br>(rpm) | $a_{HC}$     | $b_{HC}$ | $c_{HC}$ | $d_{HC}$ | $e_{HC}$ |
| 0.4170                   | 238.4465               | 167                    | -0.0595      | -0.0088  | 1.6009   | 0.7635   | -0.0424  |

(a) NO<sub>x</sub> emission Flow(b) Specific NO<sub>x</sub> emissionFigure A. 5: NO<sub>x</sub> emission (main engine)

(a) HC emission flow



(b) Specific HC emission flow

Figure A. 6: HC emission (main engine)

Table A. 7: Coefficients of NOx emission model of auxiliary engine.

| Nominal Parameters        |                        |                        | Coefficients |           |           |           |           |
|---------------------------|------------------------|------------------------|--------------|-----------|-----------|-----------|-----------|
| $\Phi_{NOx,nom}$<br>(g/s) | $M_{eng,nom}$<br>(kNm) | $n_{eng,nom}$<br>(rpm) | $a_{NOx}$    | $b_{NOx}$ | $c_{NOx}$ | $d_{NOx}$ | $e_{NOx}$ |
| 1.8750                    | 7.9577                 | 900                    | 0.6642       | 0.2174    | 0.8867    | -0.0267   | 0.3099    |

Table A. 8: Coefficients of HC emission model of auxiliary engine.

| Nominal Parameters       |                        |                        | Coefficients |          |          |          |          |
|--------------------------|------------------------|------------------------|--------------|----------|----------|----------|----------|
| $\Phi_{HC,nom}$<br>(g/s) | $M_{eng,nom}$<br>(kNm) | $n_{eng,nom}$<br>(rpm) | $a_{HC}$     | $b_{HC}$ | $c_{HC}$ | $d_{HC}$ | $e_{HC}$ |
| 0.0271                   | 7.9577                 | 900                    | 1.0213       | 0.1307   | 0.2600   | -0.4000  | 0.2703   |

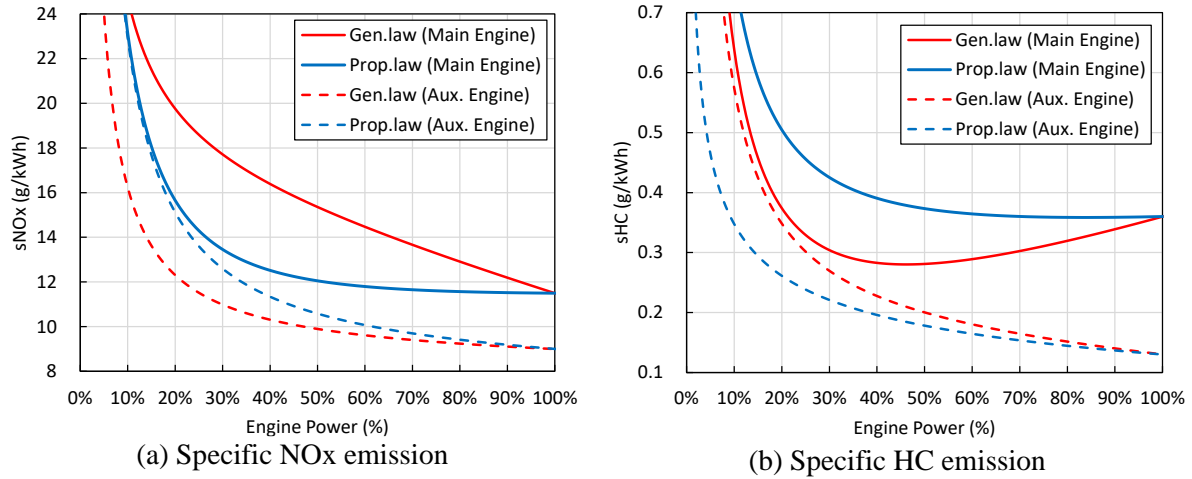


Figure A. 7: Specific NOx and HC emissions of main engine and auxiliary engines

## A.2.2 Ship resistance

The calibration results of ship resistance model are shown in Table A. 9, Figure A. 8 and Figure A. 9. Note that the original model test data of ship effective power presented in Figure A. 9 have been corrected together with the original model test data of the propeller open water characteristics according to the real ship sea trial test results and the correction method as shown in Section A.1. In addition, the available test data are limited in the high ship speeds range, namely from 11.5kn to 15kn, and there is no data available for the low ship speeds below 11.5kn. Therefore, only the specific ship resistance model at high ship speeds is calibrated using the available test data while the model at low ship speeds is fitted according to the ship resistance calculation method presented in (Holtrop and Mennen, 1982; Holtrop, 1984) carried out by the authors but not presented here.

Table A. 9: Coefficients of Ship Resistance Model

| Nominal Parameters  |                  | Coefficients |          |          |          |          |
|---------------------|------------------|--------------|----------|----------|----------|----------|
| $1000C_{E,nom}$ [-] | $v_{s,nom}$ [kn] | $a_{CE}$     | $b_{CE}$ | $c_{CE}$ | $d_{CE}$ | $k_{CE}$ |
| 10.6863             | 15               | 0.333        | 10.2     | 0.07     | -15      | -0.06    |

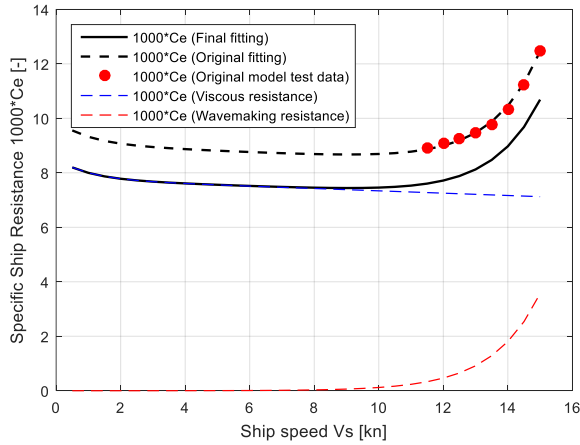


Figure A. 8: Specific Ship Resistance

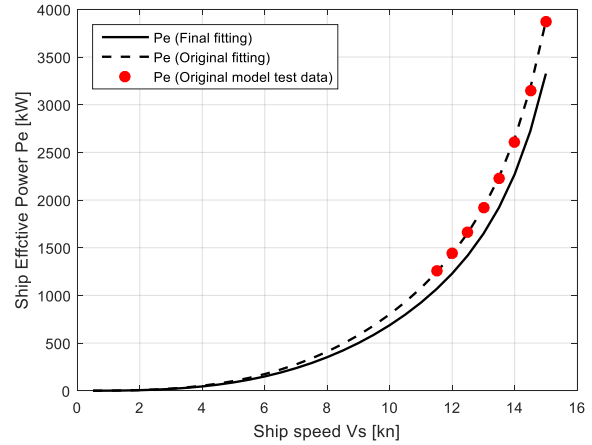


Figure A. 9: Ship Effective Power

### A.2.3 Propeller open water characteristics

The calibration results of propeller model are shown in Table A. 10 and Figure A. 10. Note that as mentioned before, the original model test data of the propeller open water characteristics have been corrected together with the original model test data of the ship effective power according to the ship sea trial test results as show in Section A.1.

Table A. 10: Coefficients of Propeller Model

| Nominal Parameters |                   |               | Coefficients |            |            |            |
|--------------------|-------------------|---------------|--------------|------------|------------|------------|
| $K_{T,nom}$ [-]    | $10K_{Q,nom}$ [-] | $J_{nom}$ [-] | $a_{prop}$   | $b_{prop}$ | $c_{prop}$ | $d_{prop}$ |
| 0.1597             | 0.1942            | 0.4072        | -1.0551      | -0.8018    | -0.1227    | -0.1346    |

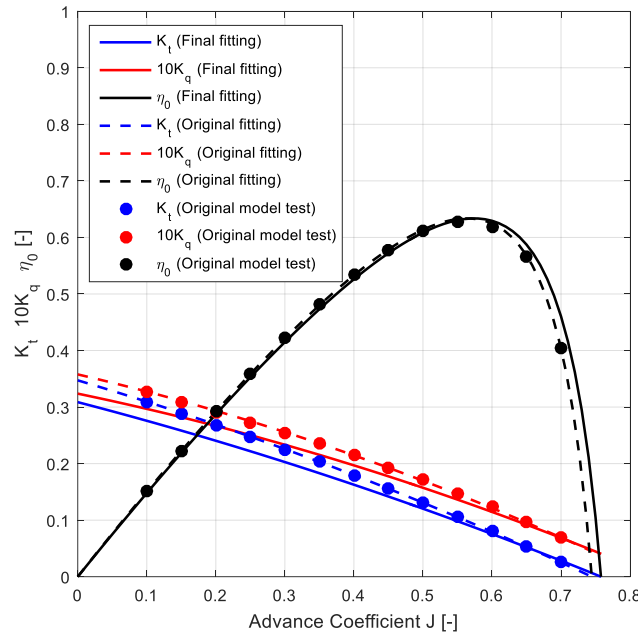


Figure A. 10: Propeller Open Water Characteristics

### A.2.4 Wake factor, thrust deduction factor and relative rotative efficiency

The calibration results of models of wake factor, thrust deduction factor and relative rotative efficiency are shown in Table A.11, Figure A. 11 and Figure A. 12. Note that the model test data of the wake factor, thrust deduction factor and relative rotative efficiency remains the same as the original model test data while the delivered power, propeller speed, ship effective power and propeller characteristics of the original model test data have been corrected according to the real ship sea trial test data as shown in Section A.1.

Table A.11: Coefficients of wake factor, thrust deduction factor and relative rotative efficiency models

| (a) Coefficients of wake factor model |                  |              |        |
|---------------------------------------|------------------|--------------|--------|
| Nominal Parameters                    |                  | Coefficients |        |
| $w_{nom}$ [-]                         | $v_{s,nom}$ [kn] | $c_w$        | $d_w$  |
| 0.2781                                | 12.5             | 0.0880       | 0.1059 |

| (b) Coefficients of thrust deduction factor model |                  |              |        |
|---|------------------|--------------|--------|
| Nominal Parameters                                |                  | Coefficients |        |
| $t_{nom}$ [-]                                     | $v_{s,nom}$ [kn] | $c_t$        | $d_t$  |
| 0.2009  | 12.5             | 0.0110       | 0.0147 |

| (c) Coefficients of relative rotative efficiency model |                  |              |              |
|--|------------------|--------------|--------------|
| Nominal Parameters                                     |                  | Coefficients |              |
| $\eta_{R,nom}$ [-]                                     | $v_{s,nom}$ [kn] | $c_{\eta r}$ | $d_{\eta r}$ |
| 0.9808   | 12.5             | 0.0235       | 0.0279       |

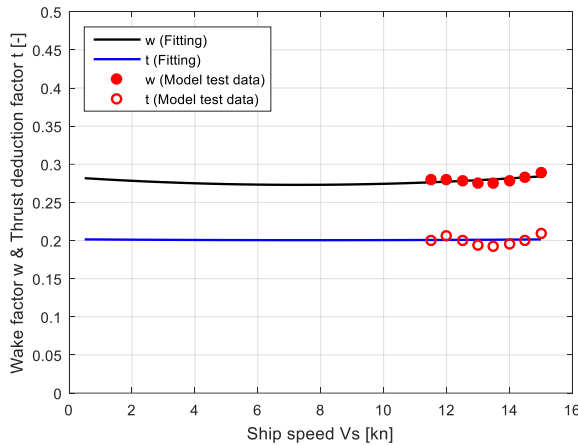


Figure A. 11: Wake factor and Thrust deduction factor

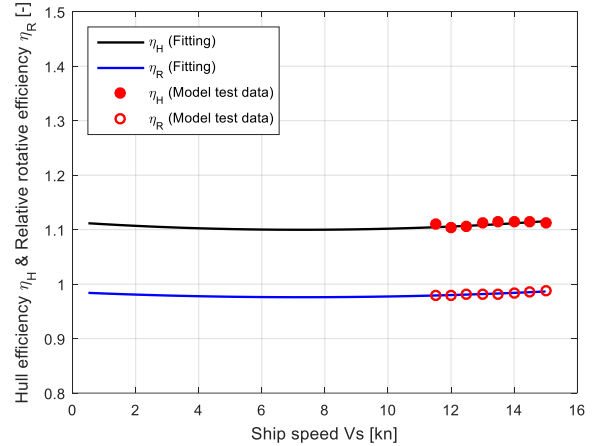


Figure A. 12: Hull efficiency and Relative rotative efficiency

### A.3 Static matching and validation of the ship propulsion system model

After the components models of the ship propulsion system have been developed and calibrated, the static matching of the ship propulsion system is analysed, matching to be understood as the relation between engine envelope and propeller/ship characteristic as fully

explained in (Klein Woud and Stapersma, 2002). The matching results have been validated by the real ship sea trial test (Figure A. 13). The original matching based on the original model test data is “heavier” compared with the sea trial test results. Note that, due to the fact that there is only one overall set of correction factors as given in equations (A. 3) to (A. 5) and presented in Table A. 1, the measured points of the sea trial are still not all exactly on the model data but at least the model now correlates in a mean sense to the measured data. Note that the ship draught during sea trial test was the same as the ship design draught. In this thesis, the service margin or sea margin (SM) is assumed to be zero ( $SM=0$ ) during the sea trial test, despite of the fact that the wind force was actually Beaufort 3-4 and the sea state was Douglas 2-3 rather than a very calm sea, however the correction on resistance would be even larger if the sea margin during sea trials was noticeably larger than one.

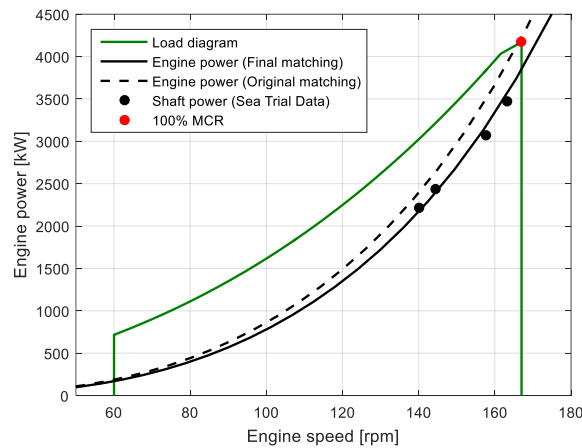


Figure A. 13: Ship Propulsion System Static Matching and Validation

## B. Selecting a Sea Margin for typical sailing condition

The added ship resistance when the ship sails in service conditions compared to sailing in sea trial condition (calm sea condition) is quantified by the sea margin (SM) (Klein Woud and Stapersma, 2002), which is defined by Equation (B. 1). According to the definition, the sea margin in the sea trial condition is zero. The sea margin in realistic sailing condition is determined by the fouling of hull and propeller, displacement, sea state and water depth as shown in Equation (B. 2).

$$SM = \frac{P_{E,service} - P_{E,trial}}{P_{E,trial}} \quad (B. 1)$$

Where,  $P_{E,service}$  is the ship effective power in service conditions and  $P_{E,trial}$  is the ship effective power in sea trial condition.

$$\begin{aligned} SM &= f(\text{fouling}, \text{displacement}, \text{sea state}, \text{water depth}) \\ &= f_1(\text{fouling}) \cdot f_2(\text{displacement}) \cdot f_3(\text{sea state}) \cdot f_4(\text{water depth}) - 1 \end{aligned} \quad (B. 2)$$

Based on 1.5 years period and 3% increase of resistance per year due to fouling, the effect of hull and propeller fouling is:

$$f_1(\text{fouling}) = (1 + 0.03)^{1.5} = 1.045 \quad (B. 3)$$

The ship resistance addition relative to that in trial condition due to sea state during realistic sailing conditions, taking wind, waves and currents in to account, is set to be 10%, so the effect of sea state is:

$$f_3(\text{sea state}) = 1.10 \quad (B. 4)$$

Clearly this is a drastic simplification of actual sea state effects, but for the current design study it is deemed sufficient.

The draught of the ship during the sea trial test is the design draught, and it is assumed that the ship also sails at the design draught in real sailing condition. So, the effect of the displacement variations on ship resistance are neglected, see Equation (B. 5). Furthermore, it is assumed that the ship sails in deep water, as during the sea trials. So, the effect of shallow water on ship resistance is also neglected, see Equation (B. 6).

$$f_2(\textit{displacement}) = 1 \quad (\text{B. 5})$$

$$f_4(\textit{water depth}) = 1 \quad (\text{B. 6})$$

The total sea margin according to Equation (B. 2) will then be:

$$SM = 1.045 \times 1 \times 1.1 \times 1 - 1 = 0.15 \quad (\text{B. 7})$$

Therefore, the sea margin (SM) in realistic sailing condition relative to sea trial condition is set to be 15%.

## **C. Corrections of Fuel Consumption and Emissions for Different Fuel Types**

The test results of fuel consumption and emissions for developing and calibrating the models of both the main engine and the auxiliary engines have been corrected at ISO (International Organization for Standardization) standard reference conditions using the standard LHV (Lower Heating Value) of the fuel oil (42,700 kJ/kg), referring to ISO 15550:2016 and ISO 3046-1:2002. However, in this thesis, the influence of sailing on different fuel types on the ship fuel consumption and emissions will be investigated. For instance, when the ship is in operation, the fuel type for the main engine can be HFO (heavy fuel oil), MDF (marine diesel fuel) or LNG (liquefied natural gas); while the fuel type for the auxiliary engines can be MDF (marine diesel fuel) or LNG (liquefied natural gas). Therefore, the fuel consumption, NO<sub>x</sub> emission and HC emission during ship operations need to be corrected accordingly by Equation (C. 1) using the multiplying correcting factors shown in Table C. 1 (and uncertainty in these factors which is in between brackets).

The underlying assumption for correcting the fuel consumption is that the efficiencies of the engines remain the same when the fuel types are changed. The correcting factors for NO<sub>x</sub> and HC emissions when using HFO and MDF are set based on the internal dataset. When using LNG as the fuel, the NO<sub>x</sub> emission will be significantly reduced by approximately 80% compared to diesel fuel (Burel et al., 2013); while the HC emission will be much higher than the diesel fuel because of the methane slip during engine operation (Anderson et al., 2015; Wei and Geng, 2016; Lehtoranta et al., 2019). So, for a simple assumption, the correcting factors for NO<sub>x</sub> and HC emissions when using LNG are set as 0.2 and 10, respectively, based on the information in the available literature and engine specifications. Note that the formation mechanisms and the environmental and human health impacts of HC (hydrocarbons) emissions from diesel fuel and LNG are different although they are all called hydrocarbons in this thesis



as well as in other literature. The HC emissions from diesel fuel, in general, are the consequence of incomplete combustion and they are hazardous to human health (e.g., carcinogenic). However, the HC emissions from LNG are mainly methane emissions caused by “methane slip” or unburnt methane and it is mainly a greenhouse gas; it has no direct health effects on humans (in modest concentrations) (Stapersma, 2010a), but it may cause suffocation if the concentration of methane in the air is too high (Jo et al., 2013). It is assumed that the non-dimensional conversion factor between fuel consumption and CO<sub>2</sub> emission is 3.206 kg/kg for diesel fuels and 2.750 kg/kg for LNG (IMO, 2018).

$$\Phi_x = C_x \cdot \Phi_{x,ISO} \quad (C. 1)$$

where  $\Phi_x$  is the fuel consumption or the emissions of HFO, MDF and LNG (kg/s);  $\Phi_{x,ISO}$  is the fuel consumption or emissions of fuel at ISO (kg/s);  $C_x$  is the correcting factors of fuel consumption and emissions for different fuel types represented in Table C. 1.

| Fuel Type            | ISO *  | HFO *  | MDF *  | LNG *              |
|----------------------|--------|--------|--------|--------------------|
| <i>LHV</i> * (kJ/kg) | 42,700 | 41,500 | 42,000 | 48,000 (+/- 2,000) |
| $C_{fuel}$ (-)       | 1      | 1.0289 | 1.0167 | 0.8896 (+/- 0.047) |
| $C_{NOx}$ (-)        | 1      | 1.2    | 1.0    | 0.2 (+/- 0.1)      |
| $C_{HC}$ (-)         | 1      | 1.5    | 1.0    | 10.0 (+/- 6)       |

\* ISO, ISO standard reference conditions, referring to ISO 15550:2016 and ISO 3046-1:2002.\*

\* HFO, heavy fuel oil; MDF, marine diesel fuel; LNG, liquefied natural gas.\*

\* LHV, lower heating values.\*

## D. Mission Profile in Open Sea

According to the transit voyage in open sea defined in Section 3.5.1, the average sea margin over the whole voyage is defined by Equation (D. 1).

$$\overline{SM} = \frac{SM_A \cdot P_{E,A} \cdot t_A + SM_B \cdot P_{E,B} \cdot t_B + SM_C \cdot P_{E,C} \cdot t_C}{P_{E,A} \cdot t_A + P_{E,B} \cdot t_B + P_{E,C} \cdot t_C} \quad (D. 1)$$

The average ship speed over the whole voyage is defined by Equation (D. 2).

$$\overline{V} = \frac{V_A \cdot t_A + V_B \cdot t_B + V_C \cdot t_C}{t_A + t_B + t_C} \quad (D. 2)$$

The distance of the whole voyage is:

$$V_A \cdot t_A + V_B \cdot t_B + V_C \cdot t_C = 650 (\text{nmile}) \quad (D. 3)$$

### Voyage I:

The maximum ship speeds in a calm sea state ( $SM = 5\%$ ) and a normal sea state ( $SM = 15\%$ ) in Case I are 13.90 kn and 13.66 kn, respectively. The maximum ship speed in a heavy sea state ( $SM = 30\%$ ) is limited at 12 kn. In order to reach the average ship speed of 13.5 kn over the whole voyage, it is assumed that the ship sails at the maximum speeds at different parts of the voyage defined above. In Voyage I, the average sea margin over the whole voyage is 15%. According to Equations (D. 1), (D. 2) and (D. 3), the time the ship sails in different parts of the voyage in Voyage I are:  $t_{I,A} = 4.27$  (h),  $t_{I,B} = 5.26$  (h),  $t_{I,C} = 38.62$  (h).

### Voyage II:

The average sea margin of the whole voyage in Voyage II is also 15%. The ship speed over

the whole voyage is 12 kn and the corresponding ship effective power over the whole voyage is 1229.59 kW. It is assumed that the time the ship sails in a heavy sea state in Voyage II and Voyage III is the same as that in Voyage I, which is 5.26 h. Then, according to Equations (D. 1), (D. 2) and (D. 3), the time the ship sails in different parts of the voyage are:  $t_{II,A} = 7.89$  (h),  $t_{II,B} = 5.26$  (h),  $t_{II,C} = 41.02$  (h).

**Voyage III:**

Similar to Voyage II, the time the ship sails in different parts of the voyage in Voyage III, where the average ship speed is 10 kn, are:  $t_{III,A} = 7.89$  (h),  $t_{III,B} = 5.26$  (h),  $t_{III,C} = 51.85$  (h).

## **E. Details of blowdown and scavenging models of two-stroke marine diesel engine**

### **E.1 Blowdown**

The blowdown process of four-stroke diesel engines can be modelled by Zinner blowdown proposed in (Zinner, 1978), which has been improved in (Schulten and Stapersma, 2003). The traditional Zinner blowdown model assumes that the conditions, namely the temperature and pressure, in the cylinder and in the outlet receiver during blowdown are the same. The improved blowdown model in (Schulten and Stapersma, 2003) proposes that a part of the gases is pushed out of the cylinder during blowdown and the remaining part continues the polytropic expansion in the cylinder, so the temperature in the cylinder and in the outlet receiver after blowdown will be different. Both the blowdown models in (Zinner, 1978) and (Schulten and Stapersma, 2003) assume that the process happens instantaneously as soon as the exhaust valves open, i.e. at constant cylinder volume ( $V_6$ ), and the pressure in the cylinder after blowdown is the same as that in the outlet receiver.

However, for two-stroke diesel engines the blowdown process is followed by the scavenging process rather than the expelling process in four-stroke diesel engines. It is assumed that the remaining mass in the cylinder will expand to the scavenging pressure, which is higher than the pressure in the outlet receiver. So, the blowdown model needs to be adapted for two-stroke diesel engine taking into account that the pressures in the cylinder and in the outlet receiver are different during the blowdown process. The adapted blowdown model for two-stroke engines is illustrated in Figure E. 1. It is assumed that the remaining gases in the cylinder continues the polytropic expansion with an increasing cylinder volume (from  $V_6$  to  $V_7$ ) and the pressure in the cylinder  $p_7$  after blowdown will be the scavenging pressure  $p_{scav}$ . Another part of the gases that blows down out of the cylinder continues the expansion in the outlet receiver in two steps. Firstly, the blowdown-out gas in the outlet receiver expands to a pressure that is

the same as that in the cylinder, i.e the scavenging pressure  $p_{scav}$ . Secondly, the blowdown-out gas further expands to the pressure in the outlet receiver  $p_{or}$ . It is assumed that the outlet receiver is covered by a virtual piston moving against the pressure in the outlet receiver  $p_{or}$ .

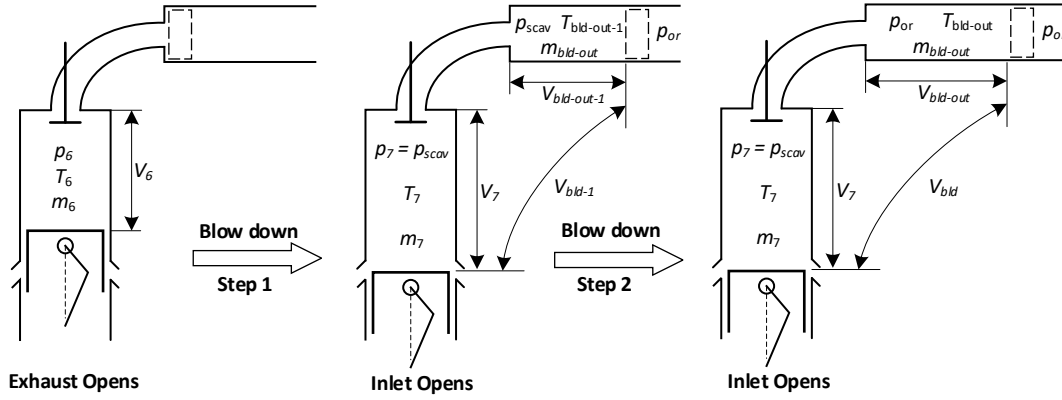


Figure E. 1: Adapted blowdown model for two-stroke diesel engines

The virtual blowdown temperature in the first step is calculated based on the assumptions of the traditional Zinner blowdown model as shown in equation (E. 1).

$$T_{bld,1} = T_6 \cdot \left( \frac{1}{n_{bld,1}} + \frac{n_{bld,1} - 1}{n_{bld,1}} \cdot \frac{p_{scav}}{p_6} \right) \quad (E. 1)$$

The temperature and the remaining mass in the cylinder after blowdown are calculated based on the assumptions by the blowdown model in (Schulten and Stapersma, 2003) as shown in equations (E. 2) and (E. 3) respectively.

$$T_7 = T_6 \cdot \left( \frac{p_7}{p_6} \right)^{\frac{n_{exp} - 1}{n_{exp}}} \quad (E. 2)$$

$$m_7 = \frac{p_{scav} \cdot V_{IO}}{R_7 \cdot T_7} \quad (E. 3)$$

With the assumption that the total blowdown volume in first step is the same as that in traditional Zinner blowdown model as shown by equation (E. 4), the mass and the temperature of the gases entering the outlet receiver after the first step of blowdown are calculated by equations (E. 5) and (E. 6) respectively.

$$V_{bld,1} = V_{bld-out,1} + V_7 \quad (E. 4)$$

$$m_{bld-out} = m_6 - m_7 \quad (E. 5)$$

$$T_{bld-out,1} = \frac{m_6 \cdot T_{bld,1} - m_7 \cdot T_7}{m_{bld-out}} \quad (E. 6)$$

The temperature of the blowdown-out mass in the outlet receiver after the second step of blowdown is calculated by equation (E. 7). The derivation of equation (E. 7) is similar to that of equation (E. 1), which has been introduced in detail in (Stapersma, 2010c).

$$T_{bld-out} = T_{bld-out,1} \cdot \left( \frac{1}{n_{bld}} + \frac{n_{bld}-1}{n_{bld}} \cdot \frac{p_{or}}{p_{scav}} \right) \quad (E. 7)$$

## E.2 Two-stage scavenging

### E.2.1 Stage I: Two-zone scavenging model

The two-zone scavenging model proposed in this thesis is applied in stage I, as the cylinder is divided into two zones, namely A zone and B zone. Parameters in A zone and B zone are calculated individually based on the mass balance, air (or composition) balance, gas law and the energy balance. The average value of the state parameters of the whole cylinder volume are calculated by mixing A zone and B zone. It is assumed that there is no mass and heat exchange between A zone and B zone, and there is no heat exchange between the two zones and the cylinder wall.

#### (1) B zone

According to the definition of B zone, there is only an ingoing mass flow entering B zone and there is no mass flow flowing out. According to the mass balance, the mass accumulation within B zone is equal to the net inflow as shown in equation (E. 8). The final solution for the normalised mass of B zone after a certain scavenging time is expressed by equation (E. 9).

$$\frac{dm_B}{dt} = \dot{m}_{sc-in} \quad (E. 8)$$

$$\frac{m_B}{m(0)} = S_B(0) + t_{sc,r} \cdot y(0) \quad (E. 9)$$

where,  $m(0)$  is the initial mass of the whole cylinder volume when the scavenging starts;  $S_B(0)$  is the initial mass ratio of B zone;  $y(0)$  is the initial temperature ratio of the temperature in the cylinder to that of the ingoing mass flow.

The temperature is normalised against the temperature of the ingoing scavenging mass flow as the temperature ratio, which is defined by equation (E. 10).

$$y \stackrel{def}{=} \frac{T}{T_{sc-in}} \quad (E. 10)$$

where,  $T_{sc-in}$  is the temperature of the ingoing scavenging mass flow, which is equal to the temperature in the inlet receiver  $T_{ir}$ .

The ideal gas law for B zone is shown in equation (E. 11).

$$p_B \cdot V_B = m_B \cdot R_B \cdot T_B \quad (E. 11)$$

According to the energy balance, the accumulation of internal energy in B zone is equal to the net inflow of enthalpy plus the work done, assuming no heat exchange with the wall.

$$\frac{dU_B}{dt} = \dot{H}_{sc-in} - p \cdot \frac{dV_B}{dt} \quad (E. 12)$$

It is assumed that the specific heat of the gases in B zone  $c_{p,B}$  is constant during the scavenging process. So, the specific heat ratio defined by equation (E. 13) will be constant with the assumption that the specific heat of the ingoing scavenging air is constant during the scavenging process.

$$\gamma = \frac{\overset{def}{c_{p,B}}}{c_{p,sc-in}} \quad (\text{E. 13})$$

Combining equations (E. 8), (E. 11) and (E. 12), the final solution for the temperature in B zone in a normalized form is shown in equation (E. 14). According to gas law, combining equations (E. 11), (E. 9) and (E. 14), the normalized volume of B zone is calculated by equation (E. 15).

$$y_B = \frac{\overset{def}{T_B}}{T_{sc-in}} = \frac{1}{\gamma} + \frac{S_B(0) \cdot \left[ y_B(0) - \frac{1}{\gamma} \right]}{S_B(0) + t_{sc,r} \cdot y(0)} \quad (\text{E. 14})$$

$$\frac{V_B}{V} = S_B(0) + \frac{1}{\gamma} \cdot t_{sc,r} \quad (\text{E. 15})$$

According to the air balance, the air mass accumulation in B zone is equal to the net air inflow as shown in equation (E. 16). The final solution for composition in B zone is calculated by equation (E. 17).

$$\frac{dm_{a,B}}{dt} = \dot{m}_{a,sc-in} \quad (\text{E. 16})$$

$$x_B = x_{sc-in} - \frac{S_B(0) \cdot [x_{sc-in} - x(0)]}{S_B(0) + y(0) \cdot t_{sc,r}} \quad (\text{E. 17})$$

## (2) A zone

There is no mass exchange between A zone and B zone, so, the composition in A zone is constant during stage I. Assume that the composition of the outgoing scavenging mass flow is the same as that in A zone during stage I as shown in equation (E. 18).

$$x_A = x(0) = x_{sc-out} \quad (\text{E. 18})$$

According to the mass balance, the mass accumulation within A zone is equal to the net inflow.

$$\frac{dm_A}{dt} = -\dot{m}_{sc-out} \quad (\text{E. 19})$$

The ideal gas law for A zone:

$$p_A \cdot V_A = m_A \cdot R_A \cdot T_A \quad (\text{E. 20})$$

According to the energy balance, the accumulation of internal energy in A zone is equal to the net inflow of enthalpy plus the work done, assuming no heat exchange with the wall.

$$\frac{dU_A}{dt} = -\dot{H}_{sc-out} - p \cdot \frac{dV_A}{dt} \quad (\text{E. 21})$$

Combining equations (E. 19), (E. 20) and (E. 21), it is proved that the temperature in A zone is constant.

$$T_A = T(0) = \text{constant} \quad (\text{E. 22})$$

With the relationship of the volumes in the cylinder, i.e.,  $V = V_A + V_B$ , the volume of A zone is calculated by equation (E. 23). According to the gas law, the mass of A zone is calculated by equation (E. 24).

$$\frac{V_A}{V} = S_A(0) - \frac{1}{\gamma} \cdot t_{sc,r} \quad (\text{E. 23})$$

$$\frac{m_A}{m(0)} = S_A(0) - \frac{1}{\gamma} \cdot t_{sc,r} \quad (\text{E. 24})$$

### (3) The whole cylinder volume

The mean parameters of the whole cylinder volume are calculated by mixing the two zones based on the mass balance, air (or composition) balance, gas law and the energy balance.

With the mass relationship in the cylinder volume, i.e.,  $m = m_A + m_B$ , the total mass in the cylinder volume is calculated by equation (E. 25). According to the ideal gas law for the whole (constant) cylinder volume, the average temperature in the cylinder is calculated by equation (E. 26).

$$\frac{m}{m(0)} = 1 + t_{sc,r} \cdot \left[ y(0) - \frac{1}{\gamma} \right] \quad (\text{E. 25})$$

$$y = \frac{\overset{\text{def}}{T}}{T_{sc-in}} = \frac{y(0)}{1 + t_{sc,r} \cdot \left[ y(0) - \frac{1}{\gamma} \right]} \quad (\text{E. 26})$$

The average composition of the whole cylinder volume is calculated by equation (E. 27). So, the final solution for the composition of the mass in the cylinder is shown in equation (E. 28).

$$x = \frac{m_A \cdot x_A + m_B \cdot x_B}{m} \quad (\text{E. 27})$$

$$x = \frac{\left[ x_{sc-in} \cdot y(0) - x(0) \cdot \frac{1}{\gamma} \right] \cdot t_{sc,r} + x(0)}{1 + t_{sc,r} \cdot \left[ y(0) - \frac{1}{\gamma} \right]} \quad (\text{E. 28})$$

### (4) End time of stage I

A zone will disappear at the end of stage I and the mass in A zone becomes zero as shown



in equation (E. 29).

$$\frac{m_A}{m(0)} = S_A(0) - \frac{1}{\gamma} \cdot t_{sc,r} = 0 \quad (t_{sc,r} = t_{sc,r,I}) \quad (\text{E. 29})$$

During stage I,  $\frac{m_A(0)}{m(0)} \geq 0$  and  $t_{sc,r} \leq \gamma \cdot S_A(0)$ , so, stage I will end at  $t_{sc,r,I} = \gamma \cdot S_A(0)$ .

### E.2.2 Stage II: Perfect mixing model

The perfect mixing model for a constant control volume (the cylinder volume) will be applied in stage II as only the perfect mixing zone (B zone) exists in the cylinder in this stage. The perfect mixing model is also based on the mass balance, air (or composition) balance, gas law and the energy balance. In the perfect mixing model introduced in (Stapersma, 1999) the heat exchange between the gas and the cylinder wall has been taken into account. However, in order to keep the assumptions consistent in this thesis, the perfect mixing model in stage II also neglects the heat exchange with the cylinder wall. The final solution for the temperature, composition and mass in the whole cylinder volume including only B zone (perfect mixing zone) is shown in equations (E. 30), (E. 31) and (E. 32).

$$y = \frac{y_{II}(0)}{1 + [y_{II}(0) \cdot \gamma - 1] \cdot \left[ 1 - e^{-\frac{1}{\gamma}(t_{sc,r} - t_{sc,r,I})} \right]} \quad (\text{E. 30})$$

$$x = x_{sc-in} - \frac{[x_{sc-in} - x_{II}(0)] \cdot e^{-\frac{1}{\gamma}(t_{sc,r} - t_{sc,r,I})}}{1 + [y_{II}(0) \cdot \gamma - 1] \cdot \left[ 1 - e^{-\frac{1}{\gamma}(t_{sc,r} - t_{sc,r,I})} \right]} \quad (\text{E. 31})$$

$$\frac{m}{m(0)} = y(0) \cdot \left\{ \gamma - \left[ \gamma - \frac{1}{y_{II}(0)} \right] \cdot e^{-\frac{1}{\gamma}(t_{sc,r} - t_{sc,r,I})} \right\} \quad (\text{E. 32})$$

where,  $x_{II}(0)$  and  $y_{II}(0)$  are the initial air mass ratio and temperature ratio of stage II, which are calculated by the two-zone scavenging model at the end of stage I ( $t_{sc,r} = t_{sc,r,I}$ ).

## F. Engine components models

### F.1 Turbocharger model

#### F.1.1 Buchi balance

The most crucial physics for a turbocharged diesel engine is the Buchi balance since it defines the cooperation between the three machines that actually make up the diesel engine: the cylinder process, the compressor and the turbine. The latter are directly cooperating through the Buchi power balance but the mass flow and turbine entry temperature in this balance interact with the cylinder process, in particular with its gas exchange. The power balance between the compressor and the turbine is governed by the “Buchi equation” (equation (F. 1)) (Stapersma, 2010c). In the Buchi balance, the turbocharger efficiency requires a good prediction of compressor and turbine efficiency and thus good models for these components and further a satisfactory model for the turbocharger mechanical losses.

$$\pi_{com} = \left[ 1 + \delta \cdot \chi \cdot \eta_{TC} \cdot \tau_{TC} \cdot \left( 1 - \frac{1}{\frac{\pi_{tur}^{\gamma_{gas}} - 1}{\gamma_{gas} - 1}} \right)^{\frac{\gamma_{air}}{\gamma_{air} - 1}} \right] \quad (F. 1)$$

Where,  $\pi_{com}$  is the compressor pressure ratio;  $\pi_{tur}$  is the turbine pressure ratio;  $\delta$  is the fuel addition factor ( $\delta = 1/(1+\lambda)$ ,  $\lambda$  is the air excess ratio);  $\chi$  is the ratio between specific heats of exhaust gas and air ( $\chi = c_{p,gas}/c_{p,air}$ );  $\eta_{TC}$  is the turbocharger efficiency;  $\tau_{TC}$  is the turbocharger temperature ratio (turbine inlet temperature divided by compressor inlet temperature);  $\gamma_{gas}$  and  $\gamma_{air}$  are the specific heat ratios of gas and air respectively.

#### F.1.2 Compressor and turbine characteristics

To predict the off-design performance, including part loads and transient operation performance, of the turbocharger as well as the turbocharged engine, the first principle

parametric compressor and turbine models developed in (Stapersma, 2013) have been used. The compressor and turbine models are capable of modelling the turbocharger characteristics, including the compressor surge, turbine choking and compressor choking at high rotational speeds. For both the compressor and turbine models, the inputs are the pressure ratio and the turbocharger rotational speed while the outputs are the mass flow, temperature ratio and the compressor or turbine efficiency.

### F.1.3 Compressor surge index

One of the safety threats to the turbocharged engine is the compressor surge, especially in part loads and dynamic operation conditions. To quantify the compressor surge behaviour, the compressor surge index (SI) indicating the nondimensional distance between the compressor operating line and the surge line is defined as illustrated in Figure F. 1. The compressor surge index is negative when the compressor operates in non-surfing area, positive when working in surging area, while zero when it is hitting the surge line (Figure F. 1).

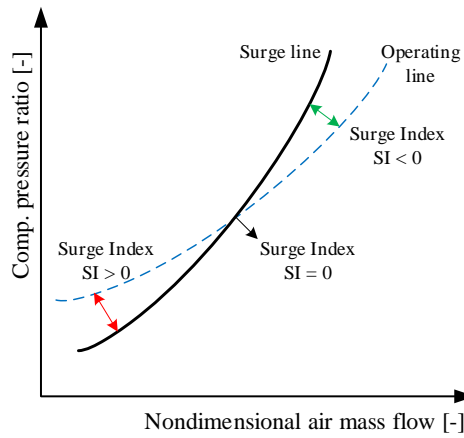


Figure F. 1: Compressor Surge Index (SI)

### F.1.4 Turbocharger mechanical efficiency

In order to model the turbocharger mechanical efficiency at various operating conditions, it is assumed that the turbocharger torque loss is a function of the turbocharger rotational speed and the compressor outlet pressure as shown in equation (F. 2).

$$M_{loss,TC}^* = 1 + a_{TC} \cdot (n_{TC}^* - 1) + b_{TC} \cdot (p_{com}^* - 1) \quad (F. 2)$$

Where,  $a_{TC}$  and  $b_{TC}$  are constants;  $M_{loss,TC}^*$ ,  $n_{TC}^*$  and  $p_{com}^*$  are the normalized torque loss, turbocharger rotational speed and the compressor outlet pressure as shown in following:

$$M_{loss,TC}^* = \frac{M_{loss,TC}}{M_{loss,TC,nom}} \quad (F. 3)$$

$$n_{TC}^* = \frac{n_{TC}}{n_{TC,nom}} \quad (F. 4)$$

$$p_{com}^* = \frac{p_{com}}{p_{com,nom}} \quad (F. 5)$$

Where,  $M_{loss,TC,nom}$ ,  $n_{TC,nom}$  and  $p_{com,nom}$  are the turbocharger torque loss, turbocharger rotational speed and the compressor outlet pressure at nominal operating condition.

## F.2 Air cooler model

The outlet temperature of the air cooler is calculated by equation (F. 6) according to the definition of the heat exchanger effectiveness  $\varepsilon_{AC}$  of the air cooler in equation (F. 7).

$$T_{CAC} = T_{ac} - \varepsilon_{AC} \cdot (T_{ac} - T_{water}) \quad (F. 6)$$

$$\varepsilon_{AC} \stackrel{def}{=} \frac{T_{ac} - T_{CAC}}{T_{ac} - T_{water}} \quad (F. 7)$$

Where,  $T_{ac}$  is the inlet temperature of the cooler;  $T_{CAC}$  is the outlet temperature of the cooler;  $T_{water}$  is the temperature of the cooling water of low temperature.

The heat exchange effectiveness  $\varepsilon_{AC}$  is modelled as a function of the air mass flow  $\Phi_{CAC}$  through the air cooler based on the theory of the effectiveness of the counter flow heat exchangers, as shown in equation (F. 8).

$$\varepsilon_{AC} = \frac{1 - \exp\left[-a \cdot (\Phi_{CAC}^*)^{-0.2} \cdot (1 - b \cdot \Phi_{CAC}^*)\right]}{1 - b \cdot \Phi_{CAC}^* \cdot \exp\left[-a \cdot (\Phi_{CAC}^*)^{-0.2} \cdot (1 - b \cdot \Phi_{CAC}^*)\right]} \quad (0 \leq b \leq 1) \quad (F. 8)$$

with,

$$a = \begin{cases} \frac{\ln\left(\frac{1 - \varepsilon_{AC,nom}}{1 - b \cdot \varepsilon_{AC,nom}}\right)}{b - 1} & (0 \leq b < 1) \\ \frac{\varepsilon_{AC,nom}}{1 - \varepsilon_{AC,nom}} & (b = 1) \end{cases} \quad (F. 9)$$

Where,  $a$  and  $b$  are constants;  $\varepsilon_{AC,nom}$  is the heat exchange effectiveness at the nominal condition; and  $\Phi_{CAC}^*$  is the normalized air mass flow through the cooler (equation (F. 10)).

$$\Phi_{CAC}^* = \frac{\Phi_{CAC}}{\Phi_{CAC,nom}} \quad (F. 10)$$

Where,  $\Phi_{CAC,nom}$  is the air mass flow through the cooler at the nominal operating condition.

## F.3 Auxiliary blower and non-return valve models

The auxiliary blower is located in parallel with the non-return valve between the charged air cooler and the inlet receiver. The blower will assist the air supply when the turbocharger is not capable of delivering sufficient air at low engine loads (Yum et al., 2017). During engine operations, when the scavenging pressure drops below a pre-set pressure (corresponding to an engine load of approximately 25-35%) the blower will start and continue to run until the scavenging pressure exceeds a certain value higher than the pre-set pressure (corresponding to an engine load of approximately 30-40%) resulting in an appropriate hysteresis (MAN, 2014).

The closing and opening of the non-return valve are automatically controlled by the pressures at two sides of the valve, i.e., the pressures at the air cooler outlet and in the inlet receiver. When the blower is not in operation, the air cooler outlet pressure is higher than the inlet receiver pressure and the valve will be open, so, the air flow will enter into the inlet receiver through the valve; otherwise, the valve is closed and the air flow will enter into the inlet receiver through the blower. The auxiliary blower is modelled as a ‘fixed speed compressor’ using the same model as that of the compressor. It is assumed that the blower operates at only two speeds, i.e., nominal speed (‘run’) and zero speed (‘stop’) and the transient processes between ‘run’ and ‘stop’ are neglected. The non-return valve is modelled as a ‘flow resistance’ element with pressure ratio of two sides of the valve as the input and mass flow through the valve as the output.

#### F.4 Exhaust valve temperature model

The model of the exhaust valve temperature for two-stroke diesel engines is updated from a model for four-stroke diesel engines introduced in (Grimmelius and Stapersma, 2000) taking the differences between the gas exchange processes of two-stroke and four-stroke diesel engines into account. It is assumed that the heating of the exhaust valve of the two-stroke engine happens during the blowdown process and the cooling of the exhaust valve happens in the second stage of the scavenging process and the (extra) expelling process. The exhaust valve temperature is calculated by equation (F. 11). Note that, the exhaust valve temperature calculated by equation (F. 11) is in effect the average temperature over the engine cycle weighted by the heating and cooling effects.

$$T_{ev} = \frac{T_6 + r \cdot T_{sc-in}}{1 + r} \quad (F. 11)$$

$$r = \begin{cases} s^{0.8} \cdot \left( \frac{T_{sc-in}}{T_6} \right)^{0.25} \cdot \left( \frac{EC - IC}{IO - EO} \right)^{0.2} & t_{sc,r} < t_{sc,r,I} \\ s^{0.8} \cdot \left( \frac{T_{sc-in}}{T_6} \right)^{0.25} \cdot \left[ \frac{EC - \left[ (IC - IO) \cdot \frac{t_{sc,r,I}}{t_{sc,r}} + IO \right]}{IO - EO} \right]^{0.2} & t_{sc,r} \geq t_{sc,r,I} \end{cases} \quad (F. 12)$$

Where,  $s$  is the slip factor of the engine;  $t_{sc,r}$  is the relative scavenging time;  $t_{sc,r,I}$  is the relative time of first stage of the scavenging process.

#### F.5 Engine mechanical and heat losses models

In the MVFPP engine model, the engine mechanical losses are modelled as a frictional mean effective pressure using the Chen & Flynn model (Chen and Flynn, 1965), while the engine heat losses are modelled using the Woschni’s model (Woschni, 1967).

## G. Correction of C4-55 Characteristics

The corrected Wageningen C4-55 propeller has been used to model the propeller of the benchmark chemical tanker. The correction of the C4-55 characteristics has been made according to the model test data of the MAN Alpha propeller open water characteristics at design pitch. The same correction method, i.e., using the nondimensional multiplying correction factors, for the propeller characteristics introduced in Appendix A.1 has been used here.

The correction philosophy is that the ship effective power  $P_E$ , wake factor  $w$ , thrust deduction factor  $t$  and the relative rotative efficiency  $\eta_R$  are assumed and kept the same as those of the model test data; and only the delivered power  $P_D$ , propeller speed  $n$  and propeller characteristics will be corrected. The correction is made by two steps: firstly, calculating the correction factors of delivered power and propeller speed; and secondly, calculating the correction factors of the propeller characteristics. Note that the model test data of both the ship and propeller used in the correction of C4-55 is the corrected test data as previously introduced in Appendix A.1.

### G.1 Correction factors of the delivered power and shaft speed

The correction factors of the delivered power and shaft speed are calculated as shown as follows:

| Procedure:   | Variable<br>[Unit] |
|--|--------------------|
| The ship effective power remains the same as the corrected model test data.              | $P_E$ [kW]         |
| The wake factor remains the same as the corrected model test data.                       | $w$ [-]            |
| The propeller thrust deduction factor remains the same as the corrected model test data. | $t$ [-]            |
| The relative rotative efficiency remains the same as the corrected model test data.      | $\eta_R$ [-]       |
| The needed propeller thrust can be calculated by:  | $T_P$ [kN]         |

$$T_P = \frac{P_E/V_S}{1-t}$$

The propeller advance speed can be calculated by:

$$V_A = V_S \cdot (1-w)$$

$V_A$  [m/s]

The propeller thrust loading coefficient  $K_T/J^2$  can be calculated by:

$$\frac{K_T}{J^2} = \frac{T_P}{\rho \cdot V_A^2 \cdot D^2}$$

$K_T/J^2$  [-]

The propeller advance coefficient  $J$  can be obtained by interpolating the original C4-55 open water characteristics using the propeller thrust loading coefficient  $K_T/J^2$ .

$J$  [-]

The propeller open water torque coefficient  $K_{Q,0}$  can be obtained by interpolating the original C4-55 open water characteristics using the propeller thrust loading coefficient  $K_T/J^2$ .

$K_{Q,0}$  [-]

The propeller behind-hull torque coefficient  $K_Q$  can be calculated by:

$$K_Q = \frac{K_{Q,0}}{\eta_r}$$

$K_Q$  [-]

The propeller rotational speed can be calculated by:

$$N_P = \frac{V_A}{J \cdot D}$$

$N_P$  [rpm]

The propeller torque can be calculated by:

$$Q_P = K_Q \cdot \rho \cdot N_P^2 \cdot D^5$$

$Q_P$  [kNm]

The delivered power can be calculated by:

$$P_d = 2\pi \cdot N_P \cdot Q_P$$

$P_d$  [kW]

The correction factors for the propeller rotational speed can be calculated by:

$$C_N = \frac{N_{P,test}}{N_P}$$

$C_N$  [-]

The correction factors for the delivered power can be calculated by:

$$C_{Pd} = \frac{P_{d,test}}{P_d}$$

$C_{Pd}$  [-]

Finally, the mean value of correction factors for the shaft speed and delivered power are:

$$C_N = 1.0427; C_{Pd} = 1.0277.$$

## G.2 Correction factors of C4-55 propeller characteristics

The correction factors for open water characteristics of propeller C4-55 are calculated as follows:

$$C_J = \frac{C_{1-w}}{C_N} = \frac{1}{1.0427} = 0.9591$$

$$C_{Kq} = \frac{C_{Pd} \cdot C_{\eta r}}{C_N^3} = \frac{1.0277 \times 1}{1.0427^3} = 0.9066$$

$$C_{Kt} = \frac{C_{pe}}{C_N^2 \cdot C_{1-t}} = \frac{1}{1.0427^2 \times 1} = 0.9198$$

And the open water characteristics of C4-55 for all pitches is corrected by:

$$J_{corrected} = C_J \cdot J_{original}$$

$$K_{t,corrected} = C_{Kt} \cdot K_{t,original}$$

$$K_{q,corrected} = C_{Kq} \cdot K_{q,original}$$

Note that the correction factors are determined by the data at design pitch, however, the same correction factors have been used for correcting the characteristics of all pitches, although in fact the correction factors for different pitches could be different.





## References

- Abkowitz, M.A., 1964. Lectures on ship hydrodynamics: Steering and manoeuvrability. Hydro and Aerodynamic Laboratory. Lyngby, Denmark.
- Acciaro, M., 2014. Real option analysis for environmental compliance: LNG and emission control areas. *Transportation Research Part D: Transport and Environment*. 28, 41-50.
- Acomi, N., Acomi, O.C., 2014. Improving the Voyage Energy Efficiency by Using EEOI. *Procedia - Social and Behavioral Sciences*. 138, 531-536.
- AEsoy, V., Einang, P.M., Stenersen, D., Hennie, E., Valberg, I., 2011. LNG-fuelled engines and fuel systems for medium-speed engines in maritime applications. *SAE Technical Paper*. (No. 2011-01-1998)
- Akagi, S., 1991. Synthetic aspects of transport economy and transport vehicle performance with reference to high speed marine vehicles. *Proceeding 1st International Conference on Fast Sea Transportation - FAST 91*, Trondheim.
- Akagi, S., Morishita, M., 2001. Transport economy-based evaluation and assessment of the use of fast ships in passenger-car ferry and freighter systems. *Proceeding 6th International Conference on Fast Sea Transportation - FAST 2001*, London.
- Altosole, M., Borlenghi, M., Capasso, M., Figari, M., 2007. Computer-based design tool for a fuel efficient-low emissions marine propulsion plant. *ICMRT Proceedings*.
- Andersen, F.H., Hult, J., Nogenmyr, K., Mayer, S., 2013. Numerical investigation of the scavenging process in marine two-stroke diesel engines. *SAE Technical Paper*. No. 2013-01-2647
- Anderson, M., Salo, K., Fridell, E., 2015. Particle- and Gaseous Emissions from an LNG Powered Ship. *Environmental Science & Technology*. 49(20), 12568-12575.
- Andersson, K., Baldi, F., Brynolf, S., Lindgren, J.F., Granhag, L., Svensson, E., 2016. *Shipping and the Environment*. Springer. Berlin/Heidelberg, Germany. p.3-27.
- Aoki, I., Kijima, K., Furukawa, Y., Nakiri, Y., 2006. On the Prediction Method for Maneuverability of a Full Scale Ship (in Japanese). *Journal of the Japan Society of Naval Architects and Ocean Engineers*. 3, 157-165.
- Armstrong, V.N., Banks, C., 2015. Integrated approach to vessel energy efficiency. *Ocean Engineering*. 110, 39-48.

- Asprion, J., Chinellato, O., Guzzella, L., 2013. A fast and accurate physics-based model for the NO<sub>x</sub> emissions of Diesel engines. *Applied Energy*. 103, 221-233.
- Aung, M.Z., Umeda, N., 2020. Manoeuvring simulations in adverse weather conditions with the effects of propeller and rudder emergence taken into account. *Ocean Engineering*. 197, 106857.
- Barrass, B., 2004. Ship design and performance for masters and mates. Butterworth-Heinemann, Barton, P.I., 1992. The modelling and simulation of combined discrete/continuous processes. PhD Thesis. Imperial College of Science, Technology and Medicine. London.
- Bennabi, N., Charpentier, J.F., Menana, H., Billard, J.Y., Genet, P., 2016. Hybrid propulsion systems for small ships: Context and challenges. 2016 XXII International Conference on Electrical Machines (ICEM). IEEE. p.2948-2954.
- Bialystocki, N., Konovessis, D., 2016. On the estimation of ship's fuel consumption and speed curve: A statistical approach. *Journal of Ocean Engineering and Science*. 1(2), 157-166.
- Bitner-Gregerse, E.M., Soares, C.G., Vantorre, M., 2016. Adverse Weather Conditions for Ship Manoeuvrability. *Transportation Research Procedia*. 14, 1631-1640.
- Bossel, H., 1994. Modeling and simulation. A K Peters/CRC Press, New York.
- Bouman, E.A., Lindstad, E., Rialland, A.I., Strømman, A.H., 2017. State-of-the-art technologies, measures, and potential for reducing GHG emissions from shipping - A review. *Transportation Research Part D: Transport and Environment*. 52, 408-421.
- Brynnolf, S., Fridell, E., Andersson, K., 2014. Environmental assessment of marine fuels: liquefied natural gas, liquefied biogas, methanol and bio-methanol. *Journal of Cleaner Production*. 74, 86-95.
- Buhaug, Ø., Corbett, J.J., Endresen, Ø., Eyring, V., Faber, J., Hanayama, S., Lee, D.S., Lee, D., Lindstad, H., Markowska, A.Z., 2009. Second imo ghg study 2009. International Maritime Organization (IMO) London, UK. 20
- Burel, F., Taccani, R., Zuliani, N., 2013. Improving sustainability of maritime transport through utilization of Liquefied Natural Gas (LNG) for propulsion. *Energy*. 57, 412-420.
- Cagin, S., Fischer, X., Delacourt, E., Bourabaa, N., Morin, C., Coutellier, D., Carré, B., Loumé, S., 2016. A new reduced model of scavenging to optimize cylinder design. *SIMULATION*. 92(6), 507-520.
- Carlton, J., Aldwinkle, J., Anderson, J., 2013. Future ship powering options: exploring alternative methods of ship propulsion. London: Royal Academy of Engineering.
- Carlton, J.S., 2019. Marine propellers and propulsion (Fourth Edition). Butterworth-Heinemann, Kidlington, Oxford.
- Chapman, L., 2007. Transport and climate change: a review. *Journal of Transport Geography*. 15(5), 354-367.
- Chen, S.K., Flynn, P.F., 1965. Development of a single cylinder compression ignition research engine. 650733. SAE Technical Paper.
- Clarke, D., 1983. The application of manoeuvring criteria in hull design using linear theory. *Trans RINA*. 125, 45-68.
- Colonna, P., van Putten, H., 2007. Dynamic modeling of steam power cycles.: Part I— Modeling paradigm and validation. *Applied Thermal Engineering*. 27(2), 467-480.
- Coraddu, A., Figari, M., Savio, S., 2014. Numerical investigation on ship energy efficiency by Monte Carlo simulation. *Proceedings of the Institution of Mechanical Engineers Part M Journal of Engineering for the Maritime Environment*. 228(3), 220-234.

- Coraddu, A., Oneto, L., Baldi, F., Anguita, D., 2015. Ship efficiency forecast based on sensors data collection: Improving numerical models through data analytics. OCEANS 2015-Genova. IEEE., 1-10.
- Dallinga, R., Rapuc, S., de Jong, J., 2020. LOW-POWERED SHIPS IN HARSH WEATHER. SWZ MARITIME. 141(2), 38-42.
- Dang, J., Van den Boom, H., Ligtelijn, J.T., 2013. The Wageningen C-and D-series propellers. 12th International Conference on Fast Sea Transportation FAST2013, Amsterdam, The Netherlands.
- Dedes, E.K., Hudson, D.A., Turnock, S.R., 2016. Investigation of Diesel Hybrid systems for fuel oil reduction in slow speed ocean going ships. Energy. 114, 444-456.
- Del Re, L., Allgöwer, F., Glielmo, L., Guardiola, C., Kolmanovsky, I., 2010. Automotive model predictive control: models, methods and applications. Springer, Berlin.
- Ding, Y., 2011. Characterising Combustion in Diesel Engines using parameterised finite stage cylinder process models. PhD Thesis. Delft University of Technology.
- Ding, Y., Li, J., Xiang, L., Zhang, Y., 2019. Two-Zone Simulation Modeling of Gas Exchange Process of Super-Long-Stroke Low-Speed Diesel Engine (in Chinese). Journal of Harbin Engineering University. 40(1), 210-216.
- Dirix, T., 2002. Renewed Concept Exploration Model for Manoeuvring. Master Thesis. Delft University of Technology. Delft, The Netherlands.
- Eyring, V., Isaksen, I.S.A., Berntsen, T., Collins, W.J., Corbett, J.J., Endresen, O., Grainger, R.G., Moldanova, J., Schlager, H., Stevenson, D.S., 2010. Transport impacts on atmosphere and climate: Shipping. Atmospheric Environment. 44(37), 4735-4771.
- Faltinsen, O.M., 1980. Prediction of resistance and propulsion of a ship in a seaway. In Proceedings of the 13th symposium on naval hydrodynamics, Tokyo.
- Figari, M., Campora, U., 2003. Numerical simulation of ship propulsion transients and full-scale validation. Proceedings of the Institution of Mechanical Engineers, Part M: Journal of Engineering for the Maritime Environment. 217(1), 41-52.
- Figari, M., Guedes Soares, C., 2009. Fuel consumption and exhaust emissions reduction by dynamic propeller pitch control. Analysis and design of marine structures (Guedes Soares C & Das PK eds)., 543-550.
- Fossen, T.I., Wiley, I.O.S., 2011. Handbook of marine craft hydrodynamics and motion control. Wiley, Chichester, West Sussex, U.K.
- Foteinos, M.I., Papazoglou, A., Kyrtatos, N.P., Stamatelos, A., Zogou, O., Stamatellou, A., 2019. A Three-Zone Scavenging Model for Large Two-Stroke Uniflow Marine Engines Using Results from CFD Scavenging Simulations. Energies. 12(9), 1719.
- Fujiwara, T., Ueno, M., Ikeda, Y., 2006. Cruising performance of a large passenger ship in heavy sea. Proceedings of the International Offshore and Polar Engineering Conference. p.304-311.
- Gabrielli, G., Von Karman, T., 1950. What price speed? Specific power required for propulsion of vehicles. Mechanical Engineering. 72, 775-781.
- Geertsma, R.D., Negenborn, R.R., Visser, K., Hopman, J.J., 2017a. Design and control of hybrid power and propulsion systems for smart ships: A review of developments. Applied Energy. 194, 30-54.
- Geertsma, R.D., Negenborn, R.R., Visser, K., Loonstijn, M.A., Hopman, J.J., 2017b. Pitch control for ships with diesel mechanical and hybrid propulsion: Modelling, validation and performance quantification. Applied Energy. 206, 1609-1631.

- Geertsma, R.D., Visser, K., Negenborn, R.R., 2018. Adaptive pitch control for ships with diesel mechanical and hybrid propulsion. *Applied Energy*. 228, 2490-2509.
- Godjevac, M., Drijver, J., de Vries, L., Stapersma, D., 2016. Evaluation of losses in maritime gearboxes. *Proceedings of the Institution of Mechanical Engineers, Part M: Journal of Engineering for the Maritime Environment*. 230(4), 623-638.
- Grimmelius, H., Mesbahi, E., Schulten, P., Stapersma, D., 2007. The use of diesel engine simulation models in ship propulsion plant design and operation. *CIMAC Congress 2007*, Vienna.
- Grimmelius, H.T., Stapersma, D., 2000. Control optimisation and load prediction for marine diesel engines using a mean value simulation model. *ENSUS Conference 2000*, Newcastle upon Tyne. p.212-229.
- Guan, C., Theotokatos, G., Zhou, P., Chen, H., 2014. Computational investigation of a large containership propulsion engine operation at slow steaming conditions. *Applied Energy*. 130, 370-383.
- Guzzella, L., Onder, C., 2009. *Introduction to modeling and control of internal combustion engine systems*. Springer, Berlin.
- Hangos, K., Cameron, I., 2001. *Process modelling and model analysis*. Academic Press, London, UK.
- Harvald, S.A., 1983. *Resistance and propulsion of ships*. Wiley, New York.
- Hasegawa, K., 1980. On a performance criterion of autopilot navigation. *The Japan Society of Naval Architects and Ocean Engineers*. p.93-103.
- He, F., Wei, J., 2017. Numerical Simulation of Scavenging Process of Large 2-Stroke Marine Diesel Engine. *2nd International Conference on Automatic Control and Information Engineering (ICACIE 2017)*. Atlantis Press.
- Holt, P., Nielsen, U.D., 2021. Preliminary assessment of increased main engine load as a consequence of added wave resistance in the light of minimum propulsion power. *Applied Ocean Research*. 108, 102543.
- Holtrop, J., 1984. A statistical re-analysis of resistance and propulsion data. *International Shipbuilding Progress*. 31(363), 272-276.
- Holtrop, J., Mennen, G.G., 1982. An approximate power prediction method. *International Shipbuilding Progress*. 29(335), 166-170.
- Hou, Y.H., Kang, K., Liang, X., 2019. Vessel speed optimization for minimum EEOI in ice zone considering uncertainty. *Ocean Engineering*. 188, 106240.
- IMO, 2014. 2014 Guidelines on the method of calculation of the attained energy efficiency design index (EEDI) for new ships.
- IMO, 2015. *Third IMO Greenhouse Gas Study 2014, executive summary and final report*. International Maritime Organisation (IMO), London.
- IMO, 2016a. Results of research project "Energy Efficient Safe Ship Operation" (SHOPERA) (Submitted by Denmark, Germany, Norway and Spain). MEPC 70/INF.33.
- IMO, 2016b. Report of JASNAOE research project for determining minimum propulsion power (Submitted by Japan). MEPC 70/INF.35.
- IMO, 2018. ANNEX 5 RESOLUTION MEPC.308(73) (adopted on 26 October 2018) 2018 GUIDELINES ON THE METHOD OF CALCULATION OF THE ATTAINED ENERGY EFFICIENCY DESIGN INDEX (EEDI) FOR NEW SHIPS.
- IMO, 2019. Finalization of the revised 2013 Interim Guidelines for determining minimum propulsion power to maintain the manoeuvrability of ships in adverse conditions Submitted by ICS and RINA.

- IMO, 2020. Fourth IMO GHG Study 2020 - Final report. International Maritime Organization (IMO). London.
- Inoue, S., Hirano, M., Kijima, K., Takashina, J., 1981. A practical calculation method of ship maneuvering motion. *International Shipbuilding Progress*. 28(325), 207-222.
- ITTC, 1999. The Specialist Committee on Trials and Monitoring: Final Report and Recommendations to the 22nd ITTC.
- ITTC, 2017. ITTC-Recommended Procedures and Guidelines: Full Scale Manoeuvring Trials. 28th International Towing Tank Conference. 7.5-04-02-01.
- Jacobs, F., Visser, K., Stapersma, D., 2016. Maritime environmental performance indicators for urban waterways in Amsterdam. *Proceedings of the Institution of Mechanical Engineers, Part M: Journal of Engineering for the Maritime Environment*., 1475090216676433.
- Jafarzadeh, S., Schjøberg, I., 2018. Operational profiles of ships in Norwegian waters: An activity-based approach to assess the benefits of hybrid and electric propulsion. *Transportation Research Part D: Transport and Environment*. 65, 500-523.
- Jo, J.Y., Kwon, Y.S., Lee, J.W., Park, J.S., Rho, B.H., Choi, W., 2013. Acute respiratory distress due to methane inhalation. *Tuberculosis and respiratory diseases*. 74(3), 120-123.
- Kalikatzarakis, M., Geertsma, R.D., Boonen, E.J., Visser, K., Negenborn, R.R., 2018. Ship energy management for hybrid propulsion and power supply with shore charging. *Control Engineering Practice*. 76, 133-154.
- Kanellos, F.D., Prousalidis, J.M., Tsekouras, G.J., 2014. Control system for fuel consumption minimization – gas emission limitation of full electric propulsion ship power systems. *Proceedings of the Institution of Mechanical Engineers, Part M: Journal of Engineering for the Maritime Environment*. 228(1), 17-28.
- Kennell, C., 1998. Design trends in high-speed transport. *Marine Technology and Sname News*. 35(3), 127.
- Kern, C., Tvete, H.A., Alnes, Ø.Å., Sletten, T., Hansen, K.R., Knafl, A., Sames, P., Puchalski, S., 2019. Battery Hybrid Oceangoing Cargo Ships. CIMAC Congress 2019, Vancouver, Canada.
- Kijima, K., Katsuno, T., Nakiri, Y., Furukawa, Y., 1990. On the manoeuvring performance of a ship with the parameter of loading condition. *Journal of the society of naval architects of Japan*. 1990(168), 141-148.
- Kijima, K., Nakiri, Y., 1999. Approximate expression for hydrodynamic derivatives of ship manoeuvring motion taking into account of the effect of stern shape (In Japanese). *Transactions of the West-Japan Society of Naval Architects*. 98, 67-77.
- Kijima, K., Nakiri, Y., 2002. On the practical prediction method for ship manoeuvring characteristics. *Transactions of the West-Japan Society of Naval Architects*., 21-31.
- Kijima, K., Nakiri, Y., 2003. On the practical prediction method for ship manoeuvring characteristics (in Japanese). *Transactions of the West-Japan Society of Naval Architects*. 105, 21-31.
- Kijima, K., Nakiri, Y., Furukawa, Y., 2000. On a prediction method for ship manoeuvrability. *The international workshop on ship manoeuvrability-25 years CPMC at HSVA, Hamburg*.
- Kitamura, F., Ueno, M., Fujiwara, T., Sogihara, N., 2017. Estimation of above water structural parameters and wind loads on ships. *Ships and Offshore Structures*. 12(8), 1100-1108.
- Klein Woud, H., Stapersma, D., 2002. Design of propulsion and electric power generation systems. IMarEST, Institute of Marine Engineering, Science and Technology, London.

- Kwasieckyj, B., 2013. Efficiency analysis and design methodology of hybrid propulsion systems. Master Thesis. Delft University of Technology. Delft, the Netherlands.
- Lamas, M.I., Rodríguez Vidal, C.G., 2012. Computational fluid dynamics analysis of the scavenging process in the MAN B&W 7S50MC two-stroke marine diesel engine. *Journal of Ship Research*. 56(3), 154-161.
- Lee, C., Lee, H.L., Zhang, J., 2015. The impact of slow ocean steaming on delivery reliability and fuel consumption. *Transportation Research Part E: Logistics and Transportation Review*. 76(Supplement C), 176-190.
- Lehtoranta, K., Aakko-Saksa, P., Murtonen, T., Vesala, H., Kuittinen, N., Rönkkö, T., Ntziachristos, L., Karjalainen, P., Timonen, H., Teinilä, K., 2019. Particle and Gaseous Emissions from Marine Engines Utilizing Various Fuels and Aftertreatment Systems. CIMAC Congress 2019, Vancouver, Canada.
- Lindstad, E., Borgen, H., Eskeland, G.S., Paalson, C., Psaraftis, H., Turan, O., 2019. The Need to Amend IMO's EEDI to Include a Threshold for Performance in Waves (Realistic Sea Conditions) to Achieve the Desired GHG Reductions.
- Lindstad, H., Eskeland, G.S., 2015. Low carbon maritime transport: How speed, size and slenderness amounts to substantial capital energy substitution. *Transportation Research Part D: Transport and Environment*. 41(Supplement C), 244-256.
- Liu, H., Lu, L., Wang, Z., 2014. Evaluation analysis of scavenging process of two-stroke marine diesel engine by experiment and simulation. *Journal of Thermal Science and Technology*. 9(2), JTST0012-JTST0012.
- Liu, J., 2017. Impacts of Rudder Configurations on Inland Vessel Manoeuvrability. PhD. Delft University of Technology.
- MAN, 2014. MAN B&W S35ME-B9.3-TII Project Guide - Electronically Controlled Two-Stroke Engines with Camshaft Controlled Exhaust Valves. MAN Diesel & Turbo, Copenhagen, Denmark.
- MAN, 2018. Basic principles of ship propulsion. MAN Diesel & Turbo, Copenhagen, Denmark.
- MEPC, 2009. Guidelines for voluntary use of the ship energy efficiency operational indicator (EEOI). International Maritime Organization, Report.
- MEPC, 2011. AMENDMENTS TO THE ANNEX OF THE PROTOCOL OF 1997 TO AMEND THE INTERNATIONAL CONVENTION FOR THE PREVENTION OF POLLUTION FROM SHIPS, 1973, AS MODIFIED BY THE PROTOCOL OF 1978 RELATING THERETO. Resolution MEPC.203(62).
- MEPC, 2013. 2013 INTERIM GUIDELINES FOR DETERMINING MINIMUM PROPULSION POWER TO MAINTAIN THE MANOEUVRABILITY OF SHIPS IN ADVERSE CONDITIONS. RESOLUTION MEPC.232(65).
- MEPC, 2015. AMENDMENTS TO THE 2013 INTERIM GUIDELINES FOR DETERMINING MINIMUM PROPULSION POWER TO MAINTAIN THE MANOEUVRABILITY OF SHIPS IN ADVERSE CONDITIONS. RESOLUTION MEPC.262(68).
- MEPC, 2017. 2013 INTERIM GUIDELINES FOR DETERMINING MINIMUM PROPULSION POWER TO MAINTAIN THE MANOEUVRABILITY OF SHIPS IN ADVERSE CONDITIONS. MEPC.1/Circ.850/Rev.2.
- Misra, S.C., 2016. Design principles of ships and marine structures. CRC Press, Boca Raton.
- Molland, A.F., Turnock, S.R., 2011. Marine rudders and control surfaces: principles, data, design and applications. Butterworth-Heinemann,

- Molland, A.F., Turnock, S.R., Hudson, D.A., 2011. Ship resistance and propulsion. Practical estimation of ship propulsive power. Cambridge university press, New York.
- Moreno-Gutiérrez, J., Pájaro-Velázquez, E., Amado-Sánchez, Y., Rodríguez-Moreno, R., Calderay-Cayetano, F., Durán-Grados, V., 2019. Comparative analysis between different methods for calculating on-board ship's emissions and energy consumption based on operational data. *Science of the Total Environment*. 650, 575-584.
- Mori, M., 1995. A Note on Hull Form Design (Part 24) (In Japanese). *Journal of Ship Science*. 48, 40-49.
- Mundt, T., Wienke, J., Hawmman, L., 2019. Overcoming the Conflict of EEDI and Minimum Power for Safe Operation in Adverse Weather, the Shaft Power Limitation - Concept. CIMAC Congress 2019, Vancouver, Canada.
- Nanda, K.S., Jia, B., Smallbone, A., Roskilly, P.A., 2017. Fundamental Analysis of Thermal Overload in Diesel Engines: Hypothesis and Validation.
- Ogawa, A., Koyama, T., Kijima, K., 1977. MMG report-I, on the mathematical model of ship manoeuvring. *Bull Soc Naval Archit Jpn*. 575(22-28)
- Oltmann, P., 2003. Identification of hydrodynamic damping derivatives - a pragmatic approach. MARSIM - International Conference on Marine simulation and Ship Manoeuvrability, Kanazawa, Japan.
- Papanikolaou, A., 2005. Review of advanced marine vehicles concepts. *Proceedings of the Seventh International Symposium on High speed marine vehicles (HSMV 2005)*, Naples, Italy. p.21-23.
- Papanikolaou, A., 2014. Ship design: methodologies of preliminary design. Springer, London.
- Papanikolaou, A., Zaraphonitis, G., Bitner-Gregersen, E., Shigunov, V., Moctar, O.E., Soares, C.G., Reddy, D.N., Sprenger, F., 2016. Energy Efficient Safe SHip Operation (SHOPERA). *Transportation Research Procedia*. 14, 820-829.
- Payri, F., Olmeda, P., Martín, J., García, A., 2011. A complete 0D thermodynamic predictive model for direct injection diesel engines. *Applied Energy*. 88(12), 4632-4641.
- Perera, L.P., Mo, B., Kristjánsson, L.A., Jønvik, P.C., Svandal, J.Ø., 2015. Evaluations on ship performance under varying operational conditions. the 34th International Conference on Ocean, Offshore and Arctic Engineering, St. John's, Newfoundland, Canada. OMAE2015-41793.
- Psaraftis, H.N., 2019a. Sustainable shipping: a cross-disciplinary view. Springer, Cham, Switzerland.
- Psaraftis, H.N., 2019b. Decarbonization of maritime transport: to be or not to be? *Maritime Economics & Logistics*. 21(3), 353-371.
- Psaraftis, H.N., Kontovas, C.A., 2010. Balancing the economic and environmental performance of maritime transportation. *Transportation Research Part D: Transport and Environment*. 15(8), 458-462.
- Psaraftis, H.N., Kontovas, C.A., 2013. Speed models for energy-efficient maritime transportation: A taxonomy and survey. *Transportation Research Part C: Emerging Technologies*. 26(Supplement C), 331-351.
- Refsgaard, J.C., Henriksen, H.J., 2004. Modelling guidelines - terminology and guiding principles. *Advances in Water Resources*. 27(1), 71-82.
- Roskilly, A.P., Palacin, R., Yan, J., 2015. Novel technologies and strategies for clean transport systems. *Applied Energy*. 157(Supplement C), 563-566.



- Safaei, A., Ghassemi, H., Ghiasi, M., 2015. Voyage Optimization for a Very Large Crude Carrier Oil Tanker: a Regional Voyage Case Study. *Scientific Journals of the Maritime University of Szczecin*. 44(116), 83-89.
- Sapra, H., Godjevac, M., Visser, K., Stapersma, D., Dijkstra, C., 2017. Experimental and simulation-based investigations of marine diesel engine performance against static back pressure. *Applied Energy*. 204, 78-92.
- Schinas, O., Butler, M., 2016. Feasibility and commercial considerations of LNG-fueled ships. *Ocean Engineering*. 122, 84-96.
- Schlesinger, S., 1979. Terminology for model credibility. *Simulation*. 32(3), 103-104.
- Schulten, P., 2005. The interaction between diesel engines, ship and propellers during manoeuvring. PhD Thesis. Delft University of Technology.
- Schulten, P.J.M., Stapersma, D., 2003. Mean Value Modeling of the Gas Exchange of a 4-stroke Diesel Engine for use in powertrain applications. SAE Technical Paper. No. 2003-01-0219
- Seiliger, M., 1922. *Graphische Thermodynamik und Berechnen der Verbrennungs-Maschinen und Turbinen*. Julius Springer, Berlin.
- Seiliger, M., 1926. *Die Hochleistungs-Dieselmotoren*. Julius Springer, Berlin.
- Sher, E., 1990. Scavenging the two-stroke engine. *Progress in Energy and Combustion Science*. 16(2), 95-124.
- Shi, W., 2013. Dynamics of Energy System Behaviour and Emissions of Trailing Suction Hopper Dredgers. PhD Thesis. Delft University of Technology. Delft, the Netherlands.
- Shigunov, V., 2018. Manoeuvrability in adverse conditions: rational criteria and standards. *Journal of Marine Science and Technology*. 23(4), 958-976.
- Shigunov, V., 2019b. Assessment of Maneuverability in Waves. *Journal of Ship Research*. 63(2), 78-93.
- Shigunov, V., 2020. Practical assessment of manoeuvrability in adverse conditions. *Ocean Engineering*. 203, 107113.
- Shigunov, V., Guo, B., Reddy, D.N., Lalovic, I., 2019a. Manoeuvrability in adverse conditions: Case studies. *Ocean Engineering*. 179, 371-386.
- Sigurdsson, E., Ingvorsen, K.M., Jensen, M.V., Mayer, S., Matlok, S., Walther, J.H., 2014. Numerical analysis of the scavenge flow and convective heat transfer in large two-stroke marine diesel engines. *Applied Energy*. 123, 37-46.
- Stapersma, D., 1999. Scavenge model for diesel engine simulation: Simultaneous cooling and cleaning in perfect mixing element (Internal report). Royal Netherlands Naval College.
- Stapersma, D., 2008. The influence of turbo charger matching on propulsion performance. INEC 2008, Embracing the future, 1-3 April 2008, Hamburg, Germany; HT Grimmeliuss.
- Stapersma, D., 2010a. Diesel Engines - A Fundamental Approach to Performance Analysis, Turbocharging, Combustion, Emissions and Heat Transfer. Emissions and Heat transfer, Part II: Diesel engines B - Combustion, Emissions and Heat Transfer. Lecture Notes NLDA/TU Delft April 2010. NLDA & Delft UT, Delft.
- Stapersma, D., 2010b. Diesel Engines - A Fundamental Approach to Performance Analysis, Turbocharging, Combustion, Emissions and Heat Transfer. Performance Analysis, Part I: Diesel engines A - Performance analysis and Turbocharging. Lecture Notes NLDA/TU Delft April 2010.
- Stapersma, D., 2010c. Diesel Engines - A Fundamental Approach to Performance Analysis, Turbocharging, Combustion, Emissions and Heat Transfer. Turbocharging, Part I: Diesel

- engines A - Performance analysis and Turbocharging. Lecture Notes NLDA/TU Delft April 2010.
- Stapersma, D., 2013. A general model for off-design performance of a single stage turbomachine (KIM-PFS-97-111, issue D) (Internal report). Delft University of Technology. Delft.
- Stapersma, D., 2016a. Some thoughts on an Energy Efficiency Design Index for naval ships. 13th International Naval Engineering Conference (INEC 2016), Bristol UK.
- Stapersma, D., 2016b. Calibrating and Matching the Mean Value First Principle Diesel Engine Model (Internal report). Delft University of Technology. Delft.
- Stapersma, D., 2017. Main Propulsion Arrangement and Power Generation Concepts. Encyclopedia of Maritime and Offshore Engineering. John Wiley & Sons, Ltd. p.1-40.
- Sui, C., de Vos, P., Stapersma, D., Visser, K., Ding, Y., 2020. Fuel Consumption and Emissions of Ocean-Going Cargo Ship with Hybrid Propulsion and Different Fuels over Voyage. Journal of Marine Science and Engineering. 8(8)
- Sui, C., Song, E., Stapersma, D., Ding, Y., 2017. Mean value modelling of diesel engine combustion based on parameterized finite stage cylinder process. Ocean Engineering. 136, 218-232.
- Sui, C., Stapersma, D., Visser, K., de Vos, P., Ding, Y., 2019a. Energy effectiveness of ocean-going cargo ship under various operating conditions. Ocean Engineering. 190, 106473.
- Sui, C., Stapersma, D., Visser, K., Ding, Y., de Vos, P., 2019b. Impact of Battery-Hybrid Cargo Ship Propulsion on Fuel Consumption and Emissions during Port Approaches. CIMAC Congress 2019, Vancouver, Canada.
- Taljegard, M., Brynolf, S., Grahn, M., Andersson, K., Johnson, H., 2014. Cost-effective choices of marine fuels in a carbon-constrained world: results from a global energy model. Environmental Science & Technology. 48(21), 12986-12993.
- Taskar, B., Yum, K.K., Steen, S., Pedersen, E., 2016. The effect of waves on engine-propeller dynamics and propulsion performance of ships. Ocean Engineering. 122, 262-277.
- Theotokatos, G., Guan, C., Chen, H., Lazakis, I., 2018. Development of an extended mean value engine model for predicting the marine two-stroke engine operation at varying settings. Energy. 143, 533-545.
- Thomson, H., Corbett, J.J., Winebrake, J.J., 2015. Natural gas as a marine fuel. Energy Policy. 87, 153-167.
- Trivyza, N.L., Rentizelas, A., Theotokatos, G., 2020. A Comparative Analysis of EEDI Versus Lifetime CO<sub>2</sub> Emissions.
- Ueno, M., Tsukada, Y., Tanizawa, K., 2013. Estimation and prediction of effective inflow velocity to propeller in waves. Journal of Marine Science and Technology. 18(3), 339-348.
- UNCTAD, 2018. 50 Years of Review of Maritime Transport 1968-2018: Reflecting on the past, exploring the future.
- UNCTAD, 2019. Review of Maritime Transport 2019. UNITED NATIONS PUBLICATION, Geneva.
- van Putten, H., Colonna, P., 2007. Dynamic modeling of steam power cycles: Part II – Simulation of a small simple Rankine cycle system. Applied Thermal Engineering. 27(14), 2566-2582.
- Ventikos, N.P., Koimtzoglou, A., Louzis, K., Eliopoulou, E., 2015. Statistics for marine accidents in adverse weather conditions. Proceedings of MARTECH 2014: 2nd International Conference on Maritime Technology and Engineering. p.243-251.

- Vrijdag, A., 2009. Control of Propeller Cavitation in Operational Conditions. PhD. Thesis. Delft University of Technology.
- Vu, T.L., Ayu, A.A., Dhupia, J.S., Kennedy, L., Adnanes, A.K., 2015. Power Management for Electric Tugboats Through Operating Load Estimation. *IEEE Trans. Contr. Syst. Technol.* 23(6), 2375-2382.
- Wei, L., Geng, P., 2016. A review on natural gas/diesel dual fuel combustion, emissions and performance. *Fuel Processing Technology.* 142, 264-278.
- Wikipedia, 2020. <https://en.wikipedia.org/wiki/Observation>.
- WMO, 2019. Manual on Codes - International Codes - Volume I.1, Annex II to the WMO Technical Regulations, Part A - Alphanumeric Codes. World Meteorological Organization.
- Woschni, G., 1967. A universally applicable equation for the instantaneous heat transfer coefficient in the internal combustion engine. 670931. SAE Technical paper.
- Yasukawa, H., Hirata, N., Matsumoto, A., Kuroiwa, R., Mizokami, S., 2019. Evaluations of wave-induced steady forces and turning motion of a full hull ship in waves. *Journal of Marine Science and Technology.* 24(1), 1-15.
- Yasukawa, H., Sakuno, R., 2020. Application of the MMG method for the prediction of steady sailing condition and course stability of a ship under external disturbances. *Journal of Marine Science and Technology.* 25(1), 196-220.
- Yasukawa, H., Yoshimura, Y., 2015. Introduction of MMG standard method for ship maneuvering predictions. *Journal of Marine Science and Technology.* 20(1), 37-52.
- Yasukawa, H., Zaky, M., Yonemasu, I., Miyake, R., 2017. Effect of Engine Output on Maneuverability of a VLCC in Still Water and Adverse Weather Conditions., 1-13.
- Yoshimura, Y., Nomoto, K., 1978. Modeling of manoeuvring behaviour of ships with a propeller idling, boosting and reversing (in Japanese). *Journal of the society of naval architects of Japan.* 1978(144), 57-69.
- Yum, K.K., Skjong, S., Tasker, B., Pedersen, E., Steen, S., 2016. Simulation of a Hybrid Marine Propulsion System in Waves. CIMAC Congress 2016, Helsinki, Finland.
- Yum, K.K., Taskar, B., Pedersen, E., Steen, S., 2017. Simulation of a two-stroke diesel engine for propulsion in waves. *International Journal of Naval Architecture and Ocean Engineering.* 9(4), 351-372.
- Zaccone, R., Ottaviani, E., Figari, M., Altosole, M., 2018. Ship voyage optimization for safe and energy-efficient navigation: A dynamic programming approach. *Ocean Engineering.* 153, 215-224.
- Zaky, M., Sano, M., Yasukawa, H., 2018. Improvement of maneuverability in a VLCC by a high lift rudder. *Ocean Engineering.* 165, 438-449.
- Zhang, C., Liu, X., Wan, D., Wang, J., 2019. Experimental and numerical investigations of advancing speed effects on hydrodynamic derivatives in MMG model, part I:  $X_{vv}$ ,  $Y_v$ ,  $N_v$ . *Ocean Engineering.* 179, 67-75.
- Zhao, F., Yang, W., Tan, W.W., Yu, W., Yang, J., Chou, S.K., 2016. Power management of vessel propulsion system for thrust efficiency and emissions mitigation. *Applied Energy.* 161, 124-132.
- Zinner, K., 1978. Supercharging of internal combustion engines. Springer-Verlag, Berlin.

# Acknowledgements

Five years ago in October, 2016, it was the first time I came to the Netherlands, and also my first time going and studying abroad. The past five years of PhD study was not an easy journey, but it was definitely a meaningful one. During the past five years studying and living in the Netherlands, I have gained new knowledge, new skills, new experiences, new perspectives and most importantly I have met new friends from different countries with different culture background. I am so grateful to all the people who have helped, supported, encouraged, motivated and accompanied me over the past five years.

To begin with, I would like to express my profound gratitude to my supervision team: Prof.ir. Hans Hopman (promotor), Dr.ir. Peter de Vos (co-promotor and daily supervisor), Rear-Admiral (ME, ret) ir. Klaas Visser, and Prof.ir. Douwe Stapersma (retired). I would like to express my sincere appreciation to my promotor Prof.ir. Hans Hopman. Dear Professor Hopman, I am very grateful to you for giving me the opportunity to conduct my PhD research under your supervision. Thank you very much for your trust and support for my PhD research project. Your valuable comments and critical questions on the research project have helped me clarify my ideas and work in the right direction.

I would like to express my great appreciation to my co-promotor / daily supervisor Dr.ir. Peter de Vos. Dear Peter, thank you so much for your supervision and support during my PhD research. Under your supervision, the research has been able to continue successfully, and the two parts of the research project have been wonderfully connected with each other. Your valuable feedback, comments, and challenging questions have helped shape my ideas and motivated me during the research. The discussions with you are always encouraging and motivating, and have helped me conduct the research on the right track.

Without the help and support from Rear-Admiral (ME, ret) ir. Klaas Visser, I would not have the opportunity to pursue my PhD research in TU Delft. Dear Klaas, your valuable trust, support and encouragement for my PhD research are greatly appreciated. You have supervised me in setting my research topic, clarifying my ideas and formulating the research plan. Thank you for encouraging me to teach and giving me the opportunities to give lectures. I am very grateful that I have joined the Vulcanus Study Trip several times and have visited many companies in maritime and other innovative industries in different countries. The study trips led by you are very educational, eye-opening and full of fun, and I have learned and enjoyed a lot during these study trips.

My special and profound gratitude goes to Prof.ir. Douwe Stapersma. This work would not be possible without the support and help from Professor Stapersma. Prof. Stapersma was my supervisor when I was a guest PhD student in TU Delft working on the first part of my PhD project, and he has provided tremendous support and help to me during my research. Dear Professor Stapersma, I have so many reasons to express my sincere and great appreciation to you. I am very grateful for your supervision, guidance, teaching and help during my PhD study over the past five years. Your scientific excellence, profound knowledge, critical and rigorous

academic attitude have been inspiring me greatly and influencing me profoundly. I have learned and enjoyed a lot from our numerous discussions through face-to-face meetings and back-and-forth emails. Almost every week mainly on Thursday in the afternoon, sitting in front of two laptops, our discussions always last for multiple hours. You are always so patient, enthusiastic and full of energy. The discussions with you are always thought-provoking, enlightening, educational and informative.

My great appreciation goes to my committee members. Dear Prof. B.J. Boersma, Prof. J. Westerweel, Prof. Y. Li and Prof. B.O. el Moctar, thank you very much for the time and efforts that you have devoted to reviewing and assessing my draft thesis. I am looking forward to our discussions during the defence.

I would like to thank all my colleagues and friends in Section Ship Design, Production and Operations, for the wonderful working environment that you have created. Dear Dr. Milinko Godjevac, Dr. Arthur Vrijdag, Dr. Harsh Sapra, Dr. Lode Huijgens, Dr. Lindert van Biert, Dr. Rinze Geertsma, Nikos Vasilakis, my sincere gratitude goes to you. Thank you for being so friendly and helpful, and I appreciate all the chats, talks and discussions that we have during the coffee breaks, lunch time and meetings. Many thanks to our secretaries, Patty, Monique, Dineke, Pauline, Anouk and Gracia, for always being so kind and helpful.

Thanks to all my friends I met in the Netherlands for making my life here happy and colourful. Dear Jie Cai, Wenbin Ma, Wenjing Guo, Xiao Lin, Xiao Li, Kai Wang, Zongchen Li, Min Zhang, Xiuhan Chen, Yimeng Zhang, Zhe Du, Mingxin Li, Yunpeng Yan, Qinqin Zeng, Jian Tan, Tingkai Guo, Henk Polinder, Niek Tramper, Speeder, Haiyan Lu, Cunquan Qu, Yapeng Li, and many others, thank you for all the unforgettable experiences and fun time I had with you, such as travelling, cycling, sporting, having meals together, having parties, playing games, chatting and so on. Thanks to all my housemates and friends I have lived with during the past five years in the Netherlands. Dear Davide Galeotti, Mohammad Mirzaali, Haohua Zong, Manvika Singh, Zhi Hong, Xinyu Zhou, Xinmiao Du, Xiaojuan Zhang, Maolong Lyu, Wenyi Lu, Yihan Ouyang, thank you for the comfortable living environment you have created and the happy time we spent together.

I express my profound gratitude to Professor Yu Ding from Harbin Engineering University, China, who have helped me and supported me tremendously over the years since I was a master student. Dear Professor Ding, thank you so much for encouraging and supporting me to pursue my PhD study in the Netherlands.

My deepest gratitude goes to my parents, who have always been working so hard to provide a better life and education for me and my younger sister. Thank you so much for everything and forever!

Congbiao Sui

27 May, 2021

Delft, The Netherlands

# Curriculum Vitae

## Congbiao SUI 随从标

06-10-1989      Born in Fuyang, Anhui, China

### EDUCATION

2009 - 2013      Bachelor of Science in Marine Engineering  
Huazhong University of Science and Technology (HUST), Wuhan, China

2013 - 2015      Master of Engineering in Power Engineering  
Harbin Engineering University (HEU), Harbin, China

2016 - 2021      Doctor of Philosophy in Marine Engineering  
Delft University of Technology (TUD), Delft, the Netherlands

### Publications

1. **Sui, C.**, de Vos, P., Hopman, H., Visser, K., Stapersma, D., Ding, Y., 2021. Effects of Adverse Sea Conditions on Propulsion and Manoeuvring Performance of Low-Powered Ocean-Going Cargo Ship. *Submitted to a journal*.
2. **Sui, C.**, de Vos, P., Stapersma, D., Visser, K., Hopman, H., Ding, Y., 2021. Mean value first principle engine model for predicting dynamic behaviour of two-stroke marine diesel engine in various ship propulsion operations. *Submitted to a journal*.
3. **Sui, C.**, de Vos, P., Stapersma, D., Visser, K., Ding, Y., 2020. Fuel Consumption and Emissions of Ocean-Going Cargo Ship with Hybrid Propulsion and Different Fuels over Voyage. *Journal of Marine Science and Engineering*. 8(8)
4. **Sui, C.**, Stapersma, D., Visser, K., de Vos, P., Ding, Y., 2019. Energy effectiveness of ocean-going cargo ship under various operating conditions. *Ocean Engineering*. 190, 106473.
5. **Sui, C.**, Stapersma, D., Visser, K., Ding, Y., de Vos, P., 2019. Impact of Battery-Hybrid Cargo Ship Propulsion on Fuel Consumption and Emissions during Port Approaches. CIMAC Congress 2019, Vancouver, Canada.
6. **Sui, C.**, Song, E., Stapersma, D., Ding, Y., 2017. Mean value modelling of diesel engine combustion based on parameterized finite stage cylinder process. *Ocean Engineering*. 136, 218-232.